A methodology based on local resolution of turbulent structures for effective modeling of unsteady flows

by

Giancarlo Lenci

M.S., Energy Engineering, Sapienza University of Rome, 2010
M.S., Nuclear Science and Engineering, Massachusetts Institute of Technology, 2013

SUBMITTED TO THE DEPARTMENT OF NUCLEAR SCIENCE AND ENGINEERING
IN PARTIAL FULFILLMENT OF THE REQUIREMENTS FOR THE DEGREE OF

DOCTOR OF PHILOSOPHY IN NUCLEAR SCIENCE AND ENGINEERING
AT THE
MASSACHUSETTS INSTITUTE OF TECHNOLOGY

June 2016

Author: _____

Giancarlo Lenci
Department of Nuclear Science and Engineering
May 6, 2016

Certified by: _____

Emilio Baglietto, PhD
Norman C. Rasmussen Associate Professor of Nuclear Science and Engineering
Thesis Supervisor

Certified by: _____

Pierre F.J. Lermusiaux, PhD
Associate Professor of Mechanical Engineering
Thesis Reader

Certified by: _____

Neil E. Todreas, ScD
KEPCO Professor of Nuclear Science and Engineering, Emeritus
Thesis Reader

Accepted by: _____

Ju Li, PhD
Battelle Energy Alliance Professor of Nuclear Science and Engineering
Chairman, Department Committee for Graduate Students

A methodology based on local resolution of turbulent structures for effective modeling of unsteady flows

by

Giancarlo Lenci

Submitted to the Department of Nuclear Science and Engineering in partial fulfillment
of the Requirements for the Degree of

DOCTOR OF PHILOSOPHY
IN NUCLEAR SCIENCE AND ENGINEERING

ABSTRACT

Computational fluid dynamics (CFD) is widely adopted to predict complex flows and to inform the design of advanced engineering systems. In particular, the industry has seen a continuous growth of CFD simulations of turbulent phenomena, which has been made possible by the tremendous reduction achieved in cost per floating point operation. The need for accurate, yet computationally effective, transient methods has drawn particular attention to hybrid turbulence models, seeking to offer significant cost reduction over large-eddy simulation (LES). Despite promising results in academic test cases, the use of hybrid modeling is still scarce in general industrial simulations. Such a low adoption is mainly driven by limitations in the ability to provide accurate, robust, reliable, and grid-convergent solutions. Hybrid models are still far from presenting a viable replacement to unsteady Reynolds-averaged Navier-Stokes (URANS).

This work investigates the key weaknesses of current hybrid approaches and develops a novel modeling strategy to overcome selected shortcomings. Hybrid approaches have mostly focused on identifying regions of the flow where LES could be recovered, based for example on a comparison between grid and flow length scales. Conversely, the new approach aims at leveraging the robustness of URANS in suitable flow regions while introducing controlled eddy resolution in regions of poor URANS applicability. This drastic change in strategy focuses on avoiding the frequent failures observed for existing hybrid methods while still enabling the effective resolution of scales.

The formulation proposed identifies critical flow regions based on the absolute value of the second invariant of the resolved velocity gradient tensor. The variable retains several useful properties, including the capability to describe scale separation, deformation, shear flow, and coherent structures (*thus motivating the name STRUCT adopted for the new approach*). The method is implemented into a finite volume, general-purpose CFD solver and tested in unsteady flow applications on URANS-like grids. Results demonstrate the capability of the model to select regions of effective hybrid activation based on local flow variables. In all flow cases tested, the hybrid model activates in areas of strong flow deformation producing large resolved structures in the solution and generating enhanced description of low-frequency phenomena compared to URANS. This observation confirms the powerful consistency between regions of low URANS performance and highly deformed structures, and supports the potential of the STRUCT approach in applications requiring selective spectral information such as fluid-structure interaction analyses.

After a controlled evaluation of the model with fixed parameters specified before the simulation, two formulations are proposed to provide full closure: one based on a local averaging operator represented by a truncated Taylor series expansion, and a second one leveraging a Lagrangian differential operator to provide a smooth averaging. Both of those methods aim at providing viable averaged fields as needed by the STRUCT formulation while relying only on local operations for ensuring a low penalty on computational cost in parallel simulations. The former method determines the hybrid activation regions but still relies on a constant coefficient for reducing the modeled turbulent scales. On the other hand, the latter method assigns both conditions automatically.

In all simulation results, significant agreement with experimental data is achieved for the first and second central moments of the velocity components. These results illustrate the potential of the STRUCT approach to provide accurate LES-like predictions with a computational cost only about 10% higher than that of URANS while orders of magnitude lower than LES. The generality of the STRUCT approach is confirmed in applied work extending its applicability to real flow cases.

The controlled STRUCT approach demonstrates significant grid consistency properties while preventing strong error increase as the grid is coarsened beyond URANS convergence. The STRUCT methodology has the potential to revert to URANS in conditions of poor hybrid model applicability while future work can design LES retrieval at the fine-grid limit. Due to those robust properties and to the safe fail-to-URANS rationale, the STRUCT concept has the potential to achieve through future tests and developments a reliable enhancement over URANS.

Thesis Supervisor: Emilio Baglietto
Title: Norman C. Rasmussen Associate Professor of Nuclear Science and Engineering

Acknowledgments

My deep gratitude goes to my thesis supervisor Prof. Emilio Baglietto, for choosing me as one of his first Ph.D. students and for providing constant guidance to my work. His impressive expertise in advanced single-phase and multi-phase flow simulation makes him an international leader of CFD. Many people around the world contact him to find answers to hard questions, so I have been very lucky to receive his time and attention during my Ph.D. He encouraged my creative thinking while providing excellent suggestions to maintain my progress on a constructive track. His rigorousness at the beginning of my Ph.D. pushed me to work hard and learn fast while after the first months he gave me great intellectual independence. He managed to achieve financial support for my project through at least four different funding sources without distracting me from my target. He taught me how to combine the rigorous learning of existing subjects with the capability to walk safely away from the paved road, building on justified steps.

It is my deepest honor and pleasure to have Prof. Neil Todreas on my doctoral committee. His advice and guidance have been inspirational for me since my first days at MIT. He taught me many skills including technical, analytical, and human ones. On the technical side, he always challenged me with hard problems, in the review of his textbook, in coursework, and in his requests as supervisor of my MS thesis. From the analytical point of view, he always encouraged my critical thinking and investigative attitude, teaching me how to never lose focus on the big picture while diving deep into the needed details. On the human side, I learned from him to express my thoughts openly, seeking feedback from others to measure my progress and find ways to improve.

I would like to thank my committee member Prof. Pierre Lermusiaux for his support during my research update meetings. He listened carefully to my presentations and identified critical details that needed deeper analysis. He is capable of making every scientific discussion productive and pleasant at the same time. He transformed my fear of presenting new ideas to an expert into a proactive willingness to identify and fix the weaker points. He represents well the MIT mentality of reacting to a challenging problem with optimism and desire towards discovery.

I am very honored to have Prof. Michael Short serving as my Ph.D. committee chair. The insightful questions he asked during my defense presentation are strongly appreciated.

I would like to thank the MIT colleagues who collaborated more closely with me in my research: Michael Acton, Jingyong Zhang, Davide Concu, Pablo Ducru, Rami Abi Akl. It has been a great pleasure for me to engage in investigative thinking with all of those smart people. Many other colleagues have made interesting and well appreciated research discussions with me, including Etienne Demarly, Benjamin Magolan, Giulia Agostinelli, and Ravikishore Kommajosyula.

Many thanks to Sylvain Lardeau from CD-adapco for providing us with software access to implement and test the new turbulence model presented here in STAR-CCM+.

This work would have not been possible without the economic support that came from various institutions and sources. This includes funds deriving from the DOE-sponsored NEAMS project, TerraPower, AREVA, and the Theos J. Thompson Memorial Fellowship at MIT.

Many thanks to my colleagues who have administered the group's cluster, allowing me to always run simulations seamlessly. Among them: Etienne Demarly, Nazar Lubchenko, Gustavo Montoya, Ravikishore Kommajosyula, and Joseph Fricano.

I owe my gratitude to all of the NSE department's professors for being inspirational teachers. In particular, I had closer interaction with: Michael Golay, Kord Smith, Jacopo Buongiorno, and Richard Lester. The memory of Professor Mujid Kazimi is a source of guidance and encouragement for me, due to his great support to students, kindness, and high standards.

I would like to thank Uuganbayar Otgonbaatar and Dr. Yvan Caffari for inviting me to very pleasant research discussions on uncertainty analysis.

My appreciation extends to all of the other people in our CFD team for being very friendly and available for discussion at any time. In particular: Mariana Rodriguez, Rosemary Sugrue, Lindsey Gilman, Ethan Bates, Yongsoo Park, Xingang Zhao, Melanie Tétreault-Friend, Roberto Formento, Eugeny Sosnovsky. Thank you Alexandre Guion, Matteo Bucci, Leigh Ann Kesler, Cody Dennett, Koroush Shirvan, Rosemary Sugrue, and Michael Acton for your help in my presentation rehearsals.

During my first two years as a graduate student, some students from classes before mine gave me significant suggestions on how to handle my new challenging tasks at MIT. Among them, I would like to thank Stefano, Jake, Brittany, Koroush, and Youho. It has been exciting to serve as ANS student section co-President together with Lindsey Gilman. I would also like to recognize the great teamwork with Chris, Federico, Alessandra, Mariapaola, Giulia, Andrea, Tommaso, and Kevin in the MITaly student group. Moreover, it has been fun to teach an IAP class with Alexandre Guion on how to code smoothed particle hydrodynamics.

During my first years at MIT, I was fortunate to have a strong "extended" group or roommates: Oguzhan, Thomas, Andrea, Arshed, Ahmed, Georgios (×2), Francesco, Henry. On the other hand, towards the end of my PhD, I was blessed to meet great friends: Juan, Rami, Giulia, Paolo, Enrique. I am sure that some of these people will remain lifelong friends. My landlady Elena is one of the people who provided the greatest support to my work. Every time she saw me in a hurry for a deadline, she cooked a delicious meal for me to help me relax and save time. I would like to thank Rossella, Michele, Angelo, and Vetri, for their lovely company and pleasant dinners. Many other MIT friends have been supportive and inspirational during these years. Among them: Alessandro, Katia, Fabio, Geoffrey, Francesco, Nathan, Mihai, Sara.

My friends in Rome have always given me great encouragement: Alex, Luca, Serafino, Barbara, Francesca, Arianna, Claudia, Gonzalo, Giovanni, Andrea, Camilla, Giulia, and many others.

I would like to give special thanks go to my parents, Ruggero and Nilda. They provide me with love, attention, and support like no one else. Sometimes I made trips home that ended up coinciding with work deadlines. In those cases, my parents have been exceptional teammates, preparing food for me and letting me find everything ready so I could be productive and still enjoy my time with them. I would also like to thank my two exceptional brothers, Francesco and Luigi, for their friendly support.

No words are enough to express my gratitude to my loving, patient, and caring fiancée Valentina. I am lucky to have met such a smart and wonderful person with whom we can be at each other's side across the adventures of life. Planning my future with her gives me happiness and energy. I am very blessed to have her as a companion, a friend, and a person I love, respect, and trust.

This thesis is dedicated to the memory of my grandmother Maria Pia. She was a biology teacher who devoted much of her energy to her grandchildren. She has always been proactive in bringing me and my brothers new readings and walking us through the discovery of new museums and exhibits, giving us the priceless gift of love for learning.

Table of contents

List of figures

List of tables

Nomenclature

Acronyms and abbreviations

1UD	First-order upwind discretization scheme
2UD	Second-order upwind discretization scheme
ARSM	Algebraic Reynolds stress model
BCD	Bounded central differencing discretization scheme
CD	Central differencing discretization scheme
CFD	Computational fluid dynamics
CFL	Courant-Friedrichs-Lewy
CPU	Central processing unit
DDES	Delayed detached-eddy simulation
DES	Detached-eddy simulation
DES97	Initial formulation of detached-eddy simulation proposed in 1997
DNS	Direct numerical simulation
EARSM	Explicit algebraic Reynolds stress model
E-DDES	Embedded DDES
ELES	Embedded large-eddy simulation
FFT	Fast Fourier transform
FSI	Fluid-structure interaction
FSM	Flow simulation methodology
FV	Finite volume discretization technique
GG	Green-Gauss method
GIS	Grid-induced separation
GTRF	Grid-to-rod fretting
GUI	Graphical user interface
IDDES	Improved delayed detached-eddy simulation
ILES	Implicit LES
LDV	Laser Doppler velocimetry
LES	Large-eddy simulation
LHS	Left-hand side
LNS	Limited numerical scales
LSQ	Least squares
MIT	Massachusetts Institute of Technology
MT	Maximum-transport model for PANS
NLEVM	Nonlinear eddy-viscosity model
NVD	Normalized-variable diagram
OES	Organized-eddy simulation
PANS	Partially averaged Navier-Stokes
PDE	Partial differential equation
PITM	Partially integrated transport model
PIV	Particle image velocimetry
PRNS	Partially resolved numerical simulation
PTS	Pressurized thermal shock
RANS	Reynolds-averaged Navier-Stokes

RDT	Rapid-distortion theory
RHR	Residual heat removal system
RHS	Right-hand side
RMS	Root mean square
RNG	Renormalization group theory
SRS	Scale-resolving simulation
RSM	Reynolds stress models
S-A	Spalart-Allmaras turbulence model
SAS	Scale-adaptive simulation
SDM	Semi-deterministic method
SI	International System of Units (in French: Système International d'Unités)
SIMPLE	Semi-implicit method for pressure-linked equations
SGS	Subgrid scale
STRUCT	Structure-based resolution of turbulence
STRUCT-L	STRUCT-Local formulation
STRUCT-T	STRUCT-Transport formulation
TDR	Turbulence dissipation rate
TKE	Turbulent kinetic energy
TRANS	Turbulence-resolving RANS
URANS	Unsteady Reynolds-averaged Navier-Stokes
VITA	Variable-interval time average
VLES	Very large-eddy simulation
WAG	Window average gradient
WALE	Wall-adapting local eddy viscosity
WM-LES	Wall-modeled LES
ZT	Zero-transport model for PANS

Tensor notation

Most of the equations in this work describe tensors by using the index notation. As an example, parameters with two subscript indices, ij, indicate components of second-order tensors. In equations adopting the vector notation, bolded font indicates tensors, and non-bolded font indicates scalars.

Equations in index notation follow the Einstein summation convention. Thus, a repeated index in a single term implies summation of that term over all values of the index.

Accents, apices, and chevrons

Unless specified otherwise, accents, apices, and chevrons identify statistical operations. Those operations applied onto a generic instantaneous flow field, $\phi(\boldsymbol{x}, t)$, are indicated as follows:

- Instantaneous field: ϕ
- Resolved field: $\bar{\phi}$
- Residual field, i.e. deviation of the instantaneous field from the resolved one: $\phi'' \equiv \phi - \bar{\phi}$
- Time-averaged field: $\hat{\phi}$
- Deviation of the instantaneous field from the time-averaged one: $\phi' \equiv \phi - \hat{\phi}$
- Deviation of the resolved field from the time-averaged one: $\tilde{\phi} \equiv \bar{\phi} - \hat{\phi}$

Chevrons indicate a generic averaging operation defined on a case-by-case basis.

Nomenclature tables

The following tables define the notation used in the equations of this work. Units are reported in the International System of Units (SI).

Table I Notation: Latin alphabet characters

Notation	Unit	Description
A	m^2	Area
A	$-$	Model coefficient
A_{ij}	s^{-2}	Velocity gradient tensor
a	$-$	Generic coefficient
a_{ij}	$\mathrm{J\,kg}^{-1}$	Anisotropic part of residual stresses tensor
C	$-$	Courant number
C	$-$	Model coefficient
C_S	$-$	Smagorinsky constant
c_K	$-$	Kolmogorov's constant
c_v	$\mathrm{J\,Kg}^{-1}\mathrm{K}^{-1}$	Specific heat at constant volume
D	m	Characteristic linear size
d	m	Wall distance
d	$-$	Number of dimensions
E	$-$	Error
E^*	$-$	Normalized error
e_t	$\mathrm{J\,kg}^{-1}$	Total energy
F_i	$\mathrm{N\,kg}^{-1}$	Force-per-unit-mass vector
F	$-$	Control function
G	$-$	Convolution kernel
f	s^{-1}	Frequency
f	(varies)	Generic function
f_ε	$-$	PANS resolution control for ε
f_k	$-$	PANS resolution control for k
f_μ	$-$	Coefficient multiplying the eddy viscosity
g	(varies)	Generic function
H	m	Linear size
h	$-$	Activation parameter
II	s^{-2}	Second invariant of the velocity gradient tensor
Kn	$-$	Knudsen number

k	$\mathrm{J\,kg^{-1}}$	Turbulent kinetic energy
L	m	Generic distance, length scale, or integral length scale
L_{K}	m	Kolmogorov length scale
L_{M}	m	Mixing length
L_{vK}	m	Von Kármán length scale
l_i	$\mathrm{m\,s^{-2}}$	Lamb vector
N	$-$	Generic number
n_i	$-$	Unit normal vector
n	$\mathrm{s^{-2}}$	Turbulent charge
P_k	$\mathrm{W\,kg^{-1}}$	Production of turbulent kinetic energy
p	Pa	Static pressure
p_{m}	Pa	Modified pressure
Q	$\mathrm{s^{-2}}$	Q-criterion
q_i''	$\mathrm{W\,m^{-2}}$	Heat flux vector
R	$-$	Relaxation (or under-relaxation) factor
$\mathrm{R_T}$	$-$	Turbulent Reynolds number
Re	$-$	Reynolds number
r	$-$	Ratio of resolved-to-total turbulent kinetic energy
S_{ij}	$\mathrm{s^{-1}}$	Rate of strain tensor
S_κ	$\mathrm{m^3\,s^{-2}}$	Energy density per unit wavenumber
s	$-$	Source term
t	s	Time
T	K	Temperature
T	s	Generic time scale or integral time scale
T_{ij}^{D}	Pa	Deviatoric stress tensor
T_{K}	s	Kolmogorov time scale
U	$\mathrm{m\,s^{-1}}$	Generic velocity
u_i	$\mathrm{m\,s^{-1}}$	Velocity vector – components occasionally also noted as: (u, v, w)
V	$\mathrm{m^3}$	Volume
x_i	m	Position vector – components occasionally also noted as: (x, y, z)

Table II Notation: Greek alphabet characters

Symbol	Unit (SI)	Description
α	$-$	Coefficient
α	rad	Angle
β	$-$	Coefficient
β	rad	Angle
Δ	m	Computational cell size or other length
Δ_t	s	Time step or other time interval
δ_{ij}	$-$	Kronecker delta
ε	$\mathrm{W\,kg^{-1}}$	Turbulence dissipation rate
ζ	$-$	Normalized variable diagram in the bounded central differencing scheme
θ	(varies)	Generic flow field
κ	$-$	Von Kármán constant
$\varkappa$	$\mathrm{m^{-1}}$	Wavenumber
μ	Pa s	Dynamic molecular viscosity
μ_t	Pa s	Dynamic eddy viscosity
ν	$\mathrm{m^2\,s^{-1}}$	Kinematic molecular viscosity
ν_t	$\mathrm{m^2\,s^{-1}}$	Kinematic eddy viscosity
ρ	$\mathrm{kg\,m^{-3}}$	Density
σ	$-$	Blending function in the bounded central differencing scheme
σ	$-$	Turbulent Prandtl number
τ	(varies)	Generalized central moment
τ_{ij}	$\mathrm{J\,kg^{-1}}$	Stress tensor, or residual stress tensor[1] (formally a stress per unit density)
τ_w	Pa	Wall shear stress
υ	$\mathrm{m^2\,s^{-1}}$	Velocity fluctuation scale in turbulence models
ϕ	(varies)	Generic flow field or STRUCT reduction function
ψ	(varies)	Generic flow field
Ω_{ij}	$\mathrm{s^{-1}}$	Rate of rotation tensor
ω	$\mathrm{s^{-1}}$	Specific turbulence dissipation rate
ω_i	$\mathrm{s^{-1}}$	Vorticity vector

[1] The units of τ_{ij} are those of a stress per unit density, not those of a stress. This traditional definition is used here consistently with the notation used most commonly in the literature. See eq. (2.7) and (2.8).

1 Introduction

1.1 Motivation

The majority of flows of practical interest are characterized by turbulence, one of the largely unsolved problems in physics; as the Clay Mathematics Institute 1 Million $ Millennium Prize for the existence and smoothness problem states:

"Mathematicians and physicists believe that an explanation for and the prediction of both the breeze and the turbulence can be found through an understanding of solutions to the Navier-Stokes equations. Although these equations were written down in the 19th Century, our understanding of them remains minimal".

From the modeler's point of view, turbulence is a mathematical phenomenon whose challenge is embedded in those partial differential equations (PDEs). This Millennium Prize award has not been assigned yet. Current research in the pure mathematical field is challenging and important. Nevertheless, those studies often proceed in a direction that is not necessarily practical for the achievement of approximated predictions of measurable quantities.

The growing need for accurate prediction of turbulence cannot wait for the availability of usable analytical progress. Therefore, modelers resort to numerical analysis. We can learn about turbulence from direct numerical simulation (DNS) of one realization of the instantaneous flow, thus solving the discretized conservation equations through computational fluid dynamics (CFD). DNS has very stringent requirements regarding computational grid size and time step. The high computational cost makes DNS impractical in most cases, due to limitations in processing power and storage capability.

Due to the inapplicability of DNS to industrial applications, statistical representation is adopted to reduce computational cost while still obtaining the needed global parameters. The loss of information related to the use of statistics is compensated by the introduction of turbulence closures.

No turbulence closure is currently accepted as optimal for all applications. Different strengths and weaknesses exist for all models proposed in the literature. An experienced CFD analyst is expected to be capable of selecting the most appropriate model suited for a certain flow, geometry, set of boundary conditions, and computational power availability.

A tradeoff exists between characteristics of different models. The tradeoff is critical in the case of unsteady simulations of complex systems, in which computational constraints often force us to make unsatisfactory choices. Advances in turbulence modeling could lift this limitation and extend the performance of CFD in complex industrial flows. The present work proposes a new direction seeking to enhance the applicability of CFD in simulating complex systems.

1.1.1 Economic benefits of turbulence modeling advance

Advances in turbulence modeling can provide significant tangible benefits. Areas that can benefit from those advances include engineering, earth and atmospheric sciences, biology, medicine, plasma science, physics, and chemistry, and many others.

The cost for society associated with limitations in turbulence modeling capabilities is often not perceived in its full importance because it is distributed across multiple entities.

The list below contains examples of economic losses caused by turbulence modeling limitations:

- Need for excessive computational power to run costly simulations
- Need for numerous sets of experiments instead of less expensive calculations
- Need for experimental acquisitions to calibrate and validate application-specific industrial codes with limited universality
- Reduced efficiency of engineering systems, due to limited design optimization
- Reduced operating performance of systems, due to conservative engineering margins introduced to compensate for our reduced understanding of physical phenomena
- Limitations in the accuracy of weather forecast, resulting in enormous costs; for example, unpredicted natural disasters, event planning uncertainties, limited capability to plan routes

As an example of cost figures, in 2014, the national weather prediction service of the United Kingdom has planned for a £97 million (about $150 million) supercomputer to be used for the weather forecast.

The cost of computations has decreased over time together with advances in computer technology. This trend has allowed for the progressive opening of new frontiers in CFD. The combination of advancements in simulation methods and reduction in computational costs will likely lead to significant steps forward in prediction capability in future generations of CFD simulations.

1.2 Challenges

1.2.1 Turbulence modeling in engineering

During the 19th century, a split occurred in the field of fluid mechanics (Schlichting, 1979). At that time, PDEs describing fluid motion were applied in academia but not directly usable by engineers. The fast industrial development required the development of usable tools. This need led to the formation and growth of the engineering discipline of hydraulics. Such a discipline uses assumptions to derive simplified equations from the complete Navier-Stokes ones.

Generations of engineers have designed systems, including nuclear reactors, leveraging significant knowledge in the field of hydraulics and predicting single-phase and multiphase flows. Only in the last half-century, progress in computer science unwrapped the capability to leverage numerical solutions to PDEs. Those developments progressed in parallel with innovations in numerical schemes, turbulence modeling, and meshing. This progress has opened the way to more advanced predictions of physical phenomena; for example, drag, flow separation, vibration, heat transfer.

Understanding complex effects of turbulence is key to designing advanced systems. For example, the aircraft industry benefits of technologies enhancing the performance of components subject to turbulent flow. Winglets and chevron nozzles represent innovations reducing respectively aircraft drag and jet engine noise (Bargsten and Gibson, 2011).

The nuclear power field has been among the first ones to use CFD. However, the adoption of CFD in such an industry is still limited due to restrictions in computational power, efficiency, and robustness of numerical methods, and to the incomplete understanding of model limitations. Since we are currently at a turning point in which significant advances have been made in dealing with the first two challenges, it is imperative to revisit and address the modeling aspect.

The multidimensional capabilities of CFD, coupled to a reliable and efficient closure for turbulence have the potential to deliver to the nuclear engineering industry a versatile simulation tool,

leveraging local instantaneous flow and temperature field predictions. This feature supports technical advancements and allows to eliminate during the design phase failure mechanisms that have often plagued the current generation of reactors. Detailed local data are necessary for example to support the analysis of component vibrations, boron mixing, grid-to-rod-fretting (GTRF), pressurized thermal shock (PTS), thermal striping, and general fluid-structure interactions (FSI).

1.2.2 The potential of hybrid approaches to model turbulence

Let us imagine a CFD analyst having to simulate a turbulent flow. A key task is to select which turbulence model to use. Such a selection is needed because a universal model does not exist. The optimal choice depends on several factors and requires experience on strengths and weaknesses of different approaches.

A not fully inclusive list of factors to be considered in the selection comprises:

- Geometry
- Flow characteristics
- Boundary conditions
- Need for steady or unsteady simulation
- Level of detail needed
- Computational grid, if available: size and characteristics
- Computational resources
- Type of solver available
- Availability of experimental data for validation
- Required robustness
- Similarity of flow conditions with other known validated test cases, if applicable
- Type of physics, e.g. single phase, multiphase, multi-physics
- Experience of the CFD analyst, including personal biases

Here we focus on single-phase unsteady simulations. A starting point in this selection is the tradeoff between computational resources and accuracy. Let us observe the simplified diagram in Figure 1.1 below, in which accuracy is plotted in the y-axis and low computational cost in the x-axis. The two most important model groups for applications are Reynolds-averaged Navier-Stokes (RANS) or its unsteady counterpart (URANS), and large-eddy simulation (LES).

The plot, which refers to unsteady computations, assigns LES to the top-left quadrant and URANS to the lower-right one. In many typical engineering simulations, neither of those two points belong to a desirable zone of the plot. The URANS point is below such a zone, and the LES one lies to the left of it. In such a situation, the engineer is forced to select a turbulence model operating outside the most desirable range.

In many applications, the geometry is too large and the Reynolds number too high to leverage LES, so URANS is selected. For example, Menter (2012) has estimated that computational requirements in turbomachinery simulations increase by a factor of $10^5 - 10^7$ switching from URANS to LES.

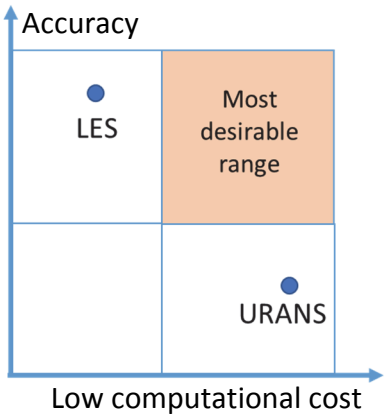

Figure 1.1 Simple diagram of the tradeoff between accuracy and low computational cost

The unsteady application of the RANS equations can describe averaged flow fields accurately when applied to simple flows. On the other hand, URANS is not applicable for flows in complex geometries or with fast-varying boundary conditions. Those cases violate the underlying assumption of URANS of scale separation between resolved and residual scales. In those cases, our CFD analyst could perhaps resort to LES, but the associated computational cost, and most importantly the very strict mesh quality and solution requirements make it in most cases not affordable for industrial simulations.

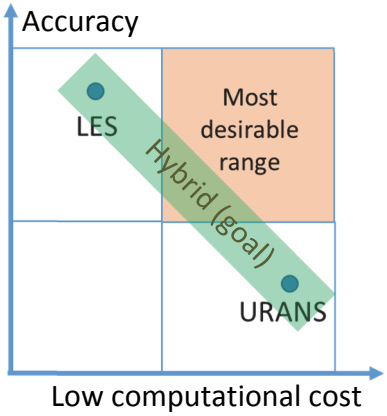

Figure 1.2 Accuracy vs. computational cost and goal of hybrid models

Hybrid models aim at bridging the gap between URANS and LES by controlling the amount of modeled turbulent kinetic energy. In Reynolds-averaged Navier-Stokes (RANS) simulations, all of the turbulent kinetic energy is modeled, while in DNS all thereof is resolved. In between those two extremes are URANS, hybrid models, and LES.

Equations for URANS and LES derive from different statistical assumptions but share significant similarities (Germano, 1999). Those similarities are leveraged in the derivation and implementation of hybrid models. Among the many hybrid models available in the literature, the most frequently encountered are: detached-eddy simulation (DES) (Spalart et al., 1997), embedded LES (ELES)

(Cokljat et al., 2009), scale-adaptive simulation (SAS) (Menter et al., 2003), and partially averaged Navier-Stokes (PANS) (Girimaji et al., 2003).

In the literature, there are many examples of simulations in which hybrid models appear to be successful in bridging URANS and LES, satisfying the condition in Figure 1.2. While those results confirm the potential benefits of hybrid models, a more general use of hybrid models beyond those known examples requires caution. The simplified two-dimensional viewpoint of Figure 1.2 does not show the full picture regarding the most important features of a model. Engineers cannot leverage a model, albeit accurate and low-cost, if it lacks other fundamental qualities.

Those additional qualities include numerical robustness, ease of implementation and use, and suitability for complex flows. Weaknesses observed in those domains explain why hybrid models have not achieved widespread adoption in engineering applications. In particular, undesirable behavior has occasionally been found in applications of hybrid models; for example, lack of grid convergence (Gant, 2010; Spalart, 2015) and generation of significant error (Davidson, 2006; Gritskevich et al., 2014; Smith et al., 2011). Users typically do not tolerate those downsides in industrial simulations – especially in cases implying a high risk or cost. In particular, engineering simulations for which experimental data are not available typically require, for quality control, grid convergence to a level not observed in current LES or hybrid models.

1.3 Proposing the STRUCT hybrid formulation

The present work proposes a new hybrid approach aimed at addressing selected shortcomings observed in current hybrid models, namely the lack of robustness, lack of consistent behavior when refining the grid, and low ease of use.

Like existing hybrid models, the new approach combines features of URANS and scale-resolving turbulence models. However, particular focus is placed upon robustness rather than on the capability of reaching full LES behavior. Therefore, the new strategy can be considered as defensive.

A key aspect of STRUCT is that unlike many existing hybrid approaches, it does not base its activation on the computational grid size, i.e. by detecting fine-grid regions suitable for an LES-like mode, rather it aims at resolving flow regions where the resolution is necessary, therefore basing its activation on flow quantities computed locally.

The model resolution is therefore controlled by comparison between resolved and modeled flow scales. The separation between those two scales results in suitable URANS application while their overlap triggers the hybrid formulation.

Resolved scales are quantified through a working parameter defined as the square root of the absolute value of the second invariant of the resolved velocity gradient tensor. Among the beneficial properties of such a parameter is the capability to identify scale separation, simple shear flow, and rapid distortion. Such a parameter is also closely related to quantities commonly used to detect coherent structures in flow solutions – hence, the name structure-based activation (STRUCT) was given to the new approach.

This work first introduces and demonstrates the applicability of the STRUCT concept in a controlled version, in which the model parameters are fixed a posteriori. This approach allows evaluating the strengths and weaknesses of the STRUCT resolution idea before introducing and validating the complete model formulations.

Validation is performed on specific flow cases which have evidenced clear limitations of existing hybrid approaches, and focus on addressing solution accuracy as well as robustness and computational cost. The baseline URANS closure for the STRUCT approach is the nonlinear eddy-viscosity k-ε model (NLEVM) proposed by Baglietto and Ninokata (2007, 2006), which offers an

advanced representation of turbulence anisotropy and, among other aspects, an enhanced capability to describe unsteady flow structures (Merzari et al., 2009).

The results presented confirm consistently improved predictions from the STRUCT solution in comparison to the baseline URANS solution, on the same coarse computational grids. The STRUCT concept shows robust generality and applicability to a wide range of flow conditions, and its fully complete implementation confirms good robustness on the tested flow cases. The model will require further evaluation on generally complex flow conditions to become a viable hybrid option for industrial applications.

1.4 Basic assumptions

1.4.1 Inherent assumptions of the equations of fluid motion

The instantaneous equations of fluid motion apply the conservation of mass, energy, and momentum to a control volume. The following basic assumptions are made:

- Continuum assumption. This assumption is acceptable for most flows of practical interest in engineering, which are characterized by a small Knudsen number.
- Non-relativistic assumption. In most engineering cases, velocities are by many orders of magnitude lower than the speed of light, so the validity of classical physics laws is assumed.

The notation used in equations is defined in the Nomenclature section. All flow fields are implied to be dependent on space and time, so velocity is $\boldsymbol{u} = \boldsymbol{u}(\boldsymbol{x}, t)$ and pressure is $p = p(\boldsymbol{x}, t)$. Let us write the Navier-Stokes equations in the notation used here.

The *momentum equation* is:

$$\frac{\partial \rho u_i}{\partial t} + \frac{\partial \rho u_i u_j}{\partial x_j} = -\frac{\partial p}{\partial x_i} + \frac{\partial T_{ij}^{\mathrm{D}}}{\partial x_j} + F_i \tag{1.1}$$

The *continuity equation* is:

$$\frac{\partial \rho}{\partial t} + \frac{\partial (\rho u_j)}{\partial x_j} = 0 \tag{1.2}$$

The *energy equation* is:

$$\frac{\partial \rho e_{\mathrm{t}}}{\partial t} + \frac{\partial \rho e_{\mathrm{t}} u_j}{\partial x_j} = -\frac{\partial p u_j}{\partial x_j} - \frac{\partial q_j''}{\partial x_j} + \frac{\partial u_i T_{ij}^{\mathrm{D}}}{\partial x_j} \tag{1.3}$$

where the total energy is a sum of internal and kinetic energy:

$$e_{\mathrm{t}} = c_v T + \frac{u_i u_i}{2} \tag{1.4}$$

1.4.2 Additional simplifying assumptions

It is often implied that the Navier-Stokes equations provide a full description of fluid motion, within domains consistent with their assumptions. In the description of turbulent flows, it is standard practice to make simplifications, to make the equations more manageable while preserving the relevant physics.

The following simplifying assumptions are made here, as often done in the literature (Nelkin, 1992):

- Incompressible flow
- Newtonian fluid, with constant isotropic molecular viscosity
- Negligible thermal effects
- Negligible effects of electric and magnetic fields

By applying those assumptions, we obtain the basic form of the equations used in this work. The deviatoric stress tensor in (1.1) and (1.3), representing viscous forces, becomes:

$$T_{ij}^{\mathrm{D}} = 2\mu S_{ij} \tag{1.5}$$

where the instantaneous strain rate is written, along with the rotation rate, as:

$$S_{ij} = \frac{1}{2}\left(\frac{\partial u_i}{\partial x_j} + \frac{\partial u_j}{\partial x_i}\right) \quad , \quad \Omega_{ij} = \frac{1}{2}\left(\frac{\partial u_i}{\partial x_j} - \frac{\partial u_j}{\partial x_i}\right) \tag{1.6}$$

Instantaneous equations are rewritten as shown below. Let us also assume no external forces, F_i.

The *momentum equation* becomes the following:

$$\frac{\partial u_i}{\partial t} + u_j \frac{\partial u_i}{\partial x_j} = -\frac{1}{\rho}\frac{\partial p}{\partial x_i} + \nu \frac{\partial^2 u_i}{\partial x_j \partial x_j} \tag{1.7}$$

The *continuity equation* is written, by considering the null density assumption, as a solenoidal field:

$$\frac{\partial u_j}{\partial x_j} = 0 \tag{1.8}$$

The energy equation is not needed anymore since thermal effects are neglected. The present work uses all the assumptions listed above and focuses on high-Re flows.

1.5 Thesis organization

The logical organization of this thesis moves through the following steps: identifying the challenge, proposing a solution, implementing it, and testing it. The Content for each chapter is outlined below:

Chapter 2 – Challenges of hybrid turbulence modeling

> The chapter focuses on the discussion of the overall challenge of hybrid turbulence modeling, both reviewing the underlying RANS closure and the hybridization concepts and briefly discussing strengths and limitations of relevant approaches.

Chapter 3 – Rationale and goals of the proposed method

> The chapter starts by discussing the limitations of current hybrid turbulence modeling, evidenced in fundamental flow cases. It then introduces the fundamental rationale and goals that have driven the new modeling work.

Chapter 4 – Proposing the STRUCT approach

> The novel STRUCT approach is introduced, starting from the selected objectives and constraints, and leading to its fundamental logic and mathematical formulation.

Chapter 5 – Numerical implementation

> The solver leveraged for the model implementation and validation is discussed, covering relevant details of the numerical methods and simulation approaches adopted.

Chapter 6 – Controlled model demonstration

The STRUCT approach is demonstrated in its controlled version, with variables optimized a posteriori. This validation allows us to separate the general features of the STRUCT approach from the influence of a specific implementation of its complete closure.

Chapter 7 – Complete local Taylor-expansion-based model STRUCT-L

A complete STRUCT approach is proposed and evaluated, where a local truncated Taylor series expansion approach is used to approximate the local flow averaging. The averaging is required to derive some of the model coefficients.

Chapter 8 – Complete transport-averaging-based model STRUCT-T

A transport-based-averaging complete STRUCT approach is proposed and validated in this chapter. The averaging operation used is based on a convective-diffusive transport equation and offers increased robustness and flexibility.

Chapter 9 – Conclusions

The conclusive chapter contains a summary of the thesis findings and a list of key contributions. Future scenarios are outlined, and additional work is suggested.

Appendix A – Additional discussions on equations

This appendix discusses key equations used in this thesis.

Appendix B – Applications of the STRUCT models

This appendix shows further collaborative validation of the STRUCT model closures in complex test cases. The focus is towards practical industrial applications.

Appendix C – Historical highlights

A summary of the historical importance of the concepts discussed in this thesis is included for reading pleasure.

Appendix D – STRUCT equations used here

The equations for the three STRUCT models presented in this work are summarized.

2 Challenges of hybrid turbulence modeling

2.1 Chapter overview

The proposed hybrid turbulence approach modifies an existing NLEVM URANS formulation by enabling local control of the ratio between resolved and modeled scales. Before introducing the method in Chapter 4, we focus on the two following chapters on the evidence and reasoning that have guided its development. We will first discuss why hybrid modeling is chosen over other strategies, what specific path has been selected, and what goals are being pursued.

Rationally, we start from identifying fundamental existing modeling strategies that have relevance for this work and describe their key features, objectives, and weaknesses. This discussion is provided in the present chapter. In the next chapter, we then combine concepts deriving from single models into overall ideas, identifying limitations of current hybrid and non-hybrid formulations, and defining a rationale for the new approach.

The present chapter begins with a discussion of a common statistical framework that can be leveraged to derive the mathematical formulation for many URANS, LES, and hybrid methods consistently. We then focus on the relevant examples in the three categories and highlight key features in their formulations, including how they can be leveraged and where they will fail.

2.2 Statistical description

The primary interest of the present work is in hybrid models, which are usually based on statistical operations combining the ensemble averaging of URANS and the partial averaging or filtering used in scale-resolving models. Let us devote this section to discussing a statistical framework that can be used to derive many hybrid and non-hybrid turbulence models.

Statistical operations are applied to the equations of fluid motion to reduce the computational burden of numerical solution over DNS, as identified in the seminal work by O. Reynolds (1895). In most engineering applications, we are not interested in the vast amount of information delivered by DNS. Even if such information were available, we would still need to apply statistical operations to gather averaged variables as useful to engineers. Using a metaphor borrowed from Borges (1999) and his short story "On Exactitude of Science", let us say that the full information of DNS is as useful to engineers as a map of an empire that is large like the empire itself. To reduce the computational cost requirements, turbulence models solve directly for statistical quantities instead of applying the statistics after the simulation. This averaging process results in an inevitable loss of information, which depends on the closure.

2.2.1 Applying no statistics: direct numerical simulation

Direct numerical simulation solves the Navier-Stokes equations for all scales of turbulence, with no need for additional models. DNS is practically limited to small geometries and moderate Re. Argyropoulos and Markatos (2014) estimated that simulation of a channel flow with Reynolds number 800,000 would require computational resources half a million times larger than a current generation's supercomputer. Computational cost increases sharply with the Reynolds number, being approximately proportional to $\mathrm{Re}^{11/4}$. The most stringent discretization requirements for DNS are

obtained directly by the Kolmogorov (1941) spatial and temporal scales, characteristic of the smallest eddies in the flow (in reality, it is shown (Moin and Mahesh, 1998) that this is not strictly necessary, and it is sufficient to resolve most of the dissipation):

$$L_K = \left(\frac{\nu^3}{\varepsilon}\right)^{1/4} \tag{2.1}$$

$$T_K = \left(\frac{\nu}{\varepsilon}\right)^{1/2} \tag{2.2}$$

In addition to those discretization requirements, the computational domain must be able to resolve the largest length scales. DNS results can be considered as deterministic "numerical experiments," generating one of the infinite possible realizations of turbulence, based on first principles. Results from DNS allow us to obtain information on the flow at a level of detail impossible to measure. Therefore, DNS is a valuable resource for the study of the fundamental physics of turbulence, assuming appropriate knowledge of the numerical error and the error associated with modeling assumptions.

2.2.2 Generalized statistical description

Let us introduce a generalized statistical description for the equations of fluid motion, following to a large extent the work by Germano (1992). This generalized description is valid for many RANS and LES closures, so it is suitable for hybrid models. Let us consider a linear and constant-preserving statistical operation that applies to flow fields and commutes with temporal and spatial differentiation. Such an operation is marked with an overbar. For two generic flow fields, ϕ and ψ, and a generic scalar, a, the condition for an operator to be linear and constant-preserving is (Germano, 1992):

$$\overline{\phi + \psi} = \bar{\phi} + \bar{\psi} \quad , \quad \overline{a\phi} = a\bar{\phi} \tag{2.3}$$

The condition of commutation with spatial and temporal differentiation is (Speziale, 1998):

$$\frac{\overline{\partial \phi}}{\partial x_\iota} = \frac{\partial \bar{\phi}}{\partial x_i} \quad , \quad \frac{\overline{\partial \phi}}{\partial t} = \frac{\partial \bar{\phi}}{\partial t} \tag{2.4}$$

The overbar operation has a different meaning in URANS and LES. It usually denotes ensemble averaging in URANS and spatial filtering by convolution of the velocity and pressure fields with a kernel $G_\Delta(x_i)$ in LES (Leonard, 1974). Let us only consider for LES linear commuting filters.

In LES, the *resolved* fields $\bar{u}_i$ and $\bar{p}$ are random, three-dimensional and unsteady, even in a statistically stationary and homogeneous steady flow. On the other hand, in a statistically stationary and homogeneous steady URANS case, resolved fields are steady and uniform (Pope, 2000). *Residual* fields are defined as the deviation between instantaneous and resolved fields:

$$\begin{aligned} u_i'' &= u_i - \bar{u}_i \\ p_i'' &= p_i - \bar{p}_i \end{aligned} \tag{2.5}$$

The terms resolved and residual are used in the present work instead of model-specific ones such as "mean", "fluctuating", "filtered". Definitions are kept general and apply to both URANS and LES, thereby being suitable for hybrid models. The statistical operation marked with an overbar can be applied to the whole equations for momentum and mass conservation. The resulting *resolved continuity equation* is:

$$\frac{\partial \bar{u}_j}{\partial x_j} = 0 \tag{2.6}$$

The instantaneous continuity equation is linear, while the momentum equation contains the nonlinear convective term, making the averaging operation more complex and introducing unknowns. It is common practice to introduce a *residual stress tensor*, which is symmetric and defined as follows:

$$\tau_{ij} \equiv \overline{u_i u_j} - \bar{u}_i \bar{u}_j \tag{2.7}$$

We can rearrange the *resolved momentum equation* in a way that resembles the instantaneous one:

$$\frac{\bar{\mathrm{D}}\bar{u}_i}{\bar{\mathrm{D}}t} = -\frac{1}{\rho}\frac{\partial \bar{p}}{\partial x_i} + \nu \frac{\partial^2 \bar{u}_i}{\partial x_j \partial x_j} - \frac{\partial \tau_{ij}}{\partial x_j} \tag{2.8}$$

where the material derivative marked with an overbar is defined, based on resolved velocity, as:

$$\frac{\bar{\mathrm{D}}\psi}{\bar{\mathrm{D}}t} = \frac{\partial \psi}{\partial t} + \bar{u}_j \frac{\partial \psi}{\partial x_j} \tag{2.9}$$

The only differences between the averaged momentum equation in (2.8) and the instantaneous one are the overbar operation on velocity and pressure, and the residual stress term. The residual stress tensor is not a real physical stress. It represents the transfer of momentum into the resolved flow due to acceleration in the residual velocity field. Strictly speaking, considering units and sign, the residual stress tensor should be: $-\rho\tau_{ij}$. However, this work uses the traditional nomenclature: τ_{ij}. The system described above has 4 equations and 10 unknowns. Engineering closures are sought after to obtain the 6 missing pieces of information. The residual stress tensor can be interpreted in a more general way, following Germano (1992), through the concept of generalized central moment. The second- and third-order generalized central moments for two generic variables are defined respectively as:

$$\tau(\phi, \psi) = \overline{\phi\psi} - \bar{\phi}\bar{\psi} \tag{2.10}$$

$$\tau(\phi, \psi, \theta) = \overline{\phi\psi\theta} - \bar{\phi}\tau(\psi, \theta) - \bar{\psi}\tau(\theta, \phi) - \bar{\theta}\tau(\phi, \psi) - \bar{\phi}\bar{\psi}\bar{\theta} \tag{2.11}$$

Higher-order moments can be defined using the same logic. The residual stress tensor is:

$$\tau_{ij} = \tau(u_i, u_j) \tag{2.12}$$

Due to our limited analytical understanding of the Navier-Stokes equations, turbulence closures do not rely purely on mathematical derivations. Rather, they leverage a combination of physics-based assumptions, semi-empirical correlations, dimensional analysis, and experience. Let us assume a flow case in which boundary conditions do not vary with time. We can define the time-averaged velocity as $\hat{u}_i$. The instantaneous velocity follows a triple decomposition:

$$u_i = \underbrace{\hat{u}_i + \overbrace{\tilde{u}_i}^{u_i'}}_{\bar{u}_i} + u_i'' \tag{2.13}$$

The same reasoning made above for the three velocity components is applied to pressure. The accents describing the terms in the triple decomposition are defined in the nomenclature section.

2.2.3 Residual stress evolution and generalized turbulence energy

The assumption of a linear, constant preserving and commuting averaging operation allows expanding the residual stresses analytically.

The following exact transport equation for the residual stresses is obtained from the equations and properties introduced so far (Germano, 1992):

$$\frac{\bar{\mathrm{D}}}{\bar{\mathrm{D}}t}\tau(u_i,u_j) = -\frac{\partial}{\partial x_k}\left(\tau(u_i,u_j,u_k) + \tau(p,u_i)\delta_{jk} + \tau(p,u_j)\delta_{ik} - \nu\frac{\partial}{\partial x_k}\tau(u_i,u_j)\right) + 2\tau(p,S_{ij}) - \left(\tau(u_i,u_k)\frac{\partial \bar{u}_j}{\partial x_k} + \tau(u_j,u_k)\frac{\partial \bar{u}_i}{\partial x_k}\right) - 2\nu\tau\left(\frac{\partial u_i}{\partial x_k},\frac{\partial u_j}{\partial x_k}\right) \tag{2.14}$$

The RHS terms of this equation are discussed here briefly.

- The first term defines the transport of residual stresses due to the effects of turbulence, the correlation between velocity and pressure fluctuations, and viscosity.
- The second term defines the pressure-rate-of-strain relation. Being traceless, it does not affect the total amount of energy transferred, but only the energy distribution between components of the residual stresses.
- The third term defines production of residual stresses from resolved velocity gradients. This term only involves quantities known during the calculation and does not require modeling.
- The last term describes the viscous dissipation of residual stresses.

The LHS of this equation yields the six independent components of the residual stresses. However, its RHS introduces 75 new unknowns (George, 2010). Expressions like in (2.14) carry the advantage of allowing physical interpretation of all terms. Nevertheless, the increase in unknowns makes the closure problem more complex. Due to this increase in complexity, the present work does not follow the approach of increasing the order of the statistical analysis.

A generalized residual turbulent kinetic energy can be defined as follows:

$$k \equiv \frac{1}{2}\tau_{kk} \tag{2.15}$$

Following Germano (1992), a transport equation for k is derived by combining (2.15) and (2.14):

$$\frac{\bar{\mathrm{D}}k}{\bar{\mathrm{D}}t} = -\frac{\partial}{\partial x_k}\left(\frac{1}{2}\tau(u_i,u_i,u_k) + \tau(p,u_k) - \nu\frac{\partial k}{\partial x_k}\right) - \tau(u_i,u_k)\bar{S}_{ik} - \nu\tau\left(\frac{\partial u_i}{\partial x_k},\frac{\partial u_i}{\partial x_k}\right) \tag{2.16}$$

This equation is important in turbulence modeling. Let us describe the meaning of the RHS terms.

- The first term describes the transport of generalized residual turbulent kinetic energy due to the effects of turbulent fluctuations, of the correlation between velocity and pressure fluctuations, and of molecular viscosity.
- The second term describes the production of generalized residual turbulent kinetic energy from resolved velocity gradients.
- The third term describes the dissipation rate of generalized residual turbulent kinetic energy due to viscous effects. Those effects generate heat. Such a term is also called turbulence dissipation rate ε and has the dimensions of an energy per unit mass and time.

The resolved rate of strain and rate of rotation tensors are defined analogously to their instantaneous counterparts in (1.6):

$$\bar{S}_{ij} = \frac{1}{2}\left(\frac{\partial \bar{u}_i}{\partial x_j} + \frac{\partial \bar{u}_j}{\partial x_i}\right) \quad , \quad \bar{\Omega}_{ij} = \frac{1}{2}\left(\frac{\partial \bar{u}_i}{\partial x_j} - \frac{\partial \bar{u}_j}{\partial x_i}\right) \tag{2.17}$$

2.2.4 Closures and Boussinesq eddy-viscosity assumption

Nearly[2] all turbulence closures provide equations to determine the six independent residual stresses based on known or derived flow parameters. Physical and numerical requirements of a closure are discussed in the next chapter, in Section 3.6.3.

The residual stress tensor τ_{ij} is a second-order symmetric tensor. It can be decomposed into the sum of an isotropic part, depending on k, and a traceless part, a_{ij}.

$$\tau_{ij} = \frac{1}{3}\tau_{kk}\delta_{ij} + a_{ij} = \frac{2}{3}k\delta_{ij} + a_{ij} \tag{2.18}$$

A simple yet common way of closing a_{ij} is the Boussinesq eddy-viscosity assumption, which relates a_{ij} to the resolved rate of strain, $\bar{S}_{ij}$, through the eddy viscosity ν_t (Boussinesq, 1877).

$$a_{ij} = -\nu_\mathrm{t}\left(\frac{\partial \bar{u}_i}{\partial x_j} + \frac{\partial \bar{u}_j}{\partial x_i}\right) = -2\nu_\mathrm{t}\bar{S}_{ij} \tag{2.19}$$

The assumption of residual stress anisotropy being aligned with resolved strain rate is not supported by experimental evidence (Pope, 2000). This weakness explains significant limitations of such an approach, although its simplicity and numerical stability justify its industrial success. Models implying a higher order of approximation are described in Section 2.3.6.

The features of the linear eddy-viscosity assumption can be discussed by combining its definition with the resolved momentum equation:

$$\frac{\bar{\mathrm{D}}\bar{u}_i}{\bar{\mathrm{D}}t} = -\frac{1}{\rho}\frac{\partial \bar{p}_\mathrm{m}}{\partial x_i} + (\nu + \nu_\mathrm{t})\frac{\partial^2 \bar{u}_i}{\partial x_j \partial x_j} \tag{2.20}$$

where the modified pressure $\bar{p}_\mathrm{m}$ is defined by lumping static pressure and the isotropic part of the residual stress tensor:

$$\bar{p}_\mathrm{m} = \bar{p} + \frac{1}{3}\tau_{kk} \tag{2.21}$$

Formulation for resolved momentum in (2.20) is similar to that for the instantaneous momentum, except for the overbar in the velocity and pressure fields, for the modified pressure, and for the enlarged viscous term. The enlarged viscosity in the Boussinesq assumption is the sum of molecular and eddy viscosity. The latter describes the momentum transfer between residual turbulence and resolved scales using the same simple formula as for molecular viscosity. However, while the definition of molecular viscosity leverages the significant separation between the scales of molecular interactions and those of the flow, this condition does not apply to turbulence. Indeed, the size of turbulent eddies can be of the same order of magnitude as flow scales.

2.3 Reynolds-averaged Navier-Stokes

Most hybrid approaches, including the one proposed here, are based on URANS equations, which represent a fundamental starting point of the present work. Let us now discuss the operations needed

[2] Practical solutions do not need the full residual stress tensor with its 6 independent components. They just need its divergence, which has 3 components (Perot, 1999; Wu and Zhou, 1996).

to derive the URANS equations. As already mentioned, in this work we mainly refer to URANS instead of RANS, since we focus on unsteady simulations.

2.3.1 Ensemble averaging

A fluid is a complex system, and we are unable to predict the instantaneous position and velocity of every molecule. However, we can model averaged properties. An assumption is that a fluid has many states all equally likely, and all of those states produce the same averaged properties. If copies of the system are taken, each state will appear for an equal number of times. Copies are called ensemble, and averaged properties are obtained through the ensemble average.

Properties of the ensemble averaging operation lead to decomposition of velocity into a random and a non-random part. The Reynolds averaging statistical operation has specific properties in addition to those already discussed for the generic overbar operation. Those properties are (Speziale, 1991):

$$\overline{\phi''} = \overline{\psi''} = 0 \tag{2.22}$$

$$\overline{\phi\psi} = \bar{\phi}\bar{\psi} + \overline{\phi''\psi''} \tag{2.23}$$

$$\overline{\phi''\bar{\psi}} = \overline{\psi''\bar{\phi}} = 0 \tag{2.24}$$

By applying the property directly in (2.23) to the equation for the residual stress tensor, such a tensor can be reformulated as the covariance of residual fluctuations:

$$\tau_{ij} = \overline{u_i''u_j''} \tag{2.25}$$

In this case, the residual stress tensor is called Reynolds stress tensor.

2.3.2 Reynolds stress evolution

The use of transport equations for the six independent Reynolds stress components is a starting point for the derivation of many turbulence models. Closure of such an equation was first proposed by Rotta (1951). This equation is an extension of (2.14) that takes into account the additional properties of Reynolds averaging mentioned above:

$$\begin{aligned}\frac{\bar{\mathrm{D}}}{\bar{\mathrm{D}}t}\overline{u_i''u_k''} = &-\frac{\partial}{\partial x_j}\left(\overline{u_i''u_j''u_k''} + \frac{1}{\rho}\left(\overline{p''u_k''}\delta_{ij} + \overline{p''u_j''}\delta_{kj}\right) - 2\nu\left(\overline{S_{ij}u_k''} + \overline{S_{kj}u_i''}\right)\right) \\ &\overline{\frac{p''}{\rho}\left(\frac{\partial u_i''}{\partial x_k} + \frac{\partial u_k''}{\partial x_i}\right)} - \left(\overline{u_i''u_j''}\frac{\partial \bar{u}_k}{\partial x_j} + \overline{u_k''u_j''}\frac{\partial \bar{u}_i}{\partial x_j}\right) - 2\nu\left(\overline{S_{ij}\frac{\partial u_k''}{\partial x_j}} + \overline{S_{kj}\frac{\partial u_i''}{\partial x_j}}\right)\end{aligned} \tag{2.26}$$

The terms in the RHS of the equation can be interpreted analogously to (2.14).

Turbulence closures require Reynolds stresses to be determined based on known flow parameters. A distinction can be made (Shih et al., 1993) between Reynolds stress *algebraic* equation models and *Reynolds stress transport* equation models. In the former, Reynolds stresses are related algebraically to the mean flow field. This relation can be applied with the aid of transported parameters defining general local properties of turbulence. In the latter models, Reynolds stresses are computed using transport equations for each component. This work focuses on algebraic models, which serve many practical applications. Discussion on Reynolds stress transport models is made briefly in Section 2.3.6, explaining why those approaches are not selected here.

2.3.3 Turbulent kinetic energy

In the case of URANS, all turbulent fluctuations are modeled. Therefore, the generalized turbulence energy shown in (2.15) is called turbulent kinetic energy (TKE). It represents the fluctuating energy per unit mass. By applying the property in (2.25) we obtain:

$$k \equiv \frac{1}{2}\tau_{kk} = \frac{1}{2}\overline{u_k'' u_k''} \tag{2.27}$$

A transport equation for k is obtained directly from (2.26) and (2.27).

$$\frac{\overline{\mathrm{D}}k}{\overline{\mathrm{D}}t} = -\frac{\partial}{\partial x_j}\left(\frac{1}{2}\overline{u_i'' u_i'' u_j''} + \frac{1}{\rho}\overline{p u_j''} - \nu\frac{\partial k}{\partial x_j}\right) - \overline{u_i'' u_j''}\frac{\partial \bar{u}_i}{\partial x_j} - \nu\overline{\frac{\partial u_i''}{\partial x_j}\frac{\partial u_i''}{\partial x_j}} \tag{2.28}$$

The meanings of the terms in the equation above are analogous to those described for (2.15).

2.3.4 Steady and unsteady RANS

The Reynolds-averaged equations have been conceived initially (Reynolds, 1895) to be solved numerically assuming steady-state conditions. Industrial applications of turbulence models often involve flows characterized by strong unsteadiness for which it is not possible to leverage RANS. In many of those cases, unsteady RANS is the only choice (Spalart, 2000). The URANS approach comes with strong limitations, as discussed extensively in the remainder of this work.

2.3.5 Overview of industrial-strength URANS closures

Before moving into the specific URANS adopted here, it is worth briefly reviewing alternative approaches that could offer, in particular, applications and flow conditions, advantages that might make them preferred candidates for hybrid applications.

We start from linear eddy-viscosity closures, which leverage the Boussinesq assumption, benefiting of its simplicity but carrying fundamental limitations. By making such an assumption, the closure is left with only one variable to be determined: the eddy viscosity. A model is needed to predict the eddy viscosity based on other known flow variables. Let us keep in mind that even an optimal evaluation of the eddy viscosity under this simplification does not translate into perfect results, due to the assumption that the Reynolds stresses be aligned with the resolved strain rate.

Kinematic eddy viscosity has the units of length squared over time or equivalently velocity multiplied by length. Its formulation is often derived from dimensional arguments. An example of the time-averaged eddy viscosity in a pipe flow is shown in Figure 2.1 (left line).

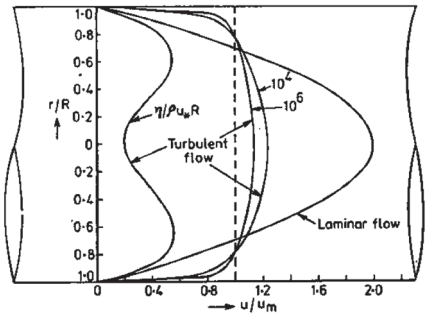

Figure 2.1 Mean eddy-viscosity and velocity profiles in a pipe flow, from Garde (1997)

Spalart-Allmaras model

The S-A model (Spalart and Allmaras, 1992) transports a working variable that has the units of a viscosity and is used to determine the eddy viscosity directly. This variable is purposely designed to eliminate the nonlinear behavior in the near-wall region by including a wall-distance-dependent correction. This characteristic makes the model particularly simple to solve and exhibits optimal numerical convergence. The model is particularly popular when a fast and coarse analysis is needed.

The terms in the original S-A model have been specifically developed for attached external flow applications, where the commonly adopted production term is for example simply proportional to the flow vorticity. It is not surprising therefore if the model does not generally demonstrate accuracy in flows with massive separation.

The Spalart-Allmaras model offers an excellent demonstration of the capability to obtain an accurate engineering solver using just one transport equation. Many alternative versions of the model have been proposed in the literature. The S-A model finds successful applications, especially in the aerospace and turbomachinery industry. However, it shares the downsides of models based on isotropic eddy viscosity, and its strengths are mainly limited to external flow applications.

Standard k-ε model

Many authors in the literature support the flow description of two-equation models, which are also widely used in industry. Debate exists in the literature on whether having two transport equations is the minimum requirement for a turbulent model to capture the strong variations that occur in turbulence both in length and in time scales (Gatski and Speziale, 1993; Spalart, 2015). The standard k-ε is one of the most widely used turbulence models in engineering applications. This success is due in part to its simplicity and robustness, and in part to the wide industrial experience accumulated over time. The model was first proposed by Jones and Launder (1972). It was then calibrated in its coefficients by Launder and Sharma (1974).

The scales of turbulence used to specify the eddy viscosity are the TKE and the turbulence dissipation rate (TDR), i.e. the dissipation of turbulent kinetic energy into heat that occurs at the molecular level per unit time. The eddy viscosity formulation is:

$$\nu_\mathrm{t} = C_\mu \frac{k^2}{\varepsilon} \tag{2.29}$$

The two following transport equations are used for TKE and TDR:

$$\frac{\overline{\mathrm{D}}k}{\overline{\mathrm{D}}t} = \frac{\partial}{\partial x_j}\left[\left(\nu + \frac{\nu_\mathrm{t}}{\sigma_k}\right)\frac{\partial k}{\partial x_j}\right] + P_k - \varepsilon \tag{2.30}$$

$$\frac{\overline{\mathrm{D}}\varepsilon}{\overline{\mathrm{D}}t} = \frac{\partial}{\partial x_j}\left[\left(\nu + \frac{\nu_\mathrm{t}}{\sigma_\varepsilon}\right)\frac{\partial \varepsilon}{\partial x_j}\right] + (C_{\varepsilon 1}P_k - C_{\varepsilon 2}\varepsilon)\frac{\varepsilon}{k} \tag{2.31}$$

The TKE equation was derived from the exact one in (2.28), except for the following assumption leveraging a gradient-diffusion hypothesis (Pope, 2000):

$$\frac{1}{2}\overline{u_i'' u_i'' u_j''} + \frac{1}{\rho}\overline{p u_j''} = -\frac{\nu_\mathrm{t}}{\sigma_k}\frac{\partial k}{\partial x_j} \tag{2.32}$$

Such an assumption neglects, among other things, accurate description of the correlation between velocity and pressure fluctuations. The TDR equation in (2.31) has not been derived directly from the exact equation but from the assumption of analogy with the TKE equation. This assumption is often made because of the complexity of the terms in the exact TDR equation (Shih et al., 1995). It is also assumed that the production and dissipation of TDR are proportional to those of TKE, multiplied by ε/k. The terms in round brackets in (2.30) and (2.31) are the diffusivities of k and ε.

Those diffusivities are formulated as molecular viscosity plus the ratio between eddy viscosity and the turbulent Prandtl numbers for k and ε.

The term describing TKE production is:

$$P_k = -\tau_{ij}\frac{\partial \bar{u}_i}{\partial x_j} \tag{2.33}$$

The model coefficients, shown in Table III, have been determined empirically based on measurements on equilibrium boundary layers and studies on the decay of isotropic turbulence (Speziale, 1991). That set of coefficients is widely used and thus considered standard for the basic k-ε model, hence the name standard k-ε.

Table III Standard k-ε model coefficients

C_μ	σ_k	σ_ε	$C_{\varepsilon 1}$	$C_{\varepsilon 2}$
0.09	1.0	1.3	1.44	1.92

The standard k-ε has the advantage of having a vast experience accumulated in industry. It also demonstrates high robustness, which makes it desirable in several engineering applications. The main downside is the excessive eddy viscosity produced by this model in complex strains. This results for example in poor behavior in test cases involving any separation (Wilcox, 1993) and in early reattachment. The same cause produces reduced accuracy in jets, severe pressure gradients, streamline curvature, rotation, swirl. The extensive use of this model can be considered as a tradeoff between the error introduced and the inherent robustness.

Realizable k-ε model

The term *realizable* in turbulence modeling refers to the capability to satisfy mathematical constraints ensuring that physical requirements be respected. The concept was introduced by Schumann (1977) and then extensively discussed by Lumley (1978). Here are the requirements.

- The three fluctuating components that make turbulent kinetic energy must be positive:

$$\tau_{ij} \geq 0 \quad \text{for} \quad i = j \tag{2.34}$$

- The Cauchy-Schwarz inequality must be respected. The Einstein summation convention is not applied in the equation below:

$$\tau_{ij}^2 \leq \tau_{ii}\tau_{jj} \quad \text{for} \quad i \neq j \tag{2.35}$$

- As stated by Schumann (1977), the Reynolds stress tensor must be real:

$$\det(\tau_{ij}) \geq 0 \tag{2.36}$$

A variant of the standard k-ε model known as the realizable k-ε has been proposed by Shih and co-workers (1995). The model modifies the standard k-ε by applying realizability and by introducing sensitivity to vortex stretching and dissipation. Eddy viscosity is calculated in the same way as for the original model, i.e. (2.29), but the C_μ coefficient varies, making the model realizable, as:

$$C_\mu = \frac{1}{A_0 + A_s \frac{k}{\varepsilon} f_{\mathrm{re}}} \tag{2.37}$$

A common implementation of parameter f_{re} is:

$$f_{\mathrm{re}} = \sqrt{\bar{S}_{ij}\bar{S}_{ij} + \bar{\Omega}_{ij}\bar{\Omega}_{ij}} \tag{2.38}$$

The two model coefficients in the denominator of (2.37) are $A_0 = 4$ and:

$$A_s = \sqrt{6}\cos\left(\frac{1}{3}\mathrm{acos}\left(\sqrt{6}\bar{S}_{ij}\bar{S}_{jk}\bar{S}_{ki}\left(\bar{S}_{ij}\bar{S}_{ij}\right)^{-1/3}\right)\right) \tag{2.39}$$

The transport equation for k is the same as for the standard k-ε while a different formulation is used in the equation for ε. The different relation introduced is derived from the exact dynamic equation for the resolved square vorticity fluctuation, through simplifying assumptions including high Reynolds number (Shih et al., 1995). This feature of the realizable k-ε allows the model to overcome partially limitations of isotropic eddy-viscosity closures. This choice results in advantages over the standard k-ε in several complex flows, including those involving a round jet, separation or swirl. Due to these advantages, the realizable k-ε is widely used for industrial simulations of internal flows. The model is not suitable in cases in which greater flow description is sought after, as achievable using higher-order or nonlinear closures.

Wilcox k-ω model

The present work is based on the selection of the k-ε framework, due to its proven robustness in internal flows. Another popular family of eddy viscosity models is instead the k-ω type. The following definition is often used for the specific turbulence dissipation rate:

$$\omega = \frac{\varepsilon}{\beta^* k} \tag{2.40}$$

Such a parameter is a rate of dissipation of TKE per unit volume, which has the units of $[\mathrm{s}^{-1}]$.The idea of transporting ω in a turbulence model dates back to Kolmogorov (1942). The same choice has been made by Wilcox (1988) in a successful model considered as a standard k-ω formulation. That model has the advantage of being physically valid in the resolved boundary layer, not requiring the use of viscous damping functions near the wall as for the k-ε. Eddy viscosity is expressed as:

$$\nu_{\mathrm{t}} = \frac{k}{\omega} \tag{2.41}$$

The transport equations used for k and ω are:

$$\frac{\bar{\mathrm{D}}k}{\bar{\mathrm{D}}t} = \frac{\partial}{\partial x_j}\left[\left(\nu + \frac{\nu_{\mathrm{t}}}{\sigma_k}\right)\frac{\partial k}{\partial x_j}\right] + \tau_{ij}\frac{\partial \bar{u}_i}{\partial x_j} - \beta^* k\omega \tag{2.42}$$

$$\frac{\bar{\mathrm{D}}\omega}{\bar{\mathrm{D}}t} = \frac{\partial}{\partial x_j}\left[\left(\nu + \frac{\nu_{\mathrm{t}}}{\sigma_\omega}\right)\frac{\partial \omega}{\partial x_j}\right] + \alpha\frac{\omega}{k}\tau_{ij}\frac{\partial \bar{u}_i}{\partial x_j} - \beta\omega^2 \tag{2.43}$$

Model coefficients are in Table IV.

Table IV k-ω model coefficients

α	β^*	β	σ_k	σ_ω
5/9	9/100	3/40	2	2

Among the multiple k-ω model formulations, the one described above is probably the most tested in the literature and practical applications. It provides partial advantages over the k-ε in wall-bounded flows with mild pressure gradients, including adverse ones producing separation. The model is built

to be sensitive to adverse pressure gradients to capture separation, but this leads to overestimated levels of shear stress, and underestimated levels of turbulent kinetic energy in simple strains. The difference between results in the k-ε and k-ω models derives from the extra term that appears in the ω equation when writing the k-ε model in k-ω form (Pope, 2000):

$$+\frac{2\nu_t}{\sigma_\omega k}\nabla\omega \cdot \nabla k \tag{2.44}$$

The most notable downside of the original k-ω model is its sensitivity to the "freestream" inlet boundary conditions for turbulence levels (Wilcox, 1993). Conversely, the k-ε appears to provide stable results with respect to the inlet conditions for k and ε. This sensitivity is undesirable in engineering simulations requiring a high degree of robustness.

SST k-ω model

The Shear Stress Transport (SST) turbulence model (Menter, 1992, 1994) combines elements of the original k-ω (Wilcox, 1988) and the standard k-ε (Launder and Spalding, 1974). The model was developed in two steps: the baseline model (Menter, 1994) and the SST itself. Its frequent implementation in hybrid turbulence models makes it particularly relevant to this discussion.

As mentioned, the k-ω model offers some advantages when compared to the k-ε approach in regions near the boundary layer (Wilcox, 1993). Nevertheless, such a model displays strong sensitivity to the inlet turbulence conditions. The idea of the SST k-ω is to combine the two models in the regions where they perform best: the k-ω near the wall and the k-ε in the free shear layers.

Both the baseline and the SST models switch between k-ω and k-ε through a blending function, F_1 multiplying the term differentiating the k-ε and k-ω equations, shown in (2.44).

The resulting equations are those of a k-ε when $F_1 = 1$ and those of a k-ω when $F_1 = 0$. The formulation for F_1 accounts for the nearest wall distance. The SST model adds a key feature to those of the baseline one in the following expression for ν_t:

$$\nu_t = \frac{a_1 k}{\max(a_1\omega, SF_2)} \tag{2.45}$$

In the expression above, F_2 is a function that depends, among other parameters, on wall distance. Such a formulation allows to avoid overestimate of the shear stress in complex boundary layers, by enforcing Bradshaw's assumption (Menter, 1994) of shear stress being proportional to TKE.

The eddy-viscosity modification and the presence of well-designed limiters in the SST provide measurable advantages on complex boundary layers, including a more robust description of separation than what is achievable with the k-ε model for this family of applications. On the other hand, the blending function behavior is arbitrary and often leads to unexpected results in internal flow applications.

The SST maintains the disadvantages of isotropic eddy-viscosity models. For example, it is not appropriate for flows involving curved surfaces, rotation, swirling, or strong deformation. The SST is leveraged in wall-resolved simulations, which come at the cost of high wall grid resolution compared to approaches using wall functions.

Other noticeable eddy viscosity models

Many other linear eddy-viscosity approaches proposed in the literature are not discussed here either because they are not relevant to this work, or they are not used widely in industry.

One class of models deriving from the k-ε approach that is certainly worth mentioning is the elliptic relaxation, proposed by Durbin (1991), to more appropriately resolve the near-wall effects without the use of arbitrary damping functions. Unlike the quasi-homogeneous k-ε, this model takes into

account non-homogeneous phenomena near the wall. An additional transport equation is solved for a scalar representing a velocity fluctuation: $\overline{v^2}$ and has been calibrated to correctly reproduce the near-wall eddy viscosity levels. The model has shown great promises but also considerable numerical challenges, and its evolution has resulted in the larger family of Elliptic Blending models. More recently, Elliptic-Blending hybrid models have been proposed (Fadai-Ghotbi et al., 2010a).

2.3.6 Relevant higher-order URANS closures

The performance of URANS-based hybrid turbulence models depends strongly on the performance of their baseline URANS formulation. In particular, linear URANS models typically result in a nonphysical evaluation of the eddy viscosity in complex strains. This effect, deriving from the eddy viscosity simplification, hinders proper resolution of the large-scale unsteady turbulent structures which are central to the success of hybrid modeling.

In this work, a NLEVM is selected instead as a baseline. Here we discuss relevant features of higher-order closures in general and NLEVM models in specific.

Linear eddy-viscosity models are based on the assumption that a_{ij} be aligned with $\bar{S}_{ij}$. Such an assumption is inaccurate not only in complex flows, but also in simple shear flows (Pope, 2000). Indeed, isotropic eddy-viscosity models have significant limitations in their physical description. The error related to the linear eddy-viscosity assumption is particularly large in flows involving complex features such as: streamline curvature, rotational strains, swirl, and turbulence-induced secondary flows. Moreover, linear models do not take into account nonlocal and history effects in the individual components of the Reynolds stress tensor (Speziale, 1991).

Models based on the isotropic eddy-viscosity assumption are designed to compute mean flow properties in simple flows. Going beyond such an assumption allows us to account more appropriately for the effects of turbulence anisotropy. As an example, isotropic RANS closures fail to describe turbulence-driven secondary flows, also called secondary flows of the second kind. Secondary flows of the second kind are different from the ones of the first kind in that they are caused by turbulence, not by a laminar velocity field. Those phenomena can be observed in non-circular straight ducts and are present in fully developed conditions (Demuren and Rodi, 1984). Turbulence produces motions perpendicular to the axial direction of the channel, as illustrated in Figure 2.2 below.

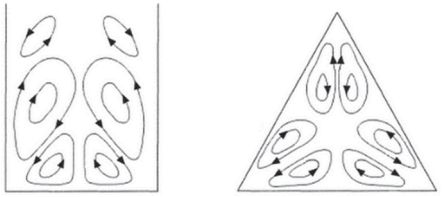

Figure 2.2 Secondary flows of the second kind, from Pattison (2011)

Reynolds stress transport models

A more general approach to close the RANS equations is to model directly the six independent Reynolds stresses, as derived from the exact solution in (2.26). Usually, an additional transport equation is used for the TDR. This approach is followed by models in Reynolds stress transport (RST) models, also called RSMs and second-order closures.

Fundamental work in the development of RSMs was done by Rotta (1951) and later generalized by Launder, Reece, and Rodi (1975), who proposed and tested a unified model. RSMs convey

significant information on nonlocal effects of turbulence and are generally more suitable than linear eddy-viscosity models for simulating complex flows that are not quasi-homogeneous. In particular, RSMs can be appropriate for flows containing strong swirl, streamline curvature, and resolved rotation (Pope, 2000). They can describe correctly flows with a rapid variation in the resolved flow field that two-equation models are unable to predict.

Nevertheless, RSMs have the disadvantage of being complex and computationally intensive. Six strongly coupled equations represent a numerical challenge for the solver, producing increased computational cost and convergence issues. Equations are generally stiff due to the large source terms so that numerical stability issues may arise; several solutions have been proposed, as discussed widely in the literature, to increase their stability. Their most relevant application drawback is the considerable sensitivity to grid cell quality and refinement. Weaknesses of RSMs in predicting complex flows can be partially attributed to inadequacies in the equilibrium formulation, or to lack of description of non-equilibrium effects (Speziale, 1996).

As we observed, if we try to derive an exact transport equation to compute the six independent residual stresses as in (2.14), we increase the number of unknowns in our problem from 6 to 75. Transporting all Reynolds stresses does not translate into increasing the number of known physical parameters. It brings the closure challenge to a higher order and increases the number of unknown parameters. The higher-order physical approximation compared to linear eddy-viscosity models is traded with more unknowns and terms complex to model. The imperfection of engineering models is not removed from simulations by using RSMs, but it is brought to a higher level of complexity.

Algebraic Reynolds stress and Nonlinear eddy-viscosity models

A family of models was introduced by Rodi (1976) involving simplification of the RSM equations into fewer PDEs and using two transport equations for general properties of turbulence (e.g. TKE and length scale). This family of approaches is called algebraic Reynolds stress models (ARSM). The simplification involves adopting the equilibrium hypothesis, based on which the convection and transport terms in the Reynolds stress equations are neglected (Gatski and Speziale, 1993).

ARSMs use an implicit relation between Reynolds stresses and resolved velocity gradients. They maintain important downsides of RSMs, such as the numerical issues in coupling multiple transport equations and the cost related to the solution of a complex coupled system. In practice, ARSMs have shown not to offer particular advantages over the full RSM models and are not commonly adopted. They are however the starting point for NLEVMs, which is the class of URANS models adopted in this work.

Pope (1975) introduced a method to express the nonlinear formulations for Reynolds stresses explicit, gathering inspiration from earlier work by Lumley (1970). Such a method is commonly referred to as NLEVM. This concept extends the eddy-viscosity assumption by adding nonlinear terms to the equation for the residual stress tensor anisotropy:

$$a_{ij} = \tau_{ij} - \frac{1}{3}\tau_{kk}\delta_{ij} = -2\nu_t\bar{S}_{ij} + f\left(\bar{S}_{ij}, \bar{\Omega}_{ij}, \dots\right) \tag{2.46}$$

The function f, which includes nonlinear terms, depends on Galilean and frame invariance properties of the resolved velocity gradient tensor and on scalar turbulence quantities, such as the transported TKE and TDR. Function f describes a nonlinear stress-strain relation.

The resolved velocity described by NLEVMs is equivalent to the instantaneous velocity of an equivalent non-Newtonian fluid with more viscous properties (Lumley, 1970). On the other hand, the linear eddy-viscosity assumption approximates the resolved flow with the instantaneous motion of a Newtonian fluid with increased viscosity.

The most general formulation for function f is derived through the Cayley-Hamilton theorem. According to such a theorem, f can be written as a weighted sum of 10 linearly independent tensor bases, symmetric, traceless, and dependent on $\bar{S}_{ij}$ and $\bar{\Omega}_{ij}$. The weighting coefficients can be expressed as a function of the invariants of $\bar{S}_{ij}$ and $\bar{\Omega}_{ij}$. Several approaches can be used to obtain the model closure.

A subset of NLEVMs is that of explicit algebraic Reynolds stress models (EARSMs). Those models are derived from ARSMs through simplifying assumptions (Hellsten and Wallin, 2009). One approach to derive EARSMs is to combine ARSMs with the expression in (2.46). A similar approach was used in two dimensions by Pope (1975) in his work introducing NLEVMs, based on the RSM of Launder, Recce and Rodi (1975) and the equilibrium assumption.

Gatski and Speziale (1993) proposed a more general three-dimensional EARSM derived from an RSM at the equilibrium limit. An EARSM was developed by Apsley and Leschziner (1998) by approximating an ARSM into a cubic formulation. Those authors use the name NLEVM.

Other NLEVMs are derived through calibration with experimental data and physical considerations like realizability (Baglietto and Ninokata, 2006; Lien et al., 1996; Shih et al., 1993; Speziale, 1987).

NLEVM approaches have been proposed using the renormalization group (RNG) theory (Rubinstein and Barton, 1990), while others leverage direct-interaction approximation tools (Nisizima and Yoshizawa, 1987).

By using NLEVMs, expressions for the residual stress tensor become fully explicit and do not require the solution of many tightly coupled equations. Such an approach reduces the computational cost and numerical stiffness compared to RSMs. The computational cost of NLEVMs is only slightly higher than that of two-equation linear models.

Additional characteristics of NLEVM justifying their adoption in the present work and details on the specific NLEVM selected are provided in Section 4.7.

2.4 Large-eddy simulation

Due to the importance of LES in hybrid turbulence modeling, it is worth identifying those features that are particularly relevant to the present work.

Often in the literature, hybrid models are described as URANS/LES since many of those models combine the URANS and LES equations. Conversely, several other hybrid formulations, including the one proposed here, do not solve the LES equations. However, those models still have scale-resolving features that use partially averaged or filtered statistics, similarly to LES.

One of the purposes of LES is to achieve higher accuracy and flow description over URANS, by making full use of the computational grid size available. In LES, the larger and most energetic eddies are resolved, and the smaller turbulent scales are modeled. The underlying consideration is that the largest scales, which carry most of the turbulent kinetic energy, are geometry-dependent, while the smallest scales, which carry a small amount of the turbulent kinetic energy, are assumed to have a universal nature. LES closures account for the momentum exchange between resolved and modeled scales. Significant savings in cell number are achieved over DNS while larger scales responsible for dominant physical effects are described more accurately than in URANS. The accuracy of URANS solutions does not increase significantly if the grid is refined beyond a degree of numerical grid convergence, due to the statistics of the model. This limitation is not present in LES, in which grid refinement increases the model's accuracy up to the DNS limit[3].

[3] However, grid convergence in LES is usually not monotonic (Spalart, 2009).

The computational cost of LES is affected by the requirement for a very fine grid near the wall compared to the boundary layer's size. Such a strict near-wall requirement is comparable with that for DNS (Durbin and Pettersson Reif, 2011). The number of grid points required for LES increases sharply with the Reynolds number. The scaling law in aerospace applications has been estimated to be roughly $N \sim \mathrm{Re}^{9/5}$ (Chapman, 1979). Those grid requirements make LES impracticable for most industrial CFD simulations (Spalart et al., 1997). LES has been steadily growing in popularity and use in the last decades due to advances in CPU technology and large-scale parallel computing.

A useful review of LES is that by Meneveau and Katz (2000), as well as the book by Sagaut (2006). Turbulence models in the LES family use for the overbar operation of Section 2.2.2 a local average in a small region around the point of interest. This averaging operation involves the integral in the spatial domain of the product of a flow function ϕ and a convolution kernel $G_\Delta(\boldsymbol{x} - \boldsymbol{x}')$.

$$\bar{\phi}(\boldsymbol{x}, t) = \int_{\mathbb{R}^3} G_\Delta(\boldsymbol{x} - \boldsymbol{x}')\phi(\boldsymbol{x}', t)\mathrm{d}^3\boldsymbol{x}' \tag{2.47}$$

This filtering operation (Leonard, 1974) averages out length scales smaller than the filter size Δ. In common LES closures, the filtering operation is typically not explicitly performed during calculations but only in the model derivation. The convolution kernel has the following property (Germano, 1992):

$$\int_{\mathbb{R}^3} G_\Delta(\boldsymbol{x} - \boldsymbol{x}')\mathrm{d}^3\boldsymbol{x}' = 1 \tag{2.48}$$

In most LES closures, the filter size is assigned based on grid spacing, to resolve turbulent scales as small as the discretization limits allow. Due to this common choice, residual scales are often referred to using the term subgrid scale (SGS). Residual stresses are not described like in URANS as the averaged product of fluctuating components unless additional assumptions are made. Several conventions exist to decompose the residual stresses, among which that by Germano (1986).

In LES, resolved parameters and residual stresses have a random-like behavior while in URANS they represent ensemble averages. To produce time-averaged solutions, LES requires collecting sufficient statistics, thus aggravating the already high computational cost deriving from the grid requirements. The largest turbulent fluctuations in LES need to be described by resolved fields. This translates into the need to simulate sufficient upstream geometrical domain to allow for turbulent field development. As this requirement is almost impracticable, an effective alternative for turbulent content at inlet boundary conditions has been to leverage synthetic eddy methods to generate turbulent structures. The sensitivity of results to inlet specifications can undermine the ease of use and robustness of LES.

LES models for SGS stresses can usually be simpler than URANS models since it is assumed that the smaller scales of turbulence carry higher universality. Simple closures translate into lower computational cost per iteration. Such a feature is desirable given the high time and space resolution required in LES. The use of simple LES closures requires that the filter length be fine enough so that the cutoff lies in the inertial range. Such a range implies that the net transfer of energy from the larger to the smaller scales does not change with small filter size variations. Another limitation is the requirement, especially in simpler LES formulations, for grids made of quasi-isotropic cells.

2.4.1 Relevant LES closures

Standard Smagorinsky SGS model

A basic SGS model has been introduced in the pioneering work by Smagorinsky (1963) and has been applied for the first time to an engineering 3D case by Deardorff (1970). In this simple closure,

residual turbulence is modeled as isotropic and in equilibrium, so production of residual turbulent energy equals dissipation. The Smagorinsky model uses the Boussinesq assumption in (2.19) and defines eddy viscosity as the product of a length scale and a velocity scale.

The length scale Δ is usually a characteristic length scale of computational cells. The velocity scale is the product of Δ and a parameter representing the resolved strain rate and is representative of a Galilean-invariant velocity difference describing eddies of size Δ (Meneveau, 2010). The eddy viscosity is thus:

$$\nu_{\mathrm{t}} = (C_{\mathrm{S}}\Delta)^2\sqrt{2\bar{S}_{ij}\bar{S}_{ij}} \tag{2.49}$$

The Smagorinsky model has several drawbacks, among which is a lack of completeness. The model constant C_{S} needs to be specified a priori before the simulation and does not adapt automatically to its optimal value. The closure in (2.49) can be interpreted as a mixing length model that uses the grid size as filter. Many models have been developed addressing the shortcomings of the Smagorinsky SGS approach. The review by Sagaut (2006) provides useful discussion.

Dynamic subgrid scale

The dynamic SGS model of Germano and co-workers (1991) addresses the issue of assigning a value for C_{S} automatically. A test filter with a size larger than the main filter is used to collect statistics on the resolved fields. Assuming that the same C_{S} be valid for the grid filter and the test filter, this operation allows to have a dynamic closure.

An approximation of the dynamic model without test filtering has been proposed by Chester, Charlette, and Meneveau (2001). Such a formulation approximates the test filtering operation through a Taylor series expansion based on single-point variables. Such a rationale has inspired an approximation of an averaging operation made in the present work and discussed in Chapter 7.

WALE

Among many LES closures proposed, the wall-adapting local eddy-viscosity (WALE) model of Nicoud and Ducros (1999) has been particularly successful in industrial simulations. The WALE model provides an advanced description of the near-wall behavior by taking into account the resolved strain and rotation rate tensors, instead of the strain only as in (2.49). The WALE model does not require explicit filtering.

Other LES closures

A large variety of additional LES closures has been developed, also including more complex transport formulation. Here we only mention some relevant ones, which have contributed in shaping this work.

In implicit LES (ILES) models, the effect of SGS turbulence accounted for through numerical error rather than a closure. Numerical methods are chosen accordingly so that an appropriate level of diffusive error is produced. ILES is suitable for very complex flows, in which explicit models are unable to capture all of the physics, so ILES would not introduce larger error (Sagaut, 2006). In those cases, the diffusive numerical scheme introduces the advantage of numerical stability.

Models exist in the LES family that use residual stress transport equations (Deardorff, 1974), which add complexity and computational cost to the solution. Other methods transport scalar properties of the residual turbulence (Deardorff, 1980). More generally, several other approaches in the literature propose closures representing SGS versions of URANS models. No clear distinction exists between those methods and hybrid turbulence modeling, as discussed in Section 2.5.1. One of the challenges of LES is the requirement for a very large number of grid points near the wall to resolve the relevant

turbulent scales. A very common alternative to this is the use of wall functions in conjunction with LES. This concept can be considered as a very simple hybrid model.

2.5 Hybrid turbulence modeling

After having reviewed the URANS component of this work, let us now analyze hybrid concepts. Such a discussion is central to this work, which identifies a new strategy for hybrid turbulence modeling. The term hybrid used here identifies models combining features of URANS and LES. This section discusses hybrid models starting with their rationale, definition, and categorization, before reviewing key aspects of selected hybrid models that can be leveraged or avoided to achieve the objectives of the present work. Such a critique is functional to the remainder of this thesis, in which a newly proposed hybrid approach addresses limitations identified in existing hybrid models.

2.5.1 Rationale and categorization

Many different formulations for hybrid models have been proposed in the literature since the first concepts appeared in the mid-1990s (e.g. Speziale, 1996). Those models are often very different from each other, spanning a wide variety of features and applicability ranges.

Definition and goals

No definition of hybrid turbulence model has gained universal acceptance in the literature. We should not be surprised about this lack of a definition, which is quite common in the study of turbulence and is related to a great extent to our limited analytical understanding of the governing equations.

For example, if we decided to define as hybrid models those approaches combining URANS and LES, then models like SAS and PANS (described later in this chapter) would be excluded because they do not imply any LES closure. Nevertheless, they both aim at achieving a behavior intermediate between URANS and DNS, which can be considered as an LES-like behavior.

Even without having a strict definition, hybrid models can be identified through their goals. Indeed, one of the main objectives of all known hybrid models is to achieve higher accuracy than what is possible through URANS, while using fewer grid points than those needed for LES. Hybrid models can be eventually designed to converge to LES when a suitable grid is available. As anticipated in the introductory chapter (Section 1.2), the accuracy/cost tradeoff only provides a simplified description of the goals of hybrid models. Many other factors play a role. More generally, hybrid models aim at retaining the desirable features in the tradeoff between URANS and LES and at rejecting the undesirable ones. Different hybrid models focus on different features. A list of desirable and undesirable features of URANS and LES that has inspired the development of the new STRUCT approach is shown in Section 3.2.3.

Hybrid Modeling Similarities

An interesting aspect of the categorization of hybrid modeling approaches is the significant similarity often found between different concepts, which are developed from differing viewpoints but in practice share similar formulations.

The term very large eddy simulation (VLES), among many uses found in the literature, identifies the extension of the applicability of LES to coarser grids. The name VLES is a way to look at hybrid modeling from an LES perspective. The wall-modeled LES (WM-LES) approach reduces computational cost over LES. This approach is the simplest form of URANS/LES coupling (Fröhlich and Von Terzi, 2008). A common characteristic of WM-LES approaches is the URANS-to-LES

interface being located in the inner part of the boundary layer. Conversely, in most other hybrid models all of the boundary layer is solved using URANS (Sagaut et al., 2013).

We can see hybrid features, in a weak sense, also in the concept of URANS. In fact, URANS, by resolving unsteady averaged parameters, seeks resolution of low-frequency structures. In this work, for the sake of clarity, the term URANS is not used to identify hybrid approaches. Nevertheless, hybrid models exist that can be interpreted as extensions of URANS (Fröhlich and Von Terzi, 2008), including the one proposed here.

Grid and energy spectrum

Hybrid models proposed in the literature are based on a variety of derivations. As a result, no unique rule for grid requirements exists, but each model has its own. The optimal grid for a test case depends on the hybrid model used. Models may be particularly sensitive to grid design features, such as the cell size in the boundary layer region in the original DES formulations.

Hybrid models are usually designed to run with grids coarser than those needed for LES. However, it is not always the case that hybrid models are designed to run on grids finer than those for URANS. In fact, many hybrid models, including the one proposed here, aim at running on computational grids typical of URANS. In a generic turbulence model, part of the energy spectrum is resolved directly from the instantaneous solution of the Navier-Stokes equations while the remaining part is evaluated with the use of models. If we sorted turbulence models based on the resolved fraction of the turbulent kinetic energy, we would have DNS and LES on one end, URANS and RANS on the opposite one. Hybrid models would fall in between those two extremes.

A qualitative picture of the flow description of URANS and LES is shown in Figure 2.3 below, in which hybrid models occupy an intermediate domain. The separation between resolved and residual scales lies in the domain of large scales in URANS and in the inertial range in LES. Hybrid approaches often place such a separation in an intermediate domain, in which complex interaction between scales exists. This choice makes hybrid modeling challenging.

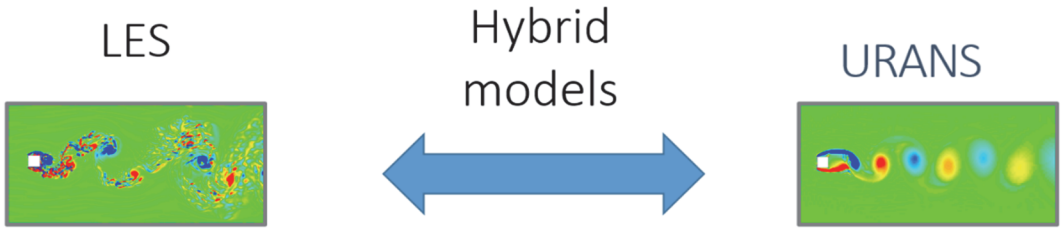

Figure 2.3 Hybrid turbulence models rationale: qualitative picture

Similarity between URANS and LES

As discussed in Section 2.2.2, if we consider a linear commuting LES filter, we can observe that URANS and LES share the same unclosed continuity and momentum equations. Nevertheless, the statistical theory and the derivations of those two approaches are very different: one is commonly based on ensemble averaging and the other on spatial filtering.

The similarity between URANS and LES allows for a simple implementation of hybrid models by using existing implementations of URANS equations but modifying the closure terms and the numerical schemes.

Categorization

Multiple authors in the literature use different approaches to categorize hybrid models. A distinction made by Gopalan and Jaiman (2015) identifies:

- *Segregated* models, by which URANS and LES equations are solved in two spatial domains, fixed before the simulation. Those models are also referred to with the term *zonal*, used for example by Pont et al. (2014).
- *Interfaced* models, by which a transition is made between URANS and LES, using an interface function f_I:

$$\tau_{ij} = f_\mathrm{I}\tau_{ij}^{\mathrm{URANS}} + (1 - f_\mathrm{I})\tau_{ij}^{\mathrm{LES}} \tag{2.50}$$

  The exact statistics for interfaced closures have been formulated by Germano (2015).

- *Blended* models, in which the hybrid residual stress tensor is provided by modifying the URANS one. This is done by using a function f_B. In these models, the LES equations are not used necessarily. Therefore, strictly speaking, these models do not hybridize URANS and LES. However, f_B could also be taken so that LES equations are retrieved.

$$\tau_{ij} = f_\mathrm{B}\tau_{ij}^{\mathrm{URANS}} \tag{2.51}$$

- *Uncategorized* models, in which the formulation is not identified by the criteria above.

Several other categorizations of hybrid models have been proposed in the literature. An important category is that identified by Fröhlich and von Terzi (2008) as *second generation URANS models*. Those are hybrid models for which no grid size dependence exists in any part of the formulation.

A different categorization has been proposed by Sagaut (2006), who proposed a distinction into:

- *Zonal decomposition* models, similar to zonal or segregated models.
- *Nonlinear disturbance* equations, in which the flow is split in the frequency domain into a low-frequency subdomain solved using URANS and a fluctuating domain solved with an LES-like model.
- *Universal* modeling, in which the model aims at extending LES to coarser meshes. This is usually done by combining URANS with an SGS approach.

Useful reviews of hybrid models can be found in the work by Fröhlich and von Terzi (2008), in the book by Sagaut (2006), and in that by Sagaut, Deck, and Terracol (2013).

2.5.2 Speziale Hybrid Methods

The VLES formulation proposed by Speziale (1996) is considered the first hybrid turbulence model proposed in the literature (Speziale, 1998), if we exclude as hybrid approaches URANS and WM-LES.

This closure aims at resolving appropriate scales in the range between DNS and URANS. The name VLES is used in the literature to refer to different concepts. In this case, it is intended as a hybrid model extending eddy-resolving capabilities to grids that are coarser than those needed for LES.

The residual stress tensor is formulated as a function of the grid size and other parameters, using the following relation:

$$\tau_{ij} = \left[1 - \exp\left(-\frac{c_1\Delta}{L_\mathrm{K}}\right)\right]^{c_2} \tau_{ij}^{\mathrm{URANS}} \tag{2.52}$$

Parameters c_1 and c_2 above are two empirical constants. When the grid size Δ is very large compared to the Kolmogorov length scale, the exponential becomes significantly smaller than 1. This leads asymptotically to a URANS solution. At the other limit, when Δ is small and comparable to L_K, DNS is retrieved. When Δ lies between these two limits, the model is designed to perform in a way that resembles LES or VLES. The URANS model used in the original work by Speziale (1996) is a NLEVM with strain-dependent coefficients.

The Speziale VLES inspired the development of many other approaches. However, its limitations explain its low success in realistic applications. The model equation in (2.52) produces a behavior close to URANS in most conditions. Very low values of Δ are needed to enable a scale-resolving mode. Moreover, as noticed by Spalart (2000), the model is not sensitive to the characteristic length scale of URANS as many other hybrid models are.

Nevertheless, this formulation has introduced hybrid turbulence models, opening the way to a large number of models developed over the two following decades.

Limited numerical scales

The limited numerical scales (LNS) model developed by Batten, Goldberg, and Chakravarthy (2000) can be considered as an evolution of Speziale's model. In both models, a multiplier is applied to residual stresses:

$$\tau_{ij}^{\mathrm{LNS}} = \alpha \tau_{ij}^{\mathrm{URANS}} \tag{2.53}$$

In LNS, a different formulation is used for α, the so-called latency parameter, than in Speziale's model. According to the authors of LNS, the formulation in (2.52) is undesirable, because it requires the selection of arbitrary constants. Moreover, such a formulation requires Δ to be very small, approaching the Kolmogorov scale, to obtain effective hybrid behavior. A different formulation was proposed for the latency parameter in (2.53) (described here using the notation by Fröhlich and Von Terzi, 2008):

$$\alpha = \frac{\min\left(\nu_{\mathrm{t}}^{\mathrm{LES}}, \nu_{\mathrm{t}}^{\mathrm{URANS}}\right)}{\nu_{\mathrm{t}}^{\mathrm{URANS}}} \tag{2.54}$$

Such a formulation switches from URANS to LES for sufficiently fine grids, since it contains the LES eddy viscosity, which depends on the grid size.

The formulation in (2.54) shows a straightforward approach to switch between URANS and LES based on flow conditions and grid size. To operate in LES mode, LNS requires a suitably fine grid in selected zones. LNS is an automatic version of a zonal model. Therefore, it can benefit from the injection of synthetic turbulence at the URANS-to-LES interface (Batten et al., 2002).

2.5.3 Detached Eddy Simulation and variants

Let us now discuss DES, a hybrid model that is at the same time one of the first developed and one of the most used in industry. The multiple versions of DES that have been proposed over time have been a significant source of inspiration for the development of many hybrid approaches, including the one introduced here.

The concept of DES was developed by Spalart and co-workers (1997). One of its purposes is to overcome weaknesses of URANS in predicting massively separated flows while keeping the computational cost significantly lower than in LES. Subsequent modifications of the original 1997 DES formulation have been made, so the initially proposed model is often referred to as DES97. When simulating massively separated flow past an obstacle using LES, the boundary layer causes a significant computational cost. In that zone, a very fine mesh, comparable to that needed for DNS,

is required. The DES concept overcomes this problem by solving URANS equations in attached boundary layer regions and reverting to an LES-type model everywhere else, i.e. in massively separated regions. The initially proposed DNS formulation is built by extending the robust S-A model. The parameter defining wall distance is replaced by the following expression, i.e. the minimum between wall distance and a parameter proportional to the grid size:

$$d_{\mathrm{DES}} = \min(d, C_{\mathrm{DES}}\Delta) \tag{2.55}$$

The model operates as S-A near the wall, where d is small. Far from the wall, the length scale is proportional to Δ. This sensitivity to the grid size is considered capable of delivering an LES-like behavior in massively separated regions in which the grid is suitable.

A value of the model coefficient C_{DES} of 0.65 was obtained by Shur and co-workers (1999) in their work introducing the first 3D application of DES. They derived the C_{DES} coefficient by assuming homogeneous turbulence and adjusting the model's behavior in LES mode. The approach is zonal, because the flow region is partitioned into *attached* and *detached* zones.

In several models, the parameter defining grid spacing is the geometric mean of the spacing in the three directions. In DES, the largest among the three dimensions is used instead.

$$\Delta = \max(\Delta_x, \Delta_y, \Delta_z) \tag{2.56}$$

Based on the above equation, DES running in LES mode uses a filter based on the largest of the three dimensions and does not use the extra resolution in case of strongly anisotropic grids.

The original DES has shown success in predicting time-averaged values in many test cases, especially those including massive separation while exhibiting several limitations. Thick boundary layers are especially challenging because DES tends to switch to LES prematurely. This switch produces modeled-stress depletion (MSD), i.e. a decrease in residual stresses not compensated by the needed resolved turbulence. In such a case, nonphysical solutions may produce unwanted adverse pressure gradients known as grid-induced separation (GIS) (Menter and Kuntz, 2004). Due to this issue, grid generation for DES is not easy for CFD users. It is important that computational grids be built specifically for running with DES, with flattened cells closer to the boundaries to avoid near-wall issues such as MSD or GIS. Quasi-isotropic cells are preferred in separated regions. This strong grid sensitivity near the wall represents a limitation of DES in engineering applications.

It is also recognized that a limitation of DES, common with LES and with other hybrid models, is the lack of monotonic grid convergence (Spalart, 2009).

As a lesson learned from DES, the approach proposed in the present work aims at eliminating the grid size dependency in the model formulation to avoid excessive sensitivity to the grid size and cell geometry, seeking ease of use and grid convergence.

Besides its known limitations, DES has the advantage of achieving a substantial reduction in computational cost over LES. Moreover, DES converges as desired to LES and DNS behavior as the grid is refined. The computational cost reduction over LES is sought after in the present work while LES or DNS convergence is not pursued and could be explored in future work.

The DES approach has been extended past the S-A model to leverage different URANS models, notably two-equation ones (Strelets, 2001; Travin et al., 2002). Those formulations modify the characteristic length scale of the model instead of the d parameter:

$$L_{\mathrm{DES}} = \min(L_{\mathrm{URANS}}, C_{\mathrm{DES}}\Delta) \tag{2.57}$$

where L_{URANS} is the length scale according to the URANS model, formulated as a function of the two transported parameters. Implementation of DES consists in substituting L_{URANS} with L_{DES}. The present work also implements a hybrid formulation starting from a two-equation URANS.

Models in the DES family are designed to trigger the LES-like mode far from the boundary layer, and to use URANS near the wall. In this sense, DES can be seen as an advanced extension of the concept of WM-LES. DES still requires an LES-like fine grid far from the wall, even in stable high-Re flows. Conversely, the present work aims at operating on URANS-like grids, without aiming at all at providing an advanced version of WM-LES.

Delayed Detached Eddy Simulation

The Delayed Detached Eddy Simulation (DDES) model is a modification of DES proposed by Spalart and co-workers (2006) and originally inspired by earlier work by Menter and Kuntz (2004). The goal of DDES is to keep DES in URANS mode even in thick boundary layers, to avoid the issues known as MDS and GIS. The logic is that, in those cases, it is preferable to run as URANS rather than as LES without the necessary resolved content.

Following Spalart and co-workers (2006), a new length scale parameter is introduced:

$$\tilde{d} \equiv d - f_d \max(0, d - C_{\mathrm{DES}}\Delta) \tag{2.58}$$

Such a length scale contains a function f_d switching the behavior of the model from URANS, when $f_d = 0$, to DES97, when $f_d = 1$. Such a function is formulated as:

$$f_d \equiv 1 - \tanh((8r_d)^3) \tag{2.59}$$

A parameter r_d appears, defined as:

$$r_d \equiv \frac{\nu_{\mathrm{t}} + \nu}{(\bar{S}^2 + \bar{\Omega}^2)\kappa^2 d^2} \tag{2.60}$$

The r_d variable is designed to be equal to 1 in the logarithmic layer and significantly lower when exiting the boundary layer. In practice, the expression in (2.59) smoothens and inverts the behavior of (2.60), in order to produce suitable values for f_d. The present work also seeks after robust physical description in the boundary layer, but it does not use DES formulations.

Improved delayed Detached Eddy Simulation

Recalibration of DDES was performed to provide consistency with WM-LES, avoiding Logarithmic Layer Mismatch (LLM) between inner URANS and outer LES. This approach is called improved DDES (IDDES) and was developed by Shur, Spalart, Strelets and Travin (2008). The IDDES formulation also introduces a modified expression for the subgrid length scale, different from the one in (2.56). The new expression for Δ is a function not only of the cell size in the three dimensions but also of the wall distance. This choice aims at producing a more steep variation of Δ near the wall, generating instabilities in the resolved field (Spalart, 2009). A lesson learned from IDDES is that a hybrid model can be supported that aims at generating the needed instabilities in the resolved flow fields, even without using artificial methods to inject momentum. A similar strategy is employed in the present work.

A version of the DDES and IDDES models has been calibrated based on the k-ω SST instead of the S-A baseline model (Gritskevich et al., 2011).

2.5.4 Embedded LES

The so-called embedded LES (ELES) is a simple zonal model that applies URANS and LES in distinct regions selected before the simulation.

In ELES, URANS behavior is typically used at the inlet and outlet of the simulation region, and LES is used in a selected area of interest. For example, the model has been applied to a T-junction test case by Gritskevich and co-workers (2014). In their work, the LES region has been selected as that on and immediately downstream the junction, where most of the most complex mixing phenomena are expected to occur. The zonal selection made by those authors is shown in Figure 2.4 below.

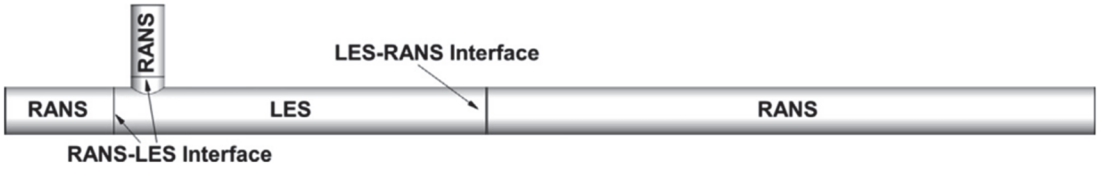

Figure 2.4 Domain decomposition in ELES of a T-junction, from Gritskevich et al. (2014). In the figure, URANS, as defined in this work, is labeled as RANS

Interfaces leading from URANS to LES are usually treated with the generation of synthetic turbulence. A wall model can be used in the LES zone to reduce further the required number of cells.

The ELES approach has the major drawback of requiring the definition of URANS and LES regions before the simulation. Such a specification makes the model incomplete and dependent upon the arbitrary distinction between the two regions.

2.5.5 Partially Averaged Navier-Stokes and similar

A particularly relevant concept in this work is that of Partially Averaged Navier-Stokes (PANS) turbulence model, introduced by Girimaji, Srinivasan, and Jeong (2003). The model was later described extensively by Girimaji (2006) and analyzed by Girimaji, Jeong, and Srinivasan (2006).. PANS can be considered to be a second-generation URANS (Fröhlich and Von Terzi, 2008) since its equations do not depend on the grid size. It is identified by its authors as a bridging model, aiming at bridging the gap between URANS and LES, and extending the capability to DNS. The derivation of the PANS equations are a way to answer the following question posed by Girimaji (2006):

"If RANS represents the closure for fully averaged statistics, what is the corresponding closure for partially averaged statistics?"

In PANS, the decomposition of resolved and residual flow variables in (2.5) is made using an arbitrary filter. This choice leads to the definition of a generalized central moment as in (2.12). Two key parameters are introduced. Parameter f_k is the ratio between residual and total TKE, while f_ε is the ratio between residual and total TDR. This work uses the subscript m for modeled.

$$f_k = \frac{k_\mathrm{m}}{k} \tag{2.61}$$

$$f_\varepsilon = \frac{\varepsilon_\mathrm{m}}{\varepsilon} \tag{2.62}$$

When both of these parameters are equal to one, all of the turbulent kinetic energy and turbulence dissipation rate are residual, so the model behaves as URANS. In particular, if f_ε is unity, then the smallest scales in PANS are equal to those in URANS (Girimaji, 2006). Parameter f_ε is set to unity

in high-Re flows, such as those treated in this work. Therefore, let us only focus on the variation of f_k and assume $f_\varepsilon = 1$.

When f_k is null, no turbulence is left unresolved, which corresponds to a DNS or a quasi-DNS if grid requirements are not met for DNS. When f_k is in the range between 1 and 0, hybrid behavior is triggered. PANS is meant to be used with coarser grids than those required for LES, aiming at minimizing computational cost.

The transport equations for the unresolved, or residual, turbulent kinetic energy and turbulence dissipation rate are shown below.

$$\frac{\bar{\mathrm{D}}k_\mathrm{m}}{\bar{\mathrm{D}}t} = \frac{\partial}{\partial x_j}\left[\left(\nu + \frac{\nu_{\mathrm{t,m}}}{\sigma_{k,\mathrm{m}}}\right)\frac{\partial k_\mathrm{m}}{\partial x_j}\right] + P_{k,\mathrm{m}} - \varepsilon_\mathrm{m} \tag{2.63}$$

$$\frac{\bar{\mathrm{D}}\varepsilon_\mathrm{m}}{\bar{\mathrm{D}}t} = \frac{\partial}{\partial x_j}\left[\left(\nu + \frac{\nu_{\mathrm{t,m}}}{\sigma_{\varepsilon,\mathrm{m}}}\right)\frac{\partial \varepsilon_\mathrm{m}}{\partial x_j}\right] + C_{\varepsilon 1}\frac{\varepsilon_\mathrm{m}}{k_\mathrm{m}}P_{k,\mathrm{m}} - C^*_{\varepsilon 2}\frac{\varepsilon_\mathrm{m}^2}{k_\mathrm{m}} \tag{2.64}$$

Those equations are the same as in the standard k-ε model, except that parameters refer to the modeled part of turbulence only. Moreover, the dissipation coefficient differs from the one in the standard k-ε according to the following equation:

$$C^*_{\varepsilon 2} = C_{\varepsilon 1} + f_k(C_{\varepsilon 2} - C_{\varepsilon 1}) \tag{2.65}$$

The formulations for the kinetic energy and dissipation turbulent Prandtl numbers vary based on the assumption made for the transport of modeled TKE and TDR. Two theories (Girimaji, 2006) were derived representing two different hypotheses: the zero-transport (ZT) model and the maximum-transport (MT) model. According to the ZT, the transport of TKE and TDR is not driven by resolved fluctuations. The two resulting turbulent Prandtl numbers are:

$$\sigma_{k,\mathrm{m}} = \sigma_k f_k^2 \quad , \quad \sigma_{\varepsilon,\mathrm{m}} = \sigma_\varepsilon f_k^2 \tag{2.66}$$

Conversely, the MT considers the transport of TKE and TDR as proportional to the eddy viscosity associated with the resolved fluctuations:

$$\sigma_{k,\mathrm{m}} = \sigma_k \quad , \quad \sigma_{\varepsilon,\mathrm{m}} = \sigma_\varepsilon \tag{2.67}$$

The modeled eddy viscosity is:

$$\nu_{t,\mathrm{m}} = C_\mu \frac{k_\mathrm{m}^2}{\varepsilon_\mathrm{m}} \tag{2.68}$$

The performance of the PANS approach depends on the URANS model on which PANS is applied. For example, PANS was applied by Basara and co-workers (2011) using a k-ε-ξ-f four-equation elliptic relaxation URANS model. Those authors achieved an enhanced description of turbulence in the near-wall region compared to a standard k-ε baseline formulation. As observed in several examples in the literature, hybrid models gain benefit from the use of underlying URANS models providing a more complete description of flow anisotropy than in simple linear two-equation models.

As another example, Liu and co-workers (2014) applied PANS over a nonlinear RNG k-ε baseline URANS. As a lesson learned, the performance of the baseline URANS is critical for hybrid models. Therefore, an advanced baseline model is leveraged in the hybrid approach proposed in this work.

Ma and co-workers (2011) developed a low-Reynolds number treatment for PANS to obtain a more physical description of modeled near-wall quantities.

Prescribing the value for f_k

In the earlier tests of PANS, the control parameter f_k was selected a-priori to be constant in the whole simulation domain. This approach is not complete since the model requires an adjustable parameter to be prescribed before the simulation. Several attempts were made after the first PANS papers to obtain a formula for optimizing parameter f_k universally.

For example, a constraint for determining the smallest value of f_k based on the grid size has been proposed by Girimaji and Abdol-Hamid (2005). Such a formulation has been obtained by applying the theory of the Kolmogorov length scale to the resolved turbulence only.

$$f_k = \frac{1}{\sqrt{C_\mu}}\left(\frac{\Delta}{L}\right)^{2/3} \approx 3\left(\frac{\Delta}{L}\right)^{2/3} \tag{2.69}$$

where $L = k^{3/2}/\varepsilon$ is the integral length scale. The formulation in (2.69) relates the resolution control parameter to the ratio between the grid size and the integral length scale. Other authors propose different variants of a formulation for f_k, usually including reference to the grid size and integral length scale (Basu et al., 2007; Elmiligui et al., 2004).

A zonal version of PANS was presented by Davidson (2014), in which f_k is switched between 1 and a lower constant value in prescribed regions. The model proposed here will also seek a formulation to prescribe locally the ratio between k_m and k. However, unlike the formulation in (2.69) and other similar ones, this is done without any direct reference to the grid size. This strategy is followed aiming at achieving robustness and grid-converging behavior.

Partially integrated transport model

The partially integrated transport model (PITM) was introduced by Schiestel and Dejoan (2005) and by Chaouat and Schiestel (2005). PITM resembles PANS in that it introduces a damping coefficient reducing the amount of modeled TKE starting from a baseline URANS. This operation modifies the term describing the destruction of TDR with no grid dependence, as in PANS. PITM has not been tested extensively on complex test cases (Sagaut et al., 2013) but mainly on simpler academic flows.

Partially resolved numerical simulation

Shih and Liu (2008, 2004) introduced the idea of partially resolved numerical simulation (PRNS). Like PANS and PITM, PRNS uses a parameter to control the fraction of resolved over total turbulent scales. The so-called resolution control parameter is selected before the simulation, to modify the eddy viscosity. The approach is in all effect extremely similar to PANS.

2.5.6 Scale-Adaptive Simulation

Scale-adaptive simulation (SAS) is, together with DES, one of the most successful hybrid models that have been implemented in engineering codes and applied to industrial flows. Similarly to PANS, SAS does not depend explicitly on the grid size so that it can be considered as a second-generation URANS (Fröhlich and Von Terzi, 2008).

SAS was developed by Menter and co-workers (2003) who, among other motivations, aimed at solving the GIS problem of DES. The SAS model is described and tested thoroughly in two papers: one by Menter and Egorov (2010), the other by Egorov, Menter, and co-workers (2010).

The authors of SAS started their analysis from the k-kL turbulence model by Rotta (1968) and removed an assumption of isotropic turbulence. As a consequence, a new term appeared in the URANS equations, which depends on the von Kármán length scale, L_vK.

This length scale is formulated based on the ratio between parameters representing the first and second spatial derivatives of resolved velocity:

$$L_{\mathrm{vK}} \equiv \kappa \frac{\bar{u}'}{\bar{u}''} \tag{2.70}$$

The von Kármán constant is $\kappa = 0.41$. We can write the first spatial derivative term as:

$$\bar{u}' \equiv \sqrt{2\bar{S}_{ij}\bar{S}_{ij}} \tag{2.71}$$

The second derivative term can be written as:

$$\bar{u}'' \equiv \sqrt{\frac{\partial^2 \bar{u}_i}{\partial x_k \partial x_k}\frac{\partial^2 \bar{u}_i}{\partial x_j \partial x_j}} \tag{2.72}$$

For the sake of brevity, let us just discuss one of the SAS formulations most used in practical cases: the one applied to the k-ω SST, as introduced by Egorov and Menter (2008). Implementation of SAS into other URANS models can be found in the literature. The SST-SAS model contains an extra production term in the ω equation of the k-ω SST. Such a term is (Menter and Egorov, 2010):

$$Q_{\mathrm{SAS}} = \max\left[\zeta_2\left(2S_{ij}S_{ij}\right)\left(\frac{L}{L_{\mathrm{vK}}}\right)^2 - C_{\mathrm{SAS}}\frac{2k}{\sigma_\Phi}\max\left(\frac{1}{\omega^2}\frac{\partial\omega}{\partial x_j}\frac{\partial\omega}{\partial x_j}, \frac{1}{k^2}\frac{\partial k}{\partial x_j}\frac{\partial k}{\partial x_j}\right), 0\right] \tag{2.73}$$

The relation in (2.73) evaluates the maximum between a difference and zero. When such a max function returns zero, then Q_{SAS} is null, and the model behaves as a k-ω SST. This occurs in regions in which the model does not switch to SAS mode. When the first term in the difference is larger than the second one, the whole difference is larger than zero and dominates, so the SAS hybrid behavior is enabled. A key role is played by the ratio between integral length scale, L, and von Kármán length scale, L_{vK}. The former parameter is:

$$L = \frac{\sqrt{k}}{\beta^{*0.25}\omega} \tag{2.74}$$

The activation criterion for hybrid turbulence in SAS does not use information on the wall distance or cell size as in DES models. The ratio between turbulence length scales and von Kármán length scale distinguishes regions of stationary flow and regions with strong instabilities such as those in massively separated flows. The former are solved with URANS and the latter through an increase of ω, thus causing a reduction of ν_t and a subsequent increase of the ratio between resolved versus modeled TKE. In the initial formulation for SAS, the ratio between length scales was elevated to the first power rather than the second one. The squared ratio was applied in a later revision of the SAS model (Egorov and Menter, 2008).

As often observed in the literature, SAS is similar to DES except that the grid spacing information is replaced with information coming from flow properties through the von Kármán length scale (Durbin and Pettersson Reif, 2011). This feature makes the model less sensitive to the grid. Moreover, parameters triggering and controlling the hybrid model in SAS are automatic and do not require arbitrary scaling factors as in PANS.

The second term in the difference of the relation in (2.73) includes a max function. Such a term detects the presence of boundary layers. Inside those layers, that term would become very large because of the gradients of ω and k being large with respect to their gradients. In this case, the difference in (2.73) would become negative, Q_{SAS} would drop to zero, leading to URANS behavior. Such an approach ensures that SAS operates in URANS mode in the boundary layer, which is the same intent as in the development of DDES versus DES (Durbin and Pettersson Reif, 2011). This is an important feature for a robust hybrid formulation, and it will be pursued in the present work.

A downside of SAS is that the transition between the URANS and scale-resolving behavior does not always produce the correct physical description unless significant unsteadiness occurs in the resolved fields. This issue is inherently built into the model, which, similarly to DES, was designed specifically assuming to capture massive unsteady separating regions, and can instead lead to substantial failure in configurations where mild separation or other complex strains exist. A representative example of this situation is described in Sections 3.2.2 and 3.2.3.

2.5.7 Formulation by Perot and Gadebusch

A hybrid model was proposed by Perot and Gadebusch (2007). Those authors modified the standard k-ε by introducing a hybrid formulation. An energy transfer variable is defined as:

$$\alpha \equiv 1.5\left(1-0.28\left(\frac{k_\mathrm{m}}{k_\mathrm{m}+k_\mathrm{r}}\right)^2\left[\left(\frac{\Delta x_i}{\sqrt{k_\mathrm{r}}}\frac{\partial\sqrt{k_\mathrm{r}}}{\partial x_i}\right)^2+0.11\right]^{-1}\right) \tag{2.75}$$

The two variables k_m and k_r represent respectively the modeled and resolved TKE. The energy transfer variable multiplies the production term in the equation for the TKE. This variable can have either positive or negative values. In the latter case, it accounts for energy backscattering.

Eddy viscosity is:

$$\nu_\mathrm{t}=C_\mu\frac{k_\mathrm{m}^2}{\varepsilon}\left(\frac{k_\mathrm{m}}{k_\mathrm{m}+k_\mathrm{r}}\right) \tag{2.76}$$

This is equivalent to the eddy viscosity of a standard k-ε for the modeled scales multiplying the ratio between modeled and total TKE. The anisotropic part of the residual stress tensor is:

$$a_{ij}=\tau_{ij}-\frac{1}{3}\tau_{kk}\delta_{ij}=2\alpha\nu_\mathrm{t}\bar{S}_{ij} \tag{2.77}$$

The model has been extended to wall-bounded flows by Pont and co-workers (2014), showing comparable accuracy with SAS and DDES. This model has promising features but very low experience in simulations to confirm its robustness. This model uses explicit statistics to determine k_r. For example, Pont and co-workers (2014) apply time averaging to the resolved fields. Due to this operation, the approach is not local in time. Some of the concepts introduced in this work have been very useful during the development of this thesis work.

2.5.8 Further selected ideas in hybrid turbulence

Among the numerous other hybrid concepts not covered in this review, a few deserve to be mentioned, as they introduce novel ideas, and have certainly, although indirectly, contributed shaping the approach proposed in this work.

- Organized-eddy simulation (OES) (Bourguet et al., 2008). This concept is similar to that called semi-deterministic method (SDM) (Sagaut et al., 2013). The flow is split into a coherent and incoherent part. The URANS formulation is modified to allow coherent motions to be resolved rather than modeled, forming a triple velocity decomposition.
- The turbulence-resolving RANS (TRANS) approach, proposed by Travin, Shur, Spalart, and Strelets (2004). Such an approach senses regions of high rotation and low strain and reduces the eddy viscosity locally.
- The flow simulation methodology (FSM) proposed by Fasel, Seidel, and Wernz (2002) as a result of a collaboration with Speziale. The model modifies the approach developed by Speziale (1996) while keeping the same conceptual framework.

- An approach by Johansen, Wu, and Shyy (2004) applies an arbitrary filter size, different than the grid size, to a baseline URANS.
- The approach proposed by Bhushan and Walters (2012). This model decomposes the residual stresses into a URANS and an LES part. The approach is used to derive a formulation for the hybrid model's residual stresses based on the residual stresses of URANS and LES.

2.6 Discussion

This chapter has discussed relevant approaches that have produced an essential knowledge in the numerical prediction of turbulence. URANS models leverage statistics to describe fluctuating quantities up to the integral length scale, which is of the order of the flow geometry. Therefore, URANS approaches model fluctuations that can be significantly larger than the computational grid.

The idea of LES is to make efficient use of a given computational grid by resolving all scales down to the grid size. This is done switching from ensemble averaging to local averaging, which is also interpreted as filtering. In practical applications, this idea is only feasible for very fine meshes, capable of resolving more than 80% of the turbulent kinetic energy. For this reason, it is argued in the literature (Sagaut et al., 2013) that the name LES should be replaced with large-and-medium-eddy simulation.

Following Sagaut (2006), grids for LES needs to be fine enough so that:

- all scales responsible for production are resolved
- turbulence is small enough so that it can be considered as isotropic and in equilibrium

This requirement leads us to the problem that, in practical industrial simulations, neither URANS nor LES models are most desirable to engineers, for opposite reasons. This issue has motivated the development of hybrid models.

Jansen's (1999) comment on RANS very well states the issue:

"though computationally efficient for some steady flows, has been disappointing for unsteady and/or complex flows."

Although still significantly limited, linear eddy-viscosity turbulence models, in particular, the k-ε, S-A, and SST, dominate the turbulence model scenario in industry. Many other turbulence models exist with promising features but are still less common due to open challenges in their robust application. A subset of them are still at the academic stage and need to undergo further testing before being applied widely. Broad industrial use is required for the turbulence community to become familiar with newer models, increasing the probability of identifying their strengths and getting to know their weaknesses. Even models proposing the most rigorous mathematical derivations require numerical testing and experience.

A danger is associated with overly relying on theoretical derivations based on the elaboration of the differential equations, rather than understanding the fundamental flow physics (Menter, 1994). This is a central concept in this thesis work. The discussion by Menter on RSMs (2012) is consistent with the idea and further justifies our decision to rely on robust two-equation RANS models:

"Considering that RANS models typically already have limitations covering the most basic self-similar free shear flows with one set of constants, there is little hope that even the most advanced Reynolds Stress Models will eventually be able to provide a reliable foundation for all such flows."

Similar dangers are associated with over-relying on dimensional analysis. As stated by Wilcox (1993):

"Historically, dimensional analysis has been one of the most powerful tools available for deducing and correlating properties of turbulent flows.

However, we should always be aware that while dimensional analysis is extremely useful, it unveils nothing about the physics underlying its implied scaling relationships. The physics is in the choice of the variables."

The need for more mature hybrid concepts is well expressed by a recent NASA report on the future of CFD (Slotnick et al., 2014), which supports the idea that hybrid models have not yet achieved in full their ambitious goal of providing industrially feasible simulation of complex flows:

"*Perhaps the single, most critical area in CFD simulation capability that will remain a pacing item by 2030 in the analysis and design of aerospace systems is the ability to adequately predict viscous turbulent flows with possible boundary layer transition and flow separation present.*"

Finally, a further requirement to guarantee the accuracy of hybrid models is the ability to describe the correct fluctuations in resolved fields. Lack of this unsteady content can result in significant error. Due to this requirement, particular attention during the assessment and validation of new models should be devoted to numerical treatment and treatment of flow boundaries.

The numerical scheme used could undermine the description of those fluctuations. Schemes with excessive diffusive error, although stabilizing for URANS models, can be detrimental for hybrids. On the other hand, numerical schemes generating dispersive error may produce enough disorder to trigger the needed instabilities artificially (this aspect is discussed in Chapter 5).

Hybrid models exist in which synthetic eddy methods are used to inject artificial fluctuations and generate the needed resolved unsteadiness. This injection is done especially at inlet boundary conditions, or at fixed interfaces as in ELES. It is more complex to introduce artificial fluctuations at interfaces that evolve over time, such as those in SAS or DES. In fact, in those models, synthetic generation of resolved fluctuations is not introduced. Multiple examples of insufficient fluctuations appear in the literature using those models.

Several other methods to simulate turbulence, not mentioned in this chapter, are studied extensively in the literature, among which (Heinz, 2007; Pecnik et al., 2012; Speziale, 1991):

- Two-point closures
- Probabilistic density function and filter density function models
- Algebraic structure-based models

Although those models may have very promising features, their use in industrial applications is still not sufficiently mature, and they have not been considered for this work.

3 Rationale and goals of the proposed method

3.1 Chapter overview

The previous chapter has provided a critical discussion of relevant models, reviewing in succession URANS, LES, and hybrid concepts. This chapter will instead start assembling the various "pieces" together and will identify the rationale motivating the development of the new hybrid approach.

The chapter begins with the discussion of limitations that have been observed in the literature during the application of current hybrid models. Strengths and limitations of URANS and LES are discussed, describing features that the new hybrid approach can leverage or should avoid. Finally, the main goals and motivations for this work are presented together with the selected requirements that have steered the development of the approach.

3.2 Observations on the performance of hybrid models

Despite the ambitious goals and promising preliminary evaluation of the significant number of hybrid turbulence concepts proposed since the mid-1990s, current hybrid closures do not reach a wide fraction of today's industrial simulations. It is, therefore, essential to first identify the general weaknesses of hybrid models leading to their limited success. To do this, we focus on their application experience. The selected test cases, while simple, are representative of fundamental flow configurations that appear in most complex industrial flows. These same flow cases are then leveraged in Chapters 6, 7, and 8, to test and demonstrate the performance of the various implementations of the newly proposed hybrid turbulence approach.

3.2.1 Flow past a square cylinder

The test case of the turbulent wake in a flow past a square cylinder represents a basic example of an external flow past an obstacle. This test case has been used extensively in the turbulence modeling literature, as it is particularly well suited to evidence the strength of hybrid models. It allows us to test the behavior of turbulence models in cases with shedding and massive separation. An illustration of a velocity profile for this flow case is shown in Figure 3.1 below.

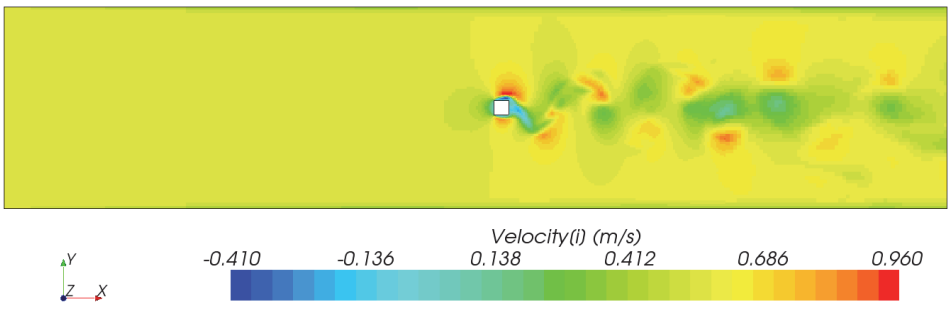

Figure 3.1 Velocity profile from simulation of the flow past a square cylinder

RANS simulations are inaccurate in this test case, as the time averaged solution is dominated by the low-frequency shedding which is not resolved in RANS. The unsteady shedding can be resolved by the URANS solution. However, such a fluctuation appears usually in a single-mode shedding instead of the complex spectrum seen in the experiment (Menter, 2012), producing a significant error. Many hybrid models have been tested in flow cases involving a square or circular cylinder, showing general success (Elmiligui et al., 2004; Jeong and Girimaji, 2010; Lakshmipathy and Girimaji, 2010; Luo et al., 2014; Song and Park, 2009). In PANS, accuracy of results increases when increasing the amount of resolved-over-total scales (Jeong and Girimaji, 2010; Song and Park, 2009).

Selected results

Results from the work by Jeong and Girimaji (2010), for PANS simulations with three values of parameter f_k, 0.4, 0.7, and 1.0, are shown in Figure 3.2 below. We can observe that simple RANS and URANS ($f_k = 1$) results using the k-ε model are the farthest from the experimental data. Meanwhile, lower values of f_k produce a closer agreement with the experiment.

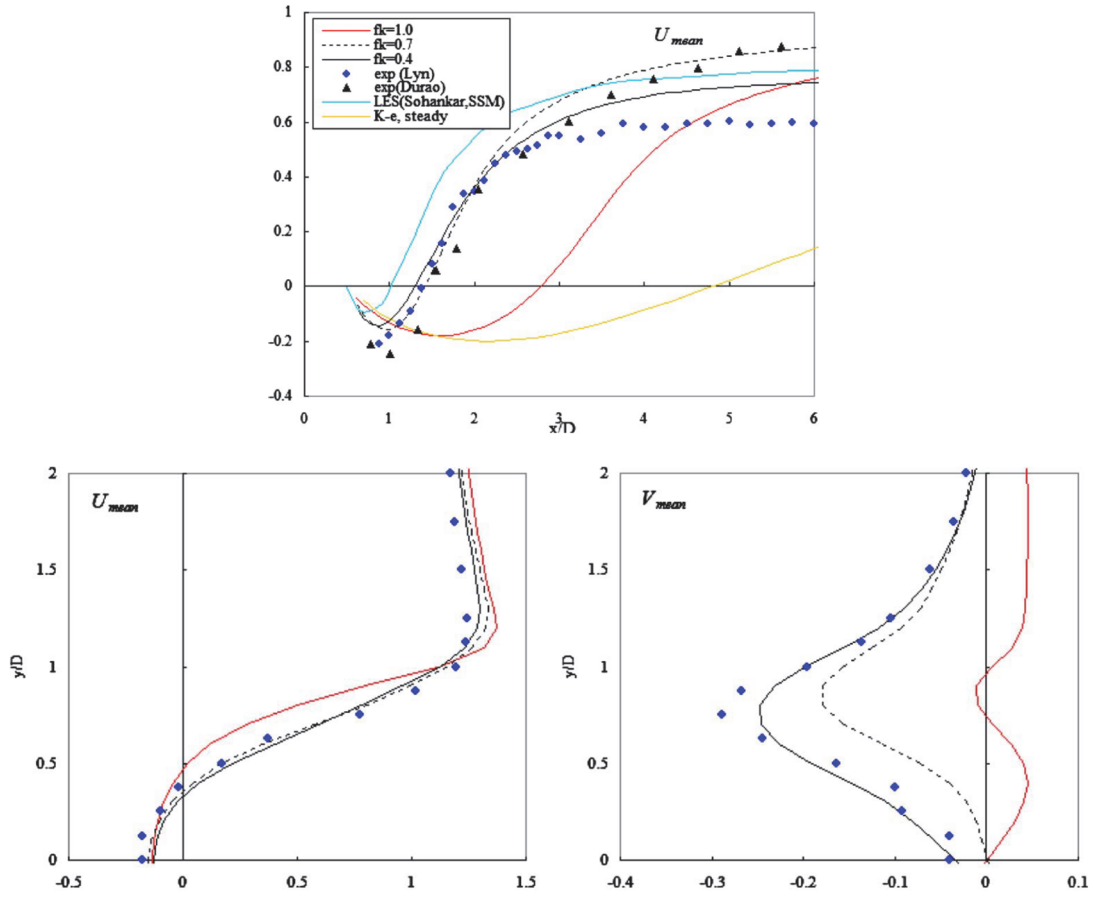

Figure 3.2 Flow past a square cylinder, PANS results from Jeong and Girimaji (2010). The top figure plots the resolved x-component of velocity as a function of position-x along the centerline of the geometry. The bottom figures plot the x (left) and y (right) component of velocity as a function of position-y at x/D=1. Velocities are normalized with reference velocity while positions are normalized with the cylinder's diameter. Details on reference parameters and a description of the geometry can be found in Section 6.2.1.

This test case is very useful in the present work since it provides us with a clear-cut distinction between regions of massive flow separation and other flow regions. Therefore, it allows us to evaluate the local response to partial resolution of turbulence effectively. An example of this analysis is shown in Section 3.5.

3.2.2 T-junction mixing – blind benchmark results

A junction with T shape with fluids mixing at different average temperatures is very common in industrial systems and has been tested extensively in the literature (e.g. Hu and Kazimi, 2006). This test case has been chosen because it represents a challenging configuration for hybrid models. A velocity profile for this flow case is shown in Figure 3.3 below.

The T-junction test case reproduces turbulent mixing of a fluid with non-uniform temperature, causing temperature fluctuations at the wall. These fluctuations will introduce cycling, thermal stresses, and the risk of fatigue cracking. Component failures due to this cause have occurred in light water reactors (Kim et al., 1993). As an example, a break resulting from thermal striping in the residual heat removal (RHR) system of the Civaux reactor in France has caused a plant shutdown in 1998 (Peniguel et al., 2003). Thermal striping can also occur in sodium fast nuclear reactors, because of the high thermal conductivity of the coolant. For example, accidents related to thermal striping have happened at both the Phénix and the Superphénix sodium fast reactors (Gelineau et al., 1994).

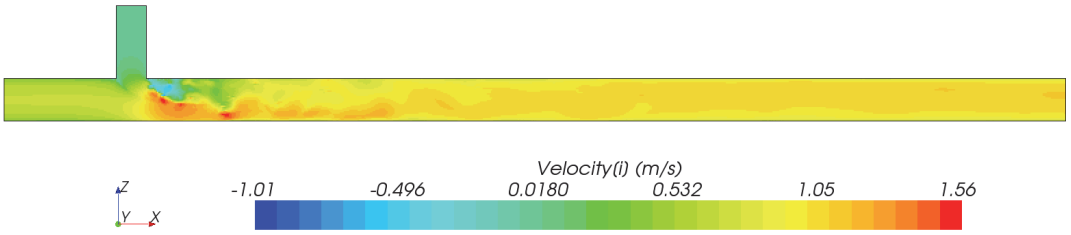

Figure 3.3 Velocity profile from simulation of the turbulent mixing in a T-junction

Selected results – blind benchmark

Due its relevance to the industry, a T-junction mixing test case was selected for the first OECD/NEA-sponsored blind CFD benchmark (Smith et al., 2011). A total of 29 participants submitted results for the benchmark. Among them, 19 chose a variant of LES for the problem, while four sets of results were obtained using the SAS-SST model with grid sizes of 5.0, 2.3, 1.1, and 1.0 million cells. Only one set of results was obtained using DES-SST, on a 2.4-million-cell grid; other results were obtained using URANS models.

Results from the benchmark (Smith et al., 2011), for a test section at 1.6 diameters distance from the junction, are shown Figure 3.4 for time-averaged velocity and in Figure 3.5 for time variance of velocity-y. Details on the geometry can be found in Section 6.3. Those results show the experimental data points, the best of four SAS results, and the DES result.

Profiles for time-averaged velocities, in Figure 3.4 below, show a significant discrepancy with the experiment for DES and SAS. Conversely, the LES and k-ω SST achieve closer agreement.

Profiles for velocity fluctuations, in Figure 3.5 below, show that all simulations are in fairly close agreement with the experiment except for SAS, which is significantly distant from it. Figure 3.4 and Figure 3.5 show examples of hybrid models generating results that are largely nonphysical. This lack of robustness exemplifies well their limited application and the more common reliance on URANS instead of hybrid models.

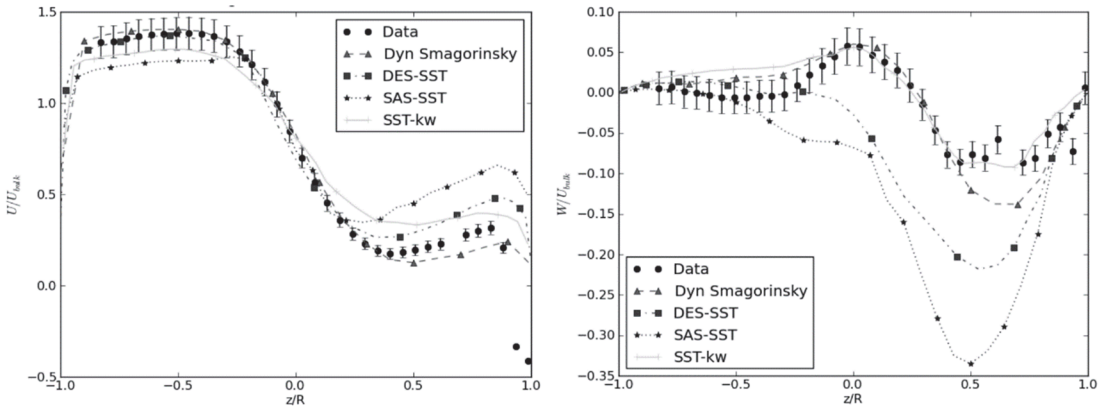

Figure 3.4 Time-averaged velocity-x at $x = 1.6D$, from Smith and co-workers (2011)

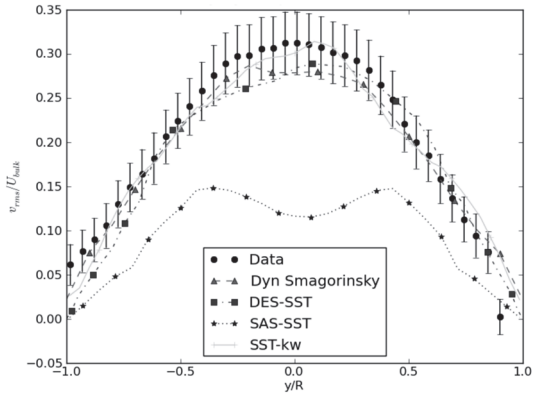

Figure 3.5 Time variance of velocity-y at $x = 1.6D$, from Smith and co-workers (2011)

As mentioned above, the SAS results shown here are the most accurate out of four submissions to the blind benchmark. The sample is large enough to support the evidence, as also concluded in the OECD report, that such an approach does not show general robustness. Although the sample is reduced to 1 in the case of DES, the same type of challenge appears in Figure 3.4.

More selected results for T-junction flow mixing

For the same T-junction configuration, open results produced after the publication of the OECD report, and obtained using hybrid models have been published by Gritskevich, Garbaruk, Frank, and Menter (2014). Three hybrid models, DDES, ELES, and SAS, were tested using two spatial interpolation schemes, central differencing (CD) and bounded central differencing (BCD). Simulations were run on a grid of about 5 million cells. Many LES simulations in the benchmark paper use a comparable grid size (Smith et al., 2011). Therefore, such a grid can be considered as an LES-like one. The LES activation regions in the ELES simulations are shown in Figure 2.4.

Results for time-averaged velocity profiles (Gritskevich et al., 2014) are shown in Figure 3.6 below. The three hybrid approaches all provide predictions in agreement with the experiment using the CD interpolation scheme. When switching to BCD, the DDES and ELES models offer similarly accurate profiles, while SAS suddenly introduces significant and nonphysical error similarly to the two previous examples. Except for this strong lack of agreement with the experiment, all the other profiles appear to agree closely with the experiment and with each other. This result is generated

with an LES-suitable fine grid, which favors models operating in LES-like mode. The blind benchmark report has shown (Smith et al., 2011) that LES, on a similarly fine grid, provides results very close to the experiment. Using hybrid models on LES-like grids defeats their purpose of being low-cost approaches since the computational cost is expected to be lower for LES than for hybrid models running with the same grid and time step.

The different behavior of SAS using the CD vs. BCD scheme is likely due to a missed activation of the hybrid LES-like mode in the BCD case. In fact, CD is known to produce more dispersive error than BCD does. The unsteadiness generated by such an error appears to be sufficient to trigger the LES-like behavior in this test case. Results for velocity fluctuations are not shown here but lead to similar conclusions as for velocities. Both for blind and open benchmark the SAS approach shows considerable deficiencies in robustness, as a small change in the grid quality, activation parameters or discretization methods will lead to sudden failure. The T-junction test case, being relevant and challenging in the testing of hybrid models, is used throughout this work.

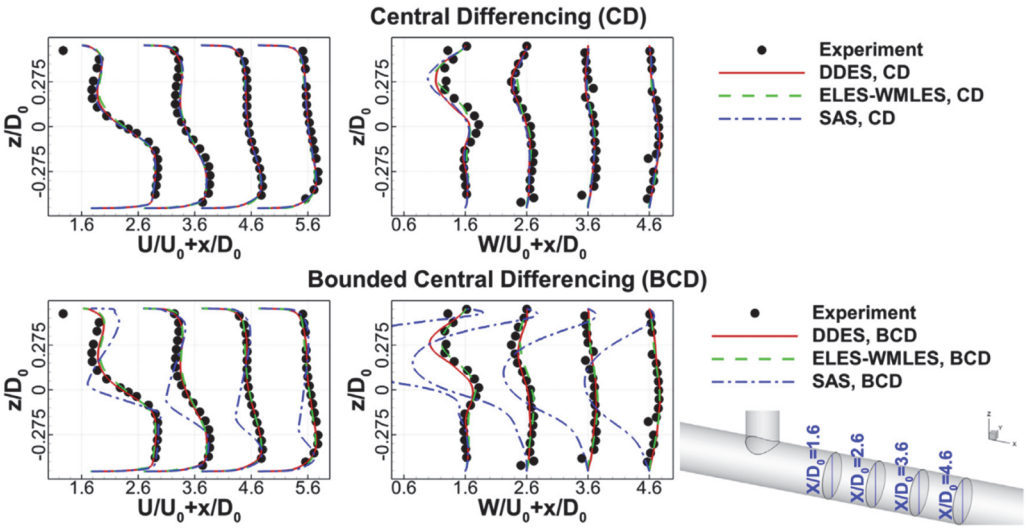

Figure 3.6 T-junction results, from Gritskevich and co-workers (2014)

3.2.3 Asymmetric diffuser flow

The flow in an asymmetric diffuser is used broadly to evaluate the capability of turbulence models to represent the challenge posed by a slight adverse pressure gradient. This test case is a challenging one for hybrid models since separation is mild. A velocity profile is shown in Figure 3.7. The phenomenon of separation is key to many engineering applications. Indeed, in many cases, we want machines to operate close to the onset of separation to maximize performance (Simpson, 1981). Nevertheless, we usually want to avoid or control separation, to prevent a sharp loss of efficiency.

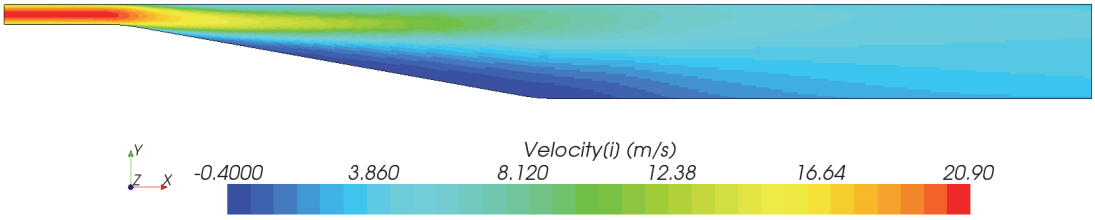

Figure 3.7 Velocity profile from simulation of the flow through an asymmetric diffuser

Flow separation violates the equilibrium assumption on which basic URANS models are formulated. This violation represents one of the reasons why many URANS models provide solutions in poor agreement with experimental data. URANS models can be capable of predicting the location of the recirculation region but without a fully accurate result in the whole domain (Berdanier, 2011).

Selected results

The work by Davidson (2006) has highlighted poor performance of SAS in such a test case. He performed coarse-grid tests using the k-ω SST model, both with and without the SAS term enabled. In a comparison, SST-SAS demonstrated poorer agreement with the experiment than SST-URANS. Such a lower accuracy of SAS can be attributed to the hybrid model operating neither in URANS mode nor full hybrid mode, but in between. Indeed, many hybrid models, including DES, are known from the literature to fail in such an intermediate domain.

Results for velocity from the same work (Davidson, 2006) are shown in Figure 3.8 below. Simulations use the central differencing scheme for spatial discretization. When the SAS term is enabled, results show high-velocity peaks in the top region of the diffuser and a strong predicted recirculation. The SST-URANS model seems to be in closer agreement with the experiment than SAS, except for near-outlet regions.

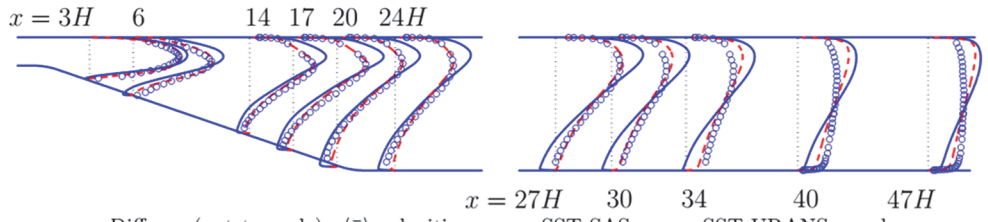

Diffuser (not to scale). $\langle\bar{u}\rangle$-velocities. —— : SST-SAS; - - - : SST-URANS; markers: experiments

Figure 3.8 Asymmetric diffuser SAS tests, velocity-x profiles, from Davidson (2006)

Results for the time variance of velocity-x in Figure 3.9 below show that the SAS term introduces a massive and nonphysical peak of resolved velocity near the beginning of the diffuser. Such a result is a clear example of a turbulence model breaking down, i.e. failing at reproducing the physical flow and introducing a very large error. This is an undesirable feature of many hybrid turbulence models and is one of the reasons why their robustness is often not relied upon in engineering applications.

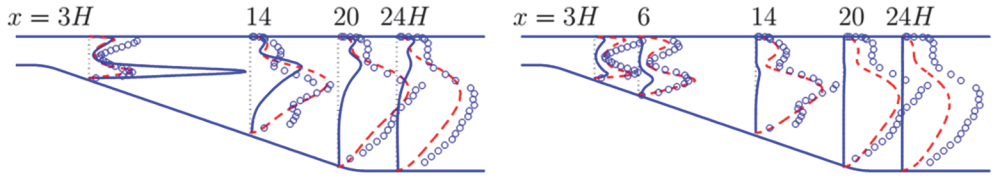

(a) SST-SAS model (b) SST-URANS model

Diffuser (not to scale). Normal stresses. —— : $\langle u'^2\rangle$; - - - : $2k/3$; markers: experiments

Figure 3.9 Asymmetric diffuser SAS tests, velocity-x variance, from Davidson (2006)

The asymmetric diffuser test case is also used in the current work and tested with the newly developed hybrid approach. Description of the flow configuration, experimental data, and results is made in Section 0.

3.3 Strengths and limitations of LES and URANS approaches

Many hybrid models combine features of URANS with features of LES, aiming at obtaining an optimal combination in the tradeoff between their strengths and weaknesses. We can list strengths and weaknesses of URANS and LES, as a starting point for proposing a new hybrid approach.

The reference URANS models considered in this discussion are two-equation formulations and in particular NLEVMs, which have been selected for this work as discussed in Chapter 2.

- SGS models are typically unable to reproduce the effects of anisotropy or non-equilibrium correctly in residual turbulence, thereby requiring a very fine grid to capture all production scales. LES filters are typically not suitable when the cutoff wavenumber lies below the inertial range. The computational requirements of LES are significantly higher than those of URANS. Such a difference is critical for internal flows. It has been estimated by Menter (2012) that, in turbomachinery, LES requirements are $10^5 - 10^7$ times higher than URANS ones.
- LES requires strong attention to the computational grid. The aspect ratio of cells needs to be approximately one. This requirement poses challenges and limitations in the grid generation process, especially in complex geometries and flows. It also limits the possibility of adopting strategies to reduce the total number of cells significantly. On the other hand, URANS does not have strong requirements regarding aspect ratio. The geometry or size of cells can be adapted based on preferential velocity directions or desired local refinement, greatly reducing computational cost.
- Wall-resolved LES requires extremely fine grids close to the wall, where the resolution needed for LES is similar to that required for DNS. As an example, LES of an airliner wing requires about 10^{11} cells, as calculated by Spalart and co-workers (1997). This requirement makes LES not affordable for high-Reynolds-number industrial simulations. URANS solved without wall functions also requires fine grids near the wall, but fewer grid points are needed than for LES due to the coarser discretization in the direction parallel to the wall.
- LES computational grids are particularly challenging to build for internal flows with numerous and complex wall boundaries. In those cases, the combined requirements of aspect ratio and wall refinement may be difficult to meet even for an expert analyst. On the other hand, suitable URANS grids can be generated more easily for those cases, even in minutes, when using automated grid generators. Moreover, the numerical error produced by a sudden change in grid size is usually more severe in LES than in URANS.
- The quality of an LES result can depend strongly on the inlet resolved turbulence. Synthetic eddy methods need to be used if resolved turbulence data are not available. On the other hand, URANS simulations of stationary processes are typically possible with simpler boundary conditions, because they do not vary with time.
- When the grid is refined, LES naturally converges to a quasi-DNS solution.
- When the mesh becomes coarser, LES models do not revert to URANS. Instead, they introduce a significant error and produce nonphysical results. This behavior is the main limitation of LES.
- URANS results converge asymptotically to the modeled solution, and not to an LES. Once reasonable convergence is reached, URANS results are not very sensitive to changes in grid size (Travin et al., 2004). Grids with a reasonable grid convergence in URANS are significantly coarser than those needed for LES.

- URANS models, especially the simpler ones, provide poor averaged results in complex flows, for example, those dominated by massive separation (Liu et al., 2014). On the other hand, LES is suitable for those simulations. This observation is related to the fact that turbulent eddies in complex cases are strongly geometry-dependent.
- URANS models are very stable numerically since they enlarge the stabilizing effect of diffusive terms.
- URANS models are not suitable for applications in which the user desires to extract detailed unsteady information from results. LES, in addition to its high potential accuracy, can provide the description of unsteady flow quantities needed in many engineering applications, for example, the study of vibrations, thermal fluctuations, and noise. Fluctuation spectra and amplitudes are typically required for fluid-structure interaction. In power engineering, unsteady features are important to predict phenomena such as vibration-induced fretting, mechanical fatigue, and thermal fatigue.
- Grid convergence in LES can be non-monotonic for complex flow cases (Spalart, 2009). This condition is not desirable for quality control of CFD results because it raises challenges in determining the order of grid convergence. On the other hand, URANS typically has grid-converging behavior in a wider range of flow cases than LES.

3.4 General relevant modeling concepts

We now discuss general concepts that apply to both URANS and LES models. Due to the similarity between URANS and LES equations mentioned in section 2.2.2, those concepts are also relevant to hybrid models. This section identifies several general concepts and discusses the potential benefits and downsides related to their use in hybrid models and the newly proposed one.

3.4.1 Isotropic eddy-viscosity assumption

The isotropic eddy-viscosity assumption is often employed in both URANS and LES closures and implies significant limitations. It considers the stress-strain relation between resolved velocity deformation and modeled turbulence as independent of angular direction. The assumption of a_{ij} being aligned with S_{ij} is proven to be far from reality even in simple shear flows (Pope, 2000). This explains causes of accuracy limitations of linear eddy-viscosity approaches in complex flows, among which those involving rotation, swirl, impingement, strong curvature, and turbulence-driven secondary flows (Hellsten and Wallin, 2009). Jones and Launder (1972) stated that their standard k-ε model shows a clear limitation in areas with significant acceleration.

On the other hand, linear eddy-viscosity models are suitable for simpler flows, for example, those involving two-dimensional boundary layers. The linear eddy-viscosity assumption offers the benefit of being easy to implement and use, and numerically stable, due to the diffusive effect of the augmented viscosity. Moreover, linear eddy-viscosity models offer a simple framework for turbulence modeling, since they only require closure for one parameter: the eddy viscosity. The upgrade of a turbulence model from linear to a higher-order closure produces higher benefits in URANS than in LES. However, the use of a higher-order LES may also provide an increase in accuracy (Deardorff, 1980).

The hybrid approach proposed here relies on a closure that is nonlinear, to gather an accurate description of complex flow features. This choice is common in many hybrid models, starting from the first one proposed by Speziale (1996).

3.4.2 Eddy-viscosity assumption, in general

The downsides of the Boussinesq assumption have been split by Pope (1975) into two components: limitations of isotropic eddy-viscosity models and limitation of the eddy-viscosity assumption, even if not isotropic. By introducing his NLEVM, Pope (1975) aimed at fixing the former issue. The resulting NLEVM class maintains the eddy-viscosity assumption while raising it to a higher order. The resolved flow behaves as an equivalent non-Newtonian fluid with increased viscous behavior rather than just a fluid with increased isotropic viscosity, as the Boussinesq assumption describes.

Several NLEVMs use an explicit variable for the eddy-viscosity scalar with a formulation that usually has the following form (Baglietto and Ninokata, 2006; Lien et al., 1996):

$$a_{ij} = \tau_{ij} - \frac{1}{3}\tau_{kk}\delta_{ij} = \nu_\mathrm{t}\left(-2\bar{S}_{ij} + f\left(\bar{S}_{ij}, \bar{\Omega}_{ij}, \ldots\right)\right) \tag{3.1}$$

It does not make any formal difference to write the equation for a_{ij} as in (3.1) or to use the formulation in (2.46), which does not use any eddy viscosity for nonlinear terms. Those two formulations can be made equivalent based on the definition of f. Indeed, the eddy-viscosity assumption, extended to nonlinear models, does not introduce any formal limitation unless we provide a specific definition for the eddy viscosity.

Models using the eddy-viscosity scalar have the advantage of being able to leverage in a simple form the extensive experience accumulated in the determination of the isotropic eddy viscosity. This feature explains why those models are selected here.

3.4.3 Equilibrium and homogeneity assumptions

Common URANS and LES closures are derived by applying statistical operations to the equations of fluid motion and by making simplifying assumptions. Two of the most common assumptions are those of equilibrium and homogeneity of statistical quantities, involving the variation of quantities in time and space respectively. Flows undergoing rapid deformation violate these assumptions. The hybrid approach proposed here aims at identifying regions in which assumptions of the baseline URANS model are violated significantly. Let us describe briefly those two assumptions.

The equilibrium assumption considers production being equal to dissipation:

$$P_k = \varepsilon \tag{3.2}$$

This assumption is key to many URANS models and is a cause of reduced accuracy in flows that are far from the equilibrium condition.

The hypothesis of nearly homogeneous turbulence implies that the resolved velocity gradient tensor be spatially constant (Sagaut, 2006):

$$\bar{A}_{ij} = \frac{\partial \bar{u}_i}{\partial x_j} = \text{const.} \tag{3.3}$$

This assumption does not undermine significantly the prediction capability of LES in cases in which the filter size is in the low inertial range. Smaller eddies in that range possess universal character, and their energy transfer is considered being at equilibrium. Moreover, their energy content is assumed to be lower than 20% of the total turbulent kinetic energy (Pope, 2000).

3.4.4 Grid-refinement behavior

A final central concept is the grid-refinement behavior of turbulence models. Experimental data are not always available to validate simulations in engineering applications. Simulations may need to be run without the support of experiments. As a consequence, grid convergence is fundamental to estimate the error component due to spatial discretization and determine a grid-converged result with its uncertainty. The hybrid model family most used in industry is arguably DES, due to its successful applicability to external flows. As discussed by Spalart (2009), a downside of DES and other known hybrid models is the lack of monotonic grid convergence in complex flows.

This limitation has been highlighted in the results by Gant (2010), related to a test case of gas release in a ventilated room. In those results, URANS and RANS have shown to be in greater agreement with experimental data than DES and SAS.

In the same study, both hybrid models have provided poorer agreement with the experiment when the grid was refined. Conversely, URANS and RANS results showed monotonic grid convergence. A histogram summarizing results from Gant (2010) is shown in Figure 3.10.

Achievement of grid consistency would be determinant for the industrial success of a hybrid model. Therefore, this feature needs to be evaluated for a new model proposal, as done later in this work.

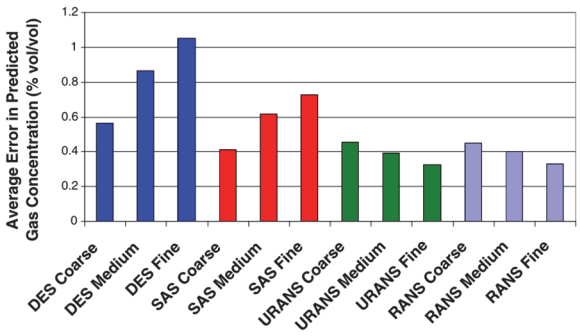

Figure 3.10 Grid convergence results using DES, SAS, URANS, RANS. From Gant (2010)

3.5 Preliminary numerical investigation

A large number of initial numerical evaluations have been performed in the early stages of this work to derive a strategy for the new hybrid approach. The studies focused on evaluating the capabilities of different flow parameters to describe regions of interest and to confirm the expected effects of adding local resolution of three-dimensional turbulence. A valuable example selected among the numerous tests is presented here.

The chosen configuration is the flow past a square cylinder (Lyn et al., 1995). The test case is introduced in Section 3.2.1 while additional numerical details are provided in Section 6.2. The reader can refer to Section 6.2 for information on the geometry and numerical conditions.

The square cylinder is a particularly useful test case for preliminary studies as it features a clear distinction between disturbed regions of the flow, involving strong shedding, and less disturbed ones, further away from the shedding zone. Fully developed flow (Re = 21,400) in a channel encounters an obstacle, generating massive separation, a wake, and flow shedding.

We select two arbitrary regions of the flow, named R1 and R2 in Figure 3.11. Region R1 stands in a zone mostly unaffected by separated flow. Region R2 stands right after the cylinder, where strong flow acceleration due to shedding is expected.

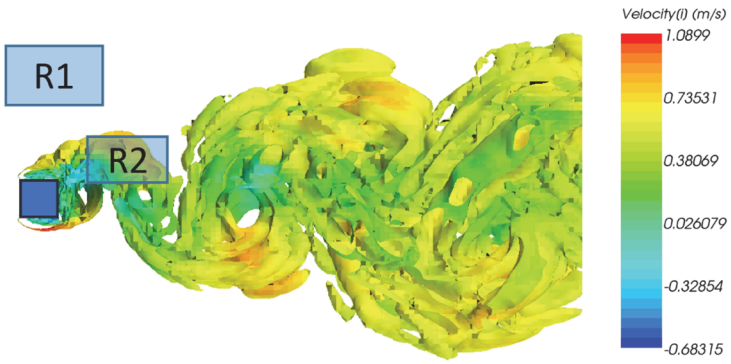

Figure 3.11 Locations of the arbitrary regions R1 and R2 in the flow past a square cylinder test case; the qualitative picture of the flow is based on velocity-x-colored surfaces of $Q = 0$

This test consists in running simulations with six different grid sizes and 11 different values of a coefficient f_μ reducing (damping) the eddy viscosity of a quadratic NLEVM URANS. The gradual reduction of this damping coefficient from 1 to 0 corresponds to a simple hybrid turbulence closure decreasing the modeled scales gradually. Grids with a cell size of 8, 12, 16, 20, 24, 28 mm are tested, refined by 50% in the wake region. Damping coefficients are tested in a range between 0 and 1, with a step of 0.1 (10^{-10} is used instead of 0, to avoid division by zero in the numerical solver used).

Section 6.2 presents simulation results using different turbulence models compared to experimental data from Lyn and co-workers (1995). The close agreement confirms that simulation conditions are closely representative of the phenomenon. The reader may refer to that section for detailed simulation results. In this discussion, results are not plotted versus the experiment but are elaborated to highlight the influence of the two working variables, grid size, and damping coefficient. An error indicator is introduced to quantify the averaged deviation between simulation and experiment for the time-averaged x-component of velocity, $\hat{u}_1$, in each region:

$$E(f_\mu) = \frac{1}{\mathrm{U_{ref}}} \frac{\sum_{i=1}^{N} \left| \hat{u}_{1,i,f_\mu} - \hat{u}_{1,i,\mathrm{exp}} \right|}{N} \tag{3.4}$$

Values are averaged throughout all N locations containing experimental data in the region of interest. For each region and grid size, values for the error in (3.4) are normalized as follows, to correct for effects caused by grid refinement:

$$E^*(f_\mu) = \frac{E(f_\mu)}{\frac{1}{N_{f_\mu}} \sum_{i=1}^{N_{f_\mu}} E(f_{\mu,i})} \tag{3.5}$$

Results for regions R1 and R2 are shown respectively in Figure 3.12 and Figure 3.13. Let us comment on the general trends shown in the two figures below. Higher values of f_μ appear to produce in most simulations a lower error in region R1, away from the shedding zone, and a higher error in the strong-shedding region, R2. Therefore, the nonlinear k-ε URANS, corresponding to a value of the damping coefficient $f_\mu = 1$, seems to be an appropriate turbulence model in region R1, which is not significantly disturbed by shedding. Conversely, in region R2, dominated by strong large-scale fluctuations, lower f_μ values produce higher agreement with the experiment. This observation suggests that region R2 would gather benefit from the use of a hybrid formulation.

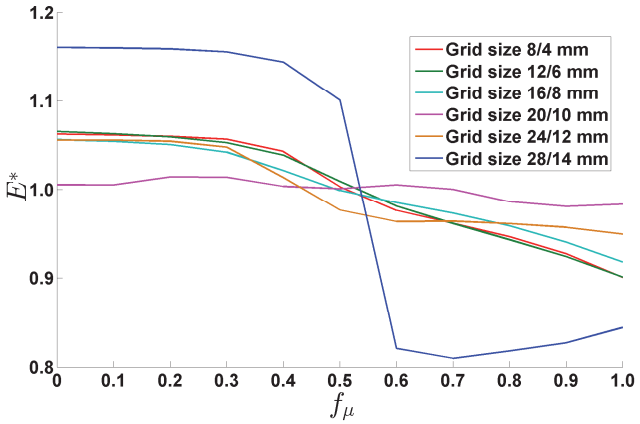

Figure 3.12 Values of E^* for different grid sizes and f_k, for region R1

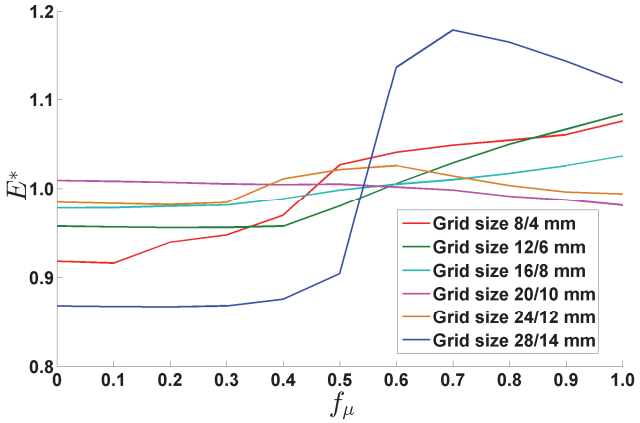

Figure 3.13 Values of E^* for different grid sizes and f_k, for region R2

Results from this example must be taken cautiously since one result cannot be extended to law. Nevertheless, these results convey a key aspect of the present work, which aims at leveraging hybrid turbulence model activation based on the statistical nature of the local flow.

3.6 Objectives and requirements of the new approach

We first define the goals that we want to pursue through the development of a new approach. Before diving into the short-term goals in this work, we start from identifying the longer-term objectives of an ideal turbulence model.

3.6.1 Long-term objectives for an ideal model

Due to the strongly application-oriented motivation of this work, a list of ideal goals is considered useful to understand if the identified shorter-term objectives are leading towards a useful research direction.

Firstly an ideal turbulence model should accomplish all of the criteria defined by Pope (2000):

- Level of description
- Completeness
- Cost and ease of use
- Range of applicability
- Accuracy

As opposed to the ideal model, a real turbulence model to be used in a given application is chosen based on a tradeoff, as described in Section 1.2. Conversely, an ideal model would not require any selection process. It would adapt automatically to any given application. It would deactivate itself and operate as DNS at the limit of a suitable fine grid, and it would apply statistics to model scales, seamlessly and increasingly, as the grid gets coarser. This gradual change would optimize results not only based on the size of cells, but also on their shape.

3.6.2 Short-term objectives of the present work

The proposed approach aims at achieving a higher flow description and accuracy than URANS and lower computational cost than LES like other hybrid models attempt to do. Also, this work aims at providing a noticeable increase in robustness compared to existing hybrid approaches. The industrial applications' needs motivate the interest in achieving robustness. The term URANS is used here referring to linear and NLEVM k-ε formulations. This work deals with high-Re turbulent flows, which are those most encountered in engineering applications.

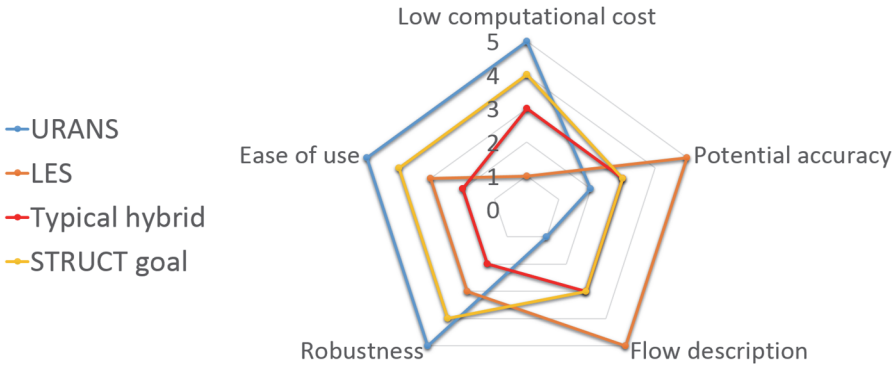

Figure 3.14 Qualitative objectives of the present work compared to other models

The paragraphs below discuss the selection of the scores provided for each category in Figure 3.14.

Potential accuracy

The score for potential accuracy identifies the capability of a model to describe time-averaged fields. The highest score is assigned to LES and the lowest one to URANS. The target performance of hybrid models, including the one proposed here, is intermediate between those two model families.

Unlike many other hybrid models, the one proposed here does not aim at reverting to LES in the fine-mesh limit. The LES-convergence capability may be sought after in future work. Hybrid models with this capability can be given the same score for potential accuracy as LES in the trivial case in which the grid and subsequent computational cost are increased to LES-like level.

Low computational cost

The qualitative score assigned to the capability to run at low computational cost is maximum for URANS and minimum for LES. Hybrid models have an intermediate score between those two. The present work aims at achieving lower cost than most hybrid formulations such as DES, ELES, SAS. Those models often require an LES-like grid in massively separated regions to operate in LES-like mode, as shown in Section 3.2.2 (Gritskevich et al., 2014). The goal here is to avoid this requirement and to design the new approach to function on coarser grids.

The new approach needs to be local, to minimize computational cost. Therefore, the equations solved at each computational node should only depend on values at the same node and local derivatives. This feature allows for efficient operations and parallelization.

Robustness

The word robustness is used here referring to the capability of a numerical model to tolerate small perturbations of simulation conditions without producing vastly different results. The opposite end of the spectrum is a chaotic system, in which small perturbations produce a large change in results. Robustness is a concept of utmost importance in industrial models. This work uses the term robustness to identify a mix of desirable qualities for applications in industry:

- Capability to achieve numerical convergence in complex geometries
- Low sensitivity to small changes in simulation conditions, e.g. grid size and cell geometry, inlet boundary condition profiles, type of solver
- Capability to converge to a consistent result as the grid is refined

The top robustness score is given to URANS, referring mainly to k-ε models, linear or nonlinear. Hybrid models are given the lowest score, due to the limitations discussed in Section 3.2. The score for LES is higher than that for hybrid models but still low compared to URANS, due to sensitivity to the grid and boundary conditions. A goal in the present work is to achieve a level of robustness higher than for LES. This objective is sought after by preserving many URANS features through the use of a defensive strategy, which is discussed further in Section 4.6.1.

This work focuses on the needs of the industrial CFD community, thereby aiming at investigating only models that are likely to be useful for applications. As a matter of fact, most industrial users are keen to adopt only robust models because non-robust alternatives imply additional testing and sensitivity studies, expensive both regarding man-hours and CPU-hours.

Flow description

Because of their statistical definition, URANS models are incapable of describing the spectral content of the most energetic eddies, so they are unsuitable for quantitatively studying vibrations and other phenomena driven by turbulent fluctuations. Therefore, Figure 3.14 assigns to URANS the lowest score in the evaluation of flow description, while the highest score is assigned to LES. Hybrid models aim at a flow description intermediate between those two, which is also a goal of the present work.

The inability of URANS to resolve the complex spectral content of unsteady flows is common to all URANS formulations, including higher-order RSMs. This limitation is a consequence of the ensemble averaging operation on which the models are based rather than approach-specific details.

The flow description of a model could be related to its accuracy in describing time-averaged flow parameters in complex geometries in which resolved structures play an important role. This link can also occur in cases in which significant FSI occurs in the turbulent spectrum range.

Ease of use

Ease of use is one of the factors driving the industrial success of a model. This quality includes: being consistent with models used in the past, being easy to learn and to implement in mainstream codes, being not susceptible to convergence problems. The k-ε model is easy to use due to its robustness and can even tolerate uncertainties in inlet turbulence specifications without producing an excessive error. Therefore, Figure 3.14 assigns to URANS top score. The lowest score is assigned to hybrid models, due to their limitations described in Section 3.2. The high error in the SAS results for a blind benchmark shown in Section 3.2.2 provides an example of this.

A score of 3 is assigned to LES because of contrasting reasons. On the one hand, significant experience exists in the industry in applying LES to suitable flow cases. On the other hand, LES requires significant care in inlet boundary conditions and grid specifications. Moreover, the high computational cost related to LES can produce significant delays in preliminary test-runs, and setting up a well-posed LES simulation in complex geometries could pose major challenges.

The present work aims at achieving a score of 4 by leveraging the ease of use of URANS, especially regarding boundary conditions and grid requirements.

The ease-of-use goal is related to completeness. Completeness is the feature of a turbulence model that does not require any case-dependent parameter to be set before running the simulation. As an example, the mixing length model is not complete because it requires knowledge of the mixing length parameter. High sensitivity to boundary conditions undermines the generality of a model in a way that resembles a lack of completeness. The main turbulence models used in engineering are all complete. The completeness challenge is addressed here in Chapters 7 and 8.

3.6.3 Properties expected from a turbulence model

Before introducing the new approach, it is important to discuss general properties that are expected from a suitable turbulence model. We can divide the properties into physical and numerical ones.

Physical properties

Following Pope (2000), a model in order not to be incorrect requires consistency with the transformation properties of the Navier-Stokes equations. Let us list important properties needed for this consistency (Pope, 2000; Sagaut, 2006):

- Reynolds-number similarity is the property of the Navier-Stokes equations of producing the same results for flows with the same Reynolds number, in terms of dimensionless variables.
- Time and space invariance implies that an experiment must provide the same results if shifted in time or space.
- Frame rotation and reflection invariance describe the property of the Navier-Stokes equations of being invariant to rotation or reflection of the frame of reference. A flow does not change if we look at it through a mirror.
- Galilean invariance is an important condition in classical physics. It implies that we must be able to describe the same phenomenon in all inertial frames. An experiment conducted on a constant-velocity flying plane must provide the same result as if the aircraft was on land, regardless of whether the experiment is described from the plane or the land.
- Asymptotic behavior implies that the model must have the same asymptotic behavior as the Navier-Stokes equations (Sagaut, 2006).

Numerical properties

A turbulence model with desirable physical properties can be used successfully in applications only if its numerical properties are favorable. Key properties are (Sagaut, 2006):

- Acceptable computational cost, implying that the number of operations per iteration is reasonably low. If a complex model introduces too high of a computational cost, such a model could become less desirable and costlier than a simpler LES run on a finer grid.
- Capability to run effectively in parallel, implying that the turbulence model must be local in time and space. The transfer of data required for non-local operations would represent a computational bottleneck.
- Capability to keep the computation stable. This requirement does not favor models with a large number of tightly coupled transport equations. Diffusive terms in equations are helpful to achieve greater stability.
- Insensitivity to the spatial and temporal discretization. Small changes in discretization must not alter the physical effects described by the model.

3.7 Discussion

The limited use of hybrid models in the industry can be justified based on a risk-related rationale. Risk can be defined as the product of the probability of a given outcome and effect thereof. Hybrid turbulence models aim at achieving high performance in flow description and accuracy. However, those models have a nonzero probability of breaking down and producing a significant error. Even if the probability of such an outcome were low, its large effect would produce a significant overall risk. We can see examples of this behavior in the analysis in Section 3.2. On the other hand, the most robust URANS models combine a lower expected performance with a low risk of producing a significant error. Engineering applications favor low-risk methods, so robust URANS models are often chosen. Indeed, robustness is identified as a key area of improvement to increase the industrial use of hybrid models. The features of URANS discussed in the present chapter are all related to two-equation linear or nonlinear models, without mentioning RSMs. Future work could extend this analysis to RSMs while here those models are not discussed due to the limitations mentioned in section 2.3.6.

4 Proposing the STRUCT approach

4.1 Chapter overview

The following chapters will introduce, implement and test the STRUCT approach. The logical flow is outlined in Figure 4.1 below. Along those chapters, the STRUCT concept is described, implemented into a numerical solver, demonstrated, extended to complete formulations, and tested.

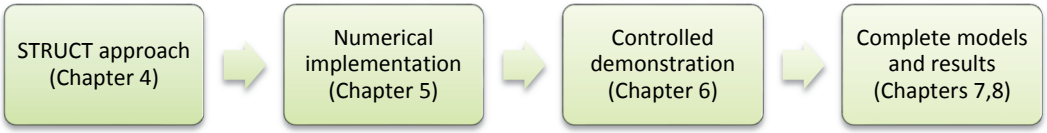

Figure 4.1 Logic used in this work for describing and testing the STRUCT approach

The present chapter begins by introducing the framework and equations for the STRUCT approach and by discussing the physical properties of the formulations used. Then, strategies are identified for the closure of the model and observations are made on the general behavior of the approach.

4.2 General framework

Many hybrid turbulence models proposed in the literature are derived from modifying URANS models with formulations that control the amount of modeled versus resolved scales. This approach can be illustrated by using the following general formulation:

$$r = \begin{cases} 1 & , \quad h \leq 1 \\ \phi & , \quad h > 1 \end{cases} \tag{4.1}$$

Parameter r is the ratio between the TKE modeled by the hybrid turbulence closure and the TKE modeled by URANS. Parameter ϕ is a reduction coefficient and h an activation parameter triggering hybrid turbulence. In the most generic formulation, the two parameters ϕ and h are arbitrary functions of space and time.

The definition used in this work for the activation parameter h is shown in the following section. Such a parameter determines whether the modeled-to-total TKE ratio is 1 or is regulated by ϕ. The former condition corresponds to URANS and the latter to hybrid mode. The choice of parameter ϕ is discussed later on, in Section 4.5.

4.3 Activation parameter, h

The early stages of this work have devoted significant effort to identifying a viable formulation for parameter h, seeking after the goals and rationale discussed in Chapter 3.

The selected concept is based on detecting resolved flow scales with a formulation that leverages the second invariant of the resolved velocity gradient tensor.

Such a parameter is defined as:

$$\overline{II} = -\frac{1}{2}\frac{\partial \bar{u}_i}{\partial x_j}\frac{\partial \bar{u}_j}{\partial x_i} \tag{4.2}$$

This choice is motivated by desirable properties identified in multiple domains, among which:

- Capability to describe regions of poor URANS performance due to lack of applicability of the scale-separation assumption
- Capability to avoid model activation in regions of simple shear flow near walls, as done in many hybrid models
- Capability to describe complex topology structures of the flow and apply partial resolution of turbulence locally
- Capability to describe regions of poor URANS performance due to flow conditions tending to the rapid distortion limit

The definition used here for h is the following:

$$h \equiv \frac{f_\mathrm{r}}{f_\mathrm{m}} = t_\mathrm{m} f_\mathrm{r} \tag{4.3}$$

where f_r and f_m both have the units the inverse of a time scale, i.e. a frequency. Those two fields are working parameters of the STRUCT approach referring respectively to the resolved and to the modeled scales of turbulence. The working variable for the resolved scales is hereby defined as

$$f_\mathrm{r} \equiv \sqrt{|\overline{II}|} \tag{4.4}$$

The working variable for the modeled flow can be expressed as a frequency f_m or as a time scale $t_\mathrm{m} = 1/f_\mathrm{m}$. Its definition is

$$\frac{1}{f_\mathrm{m}} = t_\mathrm{m} \equiv \langle t_{\mathrm{m},0} \rangle \tag{4.5}$$

where the chevrons represent a generic averaging operation, defined in the remainder of this work, applied to a parameter providing information on the modeled turbulent scales. In k-ε models let us define $t_{\mathrm{m},0}$ simply as

$$t_{\mathrm{m},0} = \frac{k_\mathrm{m}}{\varepsilon} \tag{4.6}$$

Those formulations respect the basic properties required by a model, discussed in Section 3.6.3. We can start by discussing the properties of f_r and the strategies for the generic averaging operation in (4.5) in Section 4.4.

Important properties of parameter f_r as defined in (4.4) are:

- Property 1: description of resolved flow scales
- Property 2: description of simple shear flows
- Property 3: description of flow topology structures
- Property 4: identification of the rapid distortion limit

Those properties are discussed separately in the following sub-sections. Moreover, a link between the second invariant and Poisson's equation for pressure is discussed in Appendix A.1.

4.3.1 Property 1: description of resolved flow scales

One of the properties of the formulation used here for h the capability to describe resolved flow scales and compare them to modeled flow scales through the relation in (4.3). Such a comparison is used to trigger the switching condition in (4.1) and to determine the hybrid model's behavior.

The condition of the resolved frequency being larger than the modeled one represents a case with a significant lack of scale separation. Such a condition is not expected to be represented appropriately by a URANS model. Instead, the STRUCT approach aims at identifying those regions through its two working parameters and at triggering local hybrid behavior. This logic is described in the simplified scheme of Figure 4.2 below.

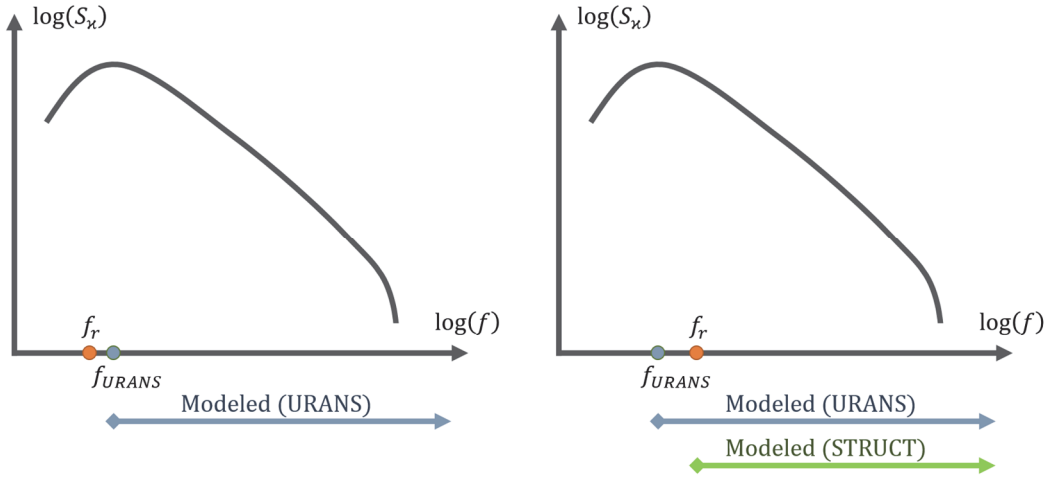

Figure 4.2 Idealized turbulent cascade and activation condition

The figure shows two plots with an idealized energy cascade. The plot on the left represents a typical case of scale separation, in which the frequency of resolved fluctuations, f_r, is smaller than the frequency of modeled fluctuations, f_m. The plot on the right represents overlap between those two frequencies. In such a case, flow scales are resolved at a frequency higher than the one of modeled turbulence. This situation violates the assumptions of URANS.

It is worth here taking the time to describe further the scale separation implications of URANS, before analyzing the use made here of the second invariant of the resolved velocity gradient tensor.

Implications of the scale-separation assumption

The applicability of URANS to complex flows is limited by its scale-separation assumption.

RANS models have been developed initially to be used in steady-state simulations in which turbulent fluctuations are statistically stationary, so resolved flow variables are constant in time while the statistical effect of residual scales is modeled. When going from RANS to URANS, the same statistics used for RANS are assumed to be valid in time-dependent flow cases.

The underlying requirement of statistically stationary residual turbulence implies that variation of resolved variables is slow compared to residual turbulent fluctuations. The term slow indicates that a spectral gap has to exist between resolved and modeled frequencies, as shown in Figure 4.3 below (Adams, 2006).

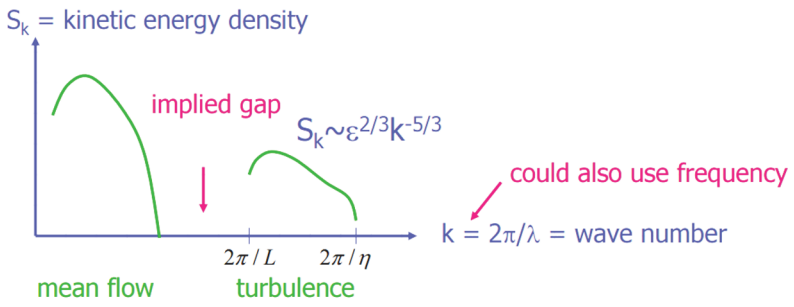

Figure 4.3 Implied gap between scales in URANS, qualitative plot from Adams (2006)

Basic URANS models are not meant to be applied in cases in which residual fluctuations are far from being statistically stationary. This condition includes flows with large-scale anisotropic vortical structures (Fröhlich and Von Terzi, 2008), curvature, swirl (Argyropoulos and Markatos, 2014), strong buoyancy, intermittency. Such cases are very frequent in engineering applications, in which it is often not affordable to resort to LES when looking for higher accuracy.

As an example, a pipe flow with slowly varying inlet velocity is characterized by scale separation. On the other hand, scale separation does not typically occur in bluff body flows. In this case, large structures are produced near the obstacle and are transported with the flow, breaking into smaller and smaller ones. Bluff body flows are usually not suitable for URANS models.

Many authors have observed limitations of URANS in complex flows. Speziale (1991) noted that most of the limitations of two-equation URANS models are due to the intrinsic assumption that a sharp separation of scales exists at the Reynolds stress tensor level. Other authors (Hedges et al., 2002; Travin et al., 2004) stated that the scale-separation assumption makes URANS dubious since it implies a separation between coherent and random eddies. Such an implication is only valid in very simple cases, not in general industrial flows.

Second invariant of the resolved velocity gradient tensor

The second invariant of the resolved velocity graduate tensor is one of the simplest parameters describing properties of the resolved velocity vector field. Such a parameter is suitable for turbulence modeling because it is a scalar with the following properties:

- Galilean invariance
- Frame-rotation invariance
- Local description in time and space

We can start from considering the three principal invariants of the resolved velocity gradient tensor.

The eigenvalues of tensor $\bar{\mathbf{A}}$ are determined by solving the following equation:

$$\det(\bar{\mathbf{A}} - \lambda \boldsymbol{I}) = 0 \tag{4.7}$$

The three principal invariants of the resolved velocity gradient tensor derive from:

$$\lambda^3 + \bar{I}\lambda^2 + \bar{II}\,\lambda + \bar{III} = 0 \tag{4.8}$$

The first principal invariant is:

$$\bar{I} = -\mathrm{tr}\bar{A}_{ij} = -\bar{A}_{ii} = -\bar{A}_{11} - \bar{A}_{22} - \bar{A}_{33} = -\lambda_1 - \lambda_2 - \lambda_3 \tag{4.9}$$

The second is:

$$\overline{II} = \frac{1}{2}\left(\left(\mathrm{tr}\bar{A}_{ij}\right)^2 - \mathrm{tr}\left(\bar{A}_{ij}\bar{A}_{ij}\right)\right) = \lambda_1\lambda_2 + \lambda_2\lambda_3 + \lambda_1\lambda_3 \tag{4.10}$$

The third is:

$$\overline{III} = -\mathrm{det}\bar{A}_{ij} = -\lambda_1\lambda_2\lambda_3 \tag{4.11}$$

The first principal invariant is zero for incompressible flows, due to the continuity condition. In the equation for the second invariant, the incompressible-flow assumption cancels out the term containing the trace of $\bar{A}_{ij}$, yielding:

$$\overline{II} = -\frac{1}{2}\mathrm{tr}\left(\bar{A}_{ij}\bar{A}_{ij}\right) = -\frac{1}{2}\bar{A}_{ij}\bar{A}_{ji} \tag{4.12}$$

The resolved velocity gradient tensor can be decomposed into the sum of two tensors: a symmetric and a skew-symmetric part. Those two parts are defined in (2.17) and have the following properties:

$$\bar{S}_{ij} = \bar{S}_{ji} \quad , \quad \bar{\Omega}_{ij} = -\bar{\Omega}_{ji} \tag{4.13}$$

The relation in (4.12) becomes thus:

$$\overline{II} = \frac{1}{2}\left(\bar{\Omega}_{mn}\bar{\Omega}_{mn} - \bar{S}_{mn}\bar{S}_{mn}\right) = \frac{1}{4}\left(\bar{\Omega}^2 - \bar{S}^2\right) \tag{4.14}$$

The scalars representing the absolute values of resolved strain and resolved vorticity are:

$$\bar{\Omega} = \sqrt{2\bar{\Omega}_{ij}\bar{\Omega}_{ij}} \quad , \quad \bar{S} = \sqrt{2\bar{S}_{ij}\bar{S}_{ij}} \tag{4.15}$$

The present work uses the second invariant, being the simplest nonzero invariant. Its square root has the units of frequency. Other approaches could consider the option of using the third invariant; however, its complexity requires higher computational effort.

As shown in (4.14), the second invariant has positive or negative values depending on the gradients of resolved velocity. In particular, values of $\overline{II}$ are positive in regions dominated by rotation and negative in regions dominated by strain. The working variable describing a resolved flow frequency used in (4.4) is a nonnegative parameter and uses the absolute value of $\overline{II}$, thereby not distinguishing shear regions from rotation ones, but conveying only information on a characteristic frequency.

4.3.2 Property 2: description of simple shear flows

As already discussed, it is desirable for a hybrid model not to act in the scale-resolving mode in regions of simple shear flow, where URANS can provide an accurate and robust solution. On the contrary, hybrid activation should only be triggered in regions of strong deformation. The formulation chosen here enforces this principle very naturally, where the parameter f_r has low values in quasi-steady shear layers. This is easily demonstrated as for simple shear flows:

$$\bar{S} = \bar{\Omega} = \frac{1}{2}\left|\frac{\partial\bar{u}}{\partial y}\right| \tag{4.16}$$

As a result, the parameter defined in (4.4) is null, yielding URANS behavior of STRUCT in simple shear layers near the wall.

The use of URANS in those regions is considered appropriate, as confirmed by similar choices made in most of the other hybrid models. The effectiveness of this concept can be observed in the results' sections in Chapters 6, 7, and 8.

4.3.3 Property 3: description of flow topology structures

An additional interpretation for the second invariant of the resolved velocity gradient tensor is related to flow topology. Indeed, the second invariant is often referred to as Q criterion and used extensively in the literature to gather an understanding of the physical structure of turbulence.

Many topology studies do not imply an averaging operation, so instead of referring to the resolved second invariant, $\overline{II}$, they refer to the instantaneous one, II, defined as:

$$II = -\frac{1}{2}\frac{\partial u_i}{\partial x_j}\frac{\partial u_j}{\partial x_i} \tag{4.17}$$

The literature uses this parameter to define eddies, shear regions, and to characterize topology elements known as coherent structures. A question that may arise is whether the topology studies for II be also valid for $\overline{II}$. This is not strictly the case, because the two parameters are significantly different: $\overline{II}$ is calculated based on resolved quantities and depends on the overbar averaging operation chosen, while II is calculated based on instantaneous quantities.

A theory for high-Re flows has been formulated by Muschinski (1996), describing the resolved flow deriving from LES equations. The resolved flow is described as the DNS solution of an equivalent non-Newtonian fluid, called 'LES fluid.' This theory can be extended to URANS (Sagaut, 2006), or to the resolved field in a hybrid model. When we analyze parameter $\overline{II}$ instead of II we look for structures in the equivalent 'resolved fluid'. Correspondence between resolved structures and instantaneous structures can only be made weakly, through a self-similarity hypothesis.

The identification of structures motivates the name given to the new approach. The name STRUCT is the truncation of structure-based hybrid activation. Given the relevance of the concept, it is worth here providing a brief discussion of coherent structures.

Coherent structures: identification and visualization

The formulation chosen for f_r uses parameters widely adopted in the literature to describe flow topology structures. A common name used throughout the literature is that of coherent structures.

Such a concept derives from the observation that in turbulent flows vortical structures can survive for a time larger than the local time scale of turbulence (Sagaut et al., 2013). This evidence suggests that turbulence is not entirely random but contains deterministic features (Tryggeson, 2007). Those features, as described by Hussain (1983), are quasi-deterministic structures randomly distributed in space and time. They appear as quasi-periodic repeating patterns (Robinson, 1991). For example, eddies downstream flow separation have similar shapes (Sagaut et al., 2013). An interesting comparison between coherent structures and galaxies was made by Lesieur and Mankbadi (1988). As an example, we can look at the measurement of coherent motions in the wake of a wind turbine, as presented by Hong and co-workers (2014). Those authors used natural snowfall and a light source to perform particle-image velocimetry (PIV) acquisitions. The flow structures of interest can be seen in the photo shown in Figure 4.4.

The concept of coherent structure has been discussed in the literature for decades. Still, no universal agreement exists on the definition of coherent structures. However, extensive evidence shows that coherent structures play a relevant role in turbulence. When studying turbulence, it is common to find concepts without a universal definition, due to our lack of full understanding of the properties of the equations. In fact, no universally accepted definition exists even to distinguish turbulence from a complex laminar flow (Mathieu and Scott, 2000). Nevertheless, we recognize the importance of predicting turbulence in engineering systems. Coherent structures have been studied to describe many phenomena, including macroscopic features such as drag and vibrations.

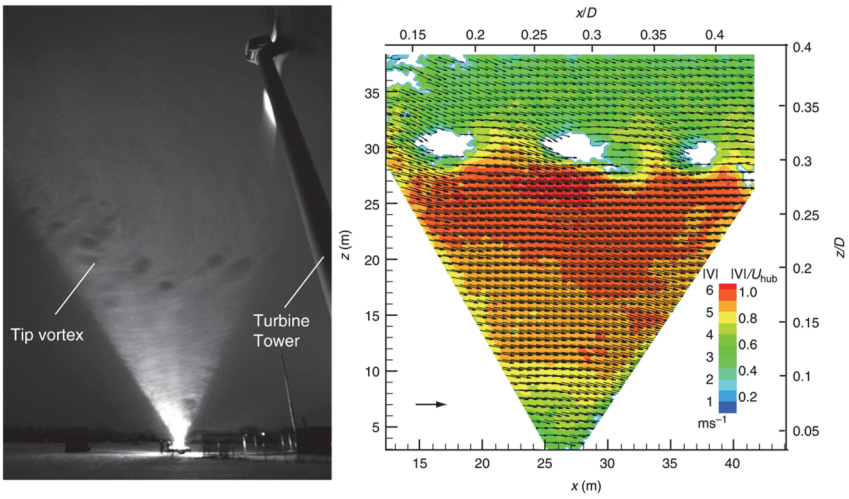

Figure 4.4 Photo (left) and instantaneous velocity measurements (right) of flow structures in the wake of a wind turbine, from Hong and co-workers (2014)

While no universal definitions exist, several attempts have been made by researchers. As an example, Hussain (1983) defined a coherent structure as:

"[...] large-scale turbulent fluid mass with a phase-correlated vorticity over its spatial extent."

Robinson (1991) provided another definition:

"For the present paper, a coherent motion is defined as a three-dimensional region of the flow over which at least one fundamental flow variable (velocity component, density, temperature, etc.) exhibits significant correlation with itself or with another variable over a range of space and/or time significantly larger than the smallest local scales of the flow."

The phase-correlation property is what makes those structures coherent, distinguishing them from other regions with high vorticity. Structures that are not coherent can be defined as phase-random motions (Hussain, 1983). A triple decomposition has been used by Hussain (1986) using a phase-averaging operation. This operation decomposes velocity into a coherent and an incoherent part.

Many authors describe turbulence as made of phases with different intensities. Those phases can take the form of bursts and lulls. This type of organization may suggest that the time-averaging operation in turbulence models is un-natural (Spalart, 2015).

Several studies exist in the literature identifying flow structures based on invariants of the velocity gradient tensor. Those methods are capable of identifying flow features instantaneously and locally in a given realization. Due to the property of being local in space and time, those methods are suitable for being used efficiently in CFD.

Hunt, Wray and Moin (1988) identified regions defined as eddy zones and convergence zones based respectively on values of II below a certain negative threshold and above a certain positive one. Rousseaux and co-workers (2007) identified vortex cores as circular regions around a vorticity peak having positive values of II.

A turbulence model based on coherent structures was proposed by Kobayashi (2005) as a SGS closure for LES. This model uses parameter $\overline{II}$ to detect the structures and modify its parameters.

Invariant-based methods are capable of describing coherent motions in structures of all sizes. However, they do not offer the advantage of extracting whole structures, as in proper orthogonal

decomposition (POD) (Kevlahan et al., 1994). The POD method is described by Aubry (1991). Disadvantages of the POD method for coherent structures have been observed in the literature. For example, Kevlahan, Hunt and Vassilicos (1994) concluded that a flow structure can be identified in the first eigenmode only if it contains most of the captured energy.

Other methods for visualizing coherent structures in addition to invariant methods and POD include the ones listed below (Hudgins and Kaspersen, 2004).

- Quadrant analysis
- Conditional sampling and stochastic estimation
- Variable-interval time average (VITA)
- Window average gradient (WAG)
- Wavelet-based methods

It is recognized in the literature that Fourier representation alone does not provide a suitable description of coherent structures (Farge et al., 1999).

4.3.4 Property 4: identification of the rapid distortion limit

The development of turbulence models has leveraged for a long time the analysis of homogeneous decaying turbulence. Strong deviations from homogeneity conditions have been studied historically using rapid distortion theory (RDT). This theory describes the short-term behavior of turbulence subjected to fast deformation. When distortions of the flow are rapid, the nonlinear and viscous terms of the equations can be neglected. The eddy-viscosity assumption is not appropriate for complex flows undergoing rapid deformation. The term fast refers to deformations with small time scales compared to those of turbulence. See Hunt and Carruthers (1990) for a review of RDT.

The rapid distortion limit is the condition in which the time scale ratio $\bar{S}^*$ between turbulence and resolved shear rate is significantly larger than 1 (Lee et al., 1990). For flows with solid body rotation, the dimensionless parameter defining rapid deformation is $\bar{\Omega}^*$ and can be defined based on resolved rotation rate (Pope, 2000). Those two parameters are:

$$\bar{S}^* = \frac{\bar{S}}{f_{\mathrm{m},0}} \quad , \quad \bar{\Omega}^* = \frac{\bar{\Omega}}{f_{\mathrm{m},0}} \tag{4.18}$$

The activation criterion used in this work can be interpreted as a combination of the criteria in (4.18). Regions with significant strain or large rotation alone will both have a large value of f_{r}.

As commented by Spalart (2015), conventional eddy-viscosity models are probably unable to produce accurate RDT behavior. One of the reasons for this is that structures exist in the flow that respond to rapid deformation with a delay (Kassinos and Reynolds, 1997). The hybrid activation approach proposed here aims at identifying regions of poor URANS performance.

As mentioned in Section 2.3.6, resolved flow variables in NLEVMs can be described as the instantaneous flow variables for an equivalent non-Newtonian viscous fluid (Lumley, 1970). If such an equivalent flow is laminar, the resolved flow is stationary or varies slowly. This case occurs in quasi-homogeneous regions, in which URANS NLEVM solutions are appropriate. In other cases, the resolved flow may undergo rapid variations that could eventually transition into turbulence of the equivalent flow. Those rapid variations may cause NLEVMs to provide inaccurate results.

RSMs can be successful in predicting the rapid variation of resolved flows (Pope, 2000). However, this work does not use RSMs for the reasons discussed in Section 2.3.6.

4.4 Strategies for the averaging operation

The previous section has discussed properties of parameter f_r as used in the STRUCT formulation. Now, two elements are left to be defined in order to close the model. One is the averaging operation used in (4.5), and the other one is the reduction parameter ϕ. Those two elements are discussed in the present two sections, starting with the averaging operation.

The product between f_r and t_m in (4.3) compares two working variables defining resolved and modeled scales. The activation criterion for the STRUCT approach in (4.1) is driven by the overlap between those two scales. While the expression for f_r derives directly from local resolved fields, the one for t_m is derived based on an averaging operation. Such an averaging operation has been assumed as generic so far, and needs definition. Among possible options, we can consider averaging in time, in space, ensemble averaging, and no averaging.

At first, this work has considered the option of not performing the averaging at all, thus using local instantaneous values of $t_{m,0}$ in (4.3). Such a strategy has shown in preliminary tests to be only suitable for very simple flow cases, while nonphysical unstable solutions are produced in more complex ones.

Conversely, the use of an averaging operation allows us to compare f_r with a value for t_m that is robust and stable but still carries relevant information on the modeled flow scales occurring within the size of a resolved eddy. The averaging operation aims at providing a solid and smooth denominator to the relation in (4.3). Preliminary tests have shown that small variations of t_m within the same order of magnitude do not introduce significant error in the solution.

The first milestone in this work uses a controlled formulation, in which a constant value for t_m is obtained by calculating the average of $t_{m,0}$ from preliminary URANS simulations. Application of such a controlled approach is meaningful only for basic flows, not for flows involving complex local phenomena. Results are shown in Chapter 6. This first milestone is considered important in the present work, because it demonstrates the physical validity of the basic STRUCT formulation regardless of the choice of the complete closure. Such a first milestone may also serve as a starting point for future work to introduce different complete closures. As a second milestone, two complete formulations are proposed. Those formulations use local approaches to calculate the average needed to determine t_m in every cell and time step. The two complete models are described in Chapter 7 and in Chapter 8.

4.5 Strategies for the reduction parameter, ϕ

The reduction parameter ϕ prescribes the ratio of resolved versus total TKE in regions of STRUCT hybrid activation. Different strategies are followed in different parts of this work.

The two initial tests, made in Chapter 6 and 7, focus on the selection of parameter h rather than on the determination of an optimal formulation for the reduction parameter ϕ. As a consequence, simulations use constant values for ϕ.

In the case of Chapter 6, such a variable is optimized a posteriori. Chapter 6 does not test a complete model but demonstrates the potential of the core STRUCT idea, opening the way to the development of complete closures.

In our first complete attempt, in Chapter 7, the focus is still mostly on the activation parameter effectiveness, while parameter ϕ is set as a constant in all simulations equal to a robust value of 0.6.

Finally, the complete model presented in Chapter 8 identifies an automatic formulation for ϕ. Simulations from that chapter are characterized by a continuous variation of ϕ in STRUCT activation regions.

4.6 Observations on the STRUCT approach

4.6.1 Defensive strategy

The STRUCT approach can be distinguished from many other hybrid approaches because of its defensive nature. The approach aims at maintaining the robust capabilities of URANS while extending them by adding partial resolution of turbulent scales in regions where URANS is weaker. The proposed approach shares similarities with SAS in that it compares resolved and residual scales to trigger the hybrid formulation without reference to the grid size. However, the similarities are mostly apparent. Instead, the model is conceptually very far from the von-Kármán-length-scale-based SAS. In many published tests of SAS, URANS mode is used near the wall while SAS mode is triggered outside the boundary layer. Fine-enough grids far from the wall are often capable of producing a behavior that resembles LES. Differently from SAS, the newly proposed approach does not enable a scale-resolving mode even on a very fine grid, unless scale-overlap regions are detected. Once again this defensive behavior is key to the robustness of the model. Many hybrid models are based on the idea of using LES far from the wall and URANS near the wall, or on variants of this logic. Many hybrid models can be considered as advanced versions of WM-LES. Conversely, this work focuses on leveraging the robustness of URANS. Unlike many other hybrid models, the hybrid trigger is not related necessarily to the presence of a wall. This feature makes STRUCT likely to be particularly suitable in complex internal flows, in which no clear distinction exists between wall-influenced and non-wall-influenced regions.

4.6.2 Resolved versus modeled scales

We now discuss the resolved and modeled scales of turbulence described by STRUCT. Length scales in turbulent flows span several orders of magnitude. The ratio between the most energetic and the smallest active length scales is roughly (see for example Sagaut, 2006):

$$\frac{L}{L_{\mathrm{K}}} = O\left(\mathrm{Re}^{3/4}\right) \tag{4.19}$$

The ratio between the largest and smallest time scales is (Durbin and Pettersson Reif, 2011, p. 18):

$$\frac{T}{T_{\mathrm{K}}} = \frac{k/\varepsilon}{\sqrt{\nu/\varepsilon}} = \sqrt{\frac{k^2}{\varepsilon\nu}} = \sqrt{\mathrm{R_T}} \tag{4.20}$$

The turbulent Reynolds number, $\mathrm{R_T}$, indicates how large the separation between time scales is. Let us make a figurative example of the length scales spanned in a turbulent flow. A flow with Re of the order of 10^5 would span about four orders of magnitude in length scales. This span is comparable to that of a 10-m-tall tree with 1-mm-long smaller blossoms. A drawing of such a tree in Figure 4.5 shows the strategy of different approaches in predicting turbulence. The size of branches corresponds to the size of eddies. Resolved scales are in full color while residual scales are faded.

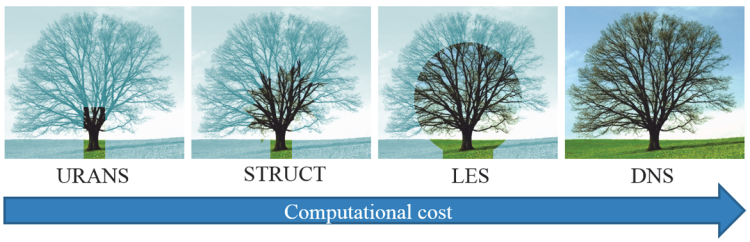

Figure 4.5 Simple illustration of the new approach's rationale

The two extremes of the figure are URANS and DNS. In the former most scales are modeled while only the tree trunk and a few larger branches are resolved. Conversely, DNS resolves all of the scales of turbulence and corresponds to the highest computational cost. By modeling smaller branches, LES achieves a lower computational cost than DNS.The boundary between colored and faded branches for LES is drawn as circular since the filter is set to cut off scales below a prescribed size. The strategy of the new approach is portrayed as an irregular shape defining the boundary between resolved and residual scales. The STRUCT approach models more scales than LES does, thus reducing grid requirements and computational cost. At the same time, selected "branches" are resolved to a greater extent than in URANS, to achieve higher accuracy and flow description. Those selected branches represent the flow structures providing poor anticipated URANS predictions.

4.6.3 Influence of computational grid

A beneficial characteristic of URANS models is their low sensitivity to computational grid resolution. In proximity of grid convergence, results are not significantly sensitive to grid size changes. The negative aspect is that the solution will not increase its accuracy significantly as the grid is refined beyond reasonable convergence.

On the other hand, most LES solvers use a filter width related to the grid size. This choice translates into a significant sensitivity of LES results to changes in grid size and cell geometry. Many hybrid turbulence models use formulations containing the grid spacing, and a subset of those are designed to perform as LES in specific regions. This dependence of the model on grid spacing is a cause of grid sensitivity and may undermine robustness.

Users of models in the DES family do not have significant freedom in choosing the grid size to use in "detached" regions far from the wall. Those regions require a grid fine enough for LES (see for example Strelets, 2001). Therefore, such hybrid models do not gain significant advantages compared to LES in detached regions.

The present work aims at achieving robustness by re-introducing in the model the influence of all length scales that fall in between the URANS integral scales and the resolved LES scales. Figure 4.6 gives a qualitative picture of the STRUCT activation regions, where the largest modeled eddy is large enough to achieve low grid sensitivity but sufficiently small to allow resolving complex flow structures.

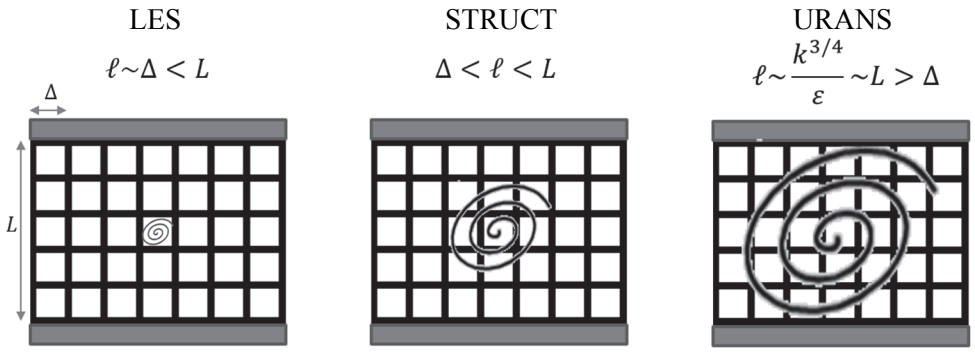

Figure 4.6 Graphical qualitative representation of the largest residual length scale in LES, in the new approach, and in URANS

It is clear that a consequence of the STRUCT method is that there will exist regions in the solution having a grid size smaller than the model's filter. While this means not leveraging all the potential

of the grid resolution, in contrast to LES, it introduces the fundamental benefit of reducing sensitivity to the cell aspect ratio and quality, which is key to large-scale industrial applications.

The model resolution independence from the mesh size has the potential to enable consistent grid convergence. As shown by Geurts (2006), LES grid convergence can be achieved using a constant filter size and reducing the grid size. This corresponds to a case in which the filter size is larger than the grid size, as illustrated in Fig. 4.6.

Fröhlich and von Terzi (2008), in their categorization of hybrid turbulence models, introduced the category of second-generation URANS models. Models in this category, which includes SAS and PANS, do not contain an explicit dependence on the computational grid size, thereby not being, strictly speaking, a combination of URANS and LES. In those models, LES equations are not solved. The STRUCT approach could be placed into this same category. Models of this kind do not revert to a strict LES formulation unless their implementation contains LES-like parameters. Those models are therefore not guaranteed to converge strictly to LES accuracy in cases in which a suitable grid is available.

4.7 Selection of the baseline URANS

The performance of a URANS-based hybrid simulations depends strongly on the suitability and accurate physical representation of the baseline URANS model.

The discussion on underlying RANS closure in Chapter 2 has made the point that two-equation turbulence models are currently the most reliable industrial approach, and are naturally also the most adopted, covering the largest possible spectrum of applications. In particular, the k-ε approach is selected here to leverage its overall consistency, where its limitations are mostly related to the linear eddy-viscosity assumption. These limitations are then addressed by the adoption of an accurate explicit representation of the stress-strain correlations rather than through an ad-hoc modification of the basic transport equations.

It is interesting to note that the importance of the selection of an effective URANS closure in the overall performance of a hybrid approach has been recognized very early. The pioneering hybrid turbulence model proposed by Speziale (1996), was for example based on a NLEVM rather than a linear model. Several studies in the literature show examples in which hybrid models based on NLVEMs achieve superior performance compared to the same hybrid models based on linear URANS. Gopalan and Jaiman (2015), for example, demonstrated increased accuracy of a hybrid NLEVM compared to its hybrid linear counterpart on a tandem cylinder flow. NLEVMs can achieve measurable advantages in terms of accuracy while preserving robustness, ease of use, low cost, and numerical stability. The computational cost of NLEVMs is only slightly higher that of linear formulations. Here we support the idea described by Hellsten and Wallin (2009) that linear URANS should be replaced completely with NLEVMs in industrial simulations.

In this work, the NLEVM formulation by Baglietto and Ninokata (2007, 2006) is selected, where the underlying nonlinear formulation was originally proposed by Shih, Zhu and Lumley (1993), and has become a common NLEVM standard. Coefficients have been reformulated by Baglietto and Ninokata leveraging a combination of experiments and DNS data, and demonstrating increased accuracy and generality on a large variety of test cases.

In the model, the residual stress anisotropy tensor equation is expanded by adding nonlinear terms to the linear formulation – in this case, quadratic q_{ij} and cubic c_{ij} ones:

$$a_{ij} = \tau_{ij} - \frac{2}{3} k_{\mathrm{m}} \delta_{ij} = \nu_{\mathrm{t}} \left(-2\overline{S}_{ij} + q_{ij} + c_{ij} \right) \tag{4.21}$$

The quadratic term used here is (Baglietto and Ninokata, 2007, 2006):

$$q_{ij} = 4C_1\frac{k_\mathrm{m}}{\varepsilon}\left[\overline{S}_{ik}\overline{S}_{kj} - \frac{1}{3}\delta_{ij}\overline{S}_{kl}\overline{S}_{kl}\right] + 4C_2\nu_\mathrm{t}\frac{k_\mathrm{m}}{\varepsilon}\left[\overline{\Omega}_{ik}\overline{S}_{kj} + \overline{\Omega}_{jk}\overline{S}_{ki}\right] + 4C_3\frac{k_\mathrm{m}}{\varepsilon}\left[\overline{\Omega}_{ik}\overline{\Omega}_{jk} - \frac{1}{3}\delta_{ij}\overline{\Omega}_{kl}\overline{\Omega}_{kl}\right] \tag{4.22}$$

The cubic term is:

$$c_{ij} = 8C_4\frac{k_\mathrm{m}^2}{\varepsilon^2}\left[\overline{S}_{ki}\overline{\Omega}_{lj} + \overline{S}_{kj}\overline{\Omega}_{li}\right]\overline{S}_{kl} + 8C_5\frac{k_\mathrm{m}^2}{\varepsilon^2}\left[\overline{S}_{kl}\overline{S}_{kl} + \overline{\Omega}_{kl}\overline{\Omega}_{kl}\right]\overline{S}_{ij} \tag{4.23}$$

If the cubic term is set to zero, the model can be used in its quadratic configuration. If both terms are set to zero, the model functions as a standard k-ε.

The non-constant model parameters used in the equations above are defined as follows:

$$C_\mu = \frac{C_{\mathrm{a0}}}{C_{\mathrm{a1}} + C_{\mathrm{a2}}\overline{S}^*} \tag{4.24}$$

$$C_1 = \frac{C_{\mathrm{NL1}}}{\left(C_{\mathrm{NL6}} + C_{\mathrm{NL7}}\overline{S}^{*3}\right)C_\mu} \tag{4.25}$$

$$C_2 = \frac{C_{\mathrm{NL2}}}{\left(C_{\mathrm{NL6}} + C_{\mathrm{NL7}}\overline{S}^{*3}\right)C_\mu} \tag{4.26}$$

$$C_3 = \frac{C_{\mathrm{NL3}}}{\left(C_{\mathrm{NL6}} + C_{\mathrm{NL7}}\overline{S}^{*3}\right)C_\mu} \tag{4.27}$$

$$C_4 = C_{\mathrm{NL4}}C_\mu^2 \tag{4.28}$$

$$C_5 = C_{\mathrm{NL5}}C_\mu^2 \tag{4.29}$$

Recall that the dimensionless parameters for resolved strain and rotation rates are defined in (4.18). The formulation used in (4.1) for the eddy viscosity is the same as in the standard k-ε model, shown in (2.29), except for the variable C_μ, which derives from (4.24). The model constants employed are derived from the work of Baglietto and Ninokata (2006), except that the coefficients C_{NL4} and C_{NL5} have been calculated in order to obtain agreement between the formulations by Baglietto and Ninokata (2006) and those in (4.28) and (4.29), in case of null resolved rotation and strain. Those constants are shown below.

Table V Cubic NLEVM coefficients

C_{a0}	C_{a1}	C_{a2}	C_{NL1}	C_{NL2}	C_{NL3}	C_{NL4}	C_{NL5}	C_{NL6}	C_{NL7}
0.667	3.9	1.0	0.8	11.0	4.5	-5.0	-4.5	1000.0	1.0

As an example, let us look at the streamlines in a simulation of flow past a square cylinder using a linear k-ε versus the selected NLEVM. Those results are shown in Figure 4.7 below. The linear model predicts excessive eddy viscosity in the region past the cylinder, resulting in dissipation of the resolved shedding. The more consistent turbulent levels predicted by the NLEVM allow for a more accurate physical description of those fluctuations.

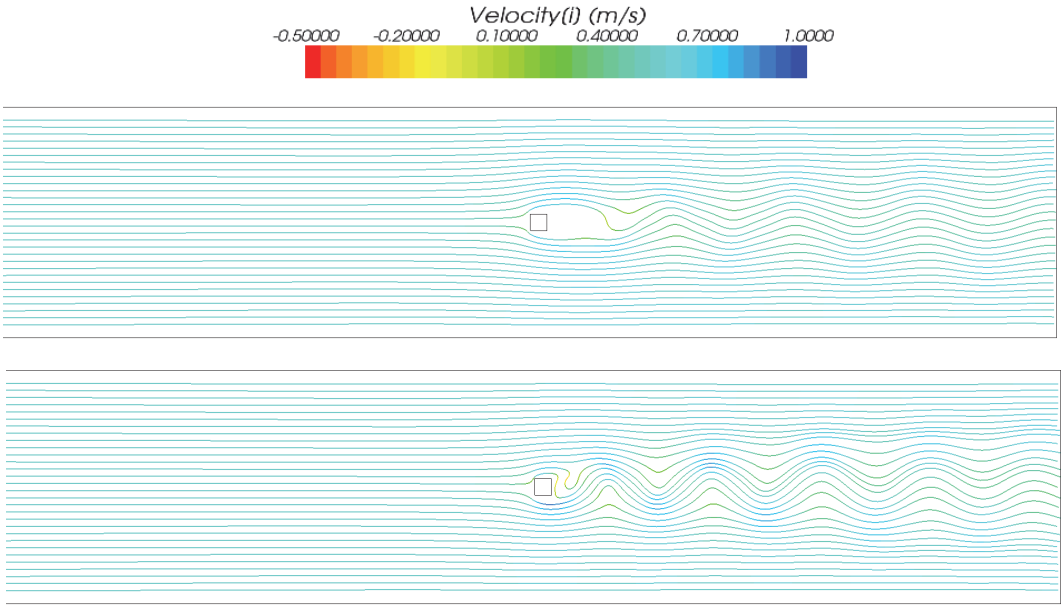

Figure 4.7 Streamlines colored based on x-component of velocity drawn on instantaneous results of linear k-ε (top) and cubic k-ε (bottom)

4.8 Discussion

This chapter has discussed several physical interpretations for identifying and selecting regions for STRUCT activation. We may notice in Section 4.3 that the rationale for the selected variables depends on the simultaneous validity of multiple properties. Interpretations based on those properties are different, and no universal theory exists.

One may wonder whether in the STRUCT approach the absence of information on the cell size would allow an LES-like behavior to trigger. The capability of obtaining LES-like results on fine grids without reference to the cell size has been already shown for example by PANS, PRNS, and in some cases SAS approach, while STRUCT results will be shown in Chapters 6, 7, and 8.

On the other hand, the STRUCT approach would inherently not suffer from the GIS problem of DES, since there is no explicit term involving the grid spacing unless a grid-based limiter is used.

The interface between URANS and LES used in ELES (see Section 2.5.4) requires the introduction of synthetic turbulence to account for the transfer of resolved energy. Meanwhile, generation of synthetic turbulence is not used in many important hybrid models, for example, DES, SAS, PANS. In those models, it is assumed that resolved motion is produced automatically by inherent flow instabilities (Gritskevich et al., 2011). A similar assumption is made in this work for STRUCT, with the additional argument that production of resolved turbulence is expected to be enhanced by the selection of regions of high deformation.

Consideration of the effect of the varying filter is essential in zonal methods in which an interface is imposed in an Eulerian framework. Interfaces using URANS upstream and LES downstream are the most sensitive. Treatments used in zonal approaches are reviewed by Sagaut, Deck, and Terracol (2013). In STRUCT, since activation regions are chosen as regions of high deformation, the resolved content is expected to be generated automatically by resolved fields. While ELES interfaces are fixed planes in the Eulerian framework, STRUCT interfaces have a Lagrangian nature described by transport equations. Consequently, the net flux density across those interfaces is not expected to be

significant compared to the global scales of the flow. The STRUCT tests of Chapter 6 will confirm the validity of these ideas. Nevertheless, it would be interesting to assess in future work the eventual need for a more complex interface treatment on STRUCT results.

From a historical point of view, it is surprising to notice how many of the URANS turbulence models introduced in Section 2.3.5 and 2.3.6 were derived around the 1970s. That was also the time when significant discussions on coherent structures appeared. Lumley (1992) wrote:

"The idea of coherent structures really took off in about 1970, with a quite irrational abandonment of nearly all other approaches."

This sentence conveys both the promise and complexity of the study of coherent structures.

The second invariant of the velocity gradient tensor, also called the Q-criterion in data visualization, has a role in existing hybrid models. It is interesting to observe then that such a criterion for visualization shares similarities with the active STRUCT formulation.

A key question, common to all turbulence closures, concerns the link between the structures observed in the resolved field and those occurring in DES or the experiment. Such an issue is pointed out clearly by Spalart (Shur et al., 1999) in his review of DES:

"The link between the DES flow field and the exact or DNS flow field should be established."

5 Numerical implementation

5.1 Chapter overview

After having introduced the STRUCT approach in the previous chapter, here we focus on its implementation, providing all the necessary details to appreciate the numerical methods adopted in the work. To evaluate the performance of the model, it is necessary to try to ensure the independence of the numerical error from the modeling error, which, in particular for scale resolving methods is not necessarily trivial. All numerical methods used in the simulations have been evaluated and selected on the basis of their expected reliability, maturity in industrial applications, and performance in combination with the physical models used in this work.

The chapter is divided into two parts: solvers and numerical schemes are briefly introduced first while all implementation details necessary to reproduce the results are discussed later.

5.2 Selection of computational tools

5.2.1 Finite volume method

Driven by the desire to allow an early industrial adoption of the approach, the model was implemented and tested into a mainstream "general purpose" commercial package, namely STAR-CCM+, developed by CD-adapco. As valid for all leading general-purpose CFD software, the flow solution is based on the finite volume (FV) discretization technique. The FV approach is widely adopted in industrial CFD because of advantages including suitability with unstructured grids and chimera meshes, parallelizability, and ease of use.

The FV solver implemented in STAR-CCM+ uses a co-located algorithm with face-based variables, capable to run on arbitrary polyhedral cells. This advantage is key in industrial simulations, for which significant challenges from the user's point of view are related to meshing complex geometries. In order to evaluate central fluxes, cell centroid values are interpolated to the face centers.

5.2.2 Software and hardware

The implementation of the STRUCT approach required the use of a STAR-CCM+ version deriving from a modified source code. A dedicated version of the software was produced as a development branch of the release 7.02. The software modification has been recently made available in a public release, 10.06, therefore allowing the model to be implemented directly in all future commercial releases. The 10.06 version of the code was recently tested confirming the independence of the results from the specific software implementation.

To further assess the portability of the approach, the STRUCT model was also implemented in the open-source solver OpenFOAM as part of a separate research project. The results of the OpenFOAM test are included in Appendix B, Sections B.4 and B.5.

The STAR-CCM+ software package contains several simulation tools, including a 3D-CAD modeler, an automatic meshing system, data post-processing utilities, and multicomponent, multiphase solvers, among which several turbulence models. Another key feature of STAR-CCM+

is the significant parallel efficiency. All of these tools are controlled through a graphical user interface (GUI). Here we only discuss the details that are relevant to the STRUCT implementation and assessment.

From the hardware standpoint, all pre/post processing was performed on a Linux workstation with 12 Intel Xeon E5-2620 cores. The 12 cores have 15 MB of cache and a 2.00 GHz base clock speed while the system is equipped with 64 GB of RAM, and an NVIDIA Quadro 2000 graphics card. Most simulations are run using a Linux cluster administered by the research group. The cluster has one head node and 33 slave nodes, whose specifications are in Table VI below. An InfiniBand connection is used to transfer data between cluster nodes.

Table VI Specifications of the Linux cluster used

Description	# Nodes	# Cores per node	Core type	Base frequency	Cache	Node RAM
Head node	1	12	Intel Xeon E5620	2.4 GHz	12 MB	32 GB
"Type 1" nodes	22	12	Intel Xeon E5620	2.4 GHz	15 MB	24 GB
"Type 2" nodes	10	12	Intel Xeon E5-2630V2	2.6 GHz	15 MB	32 GB

5.3 Solution algorithm

5.3.1 Segregated solver

A segregated pressure-velocity solution is adopted in this work, based on the semi-implicit method for pressure-linked equations (SIMPLE) algorithm (Patankar and Spalding, 1972). The SIMPLE algorithm allows for an optimal overall balance between computational efficiency and robustness for the incompressible flow cases treated in this work. The solver uses the Rhie-Chow (1983) interpolation for pressure-velocity coupling to prevent numerical oscillations affecting the solution.

The solution algorithms in the software have demonstrated to be extremely mature and have not posed any challenge in the cases presented here. For all simulations, standard under-relaxation factors are used, 0.7 for velocity, 0.3 for pressure and 0.8 for both the turbulent kinetic energy and turbulent dissipation rate. The number of outer iterations varied for each case and was selected to guarantee that iteration error is negligible.

Time advancement

The time advancement scheme is particularly important for hybrid models, where an accurate temporal discretization is required to resolve turbulence structures. Based on the extensive validation on LES application (e.g. Jayaraju et al., 2013, 2010), a second-order three-time-level scheme is used for time integration. Such a scheme uses values at the two previous time steps (CD-adapco, 2015):

$$\frac{\mathrm{d}\phi_0^{n+1}}{\mathrm{d}t} = \frac{(\alpha^2-1)(\phi_0^{n+1}-\phi_0^n)+(\phi_0^{n-1}-\phi_0^n)}{\alpha(\alpha-1)\Delta_t^{n+1}} \quad , \quad \alpha = 1+\frac{\Delta_t^{n+1}}{\Delta_t^n} \tag{5.1}$$

where Δ_t^{n+1} and Δ_t^n are respectively the time steps: $(t^{n+1}-t^n)$ and (t^n-t^{n-1}). In order to guarantee independence of the results from the temporal discretization approach, for all simulations in this work, time step is determined so that the maximum Courant number be 1. Demonstration of the influence of the time step on the solution accuracy is presented in this chapter.

Fluid properties

Fluid properties reflect the assumptions described in Section 1.4.2. In particular, density is prescribed as constant. In all test cases at a constant temperature, a constant molecular viscosity is used.

In the T-junction test case, which involves non-isothermal phenomena, the molecular viscosity is prescribed as a function of temperature. Other thermal properties are set as constant, such as specific heat, thermal conductivity, and turbulent Prandtl number. The use of the turbulent Prandtl number is related to the adoption of the simple heat-transfer-eddy-diffusivity model.

5.3.2 Choice of the spatial interpolation scheme

Selection of the spatial interpolation scheme for the computation of convective terms is important in turbulence modeling and particularly critical in hybrid simulations, due to the combination of URANS and LES features. Different types of turbulence models are known from the literature to operate optimally with different spatial interpolation schemes.

The integral form of the convective term of the transport equation for a generic variable ϕ is given by the surface integral of a flux:

$$\int_A \rho\phi\overline{\boldsymbol{u}} \cdot \boldsymbol{n}\mathrm{d}A \tag{5.2}$$

Numerical solution of (5.2) requires knowledge of the value of variable ϕ at cell faces. An interpolation method calculates face-centered values based on cell-centered ones. Referring to the notation of Figure 5.1, we need to calculate a variable in point e by only knowing the cell-centered values, indicated by capital letters.

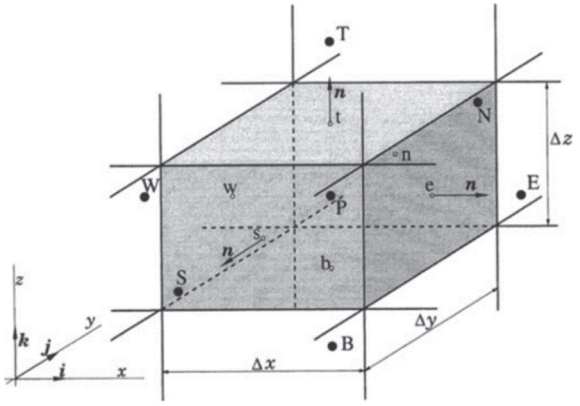

Figure 5.1 Notation used for 3D control volume, from Ferziger and Perić (2002)

Schemes important in this work are described briefly below, referring to the notation illustrated in Figure 5.1.

First-order upwind

A very simple and effective method to approximate the value of a generic field ϕ in point e is to assume it as equal to the value in the cell center upstream the face (Ferziger and Perić, 2002). This logic is used in the first-order upwind (1UD) scheme:

$$\phi_e = \begin{cases} \phi_P & \text{if} \quad (\boldsymbol{u} \cdot \boldsymbol{n})_e > 0 \\ \phi_E & \text{if} \quad (\boldsymbol{u} \cdot \boldsymbol{n})_e < 0 \end{cases} \tag{5.3}$$

The "if" condition in (5.3) ensures that the parameter value upstream the face is always taken. While the implementation is straightforward and its solution extremely stable, the method is also well known to introduce numerical diffusion, which is particularly severe in the case of flow crossing cell faces obliquely.

Central differencing

A common approach for a higher-order solution is to interpolate linearly between ϕ_P and ϕ_E to obtain ϕ_e, as done in all CD schemes:

$$\phi_e = \phi_E \frac{|\boldsymbol{x}_e - \boldsymbol{x}_P|}{|\boldsymbol{x}_E - \boldsymbol{x}_P|} + \phi_P \left(1 - \frac{|\boldsymbol{x}_e - \boldsymbol{x}_P|}{|\boldsymbol{x}_E - \boldsymbol{x}_P|}\right) \tag{5.4}$$

Differently from 1UD, the CD scheme has the advantage of being second-order accurate on grids in which faces are half-way between cell centers. This linear interpolation, however, is well known to introduce oscillatory behavior for $|\mathrm{Pe}| > 2$, and is not robustly applicable to low-quality FV grids.

Second-order upwind

In the second-order upwind differentiation (2UD) scheme, the face-centered value is calculated by extending the 1UD with another term in a Taylor series expansion, as follows:

$$\phi_e = \begin{cases} \phi_P + (\boldsymbol{x}_e - \boldsymbol{x}_P) \cdot (\boldsymbol{\nabla}\phi)_P & \text{if} \quad (\boldsymbol{u} \cdot \boldsymbol{n})_e > 0 \\ \phi_E + (\boldsymbol{x}_e - \boldsymbol{x}_E) \cdot (\boldsymbol{\nabla}\phi)_E & \text{if} \quad (\boldsymbol{u} \cdot \boldsymbol{n})_e < 0 \end{cases} \tag{5.5}$$

The 2UD equation contains gradients, thus requiring their reconstruction at the cell face. Being a second-order expansion, it is a second-order-accurate method.

As clearly stated by Godunov's theorem, a method, unfortunately, cannot be higher than first order and limited at the same time. The 2UD will, therefore, introduce new local minima and maxima which would introduce considerable stability issues and dispersive error. These issues are addressed by the introduction of limiting techniques designed to prevent the formation of local extrema. This work uses the method by Venkatakrishnan (1993).

The 2UD interpolation scheme, Being at the same time robust and more accurate than 1UD, is widely used in URANS simulations. Since URANS simulations solve for ensemble-averaged parameters, a diffusive behavior of the interpolation scheme does not compromise the solution but increases stability and convergence. Such a diffusive behavior is not desirable for scale-resolving simulations, in which CD-type schemes are often preferred.

Bounded central differencing

The CD scheme can lead, as discussed, to unphysical oscillations and local overshooting (dispersive error) in cases with high Péclet numbers and low-quality computational cells. As a consequence, stability issues can preclude solution convergence. On the other hand, scale-resolved simulations require an appropriate energy conservation in order not to dissipate the resolved turbulent kinetic energy. CD schemes have shown superior performance in this regard.

Hybrid schemes have been proposed to find an optimal solution to this tradeoff, balancing accuracy and stability. A commonly used hybrid scheme is BCD, which combines 1UD, 2UD, and CD. The following formulation is used (CD-adapco, 2015):

$$\phi_e = \begin{cases} \phi_{\mathrm{1UD}} & \text{for } \zeta < 0 \text{ or } \zeta > 1 \\ \sigma\phi_{\mathrm{CD}} + (1-\sigma)\phi_{\mathrm{2UD}} & \text{for } 0 \leq \zeta \leq 1 \end{cases} \tag{5.6}$$

The dimensionless switching parameter ζ is taken from the normalized-variable diagram (NVD). It identifies how the variable to be interpolated compares to its upstream and downstream values,

defined as D and U in the equation below (Leonard, 1988). Recall that the definition of upstream and downstream depends on the velocity direction.

$$\zeta = \frac{\phi - \phi_U}{\phi_D - \phi_U} \tag{5.7}$$

When such a variable is smaller than 0 or greater than 1, the boundedness criterion is not satisfied, so the model reverts to a robust 1UD. This is expected to happen in coarse-grid regions. When the boundedness criterion is satisfied, the model blends CD and 2UD based on a function:

$$\sigma = \sigma(\zeta) \tag{5.8}$$

Such a blending function varies smoothly with ζ and meets the requirements that $\sigma(0) = 0$, and $\sigma(\zeta) = 1$ for all values of ζ larger than an upwind blending factor, ζ_{ubf}. Such a factor can be adjusted before the simulation. Smaller values favor a less diffusive scheme, while larger values favor the robustness associated with 2UD. This approach allows limiting the blending only to those cells in which boundedness would not be respected.

The BCD scheme is used in this work for LES and for many STRUCT simulations. Variable ζ_{ubf} is taken as equal to 0.15. The physical consistency of BCD is confirmed by its wide adoption in LES. This work uses BCD in active and non-active STRUCT regions. Meanwhile, the 2UD scheme is used for URANS simulations, consistently with the most common procedure used in the industry.

5.3.3 Gradients

The integral form of transport equations governing fluid motion contains terms requiring the interpolation of gradients at the cell faces. Surface-centered gradients need to be reconstructed based on the known cell-centered values of the variables of interest.

For this purpose, a method blending the least-squares (LSQ) and the Green-Gauss (GG) approaches using a factor β is used in this work.

$$\boldsymbol{\nabla}\phi = \beta(\boldsymbol{\nabla}\phi)_{\mathrm{LSQ}} + (1-\beta)(\boldsymbol{\nabla}\phi)_{\mathrm{GG}} \tag{5.9}$$

The factor function β is calculated based on an algorithm depending on geometrical properties of cells (CD-adapco, 2015). The choice of this hybrid method is driven by the need for robustness of the solver in complex geometries and unstructured grids.

The LSQ method is known to provide more accurate gradient reconstructions in Cartesian geometries, while the G-G is known to provide higher accuracy than LSW in thin and curved cells (Shima et al., 2013). The latter kind of cell is often encountered in grids that, to save in number of cells, use wall refinement combined with coarser cells far from the wall. Therefore, this hybrid method for calculating gradients is suitable for robust low-cost simulations, as desirable based on the goals of this work.

5.3.4 Spatial interpolation scheme evaluation

To evaluate the performance of the spatial and temporal discretization schemes, a dedicated test case was performed, which provides useful qualitative and quantitative results. The configuration chosen for this test is a 2D inviscid flow simulation of a moving vortex (Moureau et al., 2005).

The setup of the test cases is relatively simple and presented in Figure 5.2. Periodic boundary conditions are applied at the two lateral sides of the domain as shown in the figure, and symmetry conditions are used at the top and bottom boundaries.

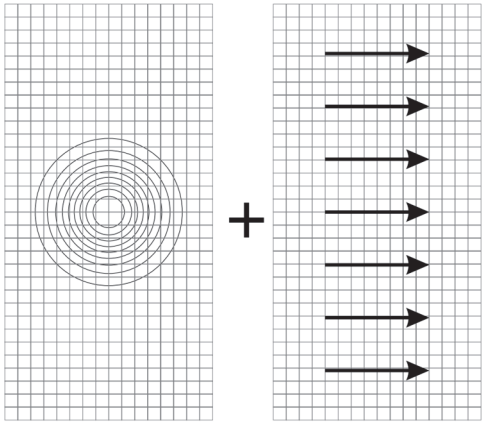

Figure 5.2 Moving vortex test case configuration, from Moureau et al. (2005)

As shown qualitatively in the figure, the initial velocity is a superposition of a field describing a vortex and a convective field. Initial conditions used for the two velocity components and for the pressure field are (Baglietto, 2013):

$$u_{x,0}(x,y) = U_{\text{conv}} - y\frac{2U_{\text{vort}}}{D_0^2}\, e^{-\frac{x^2+y^2}{D_0^2}} \tag{5.10}$$

$$u_{y,0}(x,y) = x\frac{2U_{\text{vort}}}{D_0^2}\, e^{-\frac{x^2+y^2}{D_0^2}} \tag{5.11}$$

$$p_0(x,y) = p_{\text{ref}} - \rho_0\left(\frac{U_{\text{vort}}}{D_0}\, e^{-\frac{x^2+y^2}{D_0^2}}\right)^2 \tag{5.12}$$

The constant parameters used are provided in Table VII below.

Table VII Parameters used in the moving vortex case

$\boldsymbol{U_{\text{vort}} = }$ $\mathbf{[m/s]}$	$\boldsymbol{U_{\text{conv}}}$ $\mathbf{[m/s]}$	$\boldsymbol{D_0}$ $\mathbf{[m]}$	$\boldsymbol{p_{\text{ref}}}$ $\mathbf{[Pa]}$	$\boldsymbol{\rho_0}$ $\mathbf{[kg/m^3]}$
4.6632879632	10.0	0.16	1.013×10^5	1

The flow domain is 1 m wide and 2 m tall. Due to the periodic boundary conditions, the 10 m/s convective velocity will translate the vortex out of the right boundary, and back into the domain from the left boundary. The convective time, i.e. the time required for a full return of the vortex to its initial position, is: $t_{\text{conv}} = (1\text{ m})/(10\text{ m/s}) = 0.1$ s. In an ideal inviscid solver, the velocity and pressure fields at time t_{conv} are equal to the initial conditions, assuming no interaction between vortices in the infinite domain. By observing the difference between the ideal and real solution, we quantify the error introduced by the solver. A dimensionless indicator based on the Euclidean distance ($L2$ norm) quantifies the error as:

$$L2 = \sqrt{\frac{\sum\left(\left(u_x - u_{x,0}\right)^2 + \left(u_y - u_{y,0}\right)^2\right)}{\sum\left(u_{x,0}^2 + u_{y,0}^2\right)}} \tag{5.13}$$

The four spatial discretization approaches tested are:

- 2UD
- CD
- BCD, using an upwind blending factor of 0.15
- A blended scheme that combines interpolated values from 2UD and CD. Such a model performs a weighted average of results from 2UD and CD. Here, we use a blending factor of 0.5, corresponding to an arithmetic average between the two schemes.

Six grids are tested, with three base sizes: 0.05 m, 0.025 m, and 0.0125 m, as shown in Figure 5.3.

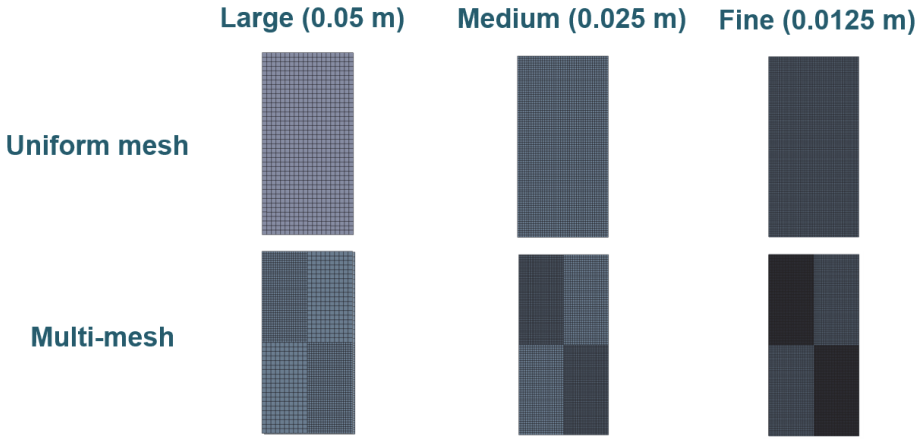

Figure 5.3 Grid styles and sizes used for the spatial discretization tests

For each base size, we test both a uniform mesh and a so-called multi-mesh. The latter grid divides the domain into four parts, as shown in Figure 5.3. In the upper left and lower right domain areas, the base size is half of the one used in the rest of the domain. The base size used as a reference in the tests is the coarser one.

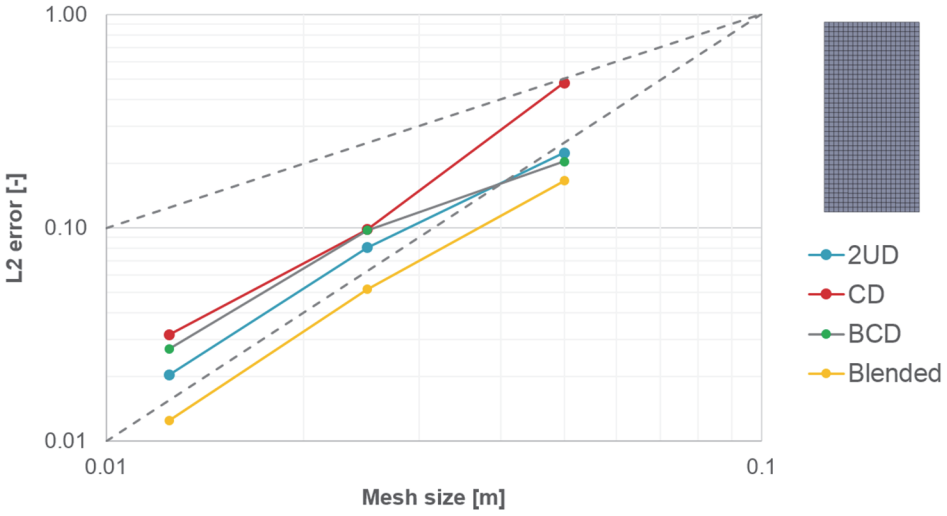

Figure 5.4 Spatial discretization scheme results, uniform mesh

Results for the L2 error as defined in (5.13) are shown in Figure 5.4 for the uniform mesh and in Figure 5.5 for the multi-mesh case. For convenience, two dashed lines are drawn in those figures identifying the slope for first- and second-order convergence. Results in Figure 5.4 show that the discretization methods tested behave roughly according to the second order of convergence on uniform grids.

Results obtained on the multi-mesh grids shown in Figure 5.5 behave according to the second order of convergence for the BCD and blended schemes. The order of convergence seems slightly lower for the CD. The BCD scheme seems to transition from a 2UD to a CD result as the grid is refined.

Overall, in all cases, the CD scheme produces the highest overall error. This expected outcome is caused by the dispersive error, which represents one of the challenges of using CD-based schemes. For the multi-mesh, the CD error is significantly higher, and the order of convergence is lower, compared to the uniform grid case.

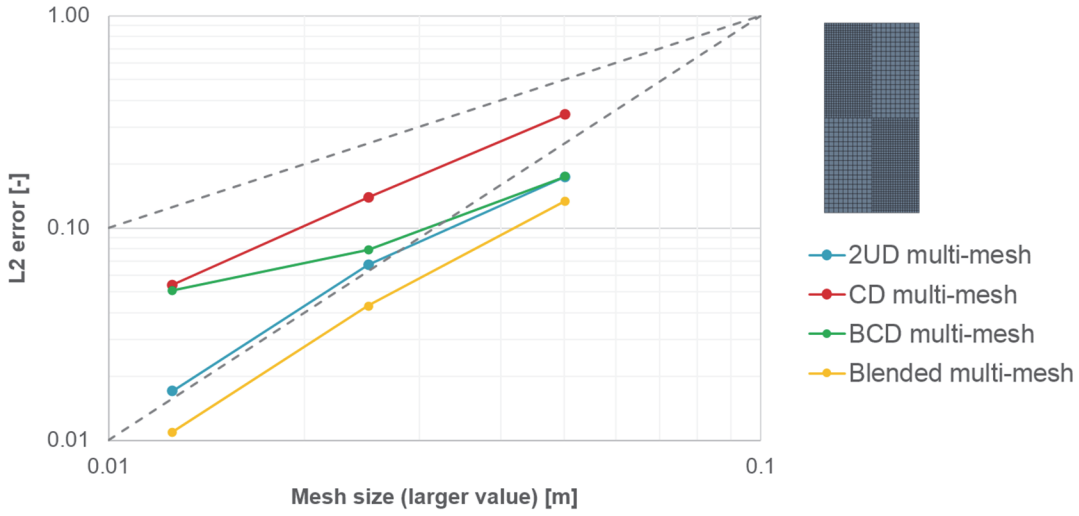

Figure 5.5 Spatial differentiation scheme results, multi-mesh

Temporal discretization analysis

Sensitivity to the temporal discretization is tested on the medium uniform grid of Figure 5.3, by varying the time step. Recall that all tests are performed with a three-time-level second-order temporal method. The Courant number is defined as:

$$C = \frac{|\overline{\boldsymbol{u}}|\Delta_t}{\Delta} \tag{5.14}$$

The Courant number can vary significantly in a complex flow domain. If simulations are run, as in this work, with a maximum Courant number of 1, most cells in the domain have a Courant number smaller than 1. Results of the sensitivity test are shown in Figure 5.6 below.

According to the figure below, a Courant number increase above 1 leads to a monotonic increase of the error for all discretization schemes. On the other hand, a Courant number decrease below 1 leads to no significant error change for the blended and the 2UD schemes. Conversely, the error decreases slightly for the BCD and increases for the CD.

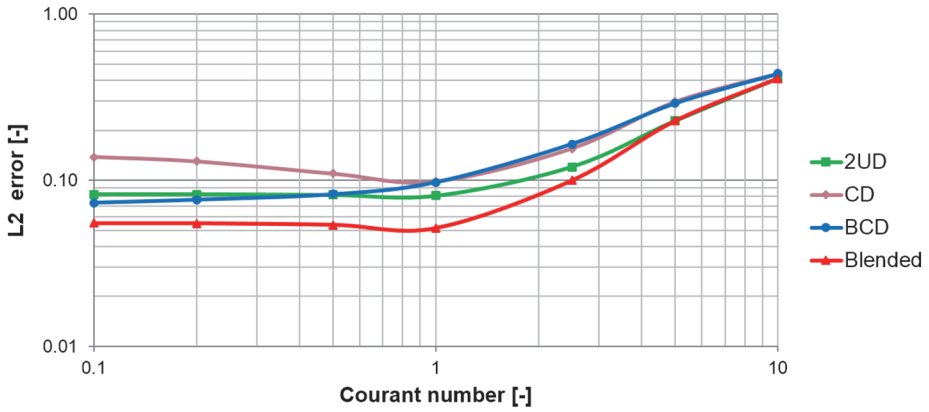

Figure 5.6 Courant number analysis, spatial differentiation scheme test

Qualitative error picture

A qualitative picture of different types of spatial discretization error is shown in Figure 5.7. The parameter shown in the figure is the magnitude of velocity calculated without taking into account the convective velocity:

$$\text{vortex plot} = \sqrt{(u_x - U_{\text{conv}})^2 + u_y^2} \tag{5.15}$$

As mentioned above, upwind schemes are expected to produce a diffusive error, while CD schemes are expected to produce dispersive one. We can verify this expectation by looking at Figure 5.7. In an inviscid simulation as performed here, a perfect solver would generate a solution identical to the starting condition. Instead, we can notice that 2UD results present a diffusion-like behavior. In particular, the peak velocity is significantly lower than the target one.

On the other hand, a dispersion of gradients compromises the shape of the vortex for the CD result. Indeed, the CD scheme can give rise to solutions outside the range of expected values and can produce nonphysical oscillations. Those oscillations introduce artificial gradients in low-gradient regions, also called dispersive error. For clarity purposes, in that figure, all velocity values exceeding the maximum initial one of 25 m/s are plotted as white, to signify that they lie outside the plausible physical range.

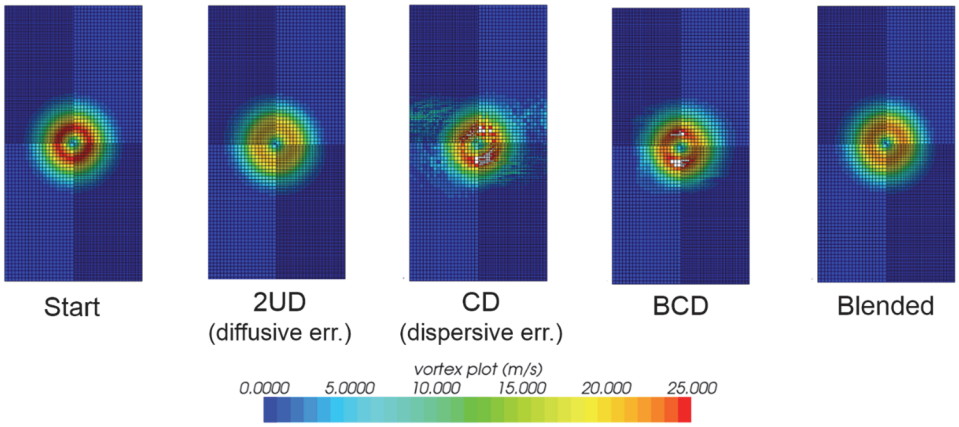

Figure 5.7 Qualitative view of the moving vortex case results

In the qualitative picture above, the BCD and blended schemes confirm their purpose of being a tradeoff between the diffusive error of 2UD and the dispersive error of CD. The dispersive error seems to prevail for the BCD scheme and the diffusive error for the blended scheme. These conclusions support the choice made in this work of running STRUCT simulations using BCD.

5.4 Implementation

This section describes the practical implementation of the STRUCT equations in the STAR-CCM+ software, as applied in all simulations shown in the following chapters.

5.4.1 Model Equations

The STRUCT approach switches between URANS and hybrid behavior based on the condition formulated in (4.1). In regions of hybrid activation, the ratio between modeled and total TKE r is assigned based on a reduction parameter, ϕ.

In the tests made in this work, the TKE ratio deriving from the STRUCT formulation is implemented into a simple hybrid approach. Future work could explore different hybrid techniques employing the general STRUCT formulation. As an example, PANS (Girimaji, 2006), discussed in Section 2.5.5, assigns the TKE ratio through a parameter r, modifying the k-ε equations:

$$C_{\varepsilon 2}^{*} = C_{\varepsilon 1} + r(C_{\varepsilon 2} - C_{\varepsilon 1}) \tag{5.16}$$

A reduction of r produces a reduction of the dissipation of TDR, thus causing an increase in TDR and a subsequent reduction of the eddy viscosity. In the model by Perot and Gadebusch (2007), described in Section 2.5.7, a different formulation is proposed:

$$\nu_{\mathrm{t}}^{\mathrm{PG}} = C_{\mu}\frac{k_{\mathrm{m}}^{2}}{\varepsilon}r \tag{5.17}$$

The formulations accounting for energy backscatter in the original model are hereby neglected. Here, we focus just on the key relation in (5.17). Such a relation prescribes a direct link between r and the eddy viscosity.

Tests made in the present work use the simple assumption in (5.17).

The TKE ratio is implemented via a damping function multiplying the eddy viscosity. The value for r is controlled as a field function in the code. This implementation has an effect on the nonlinear equation for the anisotropic part of the residual stresses, which becomes:

$$\tau_{ij} - \frac{2}{3}k_{\mathrm{m}}\delta_{ij} = r\nu_{\mathrm{t}}\left(-2\bar{S}_{ij} + q_{ij} + c_{ij}\right) \tag{5.18}$$

The equations for the TKE and TDR are also modified as follows:

$$\frac{\partial k_{\mathrm{m}}}{\partial t} + \bar{u}_j\frac{\partial k_{\mathrm{m}}}{\partial x_j} = \frac{\partial}{\partial x_j}\left[\left(\nu + \frac{r\nu_t}{\sigma_k}\right)\frac{\partial k_{\mathrm{m}}}{\partial x_j}\right] + P_k - \varepsilon \tag{5.19}$$

$$\frac{\partial \varepsilon}{\partial t} + \bar{u}_j\frac{\partial \varepsilon}{\partial x_j} = \frac{\partial}{\partial x_j}\left[\left(\nu + \frac{r\nu_t}{\sigma_\varepsilon}\right)\frac{\partial \varepsilon}{\partial x_j}\right] + C_{\varepsilon 1}\frac{\varepsilon}{k_{\mathrm{m}}}P_k - C_{\varepsilon 2}\frac{\varepsilon^2}{k_{\mathrm{m}}} \tag{5.20}$$

Results in Chapter 8 use a smooth variation of r and are obtained through the equations above. Conversely, results in Chapters 6 and 7 use a binary variation for r and the modeled turbulent kinetic energy is graphically presented as rk_{m} in all the postprocessing.

Selection of the closure parameters in the controlled approach

To assemble a fully closed version of the STRUCT model, values of the two parameters ϕ and t_m must be known. In the controlled STRUCT approach of Chapter 6, the two parameters are assigned as case-specific and constant values. Conversely, the complete models of Chapter 7 and 8 do not require any case-specific adaptation but have general applicability. As will be discussed in Chapter 6 for the controlled STRUCT, the value for t_m is determined based on averaging of URANS results for $t_{\mathrm{m},0}$. Geometric averaging is used and discussed in Section 7.3.3. Recall that the relation between t_m and $t_{\mathrm{m},0}$ is a generic averaging operation expressed as in (4.3), copied below:

$$t_\mathrm{m} = \langle t_{\mathrm{m},0} \rangle$$

The coefficient ϕ describing the TKE ratio is determined a posteriori, and optimized for each application to evaluate the limiting behavior of the model with optimal coefficient selection. This limit test allows evaluating the accuracy achievable by the STRUCT conceptual approach, independently from the specific closure implementation. The complete models introduced in Chapters 7 and 8 compute t_m during the simulation based on local approximations of the averaging operation in (4.3). The model in Chapter 7 uses a constant value for ϕ, equal in all simulations, while the one in Chapter 8 uses a function determining the local TKE reduction.

5.4.2 Data collection procedure

It is useful to provide here details on the methodology used to extract and plot simulation results. Experimental data used here are time-averaged quantities or time variances measured in flow cases with boundary conditions that are constant in time. Results obtained from our simulations are available at discrete time steps and need to be averaged over time for a consistent comparison with the experiment. If we write the triple decomposition for a generic field $\phi(\boldsymbol{x}, t)$, varying with space and time, similarly to (2.13):

$$\phi = \underbrace{\hat{\phi} + \overbrace{\tilde{\phi}}^{\phi'}}_{\bar{\phi}} + \phi'' \tag{5.21}$$

The instantaneous field, ϕ, is decomposed into a resolved component ($\bar{\phi} = \hat{\phi} + \tilde{\phi}$) and a residual one ($\phi'' = \phi - \bar{\phi}$). We are interested in extracting time-averaged fields $\hat{\phi}$, defined as:

$$\hat{\phi}(\boldsymbol{x}, t) = \frac{1}{t - t_0} \int_{t_0}^{t} \phi(\boldsymbol{x}, t') \mathrm{d}t' \tag{5.22}$$

In our solver, we can collect the time-average of the resolved field, yielding:

$$\hat{\bar{\phi}} = \widehat{\hat{\phi} + \tilde{\phi}} = \hat{\bar{\phi}} + \hat{\tilde{\phi}} + 2\widehat{\hat{\phi}\tilde{\phi}} \tag{5.23}$$

This work assumes that, for the sake of visualization of results, the two last RHS terms are zero, thereby approximating time-averaged instantaneous fields as time-averaged resolved ones:

$$\hat{\bar{\phi}} \approx \hat{\phi} \tag{5.24}$$

Simulations are run for a physical time sufficient for the appropriate collection of statistics. All quantities are monitored during simulations to ensure the appropriate convergence.

Experimental results provide information on fluctuating parameters. These results include variances of single components of velocity and covariances of two components. Some assumptions are

necessary for the comparison of simulation results to the experiment. In the triple decomposition in (5.21), deviation from the time average is defined as the sum of two components: $\tilde{\phi}$ and ϕ''. Subsequently, the variance with respect to time of ϕ, which is the value provided by the experiment, is defined as the mean square of the fluctuation about the time average:

$$\widehat{\phi'^2} = \widehat{\tilde{\phi}^2} + \widehat{\phi''^2} + 2\widehat{\tilde{\phi}\phi''} \tag{5.25}$$

We can obtain the first two terms on the RHS from the time averaging of the respective variables, during the simulation, under the assumption in (5.24). For result visualization, we assume that the last term on the RHS can be neglected. Such a term, which represents a covariance between the modeled and resolved contribution, is not expected to be significant due to the different scales covered by the resolved and residual component in the STRUCT approach.

We also assume that, for data visualization purposes, the time average of products of fluctuating velocity components be equal to the time average of residual stresses. Therefore:

$$\hat{\tau}_{ij} = \widehat{u_i''u_j''} \tag{5.26}$$

Similarly, we obtain a time covariance through simple algebra:

$$\widehat{\phi'\psi'} = \widehat{\tilde{\phi}\tilde{\psi}} + \widehat{\phi''\psi''} + \widehat{\tilde{\phi}\psi''} + \widehat{\phi''\tilde{\psi}} \tag{5.27}$$

Analogously to what is done for the variances, we assume that, for data visualization purposes, the two mixed terms, i.e. the two last terms in the RHS, be negligible. This assumption is common in URANS and many LES closures.

For LES, fluctuating parameters are calculated only by considering the resolved components, which is a valid assumption for sufficiently fine grids, as is the case for this work.

5.4.3 Abbreviated nomenclature for URANS models

In the results shown in the following chapters, for the sake of brevity, URANS models are referred to using a shortened nomenclature. The following terms are used:

- Linear URANS for the Standard k-ε
- Quadratic URANS for the Quadratic NLEVM as described in Section 4.7.
- Cubic URANS for the Cubic NLEVM as described in Section 4.7.
- STRUCT for the STRUCT approach applied to Cubic URANS

Other URANS and STRUCT models tested are described on a case-by-case basis.

5.5 Discussion

Hybrid turbulence models can be very sensitive to the spatial interpolation scheme as shown in the example of Section 3.2.2 (Gritskevich et al., 2014). In the case of DES, upwind schemes are more desirable in URANS zones, while CD schemes are more desirable in LES zones (Strelets, 2001). This discrepancy can be explained looking at the tradeoff between diffusive and dispersive error shown in Figure 5.7. The dissipative nature of 2UD is helpful for the convergence of URANS, but in LES, it dissipates desired features of the resolved flow. This issue motivates the need for hybrid numerical schemes when using hybrid turbulence models. While BCD is a popular hybrid scheme, other ones have been proposed. The blended scheme tested in Section 5.3.4 is a simple example of a different hybrid scheme.

6 Controlled model demonstration

6.1 Chapter overview

The previous chapters have introduced the overall formulation of the STRUCT approach, including its numerical implementation. The present chapter focuses on the assessment of a controlled formulation of the STRUCT model, in which pre-computed optimal model coefficients are used to demonstrate the model's capabilities. The decision to test the controlled approach before introducing the complete ones is motivated by the idea to assess the basic STRUCT concept separately from the influence of complete closures. The test cases adopted are those analyzed in chapter 3, for which the performance of existing hybrid models has been assessed and discussed in the literature.

For each flow case, details on the adopted computational grids and other relevant specifications are provided. Results are then plotted and compared with available experimental data.

6.2 Flow past a square cylinder

6.2.1 Description and experimental data

The test case of the flow past a square cylinder was introduced in Section 3.2.1. This test case is usually described successfully by hybrid models, due to their performance compared to URANS in cases with massive separation. It is considered therefore a useful first test case to assess the basic performance of the STRUCT approach.

A fully developed water flow runs through a 39 × 56 cm channel as shown in Figure 6.1. The flow encounters a square cylinder whose side is $D = 4$ cm. The Reynolds number based on D is 21,400. The reference velocity is $U_{\mathrm{ref}} = 0.535\ \mathrm{m\ s^{-1}}$.

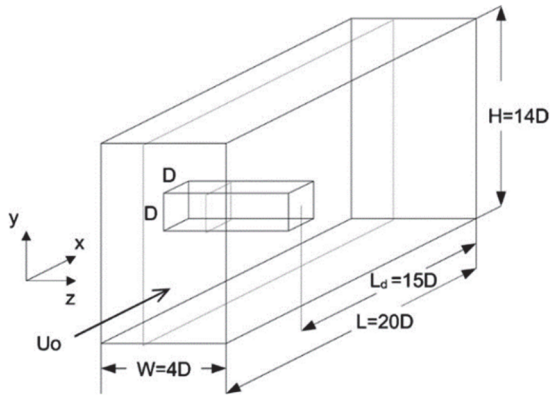

Figure 6.1 Geometry of the flow past a square cylinder, from Jeong and Girimaji (2010)

The present work plots simulation results in comparison with the experimental data collected using laser-Doppler velocimetry (LDV) by Lyn and co-workers (1995). Means and variances of velocity

are available in a matrix of measurement points inside and around the wake region. In those locations, the interaction between turbulent structures at different scales is expected to be significant.

Uncertainties in experimental results are estimated by Lyn and co-workers (1995) to be less than 5% for mean velocities and velocity fluctuations, and in the range between 15% and 25% for the covariance values $\widetilde{u_1'u_2'}$. A systematic uncertainty component is not available.

6.2.2 Computational grid, boundary conditions, and other details

The top and bottom boundaries of the domain as shown in Figure 6.1 are treated with wall functions, so a first cell with y^+ higher than 30 is used. A wall-resolved approach is used instead for wall boundaries around the square cylinder, so the first cell has y^+ around 1, and the cell growth rate is about 1.1. Periodic boundary conditions are used in the spanwise direction while a pressure outlet boundary condition is specified at the domain's exit.

One of the parameters to be defined in the simulation is the inlet velocity. The reference velocity provided by the paper of Lyn and co-workers (1995) is 0.535 m/s. More accurate information on the inlet velocity is obtained directly from LDV data at the acquisition plane $x/D = -3$.

Nevertheless, only four LDV data points are available. This level of detail was considered too low to produce a suitable profile for simulations. Therefore, a fully developed profile was calibrated to match those same four experimental points. The inlet boundary was extruded to obtain a fully developed profile. The optimal uniform inlet velocity was found to be 0.5435 m/s. This value is 1.6% higher than the nominal 0.535 m/s, so it lies within the 2% to 3% uncertainty range specified by the authors of the experiment for the nominal velocity. Velocity profiles at $x/D = -3$ for three different inlet velocities are shown in Figure 6.2, where the line in the middle has been chosen.

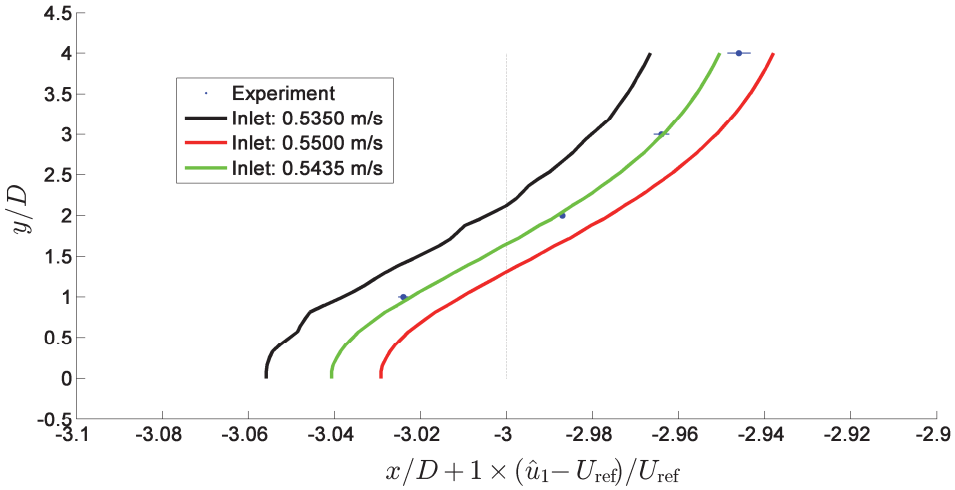

Figure 6.2 Tests in extruded geometry to determine an appropriate inlet velocity

Simulations in this work use the inlet velocity thus determined of 0.5435 m/s. Such a velocity is set as uniform at the inlet of the same extruded geometry used in the example of Figure 6.2.

The main computational grid used is trimmed with a base size of 10.5 mm. This base size is refined by 50% in the regions around and immediately after the cylinder. The total size of the mesh is 676,000 cells. Preliminary tests have shown reasonable URANS convergence on this grid. A section of such a grid is illustrated in Figure 6.3 below.

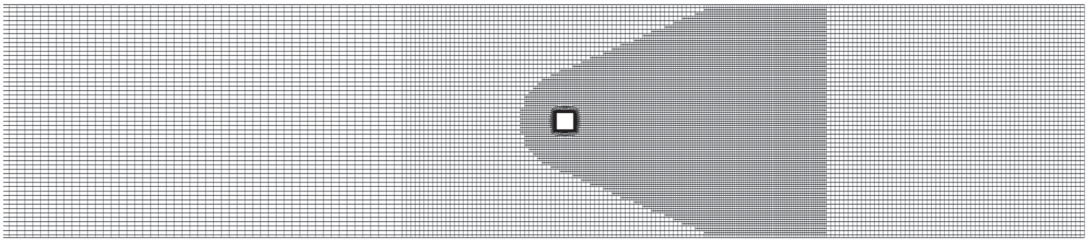

Figure 6.3 Computational grid for the square cylinder test case

A detailed view of the refined grid around the obstacle is shown in Figure 6.4 below. Significant grid refinement enables a wall-resolved treatment of that boundary.

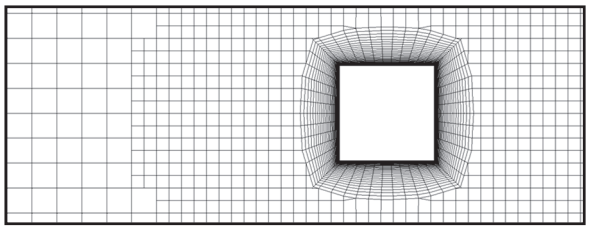

Figure 6.4 Magnified view of grid near the obstacle

6.2.3 Choice of the STRUCT parameters

The controlled STRUCT parameters used are chosen as described in Section 5.4.1. Instantaneous values of $t_{\mathrm{m},0}$ deriving from a cubic URANS simulation are shown in Figure 6.5 below. Geometric averaging of $t_{\mathrm{m},0}$ in the region around the square cylinder leads to the value used here of $t_{\mathrm{m}} = 0.33$ s. Additional precision for such a value is not needed, since results are mainly sensitive to its order of magnitude rather than its value.

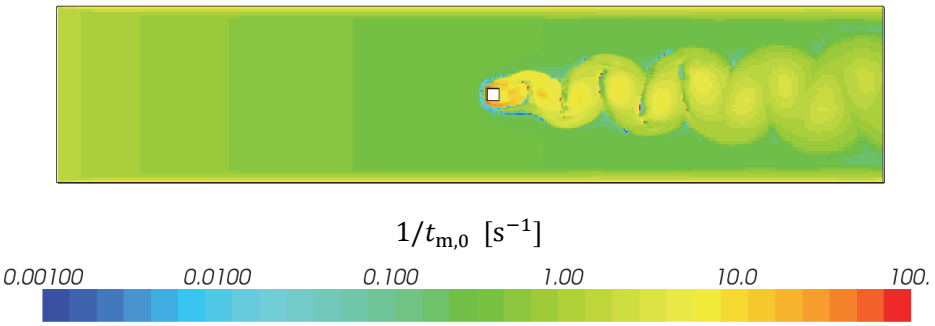

Figure 6.5 Cubic URANS results used for determining the activation condition

This case can be considered trivial for hybrid models, since results obtained without any residual stress are superior to those obtained using any k-ε model, either linear or nonlinear. Accordingly, here a damping coefficient close to zero is selected for optimal predictions: $\phi = 1 \times 10^{-10}$.

6.2.4 Results

A longitudinal section of the flow domain is shown in Figure 6.6 with the cells solved in URANS mode colored in red and those with partial resolution of turbulence are colored in blue. In that figure, we can notice how the hybrid mode is enabled only in the regions expected to be more deformed: those around and past the obstacle. On the other hand, upstream regions operate in URANS mode.

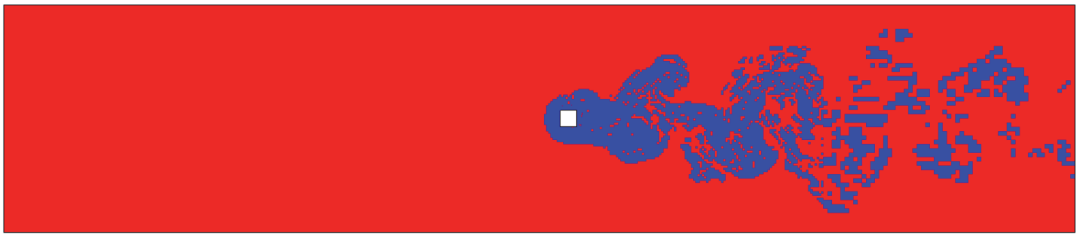

Figure 6.6 Square cylinder flow: STRUCT activation, instantaneous scalar field, in blue

We can infer from Figure 6.6 that, if the same channel had no square cylinder, the picture would be all red so that the simulation would be solved fully as URANS. Such a case would be equivalent to a simple channel flow. On such a geometry, URANS formulations have been tested extensively and are known to produce reliable time-averaged results (Wilcox, 1993). Such a result supports the idea that STRUCT follows a defensive strategy.

A graphical example of the description of shedding is shown in Figure 6.7 below. In that figure, we can notice that the cubic k-ε predicts one main shedding frequency, without evolving into more complex structures. Conversely, STRUCT produces a more irregular instantaneous picture. An analogous comparison can be found in Figure 4.7 between linear and cubic k-ε.

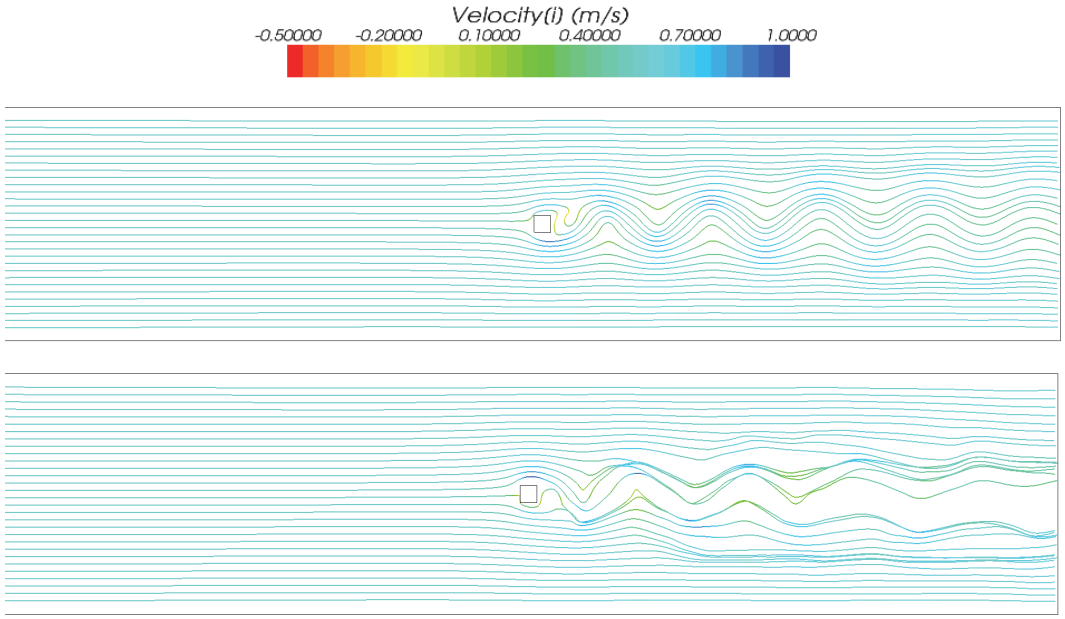

Figure 6.7 Streamlines colored based on x-component of velocity drawn on instantaneous results of cubic k-ε (top) and STRUCT (bottom)

An additional graphical example of the behavior of the STRUCT approach can be made by observing the instantaneous variation with simulated physical time of the x-component of resolved velocity, $\bar{u}$, presented in Figure 6.9. The figure compares cubic NLEVM URANS with and without the STRUCT approach enabled. All other simulation conditions are the same. Both runs start from uniform velocity and constant initial turbulence fields. Results in Figure 6.9 show the variation of $\bar{u}$ with respect to time in 5 locations in the domain, as shown in Figure 6.8. By observing the figure, we can notice the single-mode oscillations produced by URANS and the more complex ones by STRUCT.

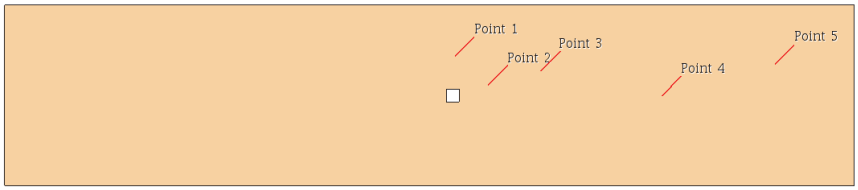

Figure 6.8 Locations of the probes used in Figure 6.9

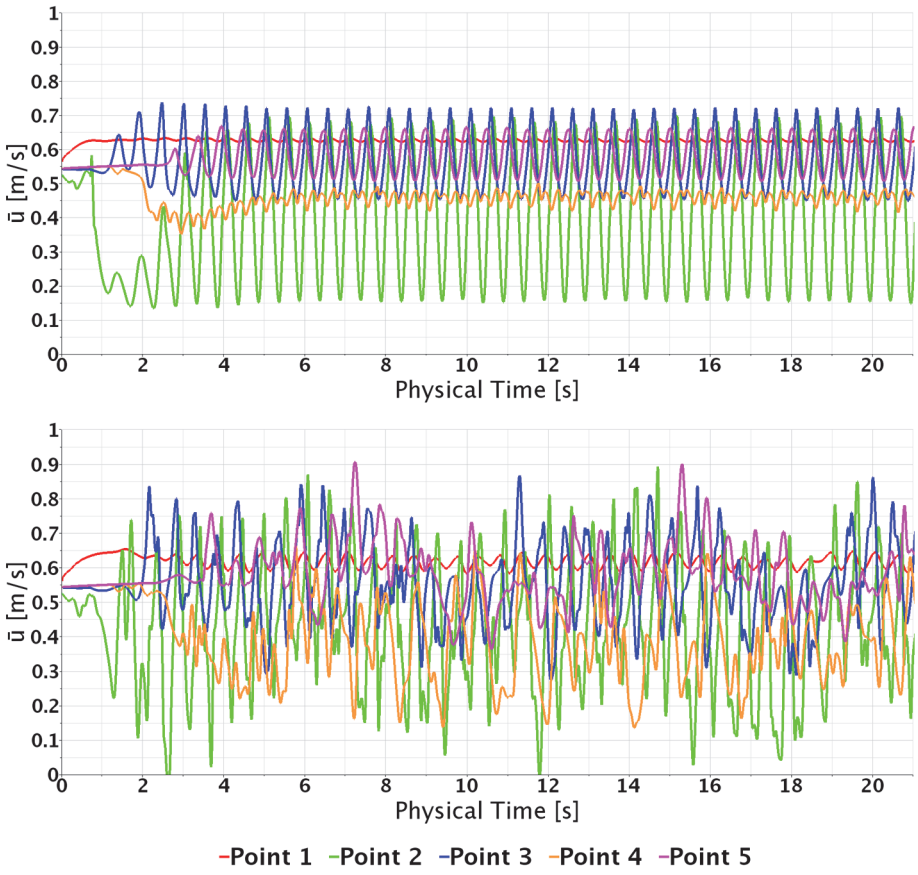

Figure 6.9 Convergence of results for cubic NLEVM (top) and STRUCT (bottom)

The runtime on an equal number of parallel cores increases by 4.9% in this test case when switching from cubic URANS to STRUCT.

We now analyze quantitatively how STRUCT results compare to experimental data and results from other turbulence models. Results for the five variables available in the experimental data set are shown in the figures below. Those variables are:

- Time average of velocity in the x-direction
- Time average of velocity in the y-direction
- Time variance of velocity in the x-direction
- Time variance of velocity in the y-direction
- Time covariance of velocity in the x-y directions

Those directions refer to the frame of reference of Figure 6.1. Recall that the short names used in the figures' legends to refer to the tested models are those described in Section 5.4.3.

By observing time-averaged velocity profiles in the x-direction in Figure 6.10 below, we can notice that the cubic URANS results are closer to the experiment than the linear URANS ones. A closer agreement with the experiment is achieved when using STRUCT. The benefits of STRUCT appear to be stronger in regions near the obstacle where the massive separation takes place, in regions in and after the wake, and in regions where the strongest shedding occurs. The URANS models, in particular the cubic one, produce results close to the experiment in low-deformation regions, especially those shown in the first and last data lines. Conversely, URANS models predict a wake characterized by negative time-averaged velocity-x that appears to be too strong compared to the experiment and displaced forward in the x-direction.

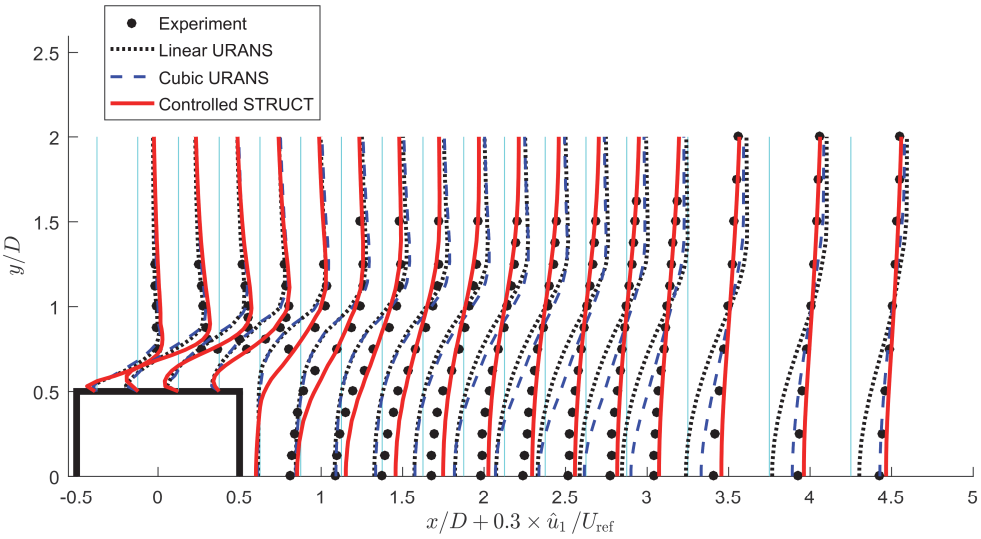

Figure 6.10 Flow past a square cylinder, time-averaged velocity $\hat{u}_1$ profiles

Results for the time-averaged y-component of velocity are shown in Figure 6.11 below. The scaling factor used for plotting velocity is slightly larger than that used for the x-direction.

The linear and cubic URANS both produce very low absolute values for mean velocity-y in and around the wake area. Conversely, in the same wake region, STRUCT predicts larger absolute values for velocity-y, obtaining closer agreement with the experiment. This trend is inverted in the downstream sets of data, in which the experiment and STRUCT results are closer to zero than the results from both URANS models, which predict negative velocity-y values.

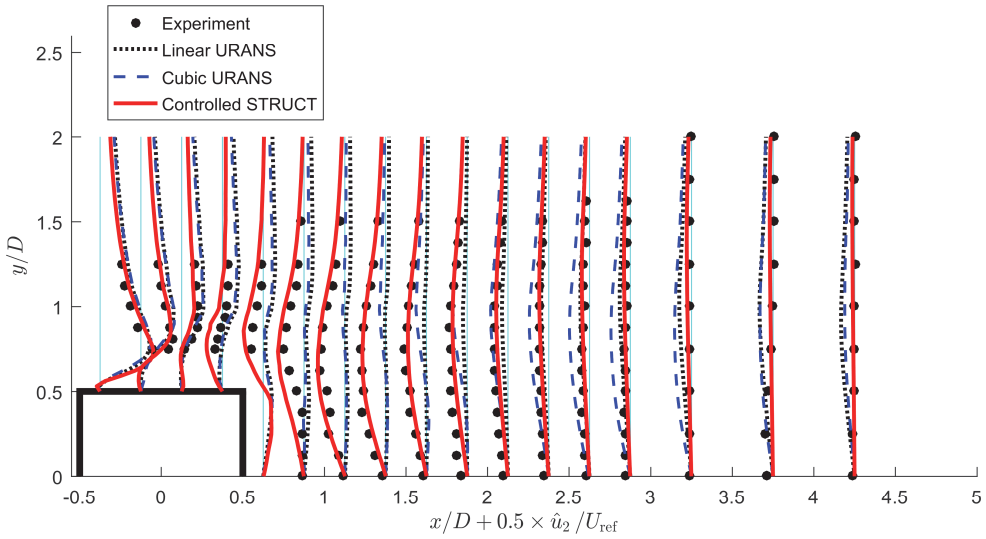

Figure 6.11 Flow past a square cylinder, time-averaged velocity $\hat{u}_2$ profiles

The variance of velocity with respect to time average is shown in Figure 6.12 below for the x-direction. STRUCT results are in close agreement with the experiment. The largest contribution for these STRUCT results comes from the resolved component of velocity variance and is clearly not captured by the URANS predictions, which show negligible profiles in the wake area. This result represents an example of scale overlap preventing accurate URANS description, for which STRUCT activation shows to be clearly beneficial.

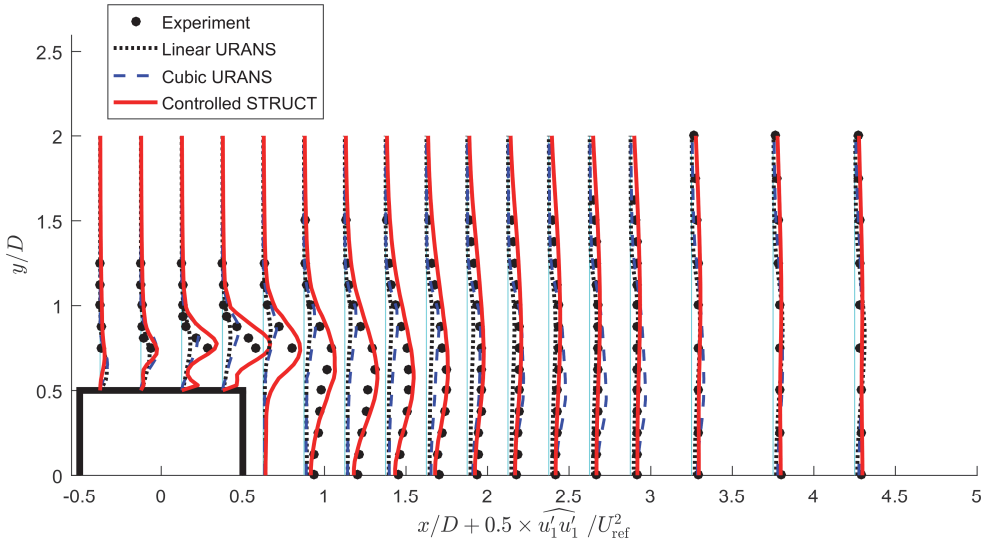

Figure 6.12 Flow past a square cylinder, time variance of velocity, $\widehat{u_1' u_1'}$ profiles

Velocity variance with respect to time average in the y-direction is shown in Figure 6.13 below. Larger values appear in and after the wake region. STRUCT results are in close agreement with the experiment while URANS produces very low values. Further away from the obstacle, the cubic

URANS seems to capture experimental turbulence levels, while the linear one produces low values. This interesting result confirms that URANS retrieves its applicability downstream the disturbance. This retrieval is observed for the advanced anisotropic model tested and not for the linear model, because of the directional nature of the shedding involved.

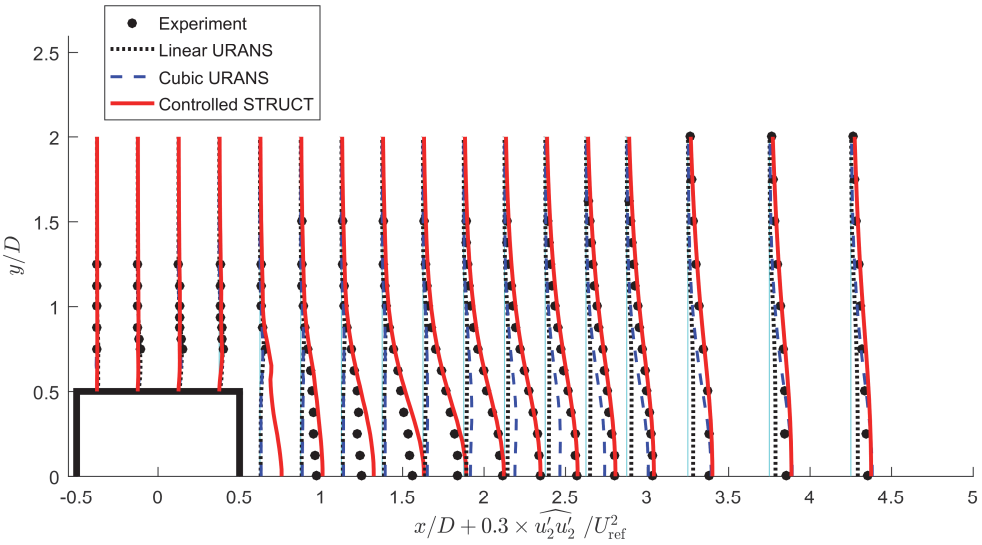

Figure 6.13 Flow past a square cylinder, time variance of velocity, $\widehat{u_2'u_2'}$ profiles

The time covariance of velocity in the x-y directions is shown in Figure 6.14 below. This variable is important because it shows whether the model is predicting the physics of turbulent eddies correctly. In fact, the joint first central moment between two velocity components provides information on any directionality existing in turbulent fluctuations. Absolute values predicted by URANS seem to be too small compared to the experiment, except for the initial and final data points. Conversely, STRUCT predictions appear to be very close to the experimental data in essentially all of the domain.

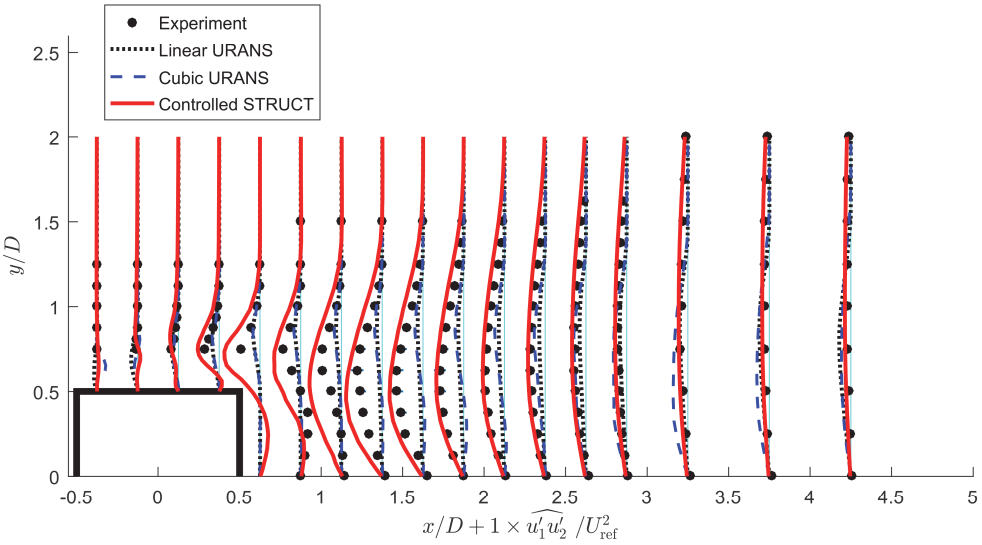

Figure 6.14 Flow past a square cylinder, time covariance of velocity, $\widehat{u_1'u_2'}$ profiles

6.2.5 Grid sensitivity

One of the key objectives of the proposed STRUCT approach is to achieve low sensitivity to the computational grids, as typical of URANS models and not achieved by existing hybrid closures. In order to assess its robust applicability, the model is evaluated on a series of grids of varying size and cell geometry. Four polyhedral grids are tested, in addition to the trimmed grid used in the previous tests. Specifications of the computational grids are described in Table VIII below.

The polyhedral grids are built using the automated meshing algorithm of the STAR-CCM+ code. Due to their lack of a regular pattern, polyhedral grids are capable of adapting to complex geometries while being generated by easy-to-use algorithms. These features make polyhedral grids a frequent and effective choice in the industry. The size specified for polyhedral cells in Table VIII below is a reference value used as an input in the automatic meshing tool used.

Table VIII Grids used in the sensitivity analysis for the square cylinder

Grid type	Reference cell size [mm]	Number of cells
Trimmed	10.50000	676,000
Polyhedral	15.75000	2,500,000
Polyhedral	23.62500	801,000
Polyhedral	35.43750	275,000
Polyhedral	53.15625	98,000

A detail of the four polyhedral grids used is shown in Figure 6.15 below.

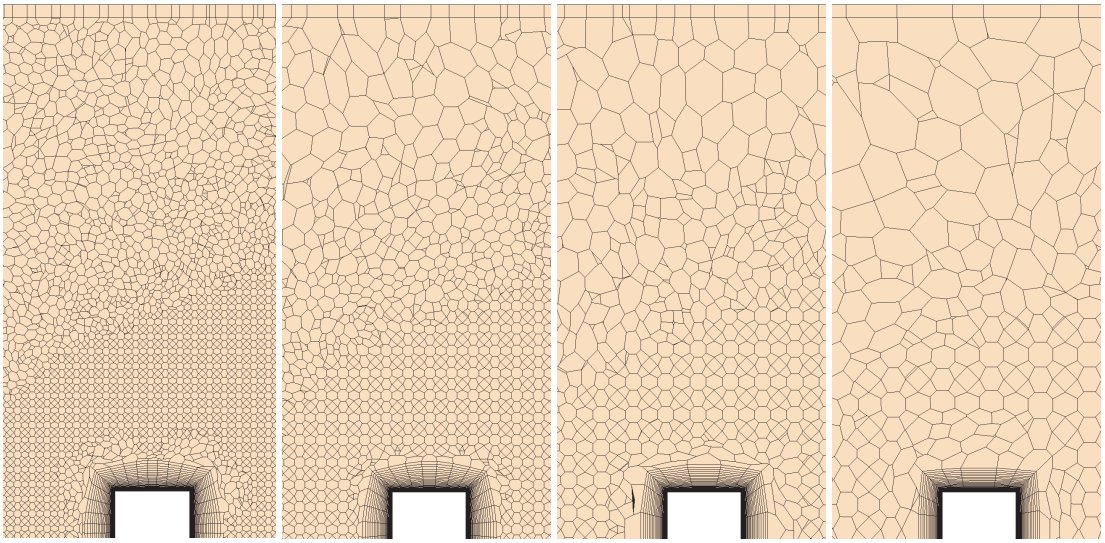

Figure 6.15 Central section showing the boundaries of the polyhedral cells used for sensitivity analysis, ordered from the finest to the coarsest one as described in Table VIII

In the tests made here, the refinement of the grid near the wall in the wall-normal direction is constant throughout all simulations, as it is designed to consistently capture the boundary layer region. Additional local grid refinement by halving the cell size is performed around and after the cylinder analogously to what is done for the trimmed mesh and shown in Figure 6.3. The total number of cells generated by the polyhedral algorithm is larger than that generated for the trimmed mesh using the same base size, as we can observe in Table VIII.

Grid sensitivity results for velocity in the x-direction are shown in Figure 6.16 below.

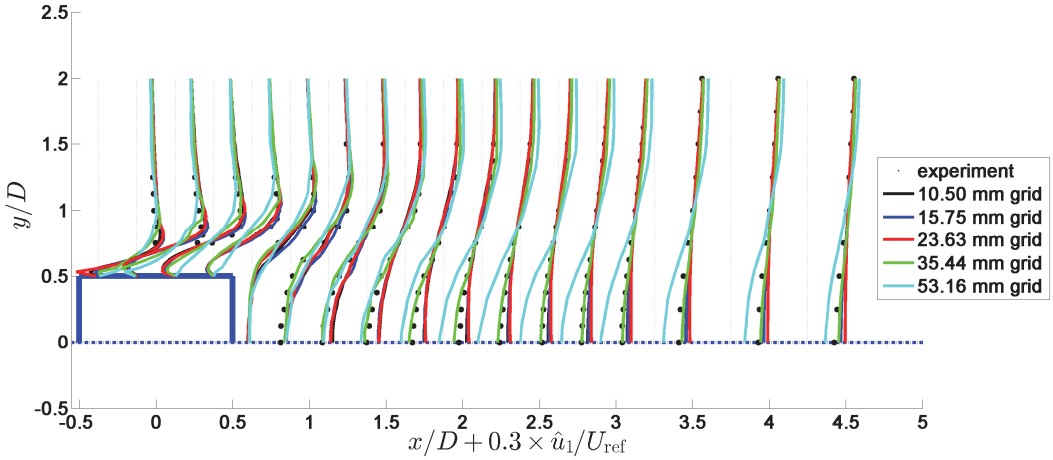

Figure 6.16 Controlled STRUCT grid sensitivity, time-averaged velocity $\hat{u}_1$ profiles

Results for the time variance of velocity in the x-direction are shown in Figure 6.17 below.

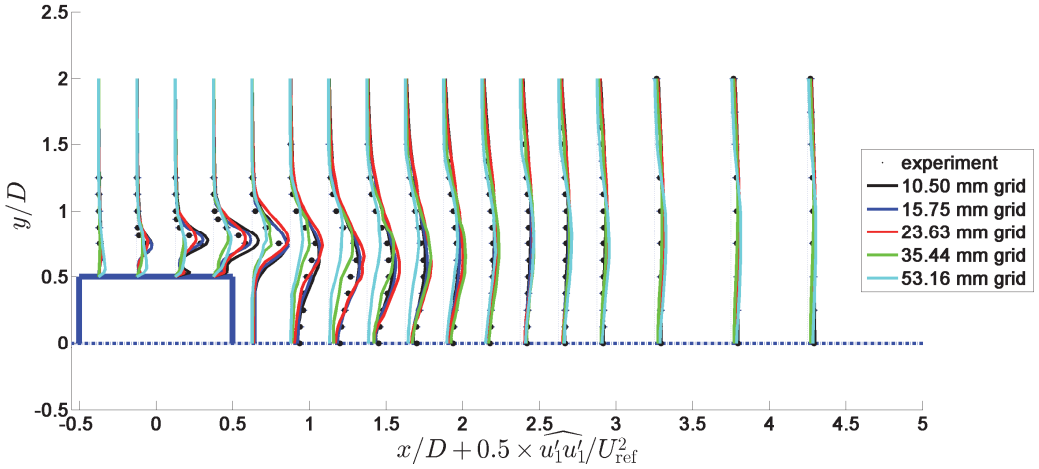

Figure 6.17 Controlled STRUCT grid sensitivity, time variance of velocity, $\widehat{u_1'u_1'}$ profiles

Results in the two figures above show a consistent grid behavior when the grid is refined. Solutions for all grids, except the two coarsest ones, are very similar to each other. It is important to underline how for very coarse grids, i.e. in the 53 mm case, results approach the predictions of a simple URANS coarse-grid behavior, which is the originally designed model behavior. The grid resolution is simply too large to allow resolution of any of the important scales and the model consistently produces URANS-approaching predictions.

The STRUCT model behavior is very well expressed by the activation regions for the four polyhedral grids of Table VIII, shown in Figure 6.18. Those regions become smaller in size as the grid becomes coarser, as a natural consequence of the inability of resolving with the grid the relevant scales. This produces a desirable behavior for hybrid models since coarser grids can be considered to be less suitable for scale-resolving simulations than finer ones.

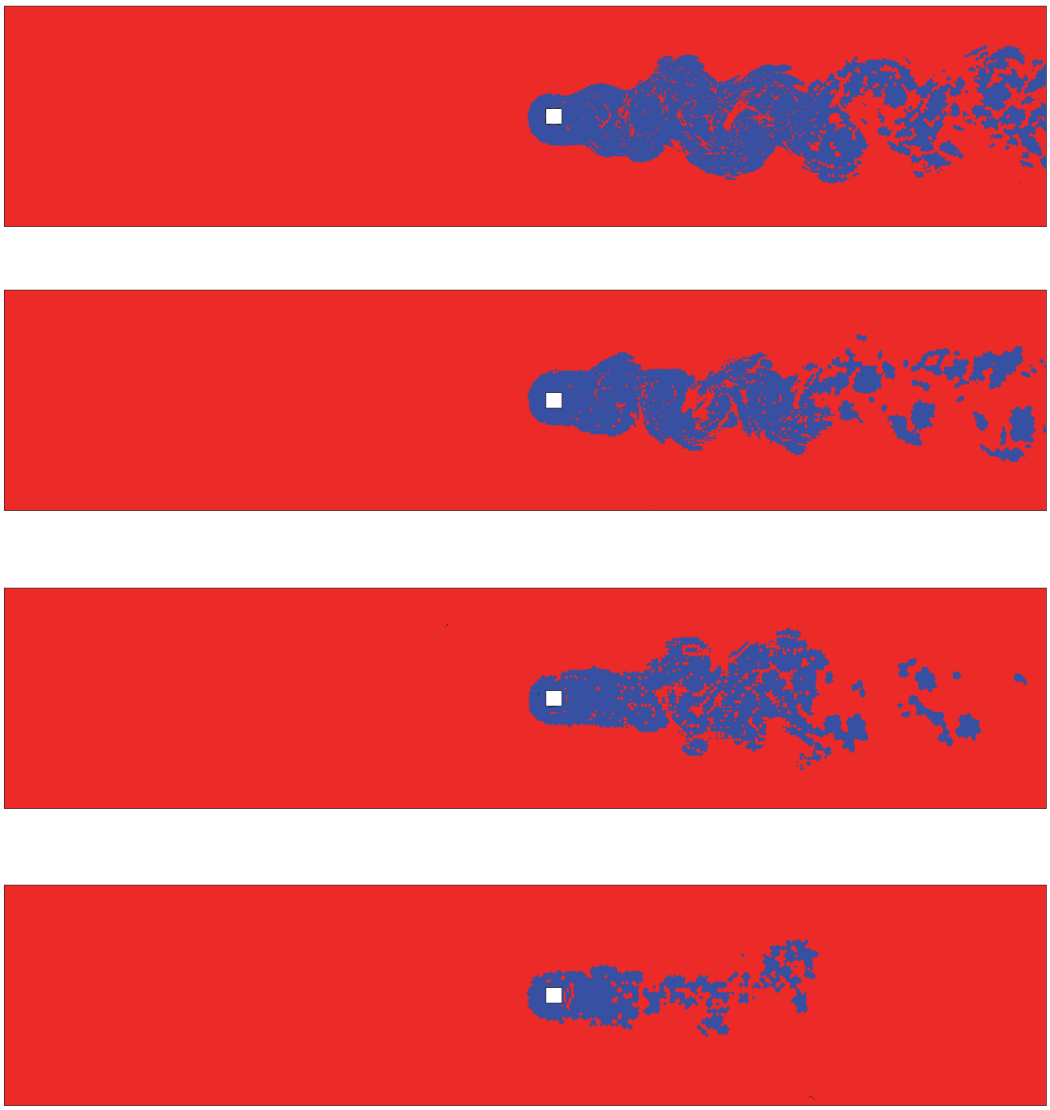

Figure 6.18 STRUCT activation regions for the four polyhedral grids of Table VIII, ordered from the finest to the coarsest

6.2.6 Qualitative comparison of resolved velocity fields

Instantaneous fields of resolved velocity can be used to verify qualitatively the behavior of the controlled STRUCT approach compared to other models. In Figure 6.19 and Figure 6.20, fields are shown for the x-component and the y-component of velocity, respectively. Those figures compare STRUCT results with those from the baseline cubic URANS and those from an LES run that required a number of core-hours approximately 115 times larger than those needed for the cubic URANS.

The URANS results show a quasi-periodic pattern of resolved vortices produced past the obstacle that continue throughout the domain until the outlet. Conversely, in LES results, significant dissipation breaks the larger vortices into smaller resolved turbulent structures along with the flow downstream the obstacle.

The STRUCT results are run on the same grid as the cubic URANS ones. A decay of large resolved structures into smaller one along with the flow is observed. The result is less detailed than for LES but retains a similar distribution of local fields.

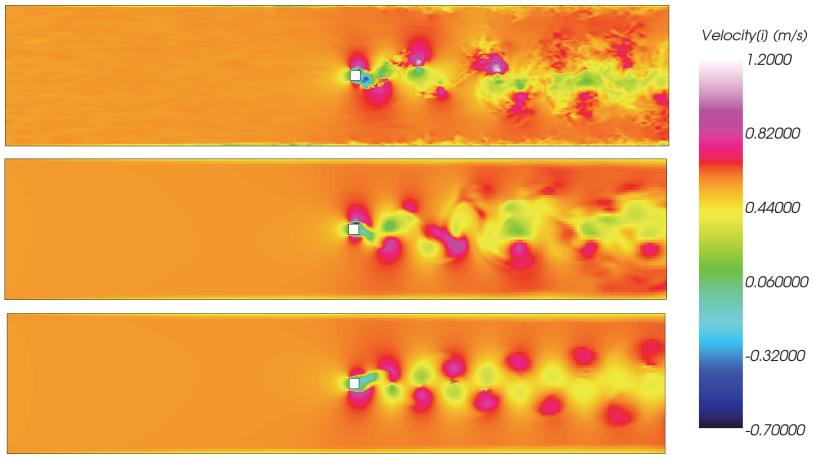

Figure 6.19 Velocity-x maps for LES (top), STRUCT (middle), cubic URANS (bottom)

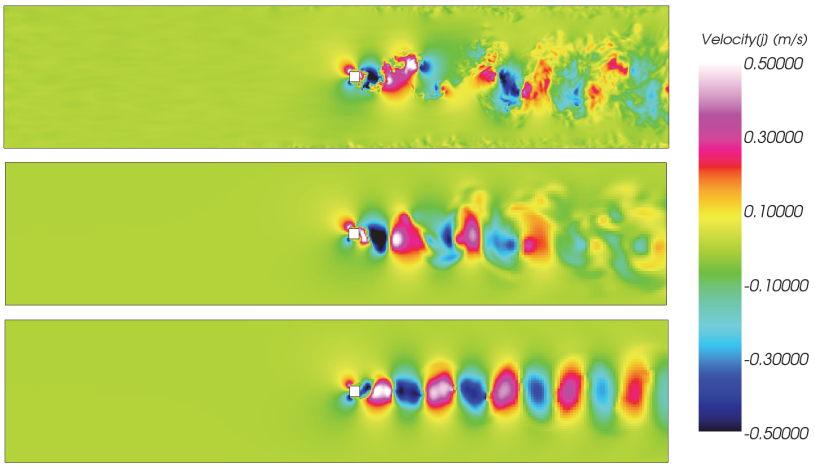

Figure 6.20 Velocity-y maps for LES (top), STRUCT (middle), cubic URANS (bottom)

6.3 Turbulent mixing in a T-junction

6.3.1 Description and experimental data

The test case representing turbulent mixing in a T-junction test was introduced in Section 3.2.2. This case has shown to be a particularly challenging one, and very importantly an extremely relevant one for industrial applications. Results from the literature discussed in Section 3.2.2 show how hybrid turbulence models achieve mixed success depending on the model, the grid, the numerical schemes used. Most importantly blind testing has shown consistent failure of hybrid closures, and only ad-hoc corrections on open benchmarks have allowed producing reasonable prediction for hybrid models, but still lacking any generality and being strongly correlate to the grid and numerical scheme selection.

In the T-junction configuration, colder (19 °C) water flowing through a 140 mm diameter pipe encounters an intersection where warmer (36 °C) water is injected through a smaller (100 mm) diameter pipe. The volumetric flow rate is 9×10^{-3} m^3/s for the cold stream and 6×10^{-3} m^3/s for the hot one. The geometry is drawn in Figure 6.21 below.

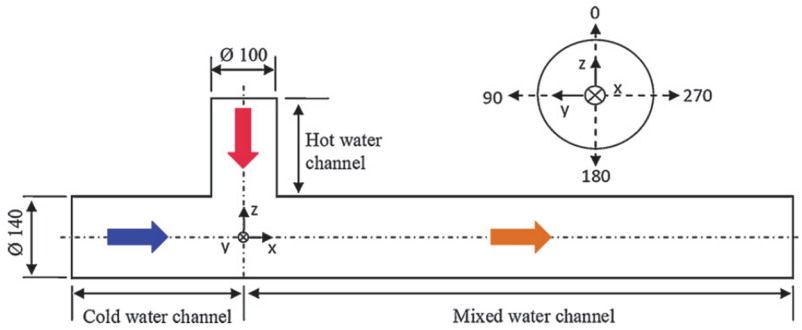

Figure 6.21 T-junction schematic, from Ayhan and Sökmen (2012)

The test case reproduced here was adopted for the 1st OECD/NEA international benchmark exercise and has been discussed extensively in the literature. Data and results have been published by Smith and co-workers (2011).

Experimental acquisitions (Smith et al., 2011) include LDV, PIV, and temperature measurements made with thermocouples. The main velocity measurements used in this work are those collected using PIV. The experimental profiles are available at four test sections, respectively at 1.6, 2.6, 3.6 and 4.6 cold-pipe diameters distance downstream the junction. Data are available for horizontal (x-y plane) and vertical (x-z plane) central sections of the pipe, as illustrated in Figure 6.22.

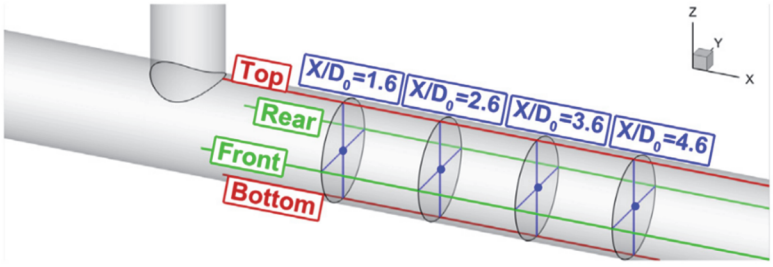

Figure 6.22 Locations of experimental data, from Gritskevich et al. (2014)

The PIV data used in this work are associated with uncertainty for velocity measurements (Smith et al., 2011) of 5% plus a systematic 0.02 m/s. Errors for velocity variance are doubled compared to those for velocity. The same report by Smith et al. (2011) states that uncertainties are likely to be even higher near the walls. In addition to this, the time variance of velocity has significant uncertainty in the central regions of the flow. This occurs because of issues with walls reflecting the PIV light sheet during the acquisitions. According to the experiment's authors (Smith et al., 2011), those issues affect the velocity variance in a systematic way but should not affect time-averaged velocity.

6.3.2 Computational grid, boundary conditions, and other details

All wall boundaries are treated with wall functions, ensuring that y+ be larger than 30 in the first cell near the wall. A similar approach was adopted in LES by Jayaraju, Komen, and Baglietto (2010) and was compared to the wall-resolved approach. The study showed that the use of wall functions leads to a consistent description of time-averaged velocity profiles and an underestimate of the gradients of velocity variance profiles near the wall.

Pressure outlet boundary conditions are used at the domain's exit. Inlet conditions are taken from the experimental LDV data, which match fully developed profile data only for the horizontal pipe.

Temperatures are treated with a segregated fluid temperature model. Buoyancy effects are neglected because of the low variation of fluid density in the range of interest,

The computational grid used for most simulations uses a trimmed mesh with a 4.5 mm base size and a total of 746,000 cells. In this grid, URANS achieves reasonable convergence. The grid is shown in Figure 6.23 below.

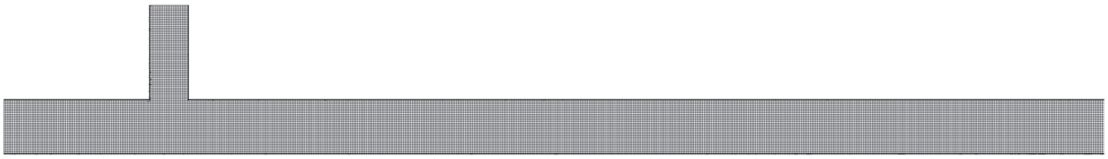

Figure 6.23 Computational grid for the T-junction test case

A magnified detail of the grid is shown in Figure 6.24 below.

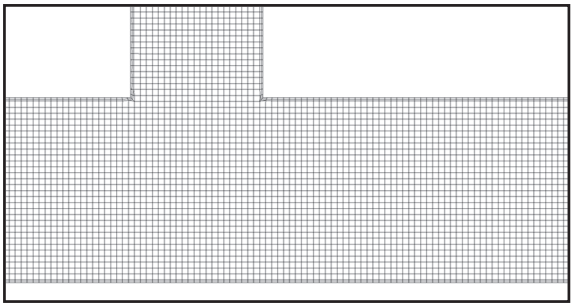

Figure 6.24 Magnified view of the grid for the T-junction test case

Such a grid is coarser than all of the grids discussed in Section 3.2.2 and used in the literature for testing hybrid turbulence models. Among those examples, the most successful application of hybrid models is run on a grid with 4.9 million cells (Gritskevich et al., 2014).

LES runs here are done using a grid finer than the one shown above, with a base size of 1.5 mm. The total size of this grid is 17.1 million cells. LES is run using the WALE SGS closure.

6.3.3 Choice of the STRUCT parameters

Activation parameters are determined as described in Section 5.4.1. A preliminary cubic URANS simulation is used to obtain instantaneous values for $t_{\mathrm{m},0}$. Geometric averaging of such a quantity around the location of interest leads to a value of $t_{\mathrm{m}} = 0.1$ s. Greater precision for this parameter is not needed, due to the low sensitivity of STRUCT results. The instantaneous values of the frequency associated with modeled scales, $t_{\mathrm{m},0}$, is shown in Figure 6.25 below.

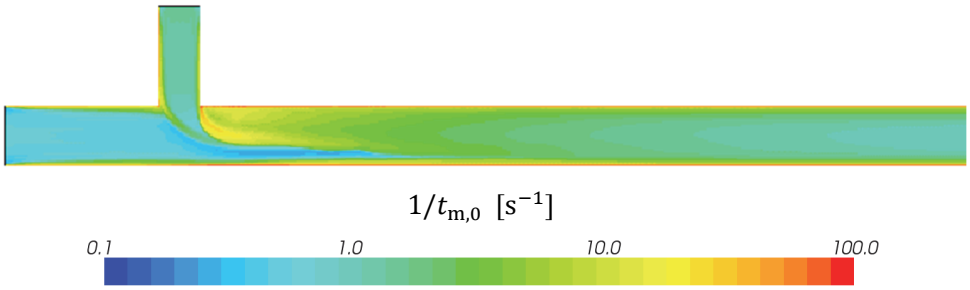

Figure 6.25 Cubic URANS results used for determining the activation condition

A suitable value for ϕ has been determined a posteriori as 0.6.

6.3.4 Results

Similarly to what is done for the square cylinder, we show the STRUCT activation regions for this test case in blue in Figure 6.26 below. Such a figure shows that the hybrid model is only activated in regions where we would expect the most disturbed flow: inside and downstream the junction. We can infer from the same figure that an undisturbed pipe flow would be solved using URANS.

Small regions of model activation occur near the inlet. This effect is likely to be due to the adaptation of the flow to a non-perfect description of velocity profiles by the inlet boundary condition.

Figure 6.26 T-junction test case: STRUCT activation, in blue, instantaneous scalar field

We can look at the variation over time of a variable defining seven arbitrary points whose locations are illustrated in Figure 6.27. The 7 points have different coordinates also in the y-direction, not shown here for the sake of brevity.

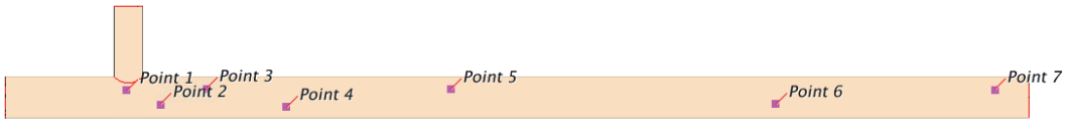

Figure 6.27 Locations of the probes used in Figure 6.28

The time history for resolved velocity in the x-direction is shown in Figure 6.28 below. The top plot shows cubic NLEVM results and the bottom plot controlled STRUCT ones. The two simulations use uniform fields as initial condition. Results show clearly how STRUCT results produce resolved scales with greater spectral content than URANS, especially inside the regions of hybrid activation.

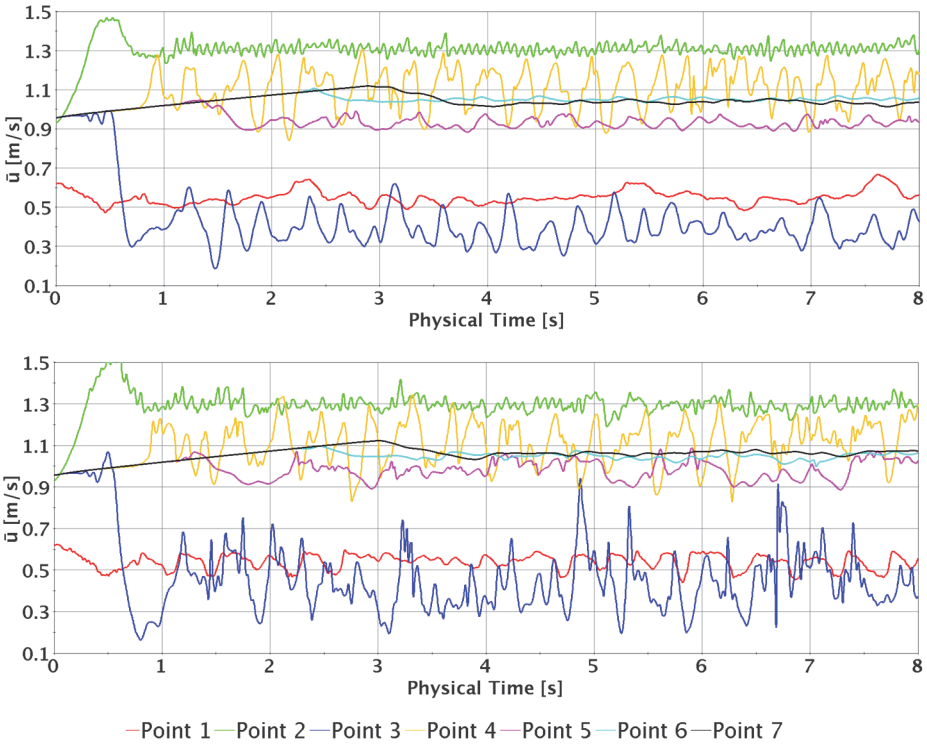

Figure 6.28 Convergence of results for cubic NLEVM (top) and STRUCT (bottom)

In this test case, STRUCT simulations run 2.6% slower than cubic URANS ones.

Experimental data for 5 variables are available for the 2 sections described above, making a total of 10 sets. All of those data sets are plotted against simulation results. The 5 variables are listed below. Information in round brackets refers to data in the x-z section, perpendicular to the x-y one.

- Time average of velocity in the x-direction
- Time average of velocity-y (velocity-z)
- Time variance of velocity in the x-direction
- Time variance of velocity in the y (z) direction
- Time covariance of velocity in the x-y (x-z) direction

All of those sets are compared with simulation results in the figures below. The abbreviated model names used in the legends are defined in Section 5.4.3.

Observing the plot for the x-component of velocity in Figure 6.29 below, we can notice that STRUCT and LES results agree closely with the experiment, while the linear and nonlinear URANS both underestimate velocities near the center of the pipe in the most downstream sections. Those velocities are overestimated in the two horizontal sides. This behavior can be interpreted as the effect of excessive eddy viscosity predicted by the model in the mixing region. The linear URANS appears to agree closely with the experiment in the first section but not in the other sections downstream.

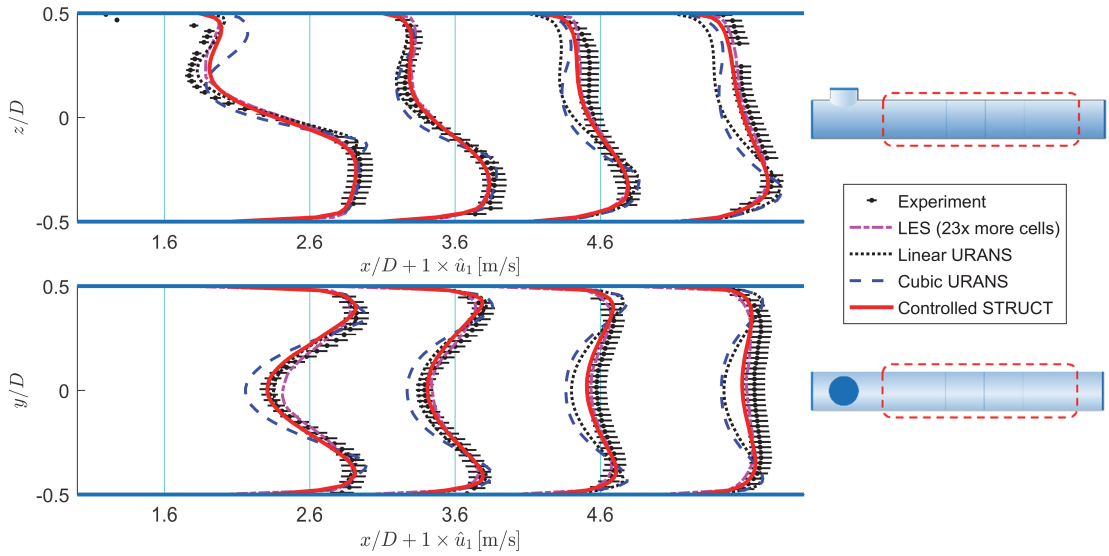

Figure 6.29 T-junction mixing, time-averaged velocity $\hat{u}_1$ profiles

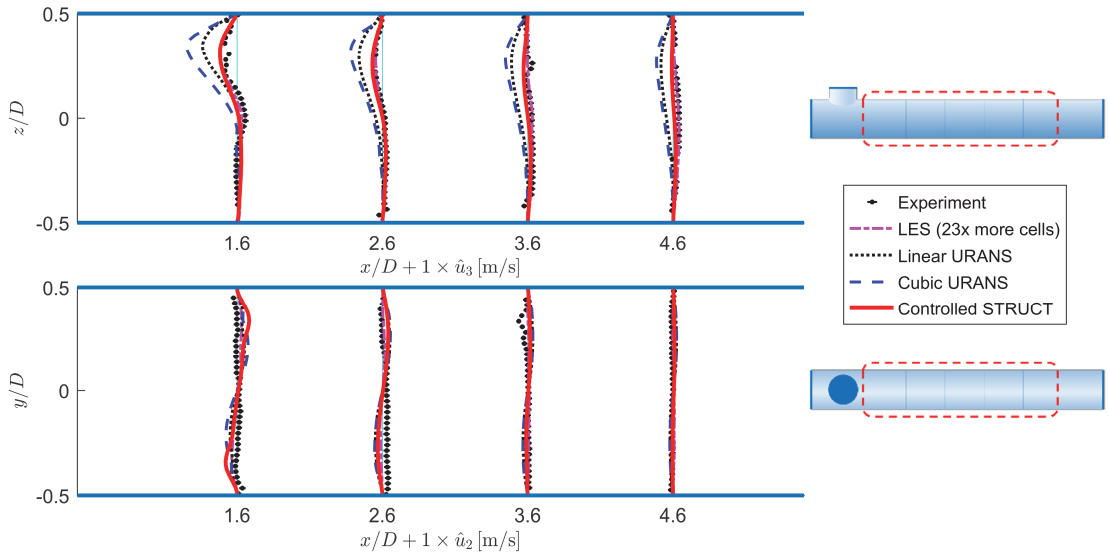

Figure 6.30 T-junction mixing, time-averaged velocity $\hat{u}_3$ and $\hat{u}_2$ profiles

Velocity components normal to the main direction and parallel to the data-collection plane are plotted in Figure 6.30 above, using the same scaling factor for velocities as in Figure 6.29. Results obtained with LES and STRUCT appear to be closer to the experiment than the two URANS results, which show a negative velocity in the z-direction in poor agreement with the experimental data.

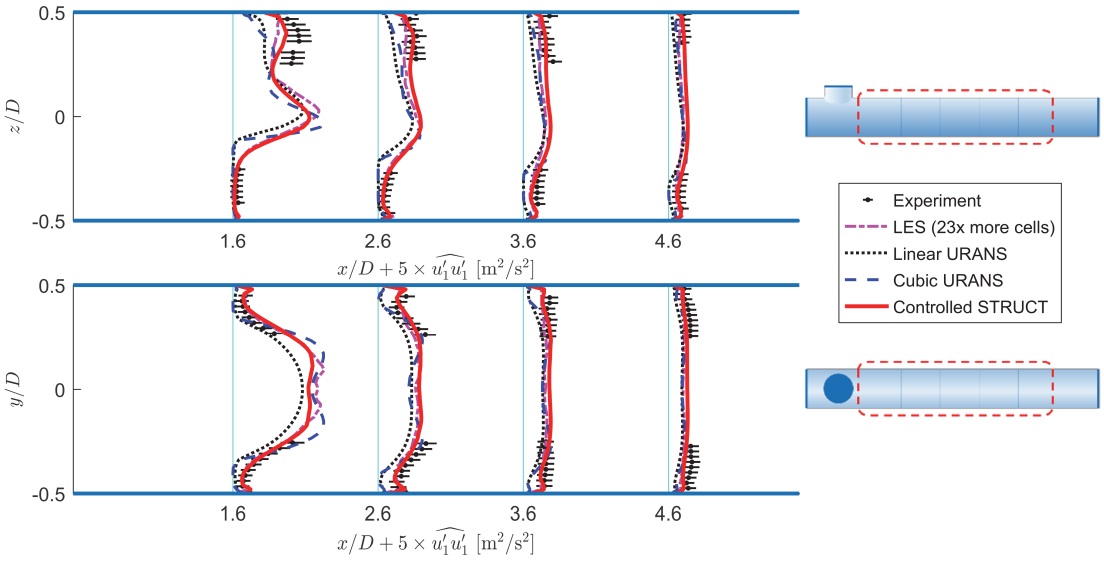

Figure 6.31 T-junction mixing, time variance of velocity, $\widehat{u_1' u_1'}$ profiles

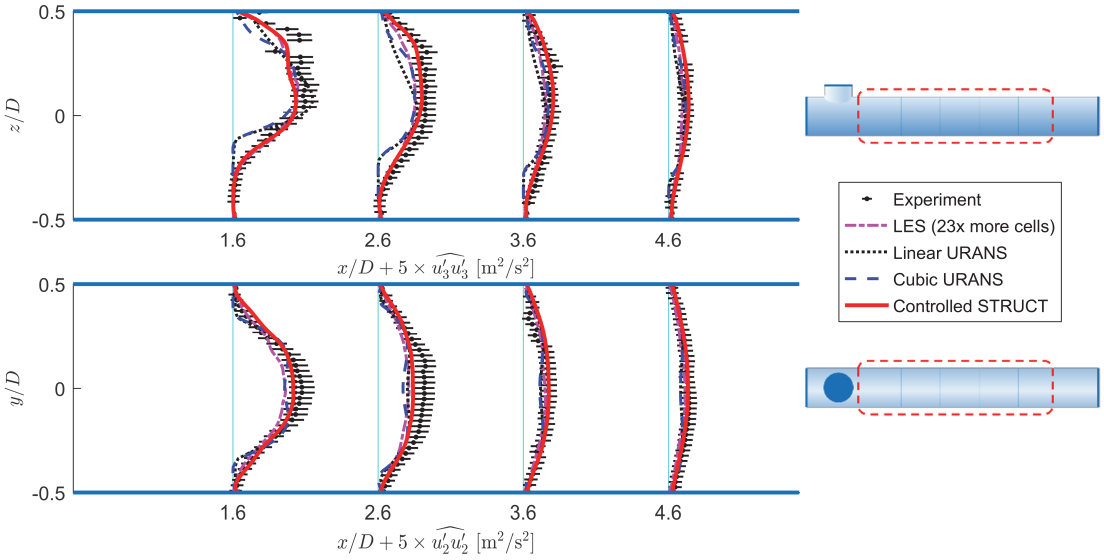

Figure 6.32 T-junction mixing, time variance of velocity, $\widehat{u_3' u_3'}$ and $\widehat{u_2' u_2'}$ profiles

Plots in Figure 6.31 above show the time variance of velocity in the x-direction. The paper presenting experimental results reports large systematic uncertainty near the center of the pipe for this variable. As mentioned above, the authors of the experiment report an overestimate of their data due to the reflection of the PIV light sheet on the walls (Smith et al., 2011). As a consequence, here those

values are omitted, so LES results are used as a reference. This choice is consistent with the benchmark report, which does not show simulation results for $\widehat{u_1'u_1'}$ (Smith et al., 2011). At the sides of the domain, LES and STRUCT results are in close agreement with each-other and are closer to the experiment than the two URANS results. In the rest of the domain, all four models seem to predict trends fairly similar to each other.

The time variance of the component of velocity parallel to the experimental sections and perpendicular to the x-direction is shown in Figure 6.32 above. Those experimental results may also be affected by systematic error as discussed for Figure 6.31 above. Overall, in that plot all four models seem to predict similar profiles. URANS results in the first section appear to have sharper gradients than STRUCT results and experimental data.

Results for the time covariance of velocity are shown in Figure 6.33 below. It is unclear whether a systematic drift also exists in this set of experimental data. The four models tested seem to provide similar results for this variable, in acceptable agreement with experimental data.

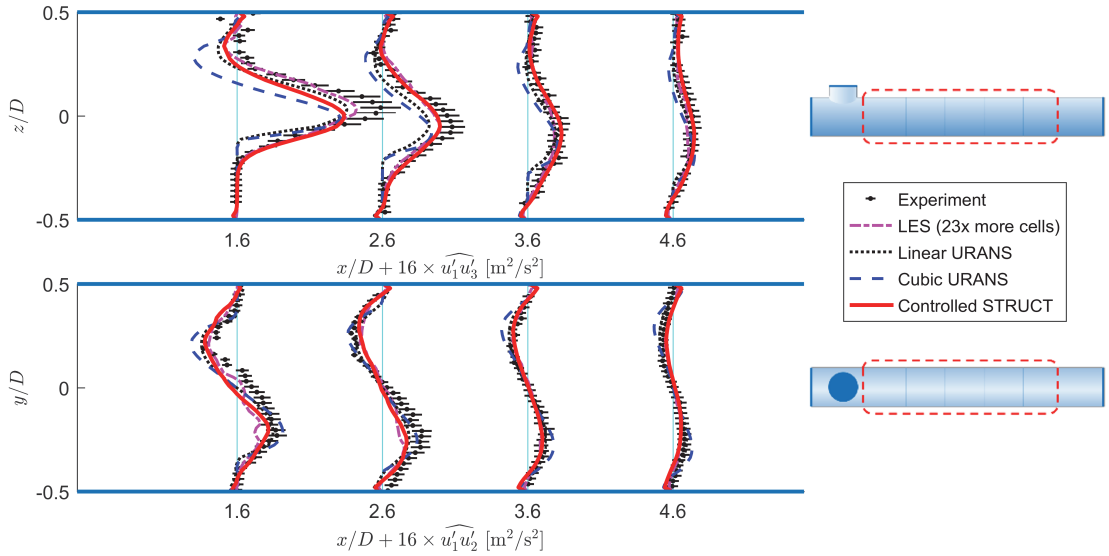

Figure 6.33 T-junction mixing, time covariance of velocity, $\widehat{u_1'u_3'}$ and $\widehat{u_1'u_2'}$ profiles

6.3.5 Grid sensitivity

Again, a grid sensitivity study for the T-junction test case is performed. In addition to the trimmed grid used in the sections above, four polyhedral grids are used, whose details are shown in Table IX below. All of those grids use the same wall-normal thickness of the first two cells. Results for the x-component of velocity and for velocity fluctuations in the x-direction are shown respectively in Figure 6.35 and Figure 6.36. By observing those results, we can draw similar conclusions as for the square cylinder test case. Results appear to converge appropriately for the finer grids while coarser grids produce an error that is comparable with that of URANS solutions for coarse grids. In particular, the two coarsest grids are inadequate for this test case and fail at converging to a consistent solution. As mentioned, when looking at the velocity variance in the x-direction, experimental data near the center in the x-y plane are affected by a positive bias (Smith et al., 2011), so results in Figure 6.36 resemble the STRUCT and LES results shown in Figure 6.31.

Results obtained with the coarsest grid tested seem to produce an irregular nonphysical behavior. Such behavior is similar to the behavior of URANS on the same very coarse grid.

Table IX Grids used in the sensitivity analysis for the T-junction

Grid type	Reference cell size [mm]	Number of cells
Trimmed	4.5000	646,000
Polyhedral	4.5000	886,000
Polyhedral	6.7500	270,000
Polyhedral	10.1250	102,000
Polyhedral	15.1875	39,000

A detailed view of the four polyhedral grids is shown in Figure 6.34 below.

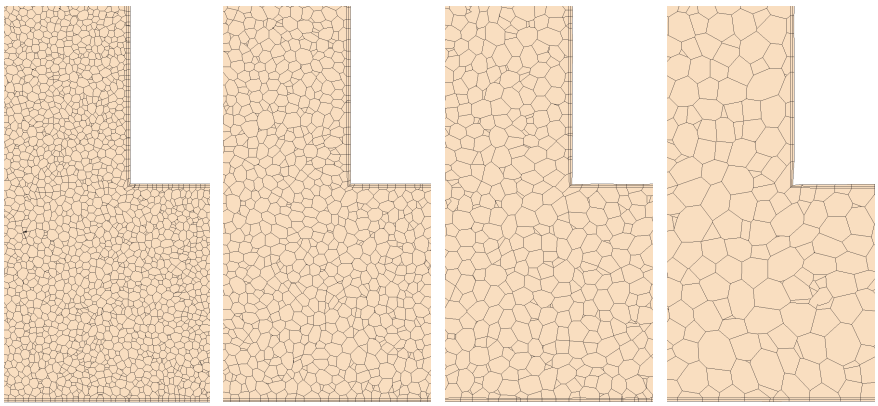

Figure 6.34 Polyhedral grids used for sensitivity analysis, ordered from the finest to the coarsest ones as described in Table IX

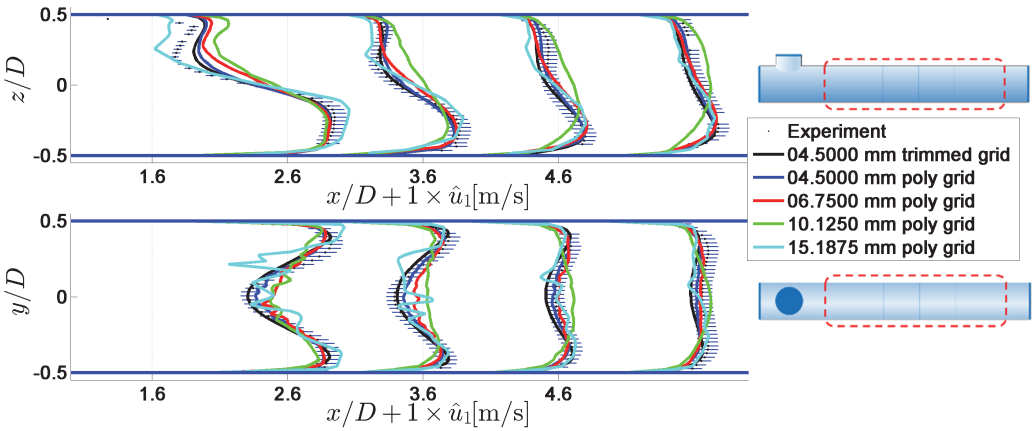

Figure 6.35 Controlled STRUCT grid sensitivity, time-averaged velocity $\hat{u}_1$ profiles

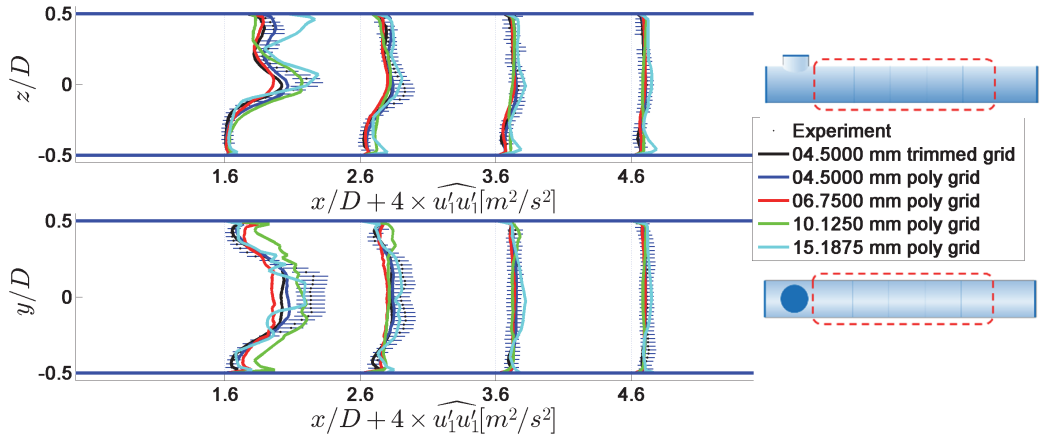

Figure 6.36 Controlled STRUCT grid sensitivity, time variance of velocity, $\widehat{u_1'u_1'}$ profiles

Activation regions for the four polyhedral grids of Table IX are shown in Figure 6.37 below. Analogously to square cylinder results, we can observe that activation regions tend to become smaller or to keep a similar size as the grid gets coarser. This confirms the capability of STRUCT of benefiting of the robustness of URANS, avoiding model breakdown on coarser grids. The error generated by STRUCT on coarser grids is comparable to that observed in preliminary URANS simulations not shown here for the sake of brevity.

In this case, the two coarsest grids tested are too coarse for producing reliable results both in STRUCT and URANS runs. They are shown here just for comparison.

Figure 6.37 STRUCT activation regions for the four polyhedral grids of Table IX, ordered from the finest to the coarsest

Mild separation in an asymmetric diffuser

6.3.6 Description and experimental data

The test case of the mild separation in an asymmetric diffuser is introduced in Section 3.2.3, and results from the literature are illustrated in the same section. Results from Davidson (2006) show very poor agreement between experimental data and SAS profiles. The mild separation features in the asymmetric diffuser test case are generally challenging for hybrid turbulence models.

A fully developed air flow runs through a 0.515×0.015 m rectangular duct. The Reynolds number is 20,000 based on the height of the inlet channel $H = 0.015$ m and on the bulk inlet velocity. In the diffuser section, the bottom wall has a slope with an angle of 10 degrees. Such a wall reverts to being horizontal when the flow domain height is greater than 4.7 times the inlet height, H. The reference inlet velocity is $U_{\mathrm{ref}} = 18.32$ m/s. The geometry sizes are drawn in Figure 6.38 below.

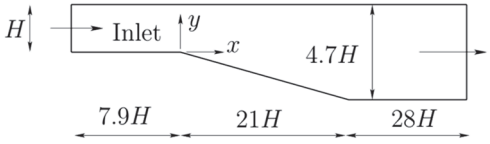

Figure 6.38 Geometry, not to scale, from Davidson (2006)

Experimental data used in this work were collected by Buice (1997) using hot wire anemometry, including cross-wire techniques and pulsed-wire anemometry. The final experimental data set is a combination of acquisitions deriving from those different techniques. The geometry used is the same as for the LDV acquisitions performed previously by Obi and co-workers (Obi et al., 1993).

Experimental results show a recirculation zone occurring towards the end of the slope close to the bottom wall, as shown in the drawing of Figure 6.39, by Buice (1997).

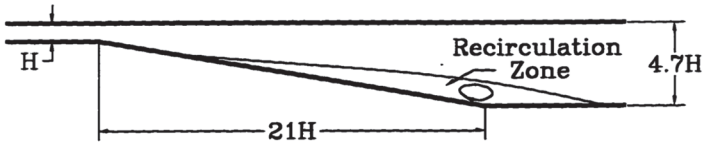

Figure 6.39 Diffuser geometry and drawing of the recirculation zone, from Buice (1997)

6.3.7 Computational grid, boundary conditions, and other details

A wall-resolved approach is used at the top and bottom walls of the domain, ensuring that y+ is smaller than 1 in the first cell near the wall and that the cell growth rate is smaller than 1.1. The wall-resolved approach is chosen because wall functions are typically not designed to be used in boundaries where separation occurs. The sides of the domain are treated with periodic boundary conditions since the geometry is defined by an extruded 2D shape.

A pressure outlet boundary condition is used (CD-adapco, 2015). Inlet conditions are taken from the experimental data by Buice (1997). The grid used in all cases, except when specified differently, has a variable cell size. A representative cell size value is 1.5 mm, with a total of about 1,800,000 cells. On this grid, URANS achieves reasonable convergence. Such a grid is shown in Figure 6.40 below.

Figure 6.40 Computational grid for the asymmetric diffuser test case

A magnified detail of the grid near the opening of the diffuser is shown in Figure 6.41 below.

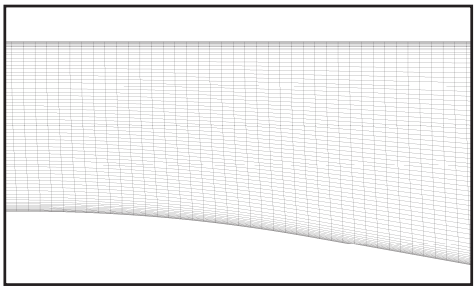

Figure 6.41 Magnified view of the grid near the opening of the diffuser

The work by Buice (1997) combines different experimental techniques and provides an estimate for the uncertainties related to each one of them. Here, we use conservatively the largest among the uncertainties reported: those for cross-wire anemometry. Those values are estimated based on a study by Anderson and Eaton (1987), reporting a 3% random error for averaged velocity, 5% for variance of velocity, and 10% for the covariance of velocity. No indication was given for a systematic uncertainty component. Such uncertainty is particularly important in regions of zero velocity, such as the recirculation zone. For this reason, the reference velocity is used to calculate error bars in the figures below, so that all error bars are equally large, even in the recirculation region. This approach is conservative since it overestimates uncertainty. It is followed for all error bars except for those for velocity covariance because values are very low compared to the reference velocity and would produce an overly conservative error bar.

6.3.8 Choice of the STRUCT parameters

The activation parameters used here for the controlled STRUCT approach are introduced as described in Section 5.4.1. Based on a preliminary URANS simulation, values for $t_{\mathrm{URANS},0}$ are obtained and then averaged through a geometric average. As a result, a value $t_{\mathrm{m}} = 0.01$ s is obtained and used here. Greater precision for this value is not needed due to the low sensitivity of the STRUCT approach to the coefficient. The instantaneous values of the frequency associated with modeled scales, $f_{\mathrm{m},0}$, is plotted in Figure 6.42 below.

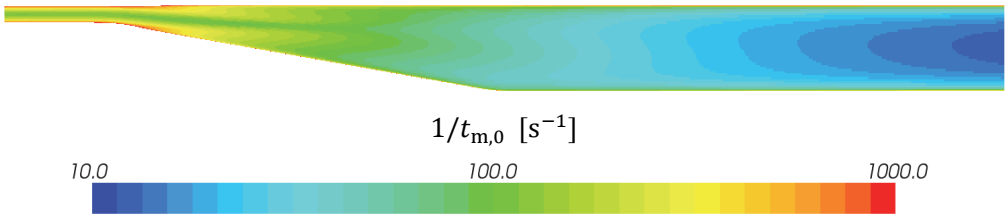

Figure 6.42 Cubic URANS results used for determining the activation condition

The optimal value for ϕ has been determined a posteriori as 0.6, which is the same value used in the T-junction test case above.

6.3.9 Results

The STRUCT activation regions for this test case are shown in Figure 6.43 below. As also observed for the previous flow cases, we can notice here that the regions of hybrid model activation are in locations in which, intuitively, we expect significant flow deformation. In particular, activation occurs near the sudden expansion. By looking at the outlet region we can infer, analogously to what is done for the previous flow cases, that an undisturbed channel would be solved as URANS. However, an exception to this concept occurs near the walls of the inlet channel.

Such an observed near-wall activation is undesired. This effect is caused by the intrinsic limitations of the controlled model. Indeed, in this simple version of STRUCT the value for t_m is constant in the whole domain. This choice is not optimal for the diffuser test case, which undergoes a significant change in the scales of turbulence between the inlet and the wider outlet. Complete versions of STRUCT, discussed in Chapters 7 and 8, use automatic adaptation of model scales based on flow variables and overcome this undesired inlet effect, as shown in Figure 7.13 and Figure 8.13.

Figure 6.43 Asymmetric diffuser: STRUCT activation, in blue, instantaneous scalar field

As done for the other test cases, we can look at the behavior of flow variables along with physical time at the beginning of a simulation. Velocity in the x-direction is monitored in the 5 points shown in Figure 6.44 below. Those points have different z coordinates, not shown here.

Figure 6.44 Locations of the probes used in Figure 6.45

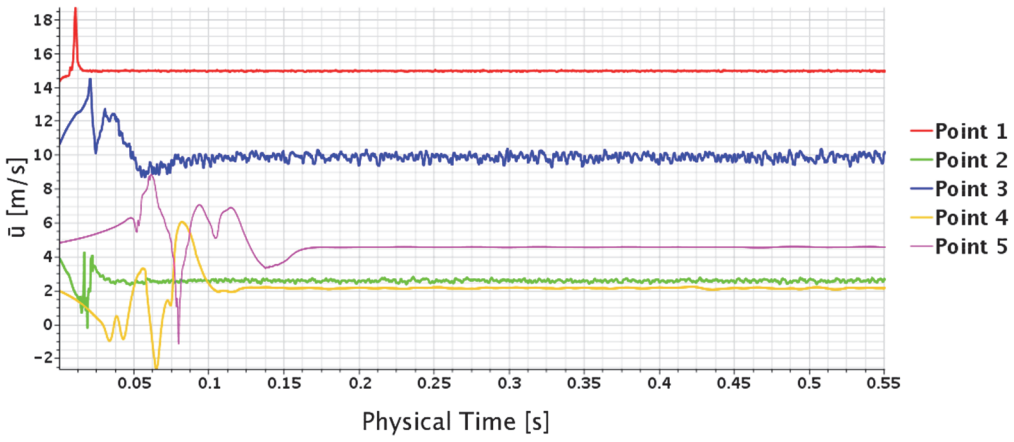

Figure 6.45 Convergence of results for STRUCT

Velocity values at those point probes are shown in Figure 6.45 above. The simulation is run using uniform initial fields. We can notice that, as expected, values further downstream from the inlet take a longer time to converge to statistically stationary results.

As opposed to the two other test cases, here velocities reach quasi-steady values. Resolved fluctuations are significantly smaller than the difference between time-averaged values shown. The largest velocity fluctuation in Figure 6.45 is observed at Point 4, which is located immediately downstream the recirculation area.

The runtime for STRUCT compared to cubic URANS on this test case is about 5.5% larger. All of the k-ε URANS models tested in this work, linear and nonlinear, did not predict any recirculation in the flow. The STRUCT results shown here produce a recirculation that resembles the one drawn based on experimental results by Buice (1997), as shown in Figure 6.46 below.

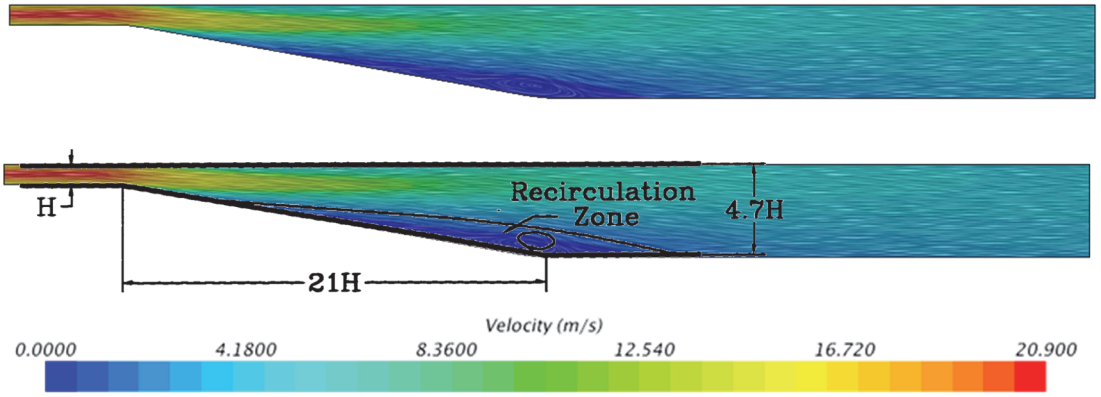

Figure 6.46 STRUCT resolved velocity vector convolution (top) and same figure with the drawing of the recirculation region from Buice (1997) superimposed (bottom)

Experimental data are plotted below for four different variables:

- Time-averaged x-component of velocity
- Time variance of velocity in the x-direction
- Time variance of velocity in the y-direction
- Time covariance of velocity in the x-y directions

The frame of reference for those directions is shown in Figure 6.38. As mentioned, in the legends below models are called with the abbreviated names defined in Section 5.4.3.

Time-averaged results for the x-component of velocity are presented in Figure 6.47 below. The locations near the inlet and outlet are predicted similarly by all the models shown and are fairly close to the experimental values. Those are the most undisturbed locations. Conversely, in the central part of the plot the only model in agreement with the experiment among the ones shown is STRUCT. Linear and nonlinear URANS do not predict any recirculation and produce low velocity gradients, maybe due to an overestimate of eddy viscosity, which is typical in standard k-ε simulations. The nonlinear URANS is closer to the experiment than the linear one while a larger jump towards the experiment is achieved when switching from nonlinear URANS to the STRUCT approach.

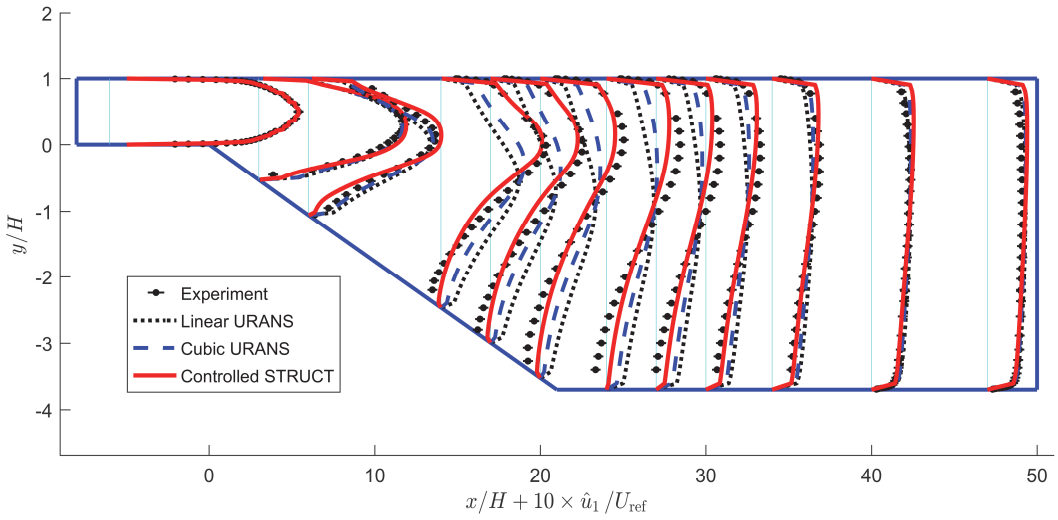

Figure 6.47 Asymmetric diffuser, time-averaged velocity $\hat{u}_1$ profiles

Time variance of velocity in the x-direction is shown in Figure 6.48 below. Among the models tested, STRUCT appears to be in closer agreement with the experiment, followed by nonlinear URANS and lastly by linear URANS.

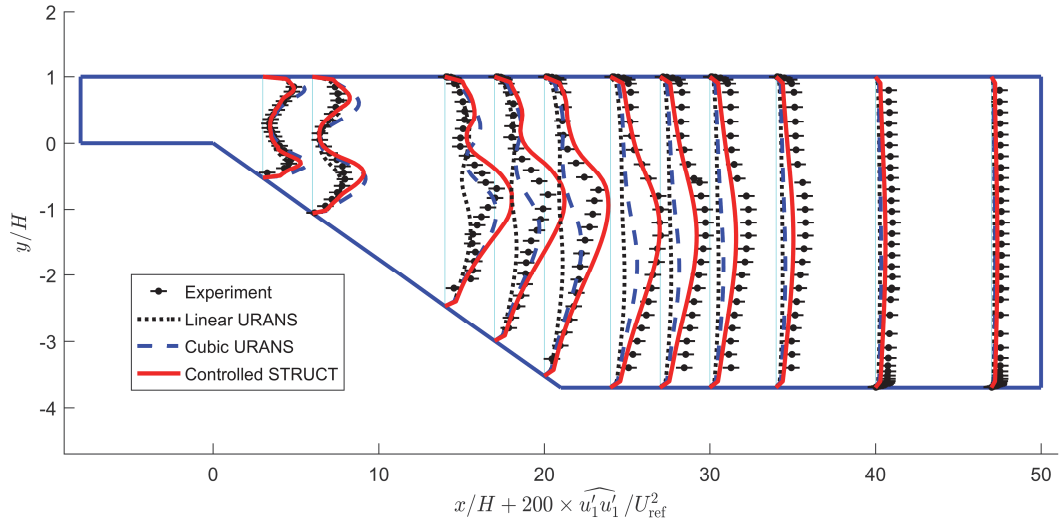

Figure 6.48 Asymmetric diffuser, time variance of velocity, $\widehat{u_1'u_1'}$ profiles

Time variance of velocity in the y direction is shown in Figure 6.49 below. Experimental data are available only in the upper part of the domain.

Values in the lower part are not provided by the authors of the experiment because their measurement conditions exceeded the uncertainty limit for reliable acquisitions using the cross-wire technique (Buice, 1997). Results from the STRUCT approach appear to be in closer agreement with the experiment than the two sets of URANS results.

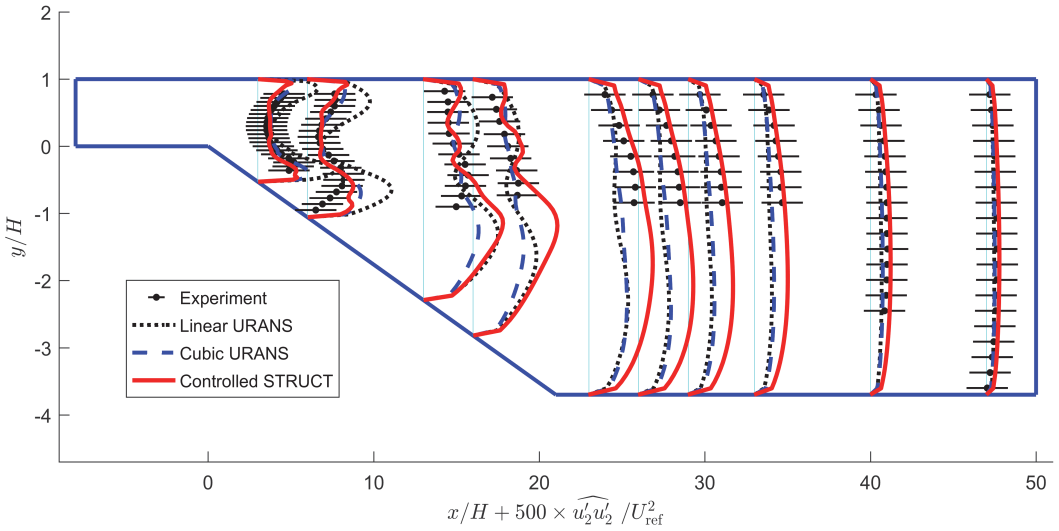

Figure 6.49 Asymmetric diffuser, time variance of velocity, $\widehat{u_2'u_2'}$ profiles

The same experimental profiles as in Figure 6.49 above are compared to LES results presented by Buice (1997) in Figure 6.50 below.

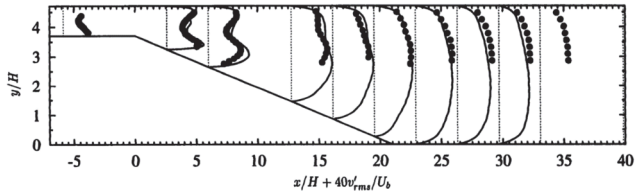

Figure 6.50 Asymmetric diffuser, $\widehat{u_2'u_2'}$ profiles from Buice (1997)

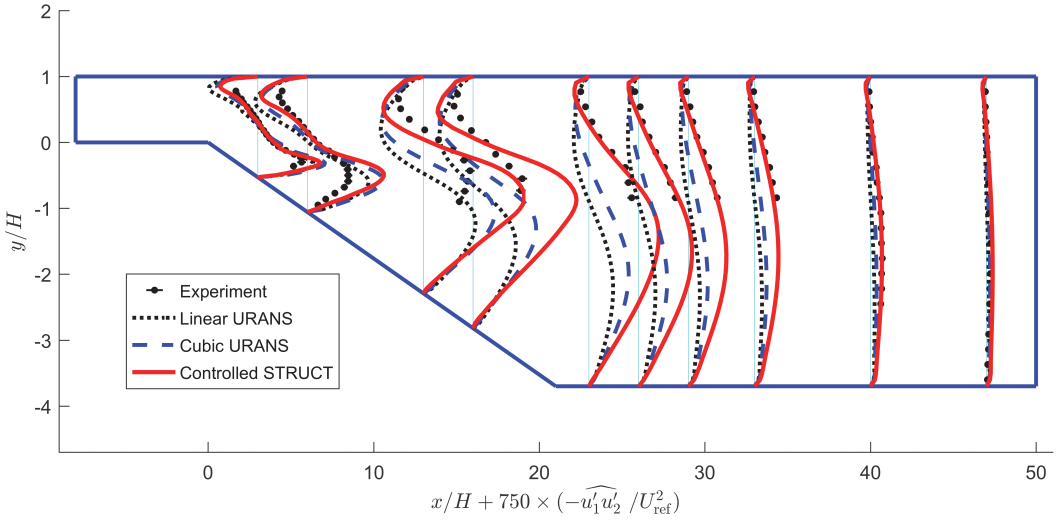

Figure 6.51 Asymmetric diffuser, time covariance of velocity, $-\widehat{u_1'u_2'}$ profiles

The time covariance of velocity is shown in Figure 6.51 above. STRUCT results appear to be in closer agreement with the experiment than results from the other two models. Observations regarding the URANS results are similar to those made for the velocity variance in Figure 6.48.

For comparison, LES results for velocity covariance presented by Buice (1997) are plotted against experimental results in Figure 6.52 below.

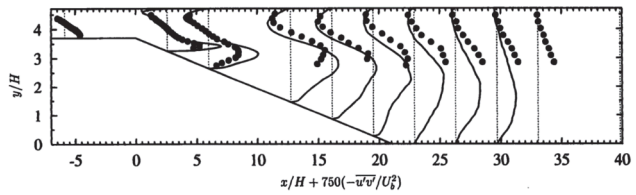

Figure 6.52 Asymmetric diffuser, $-\widehat{u_1'u_2'}$ profiles from Buice (1997)

6.3.10 Grid sensitivity

We can now look at the sensitivity of results to the choice of the grid size and cell geometry. In addition to the custom grid used in the previous tests, four polyhedral grids are used in this analysis, whose details on base sizes and number of cells are shown in Table X below.

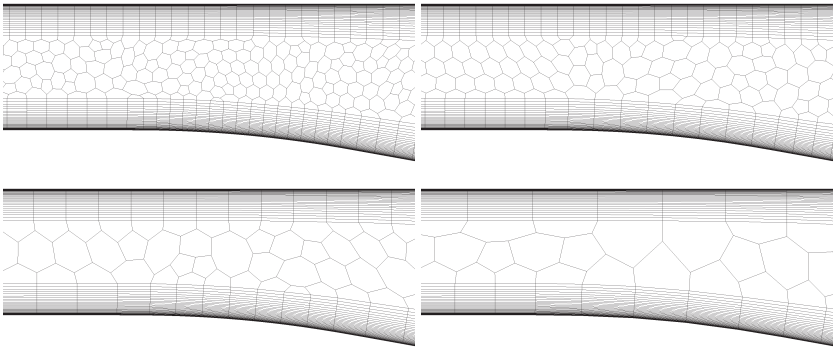

Figure 6.53 Polyhedral grids used for sensitivity analysis, ordered from the finest to the coarsest ones as described in Table X

The near-wall grid refinement in the wall-normal direction is not modified between grids. A detail showing the four polyhedral grids used is in Figure 6.53 above.

The grids shown are clearly not appropriate for LES solution due to the very large jump between the first bulk cell and the last cell in the prism layer. These grids are representative of industrial URANS meshes and are therefore relevant to the present work.

Results for the x-component of velocity are shown in Figure 6.54 below while results for velocity fluctuations in the x-direction are shown in Figure 6.55 below. Those results show that STRUCT predictions obtained using the different grids are very similar to each other. Only the coarsest grid tested seems to introduce significant error, without showing any model breakdown.

Table X Grids used in the sensitivity analysis for the asymmetric diffuser

Grid type	Reference cell size [mm]	Number of cells
Custom grid	variable	1,795,000
Polyhedral	1.5000	1,767,000
Polyhedral	2.2500	711,000
Polyhedral	3.3750	313,000
Polyhedral	5.0625	125,000

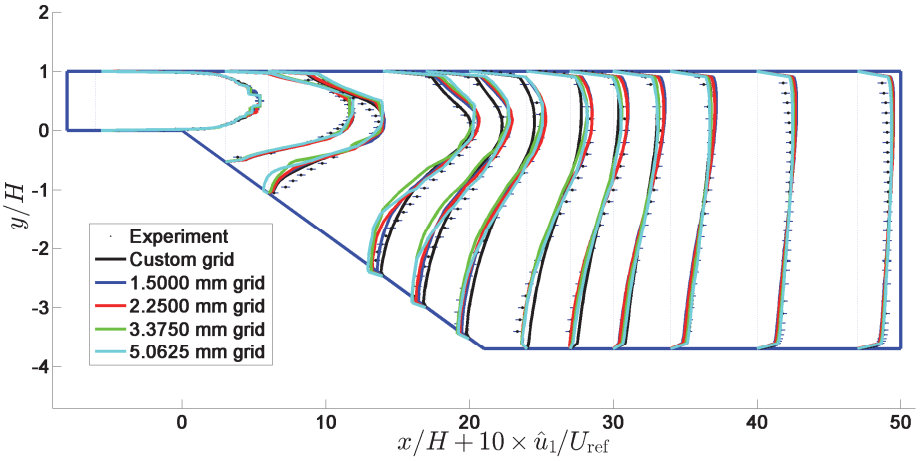

Figure 6.54 Controlled STRUCT grid sensitivity, velocity $\hat{u}_1$ profiles

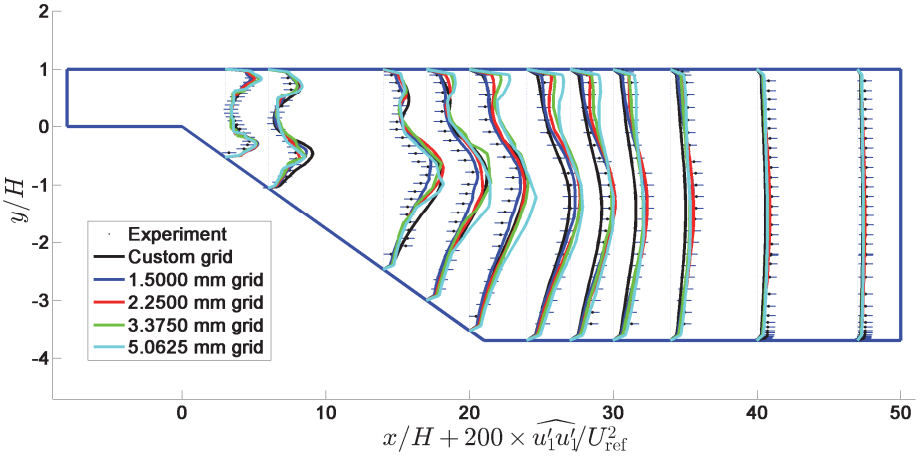

Figure 6.55 Controlled STRUCT grid sensitivity, time variance of velocity, $\widehat{u_1'u_1'}$ profiles

STRUCT activation regions using the polyhedral grids of Table X are shown in Figure 6.56 below. We can observe that, as the grid gets coarser, the activation regions appear to get thicker and shorter. This thickening behavior is opposite to the trend obtained in the previous tests. This unexpected effect can be explained by noticing that the activation in this test case is mainly caused by flow phenomena in the near-wall region, including flow separation. In such a region, the same refinement was used for all grids presented. The coarse grid used therefore predicts separation thanks to the near-wall refinement but produces regions of strong deformation when facing coarse grids outside the prism layer, resulting in STRUCT activation. This can be considered as an exasperated example of poor grid coarsening that is often applied in the industry and therefore useful.

Figure 6.56 STRUCT activation regions for the four polyhedral grids of Table X, ordered from the finest to the coarsest

6.4 Discussion

Results in this chapter provide a demonstration of the potential of the STRUCT approach. The results confirm that the simple formulation of the controlled STRUCT is capable of triggering hybrid behavior starting from the baseline cubic k-ε model selected. Such a behavior produces accurate results in the conditions tested.

The proposal and testing of a model is a fundamental step for the development of a formulation to predict a physical phenomenon. Richard Feynman used to state on the scientific method:

"It does not make a difference how beautiful your guess is, it does not make a difference how smart you are, or what your name is. If it disagrees with experiment, it is wrong."[4]

Validation is key in the process of exploring a new formulation. Successful validation does not confirm that a model is accurate, but, on the other hand, lack of agreement of a law with nature identifies flaws in the law (Popper, 1935).

A question that may arise on the STRUCT approach is whether it is more appropriate to call it a hybrid model, or a modified URANS model. As discussed in Section 2.5.1, there is significant overlap between definitions in this field. Nevertheless, STRUCT belongs more closely to the category of hybrid models. This because it is configured to behave as URANS in all the parts of the

[4] (Extract of a recorded video is available at https://www.youtube.com/watch?v=gBFZEYkzKXc)

domain without activation regions while significant resolved structures are produced inside activation regions. Those significant resolved structures are typically not observed in models carrying the name URANS.

We can observe from results in this chapter that activation regions tend to be far from the wall. Such a characteristic, related to the nature of parameter $\overline{II}$, is considered desirable for hybrid models. For example, in a review of DES Spalart (2009) states:

"Under one name or another, a form of a RANS-LES hybrid that is capable of full RANS function in boundary layers will be in use for the foreseeable future in many industries."

7 Complete Taylor-expansion-based model STRUCT-L

7.1 Chapter overview

The performance of the overall STRUCT concept, evaluated in the form of a controlled approach was tested in the previous chapter, showing promising results achieved through a preliminary yet incomplete model. This chapter and the next one will propose and implement two complete closures based on the STRUCT framework. The term "complete" refers to a model not requiring any case-dependent adjustment.

The closure developed in the present chapter approximates the averaging operation in (4.5) using a truncated Taylor series expansion. This model will be referred to as STRUCT-Local (STRUCT-L). After introducing the approach, this chapter will implement it in the same three flow cases that have been discussed in Section 3.2 and tested in Chapter 6.

7.2 Adding completeness to the STRUCT approach

The Stanford conference in 1968 highlighted the importance of focusing on complete models and motivated their subsequent development. Completeness is a required step towards the trusting of CFD predictions without the availability of experimental data. Many early approaches are not complete, including notoriously the mixing length model (Prandtl, 1925). The open version of PANS represents an example of a hybrid model being incomplete since it requires specification of the ratio between the resolved and modeled TKE.

A complete closure for the STRUCT approach can be developed by providing definitions for the two open components of the basic formulation shown in (4.1) and (4.3). Those components are: the averaging operation needed to define t_m, and the reduction parameter ϕ. The averaging operation for t_m is discussed here and the reduction parameter in Section 7.5.

Recall that t_m is defined based on the generic averaging operation in (4.5), copied below:

$$t_\mathrm{m} = \langle t_{\mathrm{m},0} \rangle$$

In the controlled tests of Chapter 6, the averaging operation was performed based on preliminary URANS results, leading to a constant value for t_m assigned before the simulation. This approach is not complete since t_m and ϕ need to be specified for each flow.

On the other hand, here we seek to make the model complete through an averaging operation computed on-the-fly during the simulation. A simple option would be to use an explicit average, e.g. an average in time, space, or ensemble. However, explicit computation of spatial averages is not desirable in the practice of common industrial simulations since it leads to significant computational burden and poor performance in parallel computations, due to the need for numerous nonlocal operations. In particular, explicit averages in time or space require operations in each cell to depend on a large number of values for different spatial locations and/or time steps. An interesting example from the literature of an explicit ensemble averaging computed during the simulation is the one

performed by Carati, Wray, and Cabot (1996). Those authors computed ensemble averaging by running the full calculation multiple times in parallel, which is only acceptable for academic simulations.

Modern FV codes are most effective when relying only on local operations, to minimize computational cost. Therefore, we seek to approximate the explicit averaging operation with a simplified one, which is local in time and space. In local operations, values are computed in each cell only depending on local parameters and local time and space derivatives. The local strategy proposed in this chapter is introduced below in Section 7.3.

7.3 The STRUCT-L approach

7.3.1 Background

Chester, Charlette, and Meneveau (2001) proposed an approximation of test filtering based on a truncated Taylor series expansion, inspired by the work by Jansen (1999). In both of those works, a Taylor series expansion approximates a Gaussian filter, reducing the computational cost compared to explicit filters. In their specific problem, Chester, Charlette, and Meneveau (2001) used a Taylor series expansion up to the second order, achieving an error below 5% for the dynamic coefficient.

7.3.2 Approximation of the arithmetic average

We can now describe the operation used here to approximate a volume averaging operation locally.

Consider a generic function of time and 3D space, $f(\boldsymbol{x}, t)$:

$$f: \begin{cases} \mathbb{R}^3 \times \mathbb{R} & \rightarrow & \mathbb{R} \\ (\boldsymbol{x}, t) & \mapsto & f(\boldsymbol{x}, t) \end{cases} \tag{7.1}$$

Assume that we are interested in the volume average of f in a sphere of radius $R > 0$ around a location of interest, say $\boldsymbol{x}_0 = (0,0,0)$. The equation for the averaged function $\langle f \rangle_R$ is written as follows using spherical coordinates:

$$\langle f \rangle_R(\boldsymbol{x}_0, t) = \frac{3}{4\pi R^3} \int_0^{2\pi} \int_0^{\pi} \int_0^{R} f(\rho,\, \alpha, \beta, t)\, \rho^2 \sin(\alpha)\, \mathrm{d}\rho\, \mathrm{d}\alpha\, \mathrm{d}\beta \tag{7.2}$$

Recall the Taylor series f_T of a generic function f with multiple variables:

$$f_\mathrm{T}(x_1, \dots, x_d) = \sum_{n_1=0}^{+\infty} \sum_{n_2=0}^{+\infty} \cdots \sum_{n_d=0}^{+\infty} \frac{(x_1 - a_1)^{n_1} \cdots (x_d - a_d)^{n_d}}{n_1! \cdots n_d!} \left(\frac{\partial^{n_1 + \cdots + n_d} f(a_1, \dots, a_d)}{\partial x_1^{n_1} \cdots \partial x_d^{n_d}} \right) \tag{7.3}$$

We can now use the generic Taylor series in (7.3) truncated after the third order to approximate the integral in (7.2) applied to a generic space-time position $(\boldsymbol{x}, t)$. This operation results in:

$$\langle f \rangle_R(\boldsymbol{x}, t) \approx f(\boldsymbol{x}, t) + \frac{R^2}{10} \boldsymbol{\nabla}^2 f(\boldsymbol{x}, t) \tag{7.4}$$

Jansen (1999) followed a similar approach, but he approximated a Gaussian filtering rather than a spherical averaging. His operation is performed generically in d dimensions on an arbitrary grid, and is truncated after the 3rd order.

7.3.3 Approximation of the geometric average

Due to the large variation of the parameter to be averaged, preliminary work indicated that a geometric averaging is more appropriate for developing a parameter representative of local flow scales compared to an arithmetic averaging. The use of a geometric average is justified by the finding that controlled STRUCT simulations are not sensitive to small variations of t_{m} within the same order of magnitude. We can then reformulate the approximation shown in Section 7.3.2 above and apply it to a geometric averaging operation. Before introducing the geometric averaging operation in a continuous domain, we can start by presenting the more familiar geometric averaging operation applied to a discrete domain. The following formulation applies to a set of n positive values f_i:

$$\left(\prod_{i=1}^{n} f_i\right)^{1/n} = \exp\left(\frac{1}{n}\sum_{i=1}^{n} \ln(f_i)\right) \tag{7.5}$$

The RHS of this equation converts a product into a summation by applying basic properties. The equation shows that the geometric mean of f_i is equivalent to the exponential of the arithmetic mean of the natural logarithm of f_i. Now, this concept can be extended from discrete to continuous domains. The product of a function $f(x)$ for x between a and b can be defined by dividing such an interval into infinitesimal bins:

$$\prod_{a}^{b} f(x)^{\mathrm{d}x} = \lim_{\Delta x \to 0} \prod_{i} f(x_i)^{\Delta x} \tag{7.6}$$

We can now use the relation in (7.6) to identify the geometric average of a continuous function $f(x)$:

$$\lim_{\Delta x \to 0}\left(\prod_{i} f(x_i)^{\Delta x}\right)^{\frac{b-a}{\Delta x}} = \exp\left(\frac{1}{b-a}\int_{a}^{b} \ln f(x)\mathrm{d}x\right) \tag{7.7}$$

The summation in (7.5) becomes an integral in the continuous domain. The geometric mean of a positive continuous function is equal to the exponential of the arithmetic mean of the natural logarithm of the same function. This conclusion equivalent to the one for a discrete function in (7.5).

We can now extend this concept to a continuous function $f(\boldsymbol{x})$ in 3D. The geometric mean is:

$$\lim_{\Delta^3 \boldsymbol{x} \to 0}\left(\prod_{i} f(x_i)^{\Delta^3 \boldsymbol{x}}\right)^{\frac{V}{\Delta^3 \boldsymbol{x}}} = \exp\left(\frac{1}{V}\int_{V} \ln f(\boldsymbol{x})\mathrm{d}^3\boldsymbol{x}\right) \tag{7.8}$$

This equation shows that, as observed in 1D, also in 3D we can express the geometric mean as the exponential of the arithmetic mean of the natural logarithm. We now apply this operation to a sphere of radius R centered around a location of interest, say $\boldsymbol{x}_0 = (0,0,0)$, as done in Section 7.3.2.

The geometric mean analogous to (7.2) is:

$$\langle f \rangle(\boldsymbol{x}_0, t) = \exp\left(\frac{3}{4\pi R^3}\int_{0}^{2\pi}\int_{0}^{\pi}\int_{0}^{R} \ln f(\rho,\, \alpha, \beta, t)\, \rho^2 \sin(\alpha)\, \mathrm{d}\rho\, \mathrm{d}\alpha\, \mathrm{d}\beta\right) \tag{7.9}$$

We now define $g = \ln f$ and use a Taylor series expansion to approximate the elements inside the exponential in (7.9) above. Analogously to (7.4), we get the following approximation for the arithmetic average of g centered in any location $\boldsymbol{x}$:

$$\frac{3}{4\pi R^3}\int_{0}^{2\pi}\int_{0}^{\pi}\int_{0}^{R} g\, \rho^2 \sin(\alpha)\, \mathrm{d}\rho\, \mathrm{d}\alpha\, \mathrm{d}\beta \approx g(\boldsymbol{x}, t) + \frac{R^2}{10}\boldsymbol{\nabla}^2 g(\boldsymbol{x}, t) \tag{7.10}$$

By substituting this relation into (7.9), we obtain a generic expression approximating the geometric average of f around any location $\boldsymbol{x}$ based on a sphere of radius R:

$$\langle f \rangle_R(\boldsymbol{x}, t) \approx \exp\left(\ln f(\boldsymbol{x}, t) + \frac{R^2}{10} \boldsymbol{\nabla}^2 (\ln f(\boldsymbol{x}, t)) \right) \tag{7.11}$$

7.3.4 Definition of the working variable for STRUCT-L

The STRUCT-L approach applies the averaging operation in (7.11) to the field $t_{\mathrm{m},0}$. This field appears in the RHS of the equation as the argument of a logarithm. Basic requirements for a logarithm's argument are to be positive and dimensionless. The first requirement is met, since $t_{\mathrm{m},0}$ is always positive. The second requirement is apparently not met because $t_{\mathrm{m},0}$ has the units of time [s]. However, in this specific case the use of a dimensional argument is acceptable because the operation in (7.11) is first-order homogeneous. This implies:

$$\langle a\psi \rangle_R(\boldsymbol{x}, t) = a \langle \psi \rangle_R(\boldsymbol{x}, t) \tag{7.12}$$

The property in (7.12) is readily derived from (7.11) and shows that the averaging operation can be scaled to any arbitrary unit that is a multiple of the previous one by multiplication with the constant positive factor a.

7.4 Averaging length

Implementation of the averaging operation in (7.11) requires the definition of parameter R, representing the radius of the sphere around the point of interest in which the average is approximated. Such a value is chosen as a multiple of the length scales of modeled turbulence:

$$R = C_R \frac{k_{\mathrm{m}}^{3/2}}{\varepsilon} \tag{7.13}$$

This formulation depends on local parameters and satisfies the requirements of Section 3.6.3. The coefficient $C_R = 2$ has been determined through a posteriori analysis of multiple flow cases. Results are not significantly sensitive to small variations of such a parameter.

7.5 Reduction parameter

The reduction parameter ϕ in (4.1) dictates the amount of resolved versus modeled scales in the regions of STRUCT activation. The STRUCT-L approach uses a constant conservative value for ϕ. A value around 0.6 is considered appropriate based on the flows tested. The next chapter will address the challenge of relaxing this assumption and determining ϕ locally in time and space.

7.6 Limiters

The local approximation of the average in (7.11) is sensitive to local gradients. Steep gradients can occur in turbulent flows and can lead to large overestimates or underestimates of the average. To avoid those occurrences in regions with sharp gradients, limiters are used bounding the approximation of the average. The formulation in (7.11) is rewritten as follows:

$$t_{\mathrm{m}} \approx \exp\left(\ln t_{\mathrm{m},0} + \min\left(\max\left(\frac{R^2}{10} \boldsymbol{\nabla}^2 \left(\ln t_{\mathrm{m},0} \right) \right), -\ln(2) \right), \ln(2) \right) \tag{7.14}$$

In the expression above, limiters ensure that the approximation of the average is constrained to the range between half and double the local value of the function. The limiters are placed inside the exponential function rather than outside to avoid overflow caused by computation of large exponentials.

The use of limiters does not introduce significant error in the solution because values computed for the variable t_{m} are only used to trigger a binary switch for hybrid mode activation.

In the next chapter, the evaluation of t_{m} is used to determine a local value for the TKE ratio. This requires the use of a local approximation for averaging different than the STRUCT-L one.

7.7 Results

We can now apply the STRUCT-L model to the same test cases of Chapter 6, using the same grids and simulation conditions. Selected results from that chapter are shown here for comparison.

7.7.1 Flow past a square cylinder

Application of the STRUCT-L approach to the flow past a square cylinder test case produces the activation regions shown in blue in Figure 7.1 below. Those regions appear to be wider than those deriving from controlled STRUCT tests, which have been shown in Figure 6.6. Such a difference is related to the use of a complete closure calculating local flow scales rather than a controlled one. Activation regions observed here are consistent with the ones that will be shown in the next chapter, deriving from another complete model.

Figure 7.1 STRUCT-L activation, instantaneous scalar field, flow past a square cylinder

Profiles for the x-component of velocity are shown in Figure 7.2 below.

The STRUCT-L approach appears to provide results closer to the experiment compared to the baseline cubic URANS. However, the agreement is not as close as that in the controlled STRUCT test of Chapter 6. The difference between controlled STRUCT and STRUCT-L results is caused by the conservative choice of $\phi = 0.6$ made in the STRUCT-L implementation. For this reason, results are shown also for a custom model called STRUCT-L-zero, for which ϕ is very small, similarly to what was done in Chapter 6. The STRUCT-L-zero provides much closer prediction of experimental values than the STRUCT-L, motivating the development of a complete version of STRUCT in which variable ϕ be not constant, as done in Chapter 8.

All of the other physical quantities shown in Chapter 6 are also tested here. Those are:

- time-averaged velocity in the y-direction, in Figure 7.3
- time variance of velocity in the x-direction, in Figure 7.4
- time variance of velocity in the y-direction, in Figure 7.5
- time covariance of velocity in the x-y directions, in Figure 7.6 below

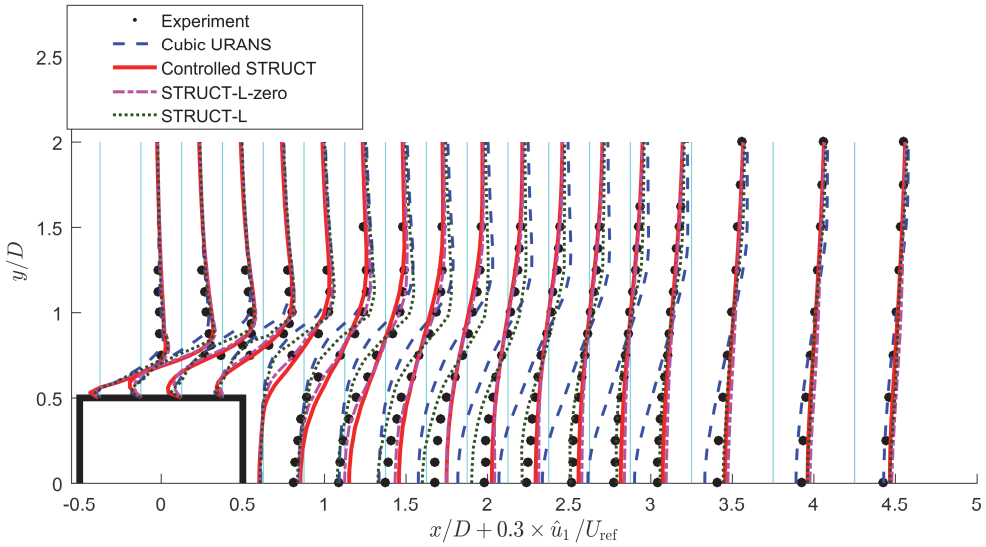

Figure 7.2 Flow past a square cylinder, STRUCT-L, time-averaged velocity $\hat{u}_1$

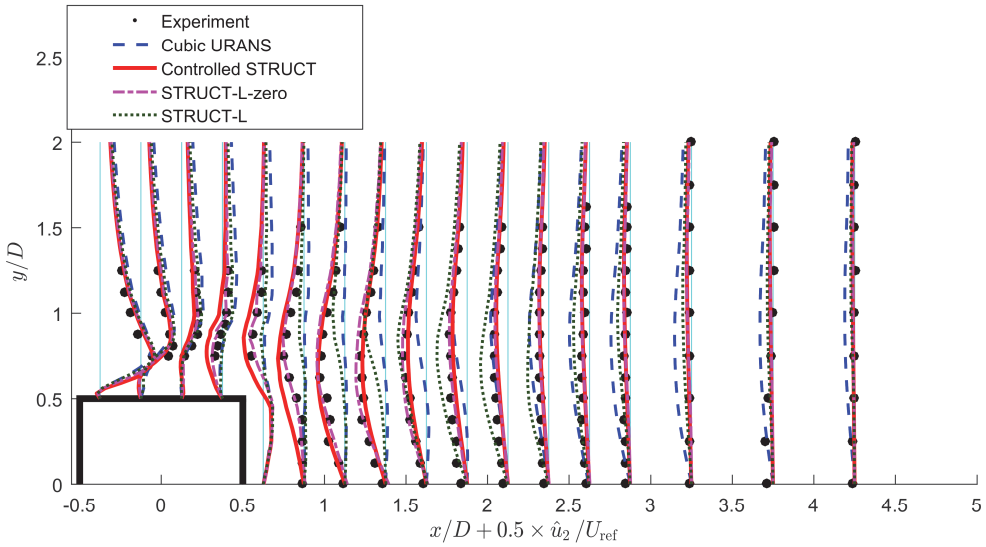

Figure 7.3 Flow past a square cylinder, STRUCT-L, time-averaged velocity $\hat{u}_2$

Results for the time-averaged components of velocity presented in the two figures above show that the STRUCT-L approach produces profiles in most cases closer to the experiment than the cubic URANS ones. However, the accuracy of those results is significantly lower than that deriving from the controlled STRUCT approach. This discrepancy is due to the choice of a constant reduction coefficient higher than that used in the controlled test. This assumption is confirmed by the observed profiles for STRUCT-L-zero results, which are very close to controlled STRUCT ones.

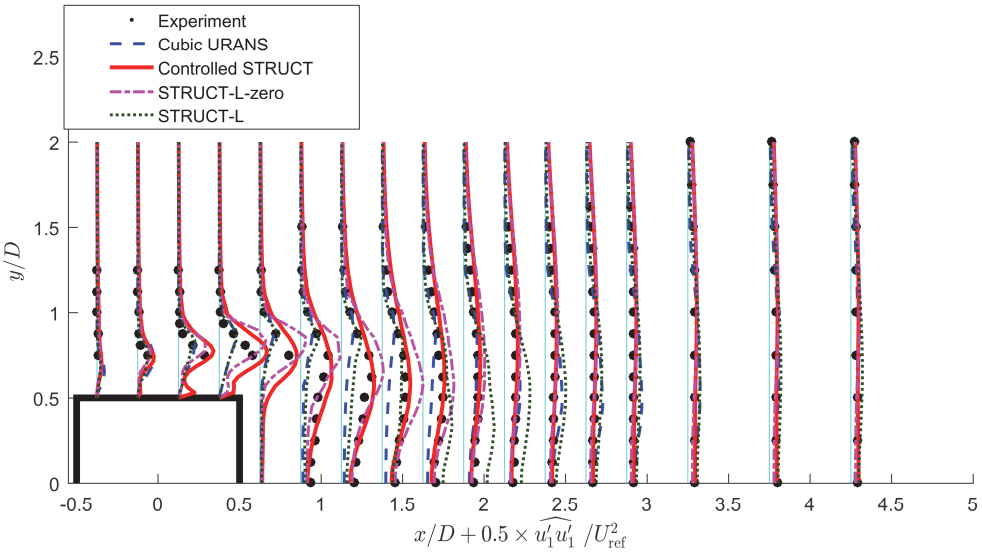

Figure 7.4 Flow past a square cylinder, STRUCT-L, time variance of velocity, $\widehat{u_1' u_1'}$

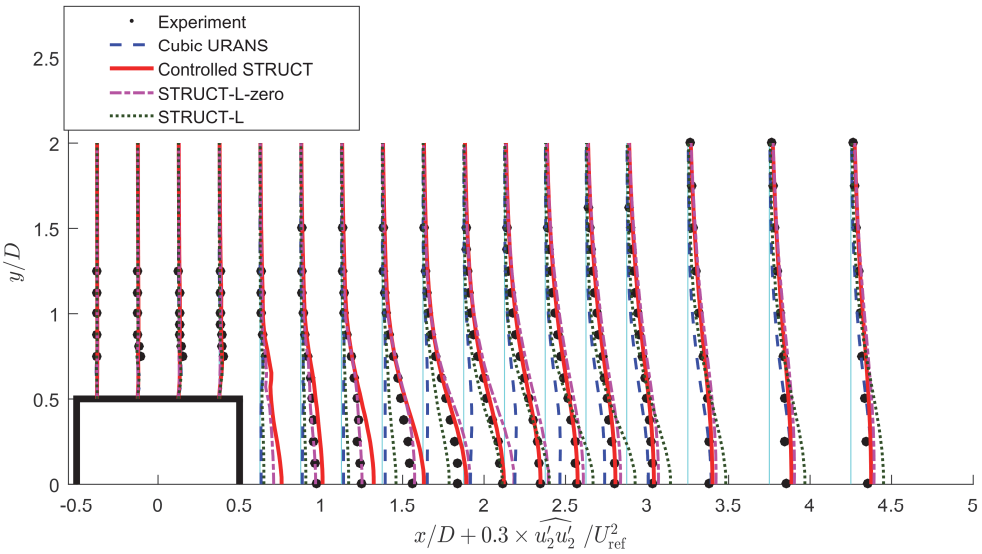

Figure 7.5 Flow past a square cylinder, STRUCT-L, time variance of velocity, $\widehat{u_2' u_2'}$

Variances of velocity presented in the two figures above show that STRUCT-L is capable of describing velocity fluctuations within the correct order of magnitude, unlike URANS. However, as observed for velocity profiles, STRUCT-L-zero results are more accurate than STRUCT-L ones.

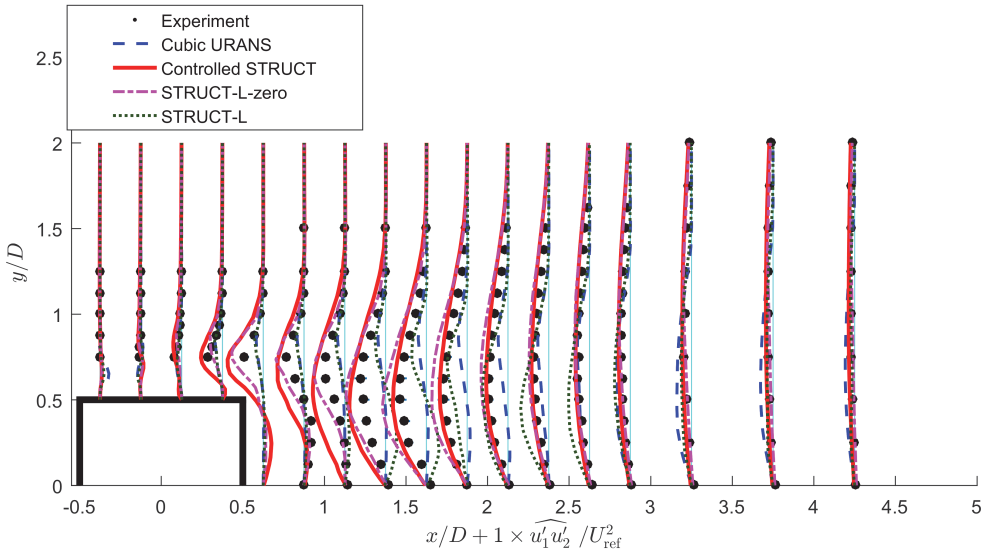

Figure 7.6 Flow past a square cylinder, STRUCT-L, time covariance of velocity, $\widehat{u_1' u_2'}$

The covariance of the two main components of velocity, shown in Figure 7.6 above, is not predicted accurately by STRUCT-L as it is by STRUCT-L-zero. In particular, the STRUCT-L results produce profiles with the wrong sign around the wake region. Nevertheless, this lack of agreement with the experiment is not more significant than that observed for the cubic URANS.

7.7.2 Turbulent mixing in a T-junction

Application of the STRUCT-L approach to the T-junction test case produces instantaneous activation regions as shown in Figure 7.7 below. From a qualitative point of view, STRUCT-L activation regions shown in the figure below resemble those deriving from controlled STRUCT tests, which are shown in Figure 6.26.

Figure 7.7 STRUCT-L activation, instantaneous scalar field, T-junction mixing

As done above for the square cylinder, we can now plot the same physical quantities as in Chapter 6 computed with the STRUCT-L approach. The results shown below are:

- Velocity profiles in the x-direction, in Figure 7.8
- Velocity profiles in the z- and y-direction, in Figure 7.9
- Profiles of the time variance of velocity in the x-direction, in Figure 7.10
- Profiles of the time variance of velocity in the z- and y-direction, in Figure 7.11
- Profiles of the time covariance of velocity in the x-z and x-y directions, in Figure 7.12

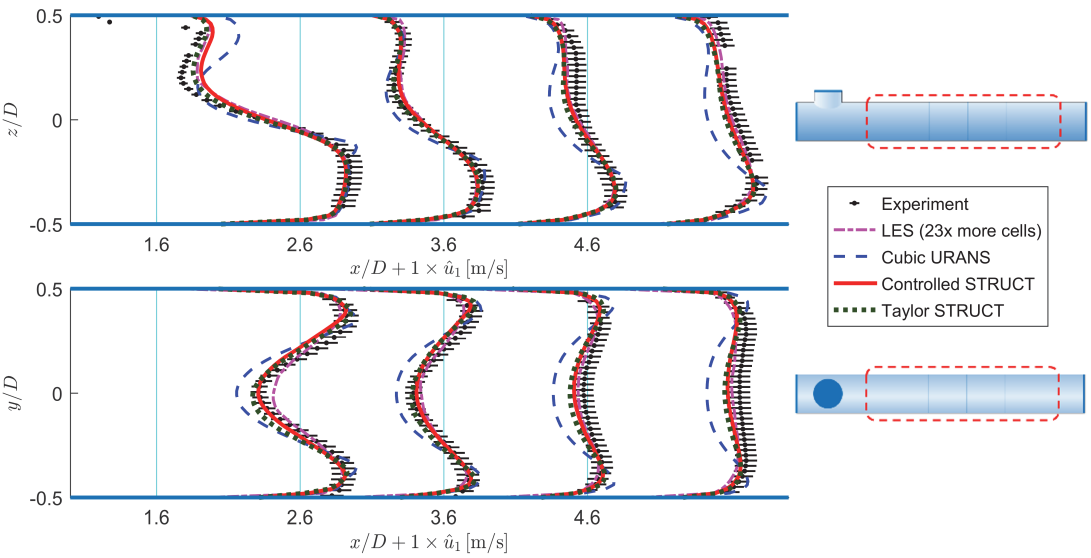

Figure 7.8 T-junction mixing, STRUCT-L, time-averaged velocity $\hat{u}_1$

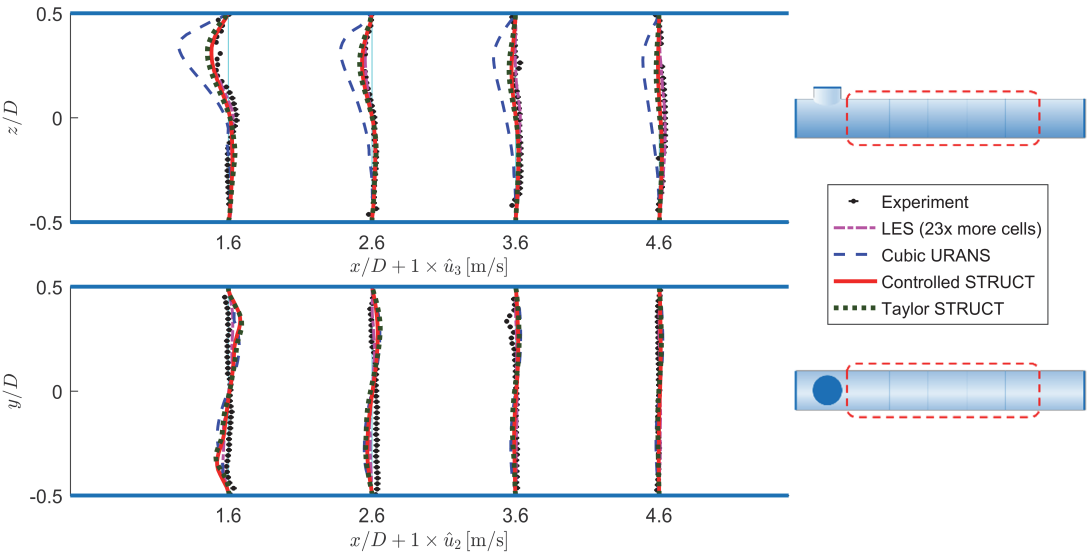

Figure 7.9 T-junction mixing, STRUCT-L, time-averaged velocity $\hat{u}_3$ and $\hat{u}_2$

The velocity profiles presented in the two figures above show an overall close agreement of the complete STRUCT-L model with experimental data, LES, and controlled STRUCT results.

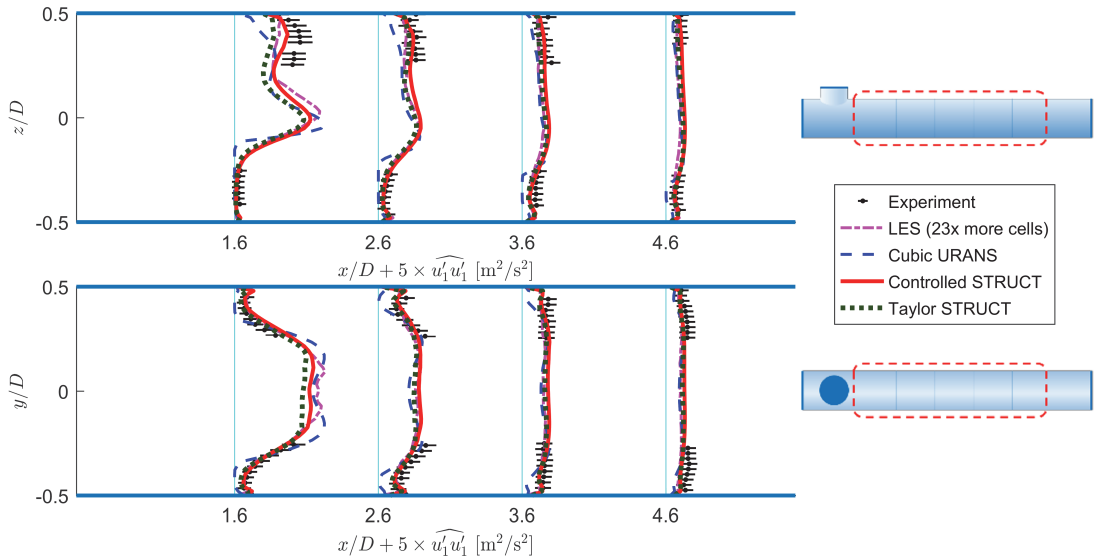

Figure 7.10 T-junction mixing, STRUCT-L, time variance of velocity, $\widehat{u_1' u_1'}$

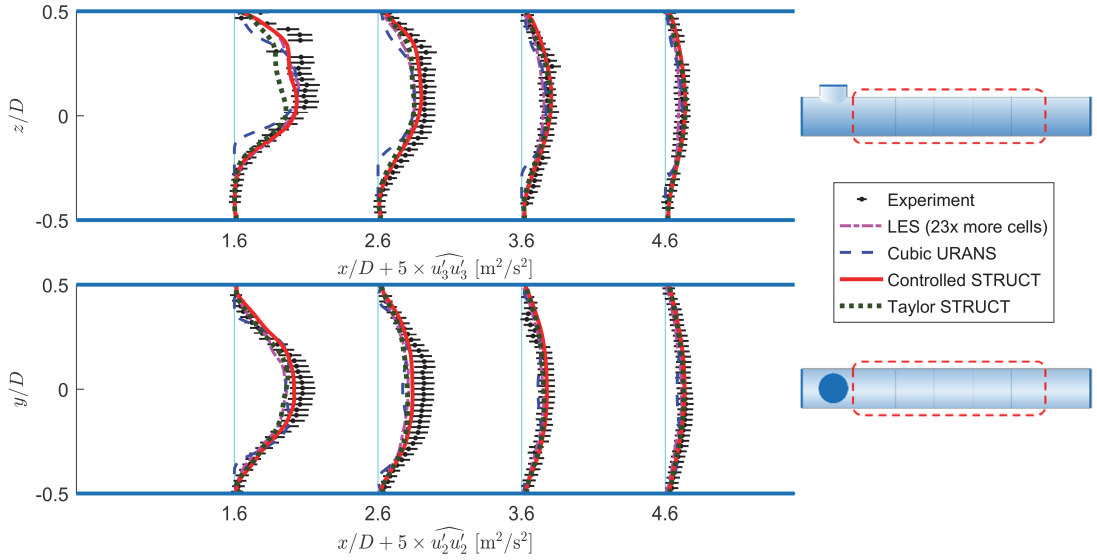

Figure 7.11 T-junction mixing, STRUCT-L, time variance of velocity, $\widehat{u_3' u_3'}$ and $\widehat{u_2' u_2'}$

The close agreement observed for STRUCT-L in velocity profiles is repeated in results for the second central moments of velocity.

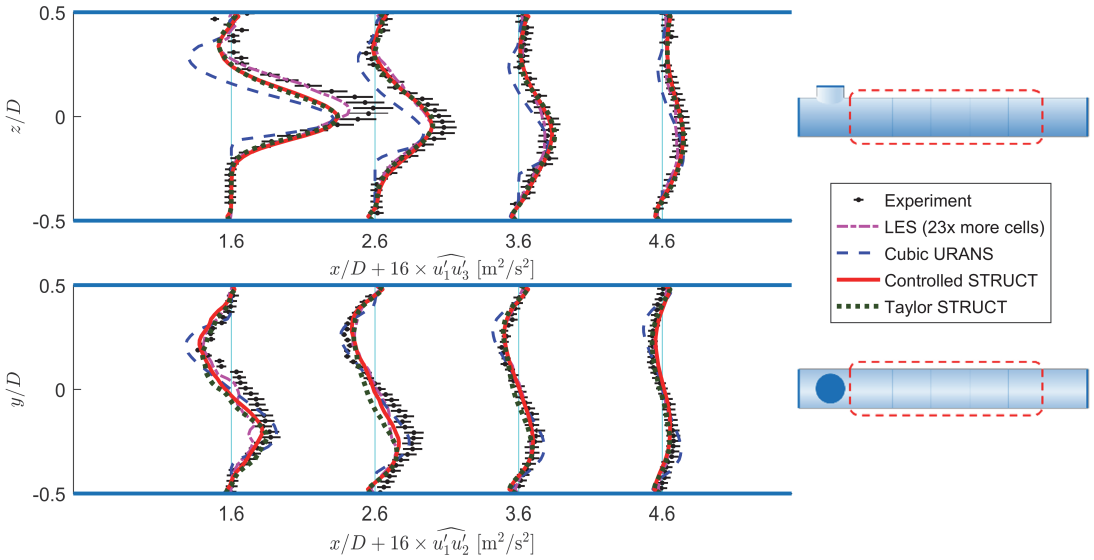

Figure 7.12 T-junction mixing, STRUCT-L, time covariance of velocity, $\widehat{u_1' u_3'}$ and $\widehat{u_1' u_2'}$

Profiles for velocity covariance shown above are also in close agreement with the experiment, LES, and the controlled STRUCT test. We can conclude that the STRUCT-L approach in the T-junction test case has proved to provide the same optimal results as in the controlled tests.

7.7.3 Mild separation in an asymmetric diffuser

Activation regions for the asymmetric diffuser test case are shown in Figure 7.13 below. Those regions appear to be different from those observed for the controlled STRUCT in Figure 6.43. Here, instead of two parallel activation regions of similar size near the beginning of the diffuser, one main longer activation region appears. The incomplete similarity between those two figures is justified by the different approach used. In the controlled model the scale for t_{m} is assigned a priori before the simulation, while in the STRUCT-L approach the choice of such a parameter is determined automatically during the simulation. In this test case a significant change in flow scales occurs due to the increase of the test section's height by 4.7 times along the diffuser. Therefore, the activation criterion of the controlled model is not considered optimal because of the use of an arbitrary scale rather than a scale-adaptive approach.

Figure 7.13 STRUCT-L activation, instantaneous scalar field, asymmetric diffuser

Profiles plotted against experimental data are shown in several figures below:

- Time-averaged velocity in the x-direction, in Figure 7.14
- Velocity variance in the x-direction, in Figure 7.15
- Velocity variance in the y-direction, in Figure 7.16
- Velocity covariance in the x-y directions, in Figure 7.17

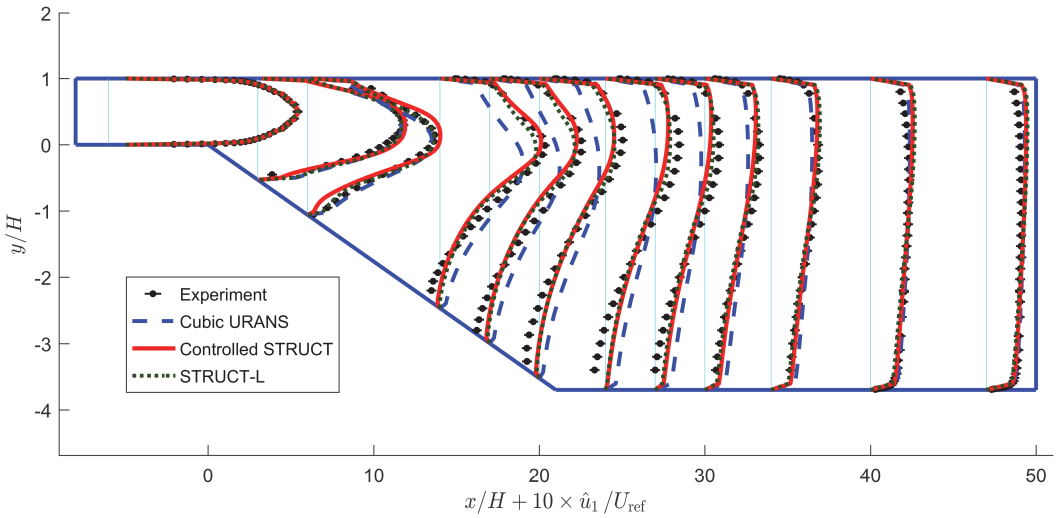

Figure 7.14 Asymmetric diffuser, STRUCT-L, time-averaged velocity $\hat{u}_1$

Velocity profiles provided above show an almost perfect agreement of STRUCT-L results with those deriving from controlled STRUCT tests.

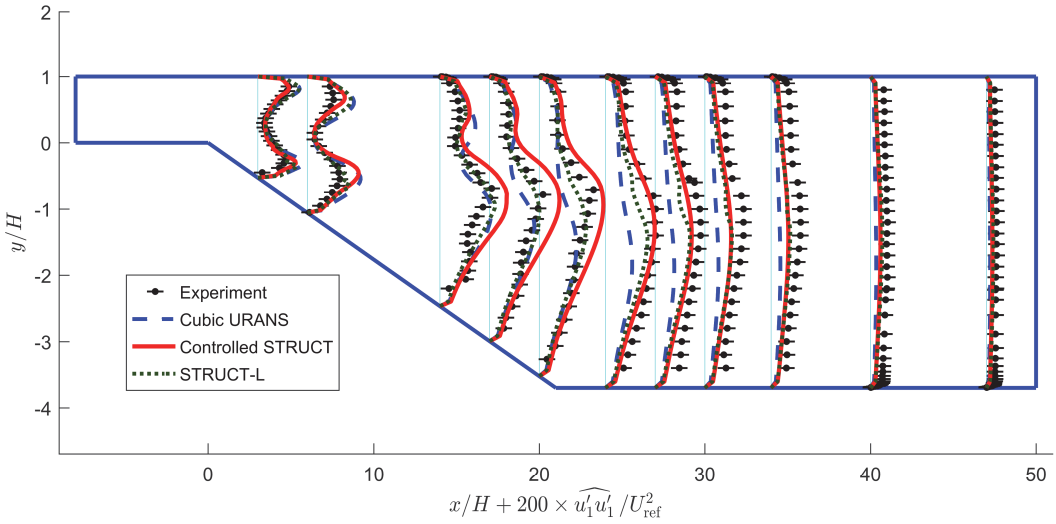

Figure 7.15 Asymmetric diffuser, STRUCT-L, time variance of velocity, $\widehat{u_1' u_1'}$

Velocity variances are presented above and below, showing an overall either equal or closer agreement with the experimental data of STRUCT-L results, compared to controlled STRUCT ones.

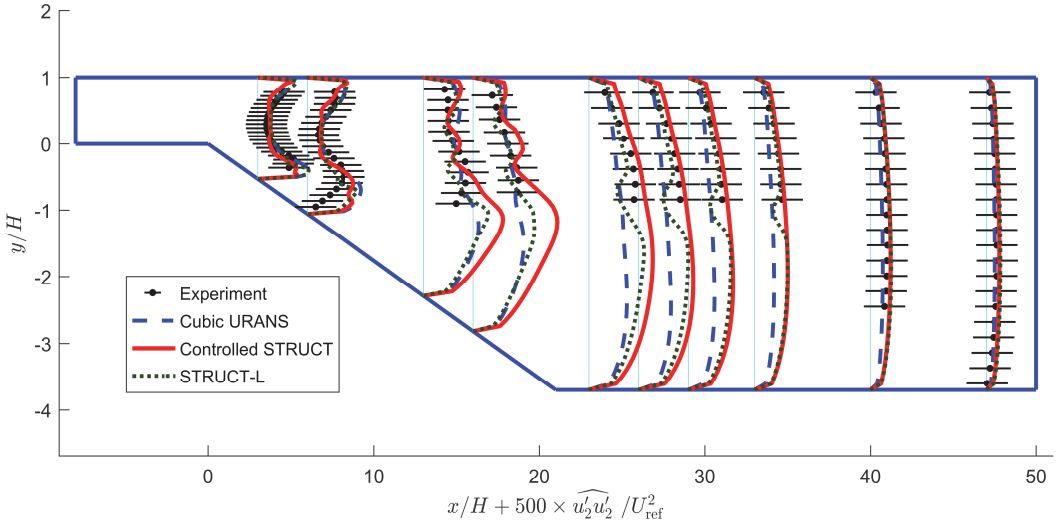

Figure 7.16 Asymmetric diffuser, STRUCT-L, time variance of velocity, $\widehat{u_2'u_2'}$

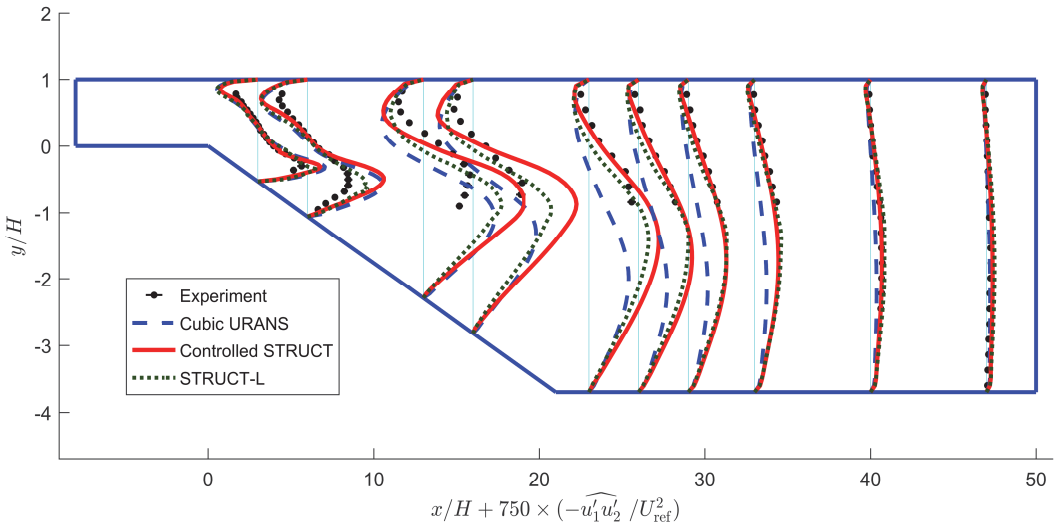

Figure 7.17 Asymmetric diffuser, STRUCT-L, time covariance of velocity, $\widehat{u_1'u_2'}$

Results for velocity variance, shown above, also reproduce very closely the trends and values of the controlled STRUCT test. The lower peaks observed in the central region move the results closer to the experiment.

7.8 Behavior in a simple straight pipe or a rectangular channel

Based on the rationale of the STRUCT approach, hybrid activation is not desired in simple flows characterized by low deformation, such as those in a straight pipe or a rectangular channel. Those kinds of flow are solved accurately using just URANS, so hybrid activation is not needed.

The achievement of this property can be checked in STRUCT-L results, focusing on the outlet regions for the T-junction and the asymmetric diffuser. The former is a circular-section pipe and the latter a rectangular-section channel. In both cases, the undisturbed flow is solved without any hybrid model activation, as shown in Figure 7.7 and Figure 7.13. A similar conclusion can be drawn looking at the inlet region of the square cylinder flow case in Figure 7.1, i.e. the region upstream the cylinder. Since STRUCT activation is not enabled, achievement of the desired property is confirmed.

7.9 Discussion

The complete STRUCT-L approach demonstrated robust performance for two test cases in which the introduction of coarse turbulent structures is key to resolving the correct flow behavior. However, the approach failed to reproduce correctly the case of the square cylinder, for which a more thorough hybrid resolution is necessary in order to reproduce the turbulent decay, as confirmed by separate tests run with the STRUCT-L-zero approach.

As Spalart (2015) wrote:

"[...] even giving the wrong answer to the right question can serve a purpose."

the STRUCT-L approach proposes an approximate solution to a problem. Such a solution can be extended and enhanced in future work. The encouraging results from STRUCT-L have motivated the development of another complete model, presented in the next chapter.

We can compare the averaging operation used here with the one encountered in the definition of turbulence closures. In URANS and LES models, averaging is usually not performed on-the-fly but only in the derivation of the equations. LES is based on the statistical operation of spatial filtering while URANS on ensemble averaging, which corresponds to time averaging in steady flows. Hybrid models, being a combination of URANS and LES, use a mixture of spatial and temporal statistics. On the other hand, here, the averaging operation in (4.5) needs to be evaluated on-the-fly in every cell and time step. The combination of temporal and spatial statistics in hybrid models motivates the development of the averaging operation presented in the next chapter, in which both time and space variables are involved.

8 Complete transport-averaging-based model STRUCT-T

8.1 Chapter overview

The STRUCT-L approach, developed in the previous chapter, approximated the averaging operation required by the model's closure via a truncated Taylor series expansion while adopting a fixed resolution scale to achieve the fundamental property of completeness.

The local averaging approach allowed efficient numerical performance and demonstrated accurate prediction capability on the two challenging cases of T-junction mixing and axisymmetric diffuser. However, the use of a fixed reduction parameter, ϕ, evidenced limitations in cases where very large flow redistribution dominates over the convected turbulent components requiring higher levels of resolution, as shown for the square cylinder test case results.

The present chapter addresses this limitation by proposing a different STRUCT formulation that employs a continuous variable to assign the TKE ratio locally to the hybrid activation regions. In this new formulation, the averaging operation is approximated through a convective-diffusive transport equation. This new complete model is referred to as STRUCT-Transport (STRUCT-T). After a brief discussion on the rationale and background of the approach, its formulation is described, and the performance of the model is assessed.

8.2 Rationale

The previous chapter has shown that the STRUCT-L approach, while offering the advantage of extremely low computational cost, is prone to strong local variations and requires the use of limiters to avoid strong over- and underestimates of the average in regions with sharp gradients. As a consequence, the working variable t_{m} produced by the approximated averaging operation is not a smooth representation of a local average of parameter $t_{\mathrm{m},0}$.

The lack of smoothness is acceptable in the model and common to similar approaches adopted for dynamic LES models, since the t_{m} variable is only leveraged to trigger a binary activation condition for the hybrid model, while the reduction parameter ϕ is fixed in the simulations. However, results for the square cylinder test case in Section 7.7.1 have presented clear limitations of this approach, motivating a dynamic evaluation of the TKE reduction.

8.3 The STRUCT-T approach

8.3.1 Background

Meneveau, Lund, and Cabot (1996) proposed a Lagrangian method to replace the explicit filtering operation in dynamic LES. The authors utilized a differential operator to approximate a Lagrangian time average, i.e. the average in time of a quantity following a fluid parcel.

Such an averaging operation is applied to a generic field f, function of time and space, yielding its averaged value $\langle f \rangle_{\mathrm{T}}$.

The operation is formulated as the solution to the following transport equation:

$$\frac{\overline{\mathrm{D}}\langle f \rangle_{\mathrm{T}}}{\overline{\mathrm{D}}t} = \frac{1}{T}(f - \langle f \rangle_T) \tag{8.1}$$

It can be shown, as given in Appendix A, that $\langle f \rangle_T$ is solution to the following operation:

$$\langle f \rangle_T(\boldsymbol{x}, t) = \int_{-\infty}^{t} f(\boldsymbol{x}, t)\, g_T(t - t')\mathrm{d}t' \tag{8.2}$$

Assuming constant parameters, the convolution kernel g_T is a negative exponential in time following a characteristic time scale, T.

$$g_T(t - t') = T^{-1}\, e^{-\frac{t-t'}{T}} \tag{8.3}$$

The averaging operation follows the fluid parcel and assigns a weight to the values of the function along the trajectory according to a negative exponential in time. Meneveau, Lund, and Cabot (1996) proposed to solve the transport equation in (8.1) during the simulation using low-order approximations to reduce its computational burden.

Overall, this Lagrangian approach has the advantage of solving a time-averaging operation without being limited to local parameters. The transport equation in (8.1) can be solved in addition to the k and epsilon ones, without adding major overhead to the overall computational cost.

8.3.2 Generalized space-time Lagrangian averaging

Here we propose a differential operator in space and time, adding a key spatial character to the method proposed by Meneveau Lund, and Cabot (1996).

The resulting operator has been briefly discussed by Germano (2000) as a promising method for differential filtering in LES but has not been further discussed or adopted in modeling.

If we consider a generic time and space function $f(\boldsymbol{x}, t)$ with the following properties:

$$f: \begin{cases} \mathbb{R}^3 \times \mathbb{R} & \rightarrow & \mathbb{R} \\ (\boldsymbol{x}, t) & \mapsto & f(\boldsymbol{x}, t) \end{cases} \tag{8.4}$$

We can define a differential Lagrangian averaging operation as the solution to the following transport equation. The equation includes a length scale, L, and a time scale, T.

$$\frac{\mathrm{d}\langle f \rangle_{T,L}}{\mathrm{d}t} + \overline{\boldsymbol{u}} \cdot \boldsymbol{\nabla}\langle f \rangle_{T,L} = \frac{L^2}{T}\boldsymbol{\nabla}^2\langle f \rangle_{T,L} + \frac{1}{T}\left(f - \langle f \rangle_{T,L}\right) \tag{8.5}$$

We may notice that the transport equation above is different from the one in (8.1) in that it contains a diffusion term in addition to the source term in the RHS. The average field $\langle f \rangle_{T,L}$ can be written as the solution to the following operation:

$$\langle f \rangle_{T,L}(\boldsymbol{x}, t) = \int_{-\infty}^{0} \int_{\mathbb{R}^3} f(\boldsymbol{x}', t') g_{T,L}(\boldsymbol{x} - \boldsymbol{x}', t - t')\mathrm{d}^3\boldsymbol{x}'\mathrm{d}t' \tag{8.6}$$

In the particular case of uniform and constant $\boldsymbol{u}, T, L$, the averaging kernel in the equation above corresponds to a Gaussian filter in space and a negative exponential in time.

$$g_{T,L}(\boldsymbol{x}-\boldsymbol{x}', t-t') = \frac{1}{T} e^{-\frac{t-t'}{T}} \frac{1}{\left(4\pi \frac{L^2}{T}(t-t')\right)^{3/2}} e^{-\frac{\left(x-x'-u(t-t')\right)^2}{4\frac{L^2}{T}(t-t')}} \tag{8.7}$$

Therefore, under those simplifying assumptions, the transport equation in (8.5) defines an averaging operation that is at the same time Gaussian in space around the point of interest and exponential in time before the time of interest. Here we use the averaging operation defined by (8.5) in arbitrary flow conditions. Such an application does not lead to the relation of (8.7) any longer, but it holds significant conservation properties, as discussed in Appendix A.

8.3.3 Definition of the working variable for STRUCT-T

The averaging operation in (8.5) is used to determine the working variable t_m as follows:

$$\frac{\mathrm{d}t_\mathrm{m}}{\mathrm{d}t} + \boldsymbol{u} \cdot \boldsymbol{\nabla} t_\mathrm{m} = \frac{L^2}{T} \boldsymbol{\nabla}^2 t_\mathrm{m} + s \tag{8.8}$$

where s is the equation's source:

$$s = \min\left(\max\left(\frac{1}{T}\left(t_{\mathrm{m},0} - t_\mathrm{m}\right), -\frac{2t_\mathrm{m}}{\Delta_t}\right), \frac{2t_\mathrm{m}}{\Delta_t}\right) \tag{8.9}$$

The source is bounded to avoid strong variations of t_m within a time step Δ_t, allowing for greater model stability and adaptation to initial conditions. The field for t_m is clipped to have a value within its physical range between a very small number, say 10^{-10} s, and 1 s.

The length and time scales used for the averaging are defined based on local flow conditions as:

$$L = \sqrt{C} \frac{k_\mathrm{m}^{3/2}}{\varepsilon} \tag{8.10}$$

$$T = \frac{1}{\beta} \frac{k_\mathrm{m}}{\varepsilon} \tag{8.11}$$

The value $C = 0.09$ derives from the standard k-ε model. The value for β used here is 0.01. Simulation results are not sensitive to small variations of β. The use of a low time constant enhances the conservation properties of the averaging operator, as shown in Appendix A.2 and A.3. This choice allows biasing the time-space averaging operation towards the space component. Boundary conditions are assigned so that at the inlet and walls $t_\mathrm{m} = t_{\mathrm{m},0}$. The same is also done for the initialization of t_m.

8.3.4 Dynamic strategy for the control coefficient

The control parameter ϕ defines the resolved-to-total TKE ratio in regions of STRUCT activation, as shown in (4.1). In the models tested in the previous two chapters, the activation parameter h was calculated as a ratio between the two working variables f_r and t_m, while the control parameter ϕ was prescribed as constant. Here, we propose instead to prescribe both h and ϕ based on the ratio between working variables. We can then replace (4.1), as follows:

$$r = \min\left(\frac{1}{\alpha t_\mathrm{m} f_\mathrm{r}}, 1\right) \tag{8.12}$$

This idea corresponds to reducing the TKE ratio in the activation regions, based on a metric identifying scale overlap. The stronger the scale overlap, the lower is r. The calibration coefficient α is assigned as constant for all flows. Such a coefficient was optimized to the value of 1.35.

8.4 Results

The STRUCT-T approach is assessed on the same flow cases and grids tested in Chapter 6 for the controlled STRUCT approach and in Chapter 7 for the STRUCT-L.

8.4.1 Flow past a square cylinder

Application of the STRUCT-T approach to the flow past a square cylinder test case produces the activation regions shown in Figure 8.1 below. The outline of the regions in which hybrid behavior is enabled is similar to that obtained from the STRUCT-L approach, shown in Figure 7.1. However, activation regions are not shown as monochrome, as they were in the controlled STRUCT and STRUCT-L tests, due to the variable reduction coefficient. The TKE ratio varies from nearly zero around the cylinder to values that increase along with the flow.

It is expected that a long extrusion of the flow domain downstream after the outlet would lead to dissipation of the vortex street and reversal of the STRUCT-T behavior to URANS mode as fully-developed conditions are retrieved. The increasing values of the TKE ratio going from the cylinder towards the outlet suggest the validity of this assumption.

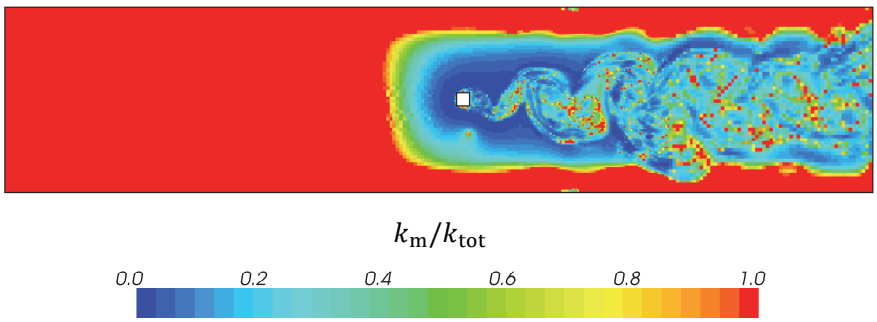

Figure 8.1 STRUCT-T activation, instantaneous scalar field, flow past a square cylinder

We can now present STRUCT-T results for this test case, by plotting the same physical values as in the last two chapters, summarized below for convenience:

- time-averaged velocity in the x-direction, in Figure 8.2
- time-averaged velocity in the y-direction, in Figure 8.3
- time variance of velocity in the x-direction, in Figure 8.4
- time variance of velocity in the y-direction, in Figure 8.5
- time covariance of velocity in the x-y directions, in Figure 8.6

Velocity profiles in Figure 8.2 and Figure 8.3 below show a behavior of STRUCT-T very close to that of the controlled STRUCT approach. This result demonstrates a significant improvement over the STRUCT-L results, for which the constant choice of the TKE reduction parameter has resulted in non-optimal velocity profiles.

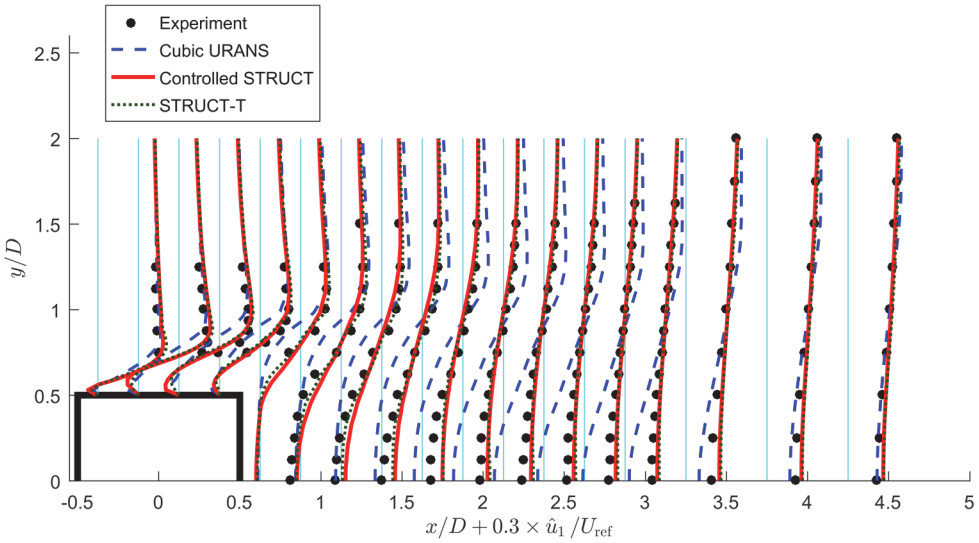

Figure 8.2 Flow past a square cylinder, STRUCT-T, time-averaged velocity $\widehat{u}_1$

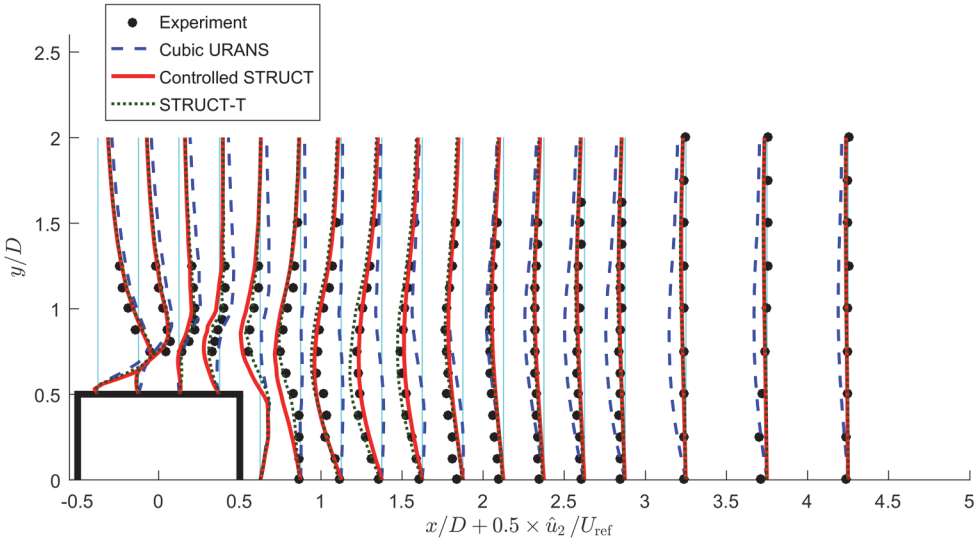

Figure 8.3 Flow past a square cylinder, STRUCT-T, time-averaged velocity $\widehat{u}_2$

The second central moments of velocity presented in Figure 8.4 and in Figure 8.5 below show results within a reasonable agreement with the experiment and with the controlled STRUCT profiles. Small discrepancies with the controlled STRUCT results are observed mainly in the region around and past the cylinder, leading to local overestimates of the fluctuations without leading to a wide error that could resemble a typical hybrid model breakdown.

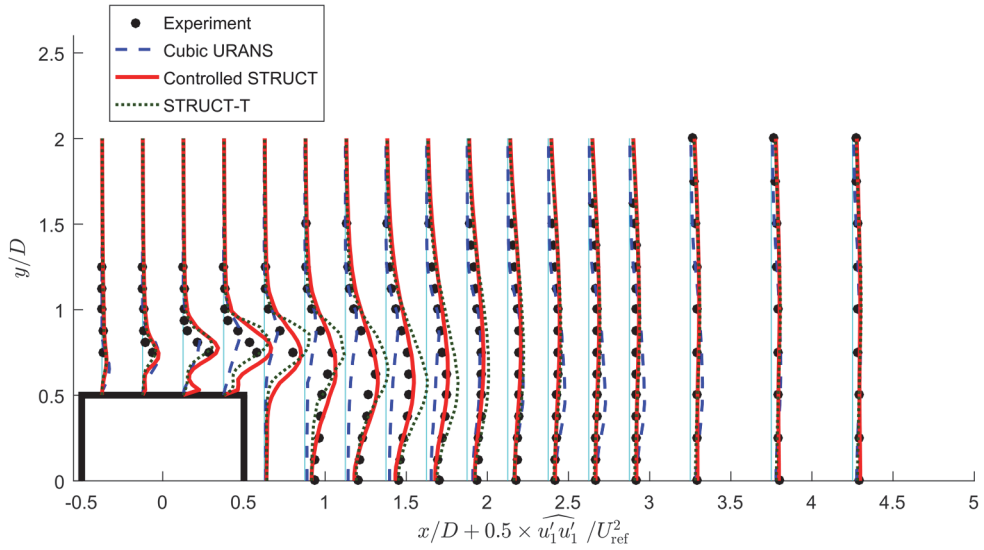

Figure 8.4 Flow past a square cylinder, STRUCT-T, time variance of velocity, $\widehat{u_1' u_1'}$

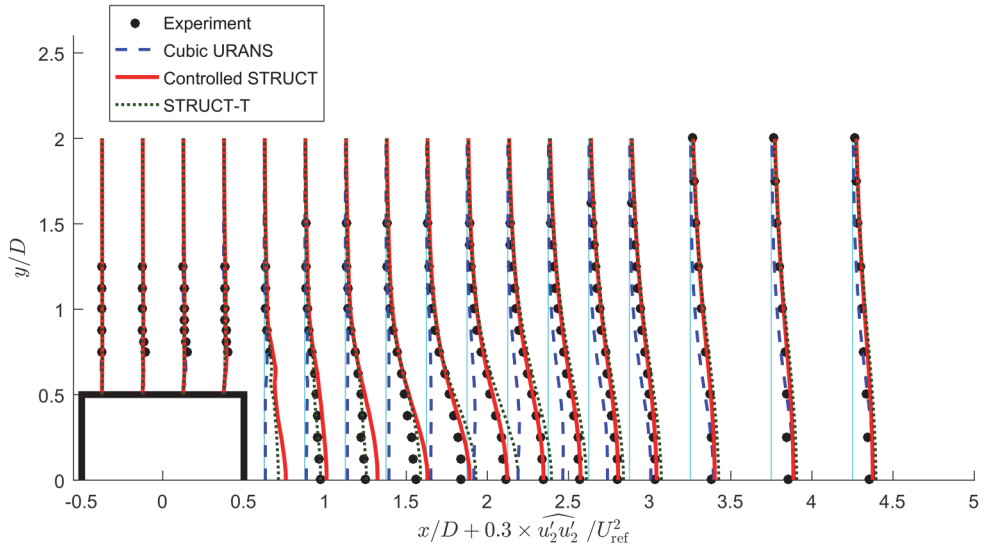

Figure 8.5 Flow past a square cylinder, STRUCT-T, time variance of velocity, $\widehat{u_2' u_2'}$

Profiles for velocity covariance in Figure 8.6 below also show similarly accurate results as the controlled STRUCT. A slightly closer agreement in the profile appears immediately downstream the cylinder while a minor overestimate of the absolute value appears further downstream. The beneficial result in the wake region could be related to the TKE reduction prescribed by the model being intermediate between 0 and 1, instead of almost zero as in the controlled approach.

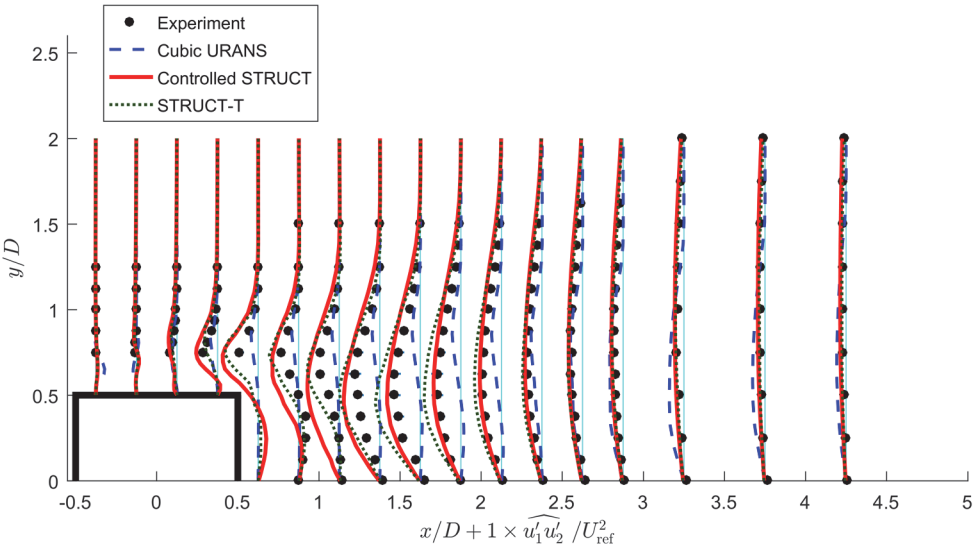

Figure 8.6 Flow past a square cylinder, STRUCT-T, time covariance of velocity, $\widehat{u_1'u_2'}$

8.4.2 Turbulent mixing in a T-junction

STRUCT-T results for the T-junction test case produce the activation regions shown in Figure 8.7. The activation regions obtained here are similar to those observed for the controlled STRUCT and the STRUCT-L approaches, shown respectively in Figure 6.26 and Figure 7.7. The TKE reduction function approaches zero around the center of the junction and has intermediate values between zero and one in the active regions downstream the junction.

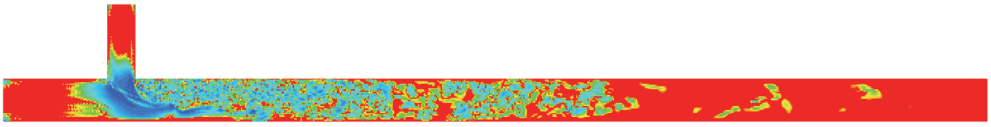

k_m/k_{tot}

Figure 8.7 STRUCT-T activation, instantaneous scalar field, T-junction mixing

We now present STRUCT-T results for the same variables shown in for the controlled STRUCT and the STRUCT-L tests. Those variables are:

- Velocity profiles in the x-direction, in Figure 8.8
- Velocity profiles in the z- and y-direction, in Figure 8.9
- Profiles of the time variance of velocity in the x-direction, in Figure 8.10
- Profiles of the time variance of velocity in the z- and y-direction, in Figure 8.11
- Profiles of the time covariance of velocity in the x-z and x-y directions, in Figure 8.12

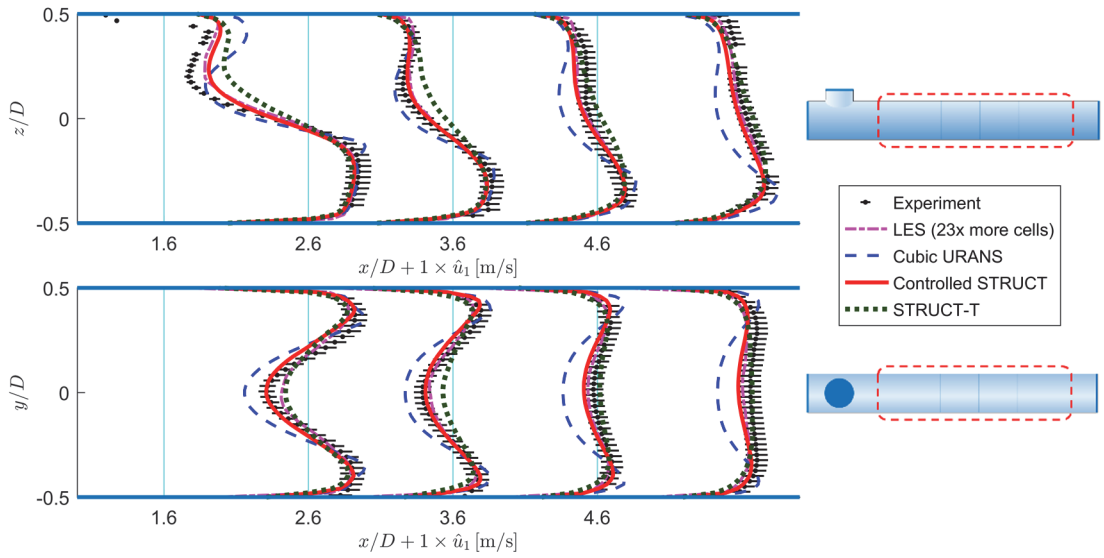

Figure 8.8 T-junction mixing, STRUCT-T, time-averaged velocity $\hat{u}_1$

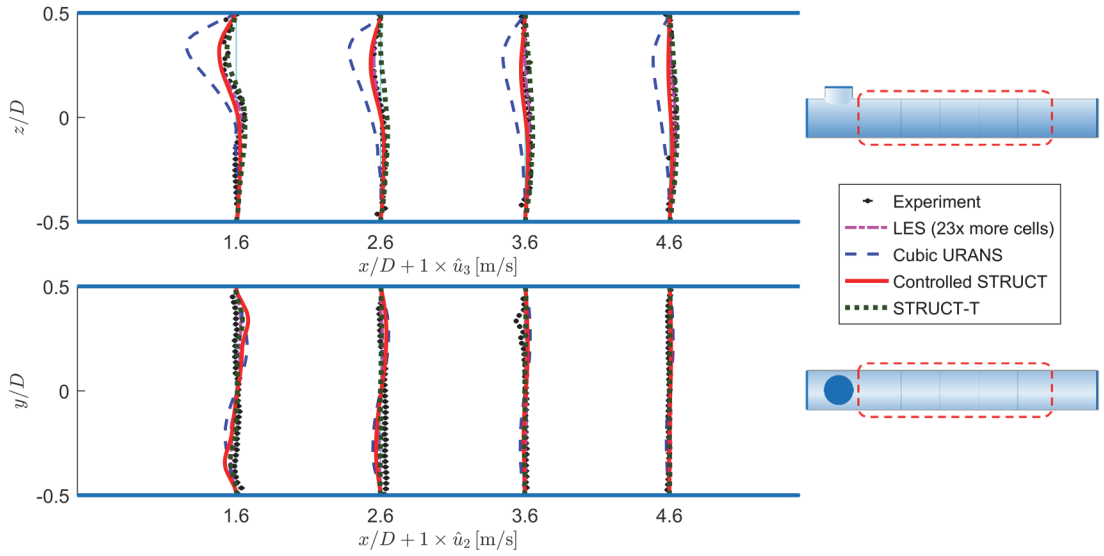

Figure 8.9 T-junction mixing, STRUCT-T, time-averaged velocity $\hat{u}_3$ and $\hat{u}_2$

Results for the main time-averaged components of velocity are shown in Figure 8.8 and Figure 8.9. Those figures show an overall close agreement of STRUCT-T results with experimental data. The first two data sections downstream the junction overestimate the velocity predicted at the center of the pipe. However, this overestimate does not lead to a large error. Future work could enhance the performance of the model complex mixing regions like this one.

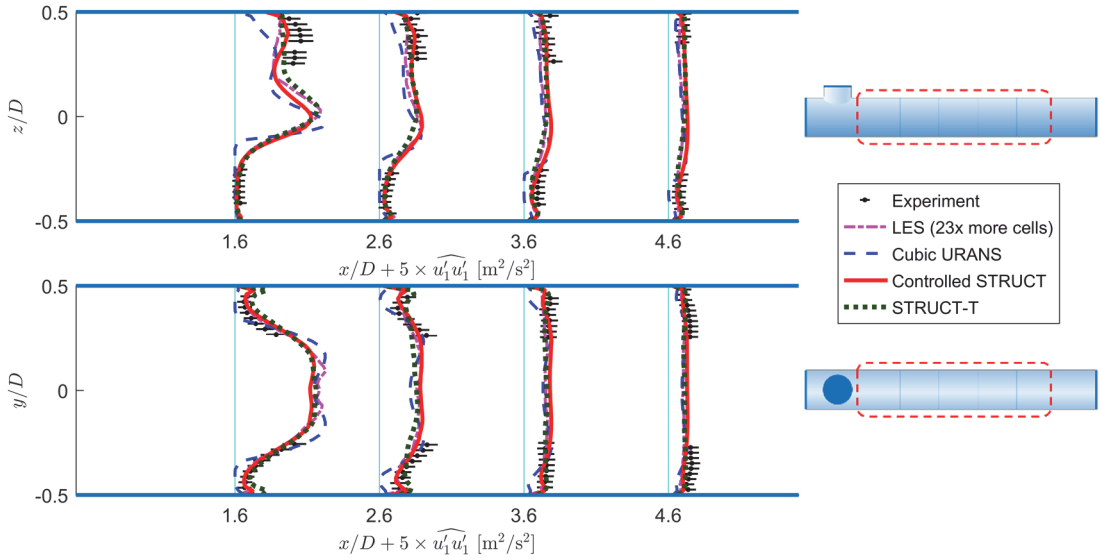

Figure 8.10 T-junction mixing, STRUCT-T, time variance of velocity, $\widehat{u_1' u_1'}$

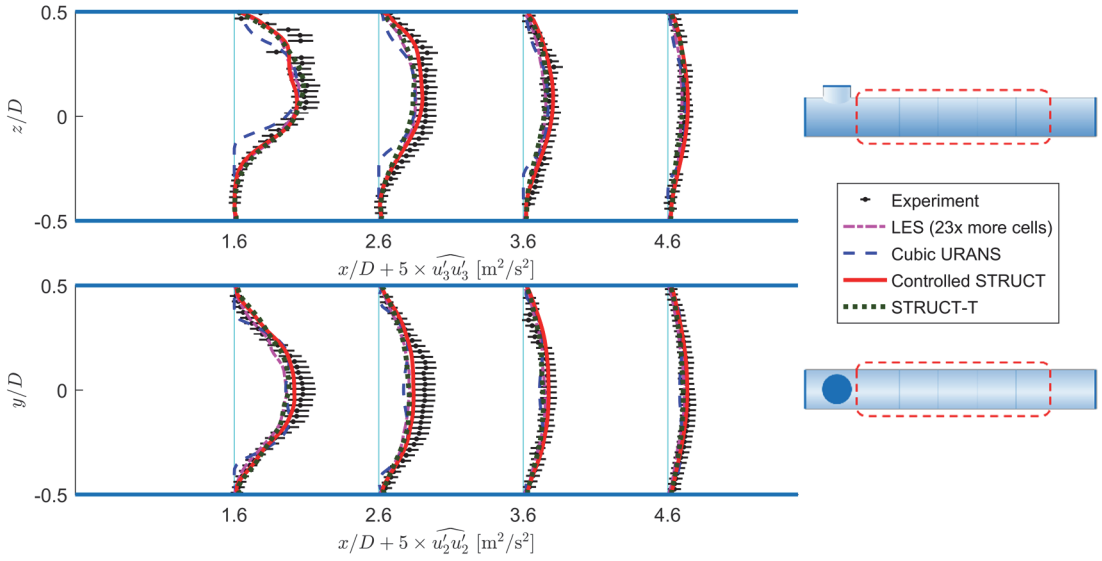

Figure 8.11 T-junction mixing, STRUCT-T, time variance of velocity, $\widehat{u_3' u_3'}$ and $\widehat{u_2' u_2'}$

First central moments of velocity are shown in Figure 8.10 and Figure 8.11 above. Those results appear to be in close agreement with available experimental data and with LES results. This agreement is very close to the one achieved by the controlled STRUCT.

The covariance of the main components of velocity is shown in Figure 8.12 below. Those profiles are in closer agreement with the experiment compared to the URANS ones. Mixed performance is achieved compared to controlled STRUCT results, without producing significant error compared to the width of experimental error bars.

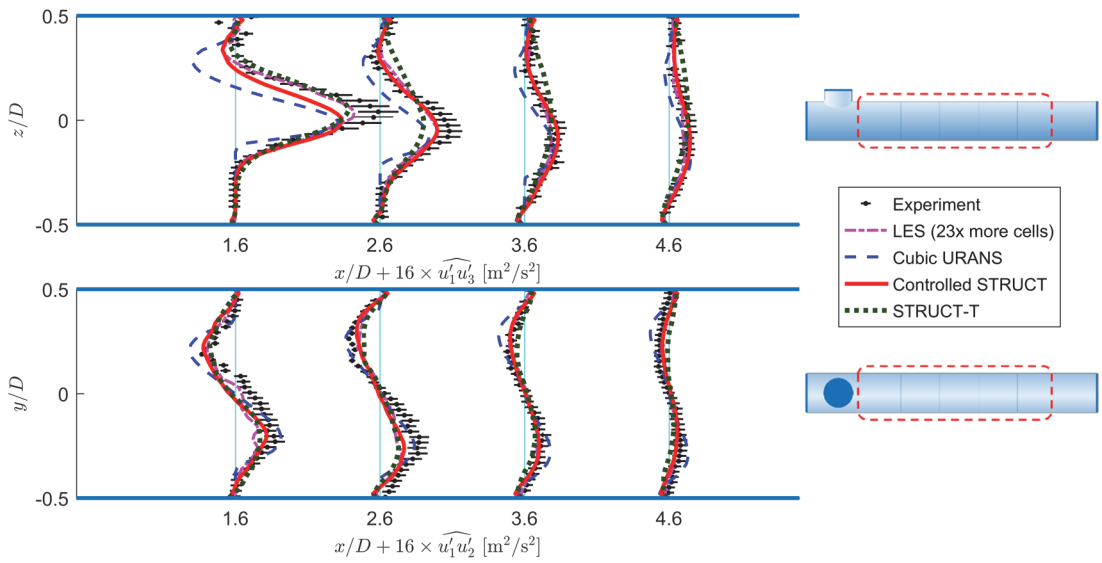

Figure 8.12 T-junction mixing, STRUCT-T, time covariance of velocity, $\widehat{u_1'u_3'}$ and $\widehat{u_1'u_2'}$

8.4.3 Mild separation in an asymmetric diffuser

Application of STRUCT-T to the test case of the mild separation in an asymmetric diffuser produces the activation regions shown in Figure 8.13 below. In that figure, we can observe a main central activation zone. Such a region has a similar shape to that obtained from the STRUCT-L approach, shown in Figure 7.13.

In the STRUCT-T activation regions shown below, most values for the TKE ratio are in the range between 0.3 and 0.9, which is the same range as for the controlled STRUCT tests made here.

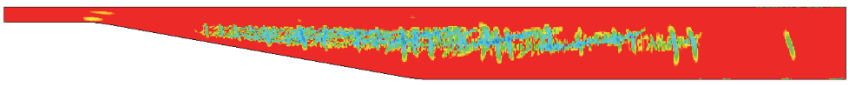

$k_{\mathrm{m}}/k_{\mathrm{tot}}$

Figure 8.13 STRUCT-T activation, instantaneous scalar field, asymmetric diffuser

Let us show STRUCT-T results for the same variables plotted in the previous chapters. Those are:

- Time-averaged velocity in the x-direction, in Figure 8.14
- Velocity variance in the x-direction, in Figure 8.15
- Velocity variance in the y-direction, in Figure 8.16
- Velocity covariance in the x-y directions, in Figure 8.17

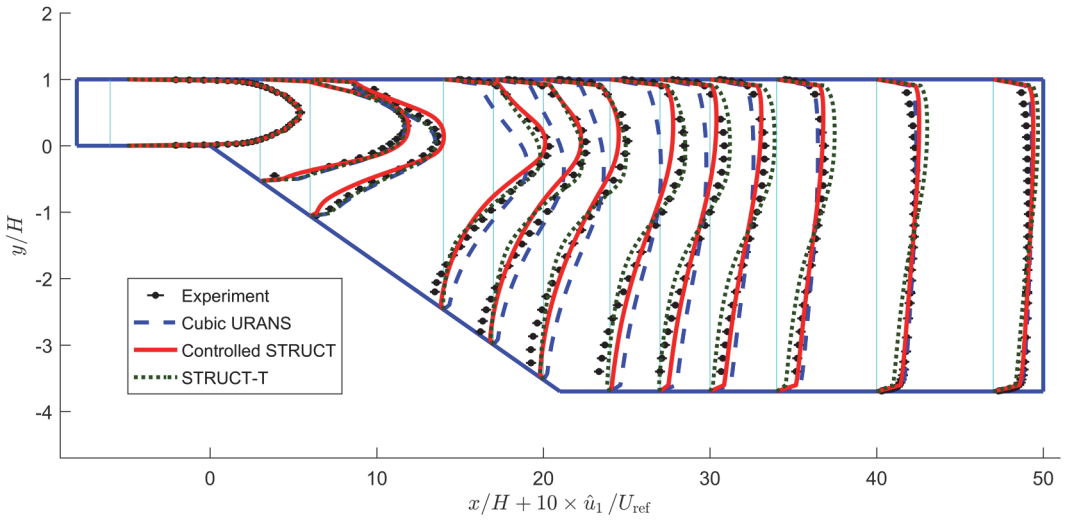

Figure 8.14 Asymmetric diffuser, STRUCT-T, time-averaged velocity $\hat{u}_1$

Results for time-averaged velocity profiles, presented in Figure 8.14 above, show an agreement with experimental data by the STRUCT-T approach even closer than that observed for the controlled STRUCT approach in most of the experimental profiles. A slight overestimate of the x-component of velocity is observed in the top regions downstream the diffuser. This overestimate may be caused by the longer activation regions compared to the controlled STRUCT.

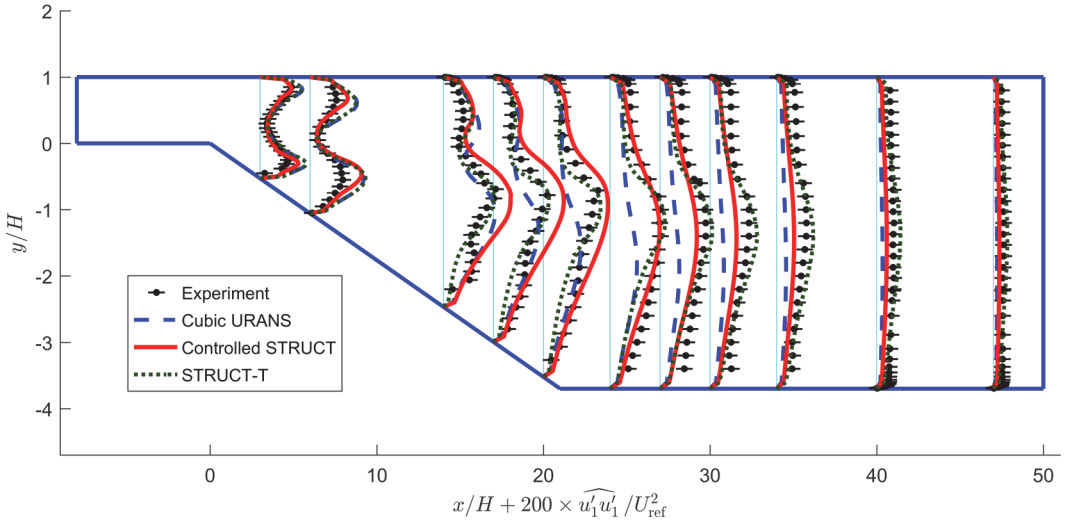

Figure 8.15 Asymmetric diffuser, STRUCT-T, time variance of velocity, $\widehat{u_1' u_1'}$

The second central moments of velocity in the x and y directions are shown in Figure 8.15 above and in Figure 8.16 below. The former figure shows that STRUCT-T results are much closer to the experiment compared to controlled STRUCT ones. The latter figure provides results within the error bars of the experiments while a peak appears in regions not captured by the experiment. Such a peak is likely caused by the presence of activation regions and may require correction in future work.

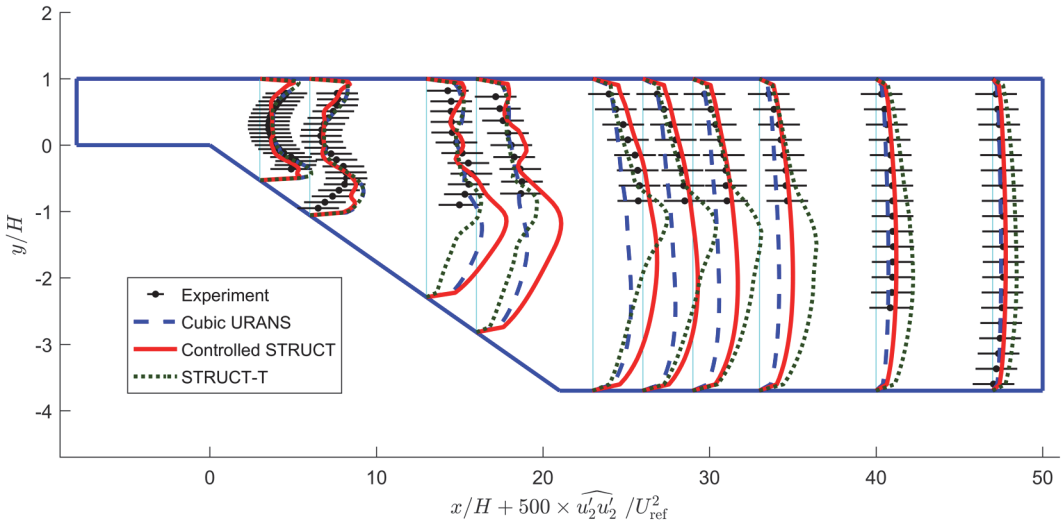

Figure 8.16 Asymmetric diffuser, STRUCT-T, time variance of velocity, $\widehat{u_2'u_2'}$

The covariance of x-y velocity components in Figure 8.17 below shows overall an accurate trend of the STRUCT-T results. A central peak appears towards the end of the domain likely caused by the presence of activation regions. Again, solution to those peaks could be addressed in future work.

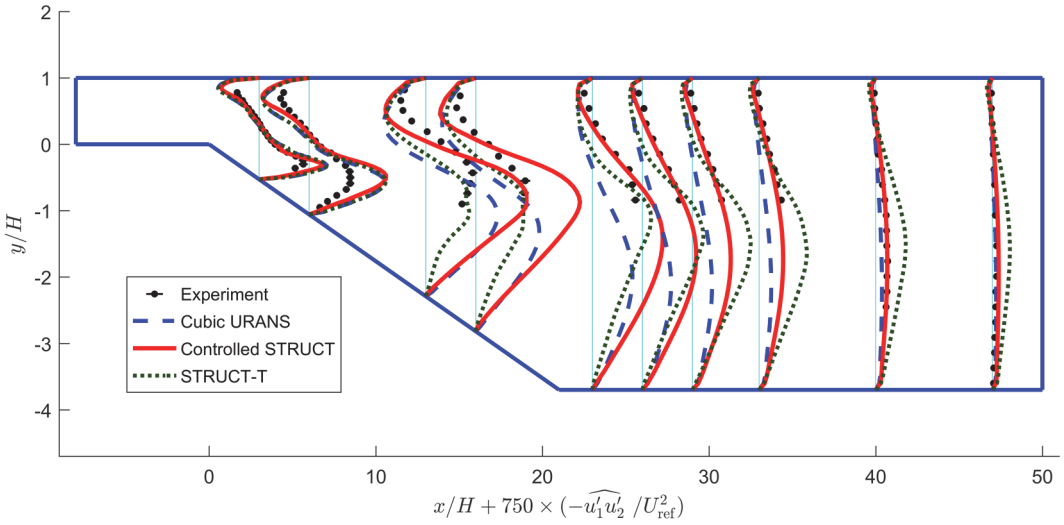

Figure 8.17 Asymmetric diffuser, STRUCT-T, time covariance of velocity, $\widehat{u_1'u_2'}$

8.5 Behavior in a simple straight pipe or a rectangular channel

As discussed already in Section 7.8, in simple flows such as those in a straight pipe or a channel, STRUCT activation is not desired. Those are flows in which the baseline NLEVM URANS usually provides accurate predictions.

As already done for the STRUCT-L approach, we can check for this feature by focusing on the regions of the flow cases already tested resembling pipe or channel flows. In particular, the inlet of the square cylinder test case and the outlet of the asymmetric diffuser one are flows through rectangular channels, while the outlet of the T-junction test case is a flow in a circular pipe. The activation regions are shown in Figure 8.1, Figure 8.7, and Figure 8.13. In all of those cases, the STRUCT-T model does not activate its hybrid behavior unless significant flow deformation occurs. We can conclude, therefore, that the desired performance is met.

8.6 Evaluation of results

The results obtained in this work can be summarized in a simplified table accounting for the root mean square (RMS) deviation between experimental data and simulation results interpolated at the locations of experimental data. The RMS deviations for a generic model M are normalized based on the RMS deviation obtained with the standard k-ε linear URANS model:

$$\mathrm{RMS}^{\mathrm{M}}_{\mathrm{normalized}} = \frac{\mathrm{RMS}^{\mathrm{M}}}{\mathrm{RMS}^{\text{linear URANS}}} \tag{8.13}$$

The values obtained using (8.13) are shown in Table XI below for different models and variables used in this work. A value of 1 would correspond to the performance of the linear URANS model.

Table XI Normalized RMS results for different models, test cases, and variables

Variable	Cubic URANS	Cont. STRUCT	STRUCT-L	STRUCT-T
Square cylinder				
$\widehat{u}_1$	0.82	0.43	0.52	0.42
$\widehat{u}_2$	1.02	0.62	0.87	0.60
$\widehat{u_1'u_1'}$	0.80	0.43	0.65	0.56
$\widehat{u_2'u_2'}$	0.73	0.26	0.46	0.30
$\widehat{u_1'u_2'}$	1.01	0.46	0.99	0.39
T-junction				
$\widehat{u}_1$ (v), $\widehat{u}_1$ (h)	0.99	0.83	0.85	0.83
$\widehat{u}_3$ (v), $\widehat{u}_2$ (h)	1.35	0.48	0.57	0.26
$\widehat{u_1'u_1'}$ (v), $\widehat{u_1'u_1'}$ (h)	0.99	0.93	0.95	0.94
$\widehat{u_3'u_3'}$ (v), $\widehat{u_2'u_2'}$ (h)	1.00	0.96	0.98	0.98
$\widehat{u_1'u_3'}$ (v), $\widehat{u_1'u_2'}$ (h)	1.00	0.99	0.99	0.99
Diffuser				
$\widehat{u}_1$	0.85	0.77	0.77	0.79
$\widehat{u_1'u_1'}$	0.82	0.57	0.62	0.53
$\widehat{u_2'u_2'}$	1.01	0.82	0.94	0.75
$\widehat{u_1'u_2'}$	1.15	1.43	1.23	1.21

The arithmetic average of the columns in Table XI leads to an averaged normalized deviation of 0.97, 0.71, 0.81, 0.68 respectively for the cubic NLEVM URANS, the controlled STRUCT approach, STRUCT-L, and STRUCT-T. Those results support the benefit of replacing the linear URANS with the NLEVM and demonstrate the capability of the STRUCT approaches of providing closer agreement with the experiment compared to the baseline URANS.

8.7 Discussion

A feature of many hybrid models is to be seamless, not requiring a sharp interface between regions with different resolution (Friess et al., 2015). The controlled STRUCT and the STRUCT-L do not meet this condition due to a sudden variation of the TKE ratio occurs between regions of active and non-active hybrid behavior. On the other hand, the STRUCT-T approach does not contain a sharp spatial boundary distinguishing between active and non-active regions. The activation occurs smoothly in a range of values of the TKE ratio. Therefore, the STRUCT-T behavior can be considered as seamless.

In the ELES approach (Cokljat et al., 2009), a fixed arbitrary interface is defined in the flow domain by the user before running the simulation, representing a boundary between URANS and LES. The fixed presence of such an interface in the Eulerian framework causes the need for the injection of artificial turbulence, to avoid a sudden depletion of turbulence when the fluid crosses it.

Conversely, in the controlled STRUCT approach the distinction between URANS and hybrid zones is defined based on local flow parameters, so it is fully Galilean invariant, without depending on any parameters in the Eulerian framework. Activation regions move with the flow and follow regions of large deformation. Such a movement reduces the mass flux across the interface compared to ELES. This large deformation has shown to generate resolved structures without any identified need for the injection of artificial turbulence.

9 Conclusions

9.1 Summary

Hybrid turbulence models have been proposed starting in the mid-1990s and combine features of URANS and LES aiming at providing an enhanced flow description and accuracy, at a reduced computational cost. The literature presents numerous examples of successful applications of hybrid models to selected test cases. However, significant weaknesses restrict their reliability for predictive simulations resulting in limited practical use, notably poor grid consistency and robustness.

The present work has evaluated the objectives and strengths of industrially relevant models and has developed a novel hybrid strategy to address a selected set of limitations. The goal of the new strategy is to preserve the robustness of URANS while adding controlled turbulence resolution in conditions of poor URANS applicability. Given the industrial interest, this work has mainly focused on robust two-equation models such as those based on the k-ε equations.

The newly proposed hybrid formulation introduces an activation condition based on a comparison between working variables representing scales associated with resolved and modeled turbulence. The parameter identified for describing resolved turbulence is the square root of the absolute value of the second invariant of the resolved velocity gradient tensor. This choice allows the hybrid behavior to be activated in regions without significant scale separation or with rapid distortion while leveraging the robust URANS equations in simple shear regions. The second invariant of the velocity gradient tensor has been used for decades in topology studies to identify coherent structures. The new approach is named STRUCT to indicate this parallel function of the parameter used.

The baseline URANS closure chosen to implement the STRUCT approach is the k-ε NLEVM by Baglietto and Ninokata (2006). As a first step, a controlled model version has been tested, which uses case-dependent parameters chosen a posteriori and constant in the whole flow region. Two closure parameters are needed, one of which derives from previous URANS results while the other one is optimized to assess the maximum resolution level achievable by the new approach.

Results have been compared with experimental data on a variety of representative flow cases running on URANS-like coarse grids. The analysis of those results has demonstrated beneficial features of STRUCT compared to the baseline URANS approach alone. Those features were measured as an increase in agreement of first and second central moments of velocity with experimental data.

The controlled applications of STRUCT have confirmed that the local resolution of turbulence provides a consistent and measurable increase in prediction accuracy. In particular, and uniquely to this approach, the results show that the improvement is obtained at all grid resolutions, and very importantly increasing prediction quality with grid refinement, which was not achievable with previous hybrid formulations. Moreover, controlled STRUCT results demonstrated no significant sensitivity to the grid cell geometry, as assessed switching from trimmed to polyhedral cells.

Those preliminary tests of the controlled approach have shown that STRUCT provides at least the same accuracy as a NLEVM URANS, as guaranteed mathematically by URANS-like parameters, and at most a significantly closer agreement with the experiment on the same coarse grid.

Two fully closed self-adaptive formulations have been proposed to extend the applicability of the proposed approach. The key aspect here is the need to obtain representative averaged values for the working variable describing modeled scales, using single-point operations. The two formulations

leverage two different conceptual approaches, one based on a Taylor series expansion, STRUCT-L, and the other one based on a convective-diffusive Lagrangian differential operator, STRUCT-T. Both of those approaches have been implemented and assessed on the same set of test cases, identifying key strengths and limitations.

The STRUCT-L approach has provided similar results as the controlled model on the cases tested. However, the model only assigns the criterion for hybrid activation based on local flow conditions, while the TKE ratio needed for hybridization is set as constant before the simulation. This leads to the downside that further optimization is possible by assigning optimal values for the TKE ratio.

The STRUCT-T approach addresses this issue by proposing an automatic closure for both conditions. This approach is made possible by the use of a smooth Lagrangian averaging relying only on local operations. Collaborative work has investigated the conservation properties of this Lagrangian operator, as shown in Appendix A.2. Results on the three flow cases tested have obtained close agreement with the experiment similarly to STRUCT-L and controlled STRUCT results.

Overall, the two complete STRUCT formulations have proven to provide accurate results on coarse grids similarly to those used for URANS and controlled STRUCT tests. The cost increase related to the use of STRUCT has been assessed to be approximately 10% in comparison to the baseline URANS implementation. This means that STRUCT simulations have a cost typically 50 times to several orders of magnitude lower than LES.

The main limitations of the STRUCT approach are the lack of LES retrieval on suitable refined grids and the need for extensive testing typical of a newly developed model.

The work has further provided useful learning on the applicability of NLEVMs. Their performance on unsteady flow applications have reached complete maturity, and their use is always preferable to two-equation linear URANS. The proposed hybrid approach and similar ideas that might be developed in the future promise to become the next step in this progression, offering a potential replacement for NLEVMs and URANS. The new approach proved to be ready for further development and testing on industrial cases. Initial assessments in this sense deriving from collaborative work are available in Appendix B.

9.2 Main contributions

Critique of selected hybrid turbulence models

The present work has analyzed hybrid turbulence models of industrial relevance determining significant weaknesses that should be addressed for improvement. Among the drawbacks identified are the poor grid consistency and the large sensitivity to variations in simulation conditions. Examples from the literature have been analyzed showing cases of hybrid models predicting unphysical behavior with errors much higher than those from two-equation URANS simulations. This investigation has determined the need for a hybrid formulation preserving the significant robustness of industrial two-equation URANS models.

Identification of a parameter describing hybrid activation regions

A formulation was developed for identifying regions of desired hybrid activation by recognizing the consistency between regions of low URANS applicability and flow regions often identified as representative of coherent flow structures. This key aspect of the work shows how the intuition-driven approach of resolving coherent flow and the analysis-driven approach of introducing hybrid activations where URANS assumptions are violated lead to the same strategy. The formulation developed is based on the second invariant of the resolved velocity gradient tensor. Such a parameter has many desirable properties for hybrid modeling, including the capability to identify scale separation, rapid deformation, and simple shear flow.

Formulation and testing of the new STRUCT approach

A new approach for hybrid turbulence modeling was developed based on a comparison between two working variables, associated with resolved and modeled turbulent scales. The new STRUCT approach leverages the robustness of URANS in most of the domain and enables hybrid activation in regions of poor URANS applicability. A controlled version of the STRUCT approach using fixed parameters determined before the simulation has been implemented and assessed in relevant flow cases to verify the limiting performance of the new approach. Results have shown a level of accuracy equal or superior to the baseline NLEVM URANS on coarse URANS-like grids. Grid consistency has been confirmed in all flows tested.

Introduction and testing of a complete STRUCT approach based on Taylor series expansion

Closure for the new hybrid approach has been developed by identifying a suitable averaging operation as required by the basic STRUCT definition. An approximation of volume averaging based only on local operations is performed using a truncated Taylor series expansion. This method identifies automatically regions of hybrid activation where a constant reduction of turbulent kinetic energy is assigned. The method has been implemented in the same flow cases as for the controlled STRUCT, achieving similar increase in accuracy and flow description over the baseline URANS.

Introduction and testing of a complete STRUCT approach based on Lagrangian averaging

A convective-diffusive Lagrangian averaging operation has been identified and analyzed in its relevant properties, determining its applicability as the averaging operation required for a complete STRUCT closure. This averaging method relies only on local operations and computes a smooth averaged field. The complete model uses such a smooth field to identify automatically not only regions of hybrid activation, but also the local reduction of turbulent kinetic energy. Results obtained by testing this model demonstrated its capability to provide similar benefit over the baseline URANS as for the controlled STRUCT while being a complete model and overcoming the STRUCT-L approach's downside of requiring a constant reduction parameter.

9.3 Perspectives

We can now peer a few decades into the past and look at an observation based on T-shirt slogans made in 1995 by Spalding (Artemov et al., 2009):

Table XII Slogans on CFD development, from Artemov et al. (2009)

Decade	Slogan	What was happening
1960s	We think we can	Imperial College research
1970s	We can!	First applications
1980s	You can too	Start of code-vending industry
1990s	Everyone can	Commercial over-sell
2000s	Everyone will	Web-based services

The slogans shown above give us a sense of the rapid evolution of CFD over four decades. It is not surprising to notice that Spalding predicted correctly what was going to happen. Indeed, today cloud-based CFD services are readily available (e.g. ESI, 2016). Extending Spalding's reasoning, we might wonder about what accomplishments are expected in the next decades in single-phase turbulence simulation. Areas of further improvement will likely concern turbulence modeling, which is usually the largest cause of modeling error due to the rapid advances in solvers that reduce numerical error.

Indeed, current turbulence models have failed to achieve a physical universality that could make a single model optimally applicable to any flow condition. CFD analysts working in engineering applications are required to select the model to use based on a tradeoff and to run significant tests to validate the chosen setup. Hybrid models represent a promising option for removing this tradeoff and achieving an optimal strategy.

We can foresee that very likely in the near future hybrid models, which are currently not widely adopted in industry, will become a primary tool. It is not uncommon that methods formerly considered limited to academic study become widely used in the industry over the necessary development time. For example, it is interesting to read a comment written in a 1976 review by W.C. Reynolds (1976):

"Zero-equation models are common practice in the more sophisticated engineering industries, and one-equation models find use there on occasion. Two-equation models, currently popular among academics, have not been used extensively for engineering applications; probably because one can do as well if not better in most problems with simpler methods."

Evidence in industrial simulations has proved that this prediction was inaccurate. Indeed, models that were popular among academics at that time have found wide application in industry later on.

Another open question is: will we need turbulence closures in the future? Extrapolating the growth in computational power based on Moore's law, a point will be reached in which LES, or even DNS, might become a practically feasible option. Based on an extrapolation, this turning point has been estimated around 2080 (Spalart, 2015). Counter-arguments to the idea that turbulence models will become obsolete support the supposition that Moore's law has been recently slowing down, and it may reach an asymptotic limit. Moreover, the use of faster processor power would still require advances in memory storage and data transfer technology to achieve an effective potential.

The preference for a specific CFD turbulence model in the industry depends not only on its formulation but also on the experience accumulated in its use over time. Experience allows us to identify strengths and limitations of models and to define usage guidelines regarding numerical schemes, mesh construction, convergence strategies, and boundary conditions. Turbulence modeling is a necessary link in the simulation chain, but not the only one.

Hybrid models so far have only been able to support a very limited class of applications. More robust and accurate hybrid models would allow us to extend the capabilities of industrial CFD to more complex applications.

This rationale has motivated the present work, whose findings have offered a potential avenue for robust hybrid modeling. Indeed, the STRUCT approach has demonstrated significant novel features. Its low sensitivity to mesh size and cell geometry is appropriate for industrial applications and defines the approach's robustness.

The future of turbulence modeling may rely strongly on hybrid methods, given their important goals and promising preliminary results. Those models, together with advances in computational tools, could provide significant benefit in future simulations of large and complex energy systems. However, this path requires two conditions to occur:

- Robust models suitable for the industrial needs need to be identified
- Significant testing and experience need to be accumulated on those models

The STRUCT approach could be developed further, aiming at satisfying the first criterion. The second criterion is not less important than the first one for a model's success. Engineers prefer a model that they know, its strengths and weaknesses, to a more promising model whose robustness is not verified extensively.

9.4 Future work

This section proposes areas of study that would be appropriate for future research.

- The baseline URANS closure could be modified or extended benefiting from the general applicability of the model. In particular, the choice of the baseline URANS could be optimized based on the industrial application analyzed.
- The STRUCT approach could be extended so that LES behavior be retrieved in the limit of a fine-enough and suitable computational grid. Convergence to LES could offer advantages in specific applications, such as combustion, in which it is often important to resolve fine turbulence scales.
- The near-wall asymptotic behavior of STRUCT could be analyzed for low-Re applications. URANS k-ε models typically use damping functions for achieving consistent performance when integrated all the way to the wall. The consistent behavior of STRUCT implemented on a baseline URANS model could be verified, and solutions could be proposed to ensure the desired performance, similarly to the PANS study by Ma and co-workers (2011).
- Strategies for the complete STRUCT approach could be investigated by using machine learning techniques together with available flow data. Those techniques could be utilized either to derive new complete formulations or to enhance the performance of the STRUCT-L or STRUCT-T ones through calibration. Interesting, relevant work has been performed on RANS closures (Duraisamy et al., 2015; Tracey et al., 2015).
- Coupling techniques could be implemented to provide a rigorous mathematical treatment of the boundary between regions with a different TKE ratio. Coupling methods for zonal hybrid models are reviewed by Sagaut, Deck, and Terracol (2013). In particular, appropriate synthetic eddy methods could be developed to inject fluctuations in flows moving from higher to lower fraction of modeled TKE. This approach is simpler to implement at inlet boundaries or pre-defined interfaces, as commonly done in ELES. It is more complex to inject resolved turbulence when the degree of resolution varies locally, as in STRUCT. Many successful hybrid models (e.g. DES, SAS) do not prescribe such a treatment, and STRUCT has demonstrated not to necessarily need it. Nevertheless, the introduction of these consistent methods would allow assessing the validity of the assumption that the high flow deformation is sufficient to enable the needed resolved instabilities.
- The STRUCT approach offers a particularly valuable approach to finding regions of significant flow deformation. This approach could naturally couple to the concept of local grid refinement and/or coarsening. The local character of the STRUCT activation criterion could be used to guide the grid adaptation. Such a technique could provide significant gains in efficiency, by concentrating the focus on the regions of higher deformation not only through the turbulence model, as in STRUCT, but also by optimizing computational grid requirements.
- The STRUCT approach was developed for high-Re turbulence analysis. Future work could relax this assumption extending the model to lower Reynolds number domains. This analysis could benefit studies of mixed and natural convection in which resolution of turbulent structures might offer significant advantages. This analysis was not included in this work, as it will require a very large and rigorous body of tests.

References

[1] Acton, M.J., Demarly, E., Lenci, G., Magolan, B., Baglietto, E., 2016. Analysis of flow-induced forces causing vibration in nuclear reactor fuel rods using the STRUCT hybrid turbulence approach, In preparation for journal submission.

[2] Acton, M.J., Lenci, G., Baglietto, E., 2015. Structure-based resolution of turbulence for sodium fast reactor thermal striping applications, in: 16th International Topical Meeting on Nuclear Reactor Thermal Hydraulics (NURETH-16). Chicago, IL, USA.

[3] Adams, E., 2006. Water quality control (MIT course 1.77, Spring 2006) lecture notes.

[4] Ahmed, S.R., Ramm, G., Faltin, G., 1984. Some Salient Features Of The Time-Averaged Ground Vehicle Wake (No. 840300), SAE Technical Paper. doi:10.4271/840300

[5] Anderson, S.D., Eaton, J.K., 1987. Experimental study of a pressure-driven, three-dimensional, turbulent boundary layer. AIAA J. 25, 1086–1093.

[6] Apsley, D.D., Leschziner, M. a., 1998. A new low-Reynolds-number nonlinear two-equation turbulence model for complex flows. Int. J. Heat Fluid Flow 19, 209–222. doi:10.1016/S0142-727X(97)10007-8

[7] Argyropoulos, C.D., Markatos, N.C., 2014. Recent advances on the numerical modelling of turbulent flows. Appl. Math. Model. 39, 693–732. doi:10.1016/j.apm.2014.07.001

[8] Artemov, V., Beale, S.B., de Vahl Davis, G., Escudier, M.P., Fueyo, N., Launder, B.E., Leonardi, E., Malin, M.R., Minkowycz, W.J., Patankar, S.V., Pollard, A., Rodi, W., Runchal, A., Vanka, S.P., 2009. A tribute to D.B. Spalding and his contributions in science and engineering. Int. J. Heat Mass Transf. 52, 3884–3905. doi:10.1016/j.ijheatmasstransfer.2009.03.038

[9] Aubry, N., 1991. On the hidden beauty of the proper orthogonal decomposition. Theor. Comput. Fluid Dyn. 2, 339–352. doi:10.1007/BF00271473

[10] Ayhan, H., Sökmen, C.N., 2012. CFD modeling of thermal mixing in a T-junction geometry using les model. Nucl. Eng. Des. 253, 183–191. doi:10.1016/j.nucengdes.2012.08.010

[11] Baglietto, E., 2013. Lecture notes from the course: Applied Computational Fluid Dynamics and Heat Transfer, MIT, class 22.315.

[12] Baglietto, E., Ninokata, H., 2007. Improved turbulence modeling for performance evaluation of novel fuel designs. Nucl. Technol. 158, 237–248.

[13] Baglietto, E., Ninokata, H., 2006. Anisotropic Eddy Viscosity Modeling for Application to Industrial Engineering Internal Flows. Int. J. Transp. Phenom. 8, 85–101.

[14] Bargsten, C.J., Gibson, M.T., 2011. NASA Innovation in Aeronautics.

[15] Basara, B., Krajnovic, S., Girimaji, S., Pavlovic, Z., 2011. Near-Wall Formulation of the Partially Averaged Navier Stokes Turbulence Model. AIAA J. 49, 2627–2636. doi:10.2514/1.J050967

[16] Basu, D., Hamed, A., Das, K., 2007. Assessment of partially averaged Navier Stokes (PANS) multiscale model in transonic turbulent separated flows, in: 5th Joint ASME/JSME Fluids Engineering Conference. pp. 1–9. doi:10.1115/FEDSM2007-37630

[17] Batten, P., Goldberg, U., Chakravarthy, S., 2002. LNS - An Approach Towards Embedded LES, in: 40th AIAA Aerospace Sciences Meeting and Exhibit.

[18] Batten, P., Goldberg, U., Chakravarthy, S., 2000. Sub-grid turbulence modeling for unsteady flow with acoustic resonance, in: Proceedings of the 38th Aerospace Sciences Meeting & Exhibit. Reno, NV, USA, pp. 1–8.

[19] Berdanier, R.A., 2011. Turbulent flow through an asymmetric plane diffuser, Class report, AAE 626. West Lafayette, IN, USA.

[20] Bhushan, S., Walters, D.K., 2012. A dynamic hybrid Reynolds-averaged Navier Stokes-Large eddy simulation modeling framework. Phys. Fluids 24. doi:10.1063/1.3676737

[21] Borges, J.L., 1999. On Exactitude in Science, in: Collected Fictions. p. 325.

[22] Bourguet, R., Braza, M., Harran, G., El Akoury, R., 2008. Anisotropic Organised Eddy Simulation for the prediction of non-equilibrium turbulent flows around bodies. J. Fluids Struct. 24, 1240–1251. doi:10.1016/j.jfluidstructs.2008.07.004

[23] Boussinesq, J., 1877. Essai sur la théorie des eaux courantes. Mémoires présentés par Divers savants à l'académie des Sci. l'institut Fr. 23-24, 1–680.

[24] Buice, C.U., 1997. Experimental investigation of flow through an asymmetric plane diffuser. Stanford University.

[25] Carati, B.D., Wray, A., Cabot, W., 1996. Ensemble averaged dynamic modeling. Cent. Turbul. Res. Proc. Summer Progr.

[26] CD-adapco, 2015. STAR-CCM+ User Manual.

[27] Chaouat, B., Schiestel, R., 2013. Partially integrated transport modeling method for turbulence simulation with variable filters. Phys. Fluids 25, 1–39. doi:10.1063/1.4833235

[28] Chaouat, B., Schiestel, R., 2005. A new partially integrated transport model for subgrid-scale stresses and dissipation rate for turbulent developing flows. Phys. Fluids 17, 1–19. doi:10.1063/1.1928607

[29] Chapman, D.R., 1979. Computational aerodynamics development and outlook. AIAA J. 17, 1293–1313. doi:10.2514/3.61311

[30] Chester, S., Charlette, F., Meneveau, C., 2001. Dynamic Model for LES Without Test Filtering: Quantifying the Accuracy of Taylor Series Approximations. Theor. Comput. Fluid Dyn. 15, 165–181. doi:10.1007/PL00013289

[31] Cokljat, D., Caridi, D., Link, G., Lechner, R., Menter, F., 2009. Embedded LES Methodology for General-Purpose CFD Solvers, in: Proceedings of 6th International Symposium on Turbulence and Shear Flow Phenomena. Seoul, Korea.

[32] Concu, D., 2016. Personal communication.

[33] Craft, T.J., Gant, S.E., Gerasimov, A. V, Iacovides, H., Launder, B.E., 2006. Development and application of wall-function treatments for turbulent forced and mixed convection flows. Fluid Dyn. Res. 38, 127–144. doi:10.1016/j.fluiddyn.2004.11.002

[34] Davidson, L., 2014. The PANS model in a zonal hybrid RANS–LES formulation. Int. J. Heat Fluid Flow 46, 112–126. doi:10.1016/j.ijheatfluidflow.2014.01.002

[35] Davidson, L., 2006. Evaluation of the SST-SAS model: Channel flow, asymmetric diffuser and axi-symmetric hill, in: Proceedings of the European Conference on Computational Fluid Dynamics (ECCOMAS CFD 2006). Egmond aan Zee, The Netherlands, pp. 1–20.

[36] Deardorff, J.W., 1980. Stratocumulus-capped mixed layers derived from a three-dimensional model. Boundary-Layer Meteorol. 18, 495–527. doi:10.1007/BF00119502

[37] Deardorff, J.W., 1974. Three-dimensional numerical study of the height and mean structure of a heated planetary boundary layer. Boundary-Layer Meteorol. 7, 199–226.

[38] Deardorff, J.W., 1970. A numerical study of three-dimensional turbulent channel flow at large Reynolds numbers. J. Fluid Mech. doi:10.1017/S0022112070000691

[39] Demuren, A., Rodi, W., 1984. Calculation of turbulence-driven secondary motion in non-circular ducts. J. Fluid Mech. 140, 189–222. doi:10.1017/S0022112084000574

[40] Ducru, P., Lenci, G., Abi Akl, R., Baglietto, E., 2016. Properties of a diffusive Lagrangian averaging operator for transported quantities, In preparation for journal submission.

[41] Duraisamy, K., Zhang, Z.J., Anand, P.S., 2015. New Approaches in Turbulence and Transition Modeling Using Data-driven Techniques, in: 53rd AIAA Aerospace Sciences Meeting. Kissimmee, FL, USA, pp. 1–14. doi:doi:10.2514/6.2015-1284

[42] Durbin, P. a., 1991. Near-wall turbulence closure modeling without "damping functions." Theor. Comput. Fluid Dyn. 3, 1–13. doi:10.1007/BF00271513

[43] Durbin, P., Pettersson Reif, B., 2011. Statistical theory and modeling for turbulent flows, 2nd ed. John Wiley and Sons, Ltd., Chichester, United Kingdom.

[44] Egorov, Y., Menter, F., 2008. Development and application of SST-SAS turbulence model in the DESIDER project, in: Notes on Numerical Fluid Mechanics and Multidisciplinary Design. pp. 261–270. doi:10.1007/978-3-540-77815-8_27

[45] Egorov, Y., Menter, F.R., Lechner, R., Cokljat, D., 2010. The Scale-Adaptive Simulation Method for Unsteady Turbulent Flow Predictions. Part 2: Application to Complex Flows. Flow Turbul. Combust. 85, 139–165. doi:10.1007/s10494-010-9265-4

[46] Elmahdi, A.M., Lu, R., Conner, M.E., Karoutas, Z., Baglietto, E., 2011. Flow Induced Vibration Forces on a Fuel Rod by LES CFD Analysis, in: 14th International Topical Meeting on Nuclear Reactor Thermal Hydraulics (NURETH-14). Toronto, ON, Canada, pp. 1–12.

[47] Elmiligui, A., Abdol-Hamid, K., Massey, S., Pao, S., 2004. Numerical Study of Flow Past a Circular Cylinder Using RANS, Hybrid RANS/LES and PANS Formulations. 22nd Appl. Aerodyn. Conf. Exhib. 1–18. doi:10.2514/6.2004-4959

[48] ESI, 2016. CFD Solutions [WWW Document]. URL http://cloud.esi-group.com/cfd (accessed 1.1.16).

[49] Euler, L., 1757. Principes generaux du mouvement des fluides. Mémoires l'Académie Sci. Berlin 11, 274–315.

[50] Evans, M.W., Harlow, F.H., 1957. The Particle-in-Cell Method for Hydrodynamic Calculations (No. LA-2139), Science (New York, N.Y.).

[51] Fadai-Ghotbi, A., Friess, C., Manceau, R., Borée, J., 2010a. A seamless hybrid RANS-LES model based on transport equations for the subgrid stresses and elliptic blending. Phys. Fluids 22, 1–19. doi:10.1063/1.3415254

[52] Fadai-Ghotbi, A., Friess, C., Manceau, R., Gatski, T.B., Borée, J., 2010b. Temporal filtering: A consistent formalism for seamless hybrid RANS-LES modeling in inhomogeneous turbulence. Int. J. Heat Fluid Flow 31, 378–389. doi:10.1016/j.ijheatfluidflow.2009.12.008

[53] Farge, M., Kevlahan, N., Perrier, V., Schneider, K., 1999. Turbulence analysis, modelling and computing using wavelets, in: Wavelets in Physics. pp. 117–200.

[54] Fasel, H.F., Seidel, J., Wernz, S., 2002. A methodology for simulations of complex turbulent flows. J. Fluids Eng. 124, 933. doi:10.1115/1.1517569

[55] Ferziger, J.H., Perić, M., 2002. Computational Methods for Fluid Dynamics, Springer. Springer-Verlag Berlin Heidelberg.

[56] Friess, C., Manceau, R., Gatski, T.B., 2015. Toward an equivalence criterion for Hybrid RANS/LES methods. Comput. Fluids. doi:10.1016/j.compfluid.2015.08.010

[57] Fröhlich, J., Von Terzi, D., 2008. Hybrid LES/RANS methods for the simulation of turbulent flows. Prog. Aerosp. Sci. 44, 349–377. doi:10.1016/j.paerosci.2008.05.001

[58] Gant, S.E., 2010. Reliability issues of LES-related approaches in an industrial context. Flow, Turbul. Combust. 84, 325–335. doi:10.1007/s10494-009-9237-8

[59] Garde, R.J., 1997. Turbulent Flow. John Wiley and Sons, Ltd., New York, NY, USA.

[60] Gatski, T.B., Speziale, C.G., 1993. On explicit algebraic stress models for complex turbulent flows. J. Fluid Mech. 254, 59–78. doi:10.1017/S0022112093002034

[61] Gelineau, O., Sperandio, M., Martin, P., Ricard, J.B., Martin, L., Bougault, A., 1994. Thermal Fluctuation Problems encountered in LMFRs, in: IAEA-IWGFR Specialists' Meeting on Correlation between Material Properties and Thermohydraulics Conditions in LMFRs. Aix-en-Provence, France, pp. 38–46.

[62] George, W.K., 2010. Lectures in Turbulence for the 21st Century, Imperial College of London and Chalmers University of Tecnhology. London, UK and Gothenburg, Sweden.

[63] Germano, M., 2015. On the hybrid RANS-LES of compressible flows. Notes Numer. Fluid Mech. Multidiscip. Des. 130, 253–263. doi:10.1007/978-3-642-31818-4

[64] Germano, M., 2000. Fundamentals of large eddy simulation, in: Advanced Turbulent Flow Computations. Springer, Vienna, Austria, pp. 81–130.

[65] Germano, M., 1999. From RANS to DNS: Towards a bridging Model, in: Direct and Large-Eddy Simulation III. Springer, pp. 225–236.

[66] Germano, M., 1992. Turbulence - The filtering approach. J. Fluid Mech. 238, 325–336. doi:10.1017/S0022112092001733

[67] Germano, M., 1986. A proposal for a redefinition of the turbulent stresses in the filtered Navier–Stokes equations. Phys. Fluids 29, 2323–2324. doi:10.1063/1.865568

[68] Germano, M., Piomelli, U., Moin, P., Cabot, W.H., 1991. A dynamic subgrid-scale eddy viscosity model. Phys. Fluids A Fluid Dyn. 3, 1760–1765. doi:10.1063/1.857955

[69] Geurts, B.J., 2006. Interacting errors in large-eddy simulation: a review of recent developments. J. Turbul. 7, 1–16. doi:10.1080/14685240600796507

[70] Girimaji, S., Abdol-Hamid, K., 2005. Partially-Averaged Navier Stokes Model for Turbulence: Implementation and Validation, in: 43rd AIAA Aerospace Sciences Meeting and Exhibit. pp. 1–14. doi:10.2514/6.2005-502

[71] Girimaji, S.S., 2006. Partially-Averaged Navier-Stokes Model for Turbulence: A Reynolds-Averaged Navier-Stokes to Direct Numerical Simulation Bridging Method. J. Appl. Mech. doi:10.1115/1.2151207

[72] Girimaji, S.S., Jeong, E., Srinivasan, R., 2006. Partially Averaged Navier-Stokes Method for Turbulence: Fixed Point Analysis and Comparison With Unsteady Partially Averaged Navier-Stokes. J. Appl. Mech. doi:10.1115/1.2173677

[73] Girimaji, S.S., Srinivasan, R., Jeong, E., 2003. PANS Turbulence model for seamless transition between RANS and LES: fixed-point analysis and preliminary results, in: Proceedings of the 4th ASME-JSME Joint Fluids Engineering Conference. Honolulu, HI, USA, pp. 1–9.

[74] Gopalan, H., Jaiman, R., 2015. Numerical study of the flow interference between tandem cylinders employing non-linear hybrid URANS–LES methods. J. Wind Eng. Ind. Aerodyn. 142, 111–129. doi:10.1016/j.jweia.2015.03.017

[75] Gritskevich, M.S., Garbaruk, A. V., Frank, T., Menter, F.R., 2014. Investigation of the thermal mixing in a T-junction flow with different SRS approaches. Nucl. Eng. Des. 279, 83–90. doi:10.1016/j.nucengdes.2014.03.010

[76] Gritskevich, M.S., Garbaruk, A. V., Schütze, J., Menter, F.R., 2011. Development of DDES and IDDES Formulations for the k-ω Shear Stress Transport Model. Flow, Turbul. Combust. 88, 431–449. doi:10.1007/s10494-011-9378-4

[77] Hedges, L.S., Travin, a. K., Spalart, P.R., 2002. Detached-Eddy Simulations Over a Simplified Landing Gear. J. Fluids Eng. 124, 413. doi:10.1115/1.1471532

[78] Heinz, S., 2007. Unified turbulence models for les and RANS, FDF and PDF simulations. Theor. Comput. Fluid Dyn. 21, 99–118. doi:10.1007/s00162-006-0036-8

[79] Hellsten, A., Wallin, S., 2009. Explicit algebraic Reynolds stress and non-linear eddy-viscosity models. Int. J. Comut. Fluid Dyn. 23, 349–361. doi:10.1080/10618560902776828

[80] Hong, J., Toloui, M., Chamorro, L.P., Guala, M., Howard, K., Riley, S., Tucker, J., Sotiropoulos, F., 2014. Natural snowfall reveals large-scale flow structures in the wake of a 2.5-MW wind turbine. Nat. Commun. 5, 4216. doi:10.1038/ncomms5216

[81] Hu, L.-W., Kazimi, M.S., 2006. LES benchmark study of high cycle temperature fluctuations caused by thermal striping in a mixing tee. Int. J. Heat Fluid Flow 27, 54–64. doi:10.1016/j.ijheatfluidflow.2005.08.001

[82] Hudgins, L., Kaspersen, J.H., 2004. Wavelets and detection of coherent structures in fluid turbulence, in: Wavelets in Physics. Cambridge University Press, Cambridge, UK, pp. 201–226.

[83] Hunt, J.C.R., Carruthers, D.J., 1990. Rapid distortion theory and the “problems” of turbulence. J. Fluid Mech. 212, 497–529. doi:10.1017/S0022112090002075

[84] Hunt, J.C.R., Wray, A.A., Moin, P., 1988. Eddies, streams, and convergence zones in turbulent flows, in: Center for Turbulence Research, Proceedings of the Summer Program. Stanford, CA, USA, pp. 193–208. doi:CTR-S88

[85] Hussain, A.K.M.F., 1986. Coherent structures and turbulence. J. Fluid Mech. 173, 303–356. doi:10.1017/S0022112086001192

[86] Hussain, A.K.M.F., 1983. Coherent structures - Reality and myth. Phys. Fluids 26, 2816–2850. doi:10.1063/1.864048

[87] Jansen, K.E., 1999. A stabilized finite element method for computing turbulence. Comput. Methods Appl. Mech. Eng. 174, 299–317. doi:10.1016/S0045-7825(98)00301-6

[88] Jayaraju, S.T., Komen, E.M.J., Baglietto, E., 2010. Suitability of wall-functions in Large Eddy Simulation for thermal fatigue in a T-junction. Nucl. Eng. Des. doi:10.1016/j.nucengdes.2010.05.026

[89] Jayaraju, S.T., Sathiah, P., Komen, E.M.J., Baglietto, E., 2013. Large Eddy Simulation for an inherent boron dilution transient. Nucl. Eng. Des. 262, 484–498. doi:10.1016/j.nucengdes.2013.05.024

[90] Jeong, E., Girimaji, S.S., 2010. Partially Averaged Navier–Stokes (PANS) Method for Turbulence Simulations: Flow Past a Square Cylinder. J. Fluids Eng. doi:10.1115/1.4003154

[91] Johansen, S.T., Wu, J., Shyy, W., 2004. Filter-based unsteady RANS computations. Int. J. Heat Fluid Flow 25, 10–21. doi:10.1016/j.ijheatfluidflow.2003.10.005

[92] Jones, W., Launder, B., 1972. The prediction of laminarization with a two-equation model of turbulence. Int. J. Heat Mass Transf. 15, 301–314.

[93] Kassinos, S.C., Reynolds, W.C., 1997. Advances in structure-based turbulence modeling. Cent. Turbul. Res. Annu. Res. Briefs 179–193.

[94] Kevlahan, N.K.-R., Hunt, J.C.R., Vassilicos, J.C., 1994. A comparison of different analytical techniques for identifying structures in turbulence. Appl. Sci. Res. 53, 339–355. doi:10.1007/BF00849109

[95] Kewlani, G., 2015. Personal communication.

[96] Kewlani, G., 2014. Large Eddy Simulations of Premixed Turbulent Flame Dynamics: Combustion Modeling, Validation and Analysis. Massachusetts Institute of Technology.

[97] Kim, J.H., Roidt, R.M., Deardorff, A.F., 1993. Thermal stratification and reactor piping integrity. Nucl. Eng. Des. 139, 83–95. doi:10.1016/0029-5493(93)90263-9

[98] Kobayashi, H., 2005. The subgrid-scale models based on coherent structures for rotating homogeneous turbulence and turbulent channel flow. Phys. Fluids 17, 2350–2360. doi:10.1063/1.1874212

[99] Kolmogorov, A.N., 1942. Equations of Turbulent Motion of an Incompressible Fluid. Izv. Acad. Sci. USSR; Phys. 6, 56–58. doi:10.1007/978-94-011-3030-1_48

[100] Kolmogorov, A.N., 1941. The local structure of turbulence in incompressible viscous fluid for very large Reynolds number. Proc. USSR Acad. Sci.

[101] Lakshmipathy, S., Girimaji, S.S., 2010. Partially Averaged Navier–Stokes (PANS) Method for Turbulence Simulations: Flow Past a Circular Cylinder. J. Fluids Eng. doi:10.1115/1.4003154

[102] Launder, B., Sharma, B., 1974. Application of the energy-dissipation model of turbulence to the calculation of flow near a spinning disc. Lett. heat mass Transf. 1, 131–137.

[103] Launder, B., Spalding, D., 1974. The numerical computation of turbulent flows. Comput. Methods Appl. Mech. Eng. 3, 269–289. doi:10.1016/0045-7825(74)90029-2

[104] Launder, B.E., Reece, G.J., Rodi, W., 1975. Progress in the development of a Reynolds-stress turbulence closure. J. Fluid Mech. 68, 537–566. doi:10.1017/S0022112075001814

[105] Lee, M.J., Kim, J., Moin, P., 1990. Structure of turbulence at high shear rate. J. Fluid Mech. 216, 561–583.

[106] Leonard, A., 1974. Energy Cascade in large-eddy simulations of turbulent fluid flows. Adv. Geophys 18A, 237–248.

[107] Leonard, B.P., 1988. Simple high-accuracy resolution program for convective modelling of discontinuities. Int. J. Numer. Methods Fluids 8, 1291–1318. doi:10.1002/fld.1650081013

[108] Lesieur, M., Mankbadi, R.R., 1988. Turbulence in Fluids. J. Appl. Mech. doi:10.1115/1.3173656

[109] Lien, F., Chen, W., Leschziner, M., 1996. Low-Reynolds-number eddy-viscosity modelling based on non-linear stress-strain/vorticity relations, in: Proceedings of the 3rd Symposium on Engineering Turbulence Modelling and Experiments. Crete, Greece, pp. 91–100.

[110] Lienhart, H., Becker, S., 2003. Flow and Turbulence Structure in the Wake of a Simplified Car Model. Notes Numer. Fluid Mech. 77. doi:10.4271/2003-01-0656

[111] Liu, J., Zuo, Z., Wu, Y., Zhuang, B., Wang, L., 2014. A nonlinear Partially-Averaged Navier-Stokes model for turbulence. Comput. fluids 102, 32–40. doi:10.1016/j.compfluid.2014.06.016

[112] Lumley, J.L., 1992. Some comments on turbulence. Phys. Fluids A Fluid Dyn. 4, 203. doi:10.1063/1.858347

[113] Lumley, J.L., 1978. Computational Modeling of Turbulent Flows. Adv. Appl. Mech. 18, 123–176.

[114] Lumley, J.L., 1970. Toward a turbulent constitutive relation. J. Fluid Mech. 41, 413. doi:10.1017/S0022112070000678

[115] Luo, D., Yan, C., Liu, H., Zhao, R., 2014. Comparative assessment of PANS and DES for simulation of flow past a circular cylinder. Jnl. Wind Eng. Ind. Aerodyn. 134, 65–77. doi:10.1016/j.jweia.2014.08.014

[116] Lyn, D. a., Einav, S., Rodi, W., Park, J.-H., 1995. A laser-Doppler velocimetry study of ensemble-averaged characteristics of the turbulent near wake of a square cylinder. J. Fluid Mech. 304, 285–319. doi:10.1017/S0022112095004435

[117] Ma, J.M., Peng, S.H., Davidson, L., Wang, F.J., 2011. A low Reynolds number variant of partially-averaged Navier-Stokes model for turbulence. Int. J. Heat Fluid Flow 32, 652–669. doi:10.1016/j.ijheatfluidflow.2011.02.001

[118] Marmanis, H., 1998. Analogy between the Navier–Stokes equations and Maxwell's equations: Application to turbulence. Phys. Fluids 10, 1428. doi:10.1063/1.869762

[119] Mathieu, J., Scott, J., 2000. An introduction to turbulent flow, Cambridge University Press. doi:10.1088/1468-5248/2/1/702

[120] Meneveau, C., 2010. Turbulence: Subgrid-Scale Modeling. Scholarpedia 5, 1–12. doi:10.4249/scholarpedia.9489

[121] Meneveau, C., Katz, J., 2000. Scale invariance and turbulence models for large-eddy simulation. Annu. Rev. Fluid Mech. 32, 1–32.

[122] Meneveau, C., Lund, T.S., Cabot, W.H., 1996. A Lagrangian dynamic subgrid-scale model of turbulence. J. Fluid Mech. 319, 353. doi:10.1017/S0022112096007379

[123] Menter, F., 2012. Best Practice: Scale-Resolving Simulations in ANSYS CFD. ANSYS Inc 1–70.

[124] Menter, F., 1992. Improved two-equation k-omega turbulence models for aerodynamic flows (No. 103975), NASA Technical Memorandum, NASA Technical Memorandum.

[125] Menter, F., Kuntz, M., 2004. Adaptation of eddy-viscosity turbulence models to un- steady separated flow behind vehicles, in: The Aerodynamics of Heavy Vehicles: Trucks, Buses, and Trains. pp. 339–352.

[126] Menter, F.R., 1994. Two-equation eddy-viscosity turbulence models for engineering applications. AIAA J. 32, 1598–1605. doi:10.2514/3.12149

[127] Menter, F.R., Egorov, Y., 2010. The scale-adaptive simulation method for unsteady turbulent flow predictions. part 1: Theory and model description. Flow, Turbul. Combust. 85, 113–138. doi:10.1007/s10494-010-9264-5

[128] Menter, F.R., Kuntz, M., Bender, R., 2003. A scale-adaptive simulation model for turbulent flow

predictions, in: 41st Aerospace Sciences Meeting and Exhibit. Reno, NV, USA, pp. 1–11. doi:10.2514/6.2003-767

[129] Merzari, E., Khakim, A., Ninokata, H., Baglietto, E., 2009. Unsteady Reynolds-averaged Navier-Stokes: toward accurate prediction of turbulent mixing phenomena. Int. J. Process Syst. Eng. doi:10.1504/IJPSE.2009.028003

[130] Moin, P., Mahesh, K., 1998. DIRECT NUMERICAL SIMULATION: A Tool in Turbulence Research. Annu. Rev. Fluid Mech. 30, 539–578. doi:10.1146/annurev.fluid.30.1.539

[131] Moureau, V., Lartigue, G., Sommerer, Y., Angelberger, C., Colin, O., Poinsot, T., 2005. Numerical methods for unsteady compressible multi-component reacting flows on fixed and moving grids. J. Comput. Phys. 202, 710–736. doi:10.1016/j.jcp.2004.08.003

[132] Muschinski, A., 1996. A similarity theory of locally homogeneous and isotropic turbulence generated by a Smagorinsky-type LES. J. Fluid Mech. 325, 239–260. doi:10.1017/S0022112096008105

[133] Navier, C.L.M.H., 1822. Mémoire sur les lois du mouvement des fluides. Mémoires l'Académie des Sci. l'Institut Fr. 6, 389–416.

[134] Nelkin, M., 1992. In what sense is turbulence an unsolved problem? Science (80-.). 255.

[135] Newton, I., 1687. Philosophiæ Naturalis Principia Mathematica, Book II. Londini: Jussu Societatis Regiae ac Typis Josephi Streater. Prostat apud plures bibliopolas.

[136] Nicoud, F., Ducros, F., 1999. Subgrid-Scale Stress Modelling Based on the Square of the Velocity Gradient Tensor. Flow, Turbul. Combust. 62, 183–200.

[137] Nisizima, S., Yoshizawa, A., 1987. Turbulent channel and Couette flows using an anisotropic k-epsilon model. AIAA J. 25, 414–420. doi:10.2514/3.9639

[138] Obi, S., Aoki, K., Masuda, S., 1993. Experimental and computational study of turbulent separating flow in an asymmetric plane diffuser, in: 9th Symp Turbulent Shear Flows. pp. 1–4.

[139] Patankar, S.., Spalding, D.., 1972. A calculation procedure for heat, mass and momentum transfer in three-dimensional parabolic flows. Int. J. Heat Mass Transf. 15, 1787–1806. doi:10.1016/0017-9310(72)90054-3

[140] Pattison, M.J., 2011. Secondary flows [WWW Document]. A-to-Z Guid. to Thermodyn. Heat Mass Transf. Fluids Eng. doi:10.1615/AtoZ.s.secondary_flows

[141] Pecnik, R., O'Sullivan, J.P., Panagiotou, K., Radhakrishnan, H., Kassinos, S., Duraisamy, K., Iaccarino, G., 2012. Towards an Accurate and Robust Algebraic Structure Based Model, in: Center for Turbulence Research: Proceedings of the Summer Program. pp. 283–293.

[142] Peniguel, C., Sakiz, M., Benhamadouche, S., Stephan, J., Vindeirinho, C., 2003. Presentation of a Numerical 3D Approach to Tackle Thermal Striping in a PWR Nuclear T-Junction, in: Proceedings of the 2003 ASME Pressure Vessels and Piping Conference. Cleveland, OH, USA, pp. 1–8. doi:10.1115/PVP2003-2191

[143] Perot, B., 1999. Turbulence modeling using body force potentials. Phys. Fluids 11, 2645–2656. doi:10.1063/1.870126

[144] Perot, B.J., Gadebusch, J., 2007. A self-adapting turbulence model for flow simulation at any mesh resolution. Phys. Fluids 19, 1–11. doi:10.1063/1.2780195

[145] Pont, G., Cinnella, P., Robinet, J., Brenner, P., 2014. Assessment of automatic Hybrid RANS/LES Models for Industrial CFD, in: 32nd AIAA Applied Aerodynamics Conference AIAA. Atlanta, GA, USA, pp. 1–16.

[146] Pope, S., 2000. Turbulent flows. Cambridge University Press. doi:10.1017/CBO9780511840531

[147] Pope, S.B., 1975. A more general effective-viscosity hypothesis. J. Fluid Mech. doi:10.1017/S0022112075003382

[148] Popper, K.R., 1935. Logik der Forschung Zur Erkenntnistheorie der modernen Naturwissenschaft, Schriften zur wissenschaftlichen Weltauffassung.

[149] Prandtl, L., 1945. Uber ein neues Formelsystem fur die ausgebildete Turbulenz. Nachr. Acad. Wiss. Gottingen Math-Phys K1, 6–19.

[150] Prandtl, L., 1925. Bericht uber Untersuchungen zur ausgebildeten Turbulenz. Zs. angew. Math. Mech. 5, 136–139.

[151] Prandtl, L., 1904. ber Flüssigkeitsbewegung bei sehr kleiner Reibung, in: Verhandlungen Des Dritten Internationalen MathematikerKongresses. pp. 484–491.

[152] Reynolds, O., 1895. On the dynamical theory of incompressible viscous fluid and the determination of the criterion. Philos. Trans. R. Soc. London.

[153] Reynolds, O., 1883. An Experimental Investigation of the Circumstances Which Determine Whether the Motion of Water Shall Be Direct or Sinuous, and of the Law of Resistance in Parallel Channels. Philos. Trans. R. Soc. London. doi:10.1098/rstl.1883.0029

[154] Reynolds, W.C., 1976. Computation of turbulent flows. Annu. Rev. Fluid Mech. 183–208.

[155] Rhie, C.., Chow, W.L., 1983. Numerical Study of the Turbulent Flow Past an Airfoil with Trailing Edge Separation. AIAA J. 21, 1525–1532.

[156] Richardson, L.F., 1922. Weather prediction by numerical process.

[157] Robinson, S.K., 1991. Coherent motions in the turbulent boundary layer. Annu. Rev. Fluid Mech. 23, 601–639. doi:10.1146/annurev.fluid.23.1.601

[158] Rodi, W., 1976. A new algebraic relation for calculating the Reynolds stresses. Gesellschaft Angew. Math. und Mech. Work. Paris Fr. 56, 219.

[159] Rotta, J., 1951. Statistische theorie nichthomogener turbulenz. Zeitschrift für Phys. 129, 547–572. doi:10.1007/BF01330059

[160] Rotta, J.C., 1968. Uber eine Methode zur Berechnung turbulenter Scherstromungen. Aerodyn. Versuchanstalt Gottingen, Rep 69 A.

[161] Rousseaux, G., Seifer, S., Steinberg, V., Wiebel, A., 2007. On the Lamb vector and the hydrodynamic charge. Exp. Fluids 42, 291–299. doi:10.1007/s00348-006-0238-2

[162] Rubinstein, R., Barton, J.M., 1990. Nonlinear Reynolds stress models and the renormalization group. Phys. Fluids A Fluid Dyn. 2, 1472. doi:10.1063/1.857595

[163] Sagaut, P., 2006. Large eddy simulation for incompressible flows: an introduction. Springer-Verlag Berlin and Heidelberg GmbH & Co. K. doi:10.1007/b137536

[164] Sagaut, P., Deck, S., Terracol, M., 2013. Multiscale And Multiresolution Approaches in Turbulence, 2nd editio. ed. Imperial College Press, London, UK. doi:10.1142/9781860948978

[165] Schiestel, R., Dejoan, A., 2005. Towards a new partially integrated transport model for coarse grid and unsteady turbulent flow simulations. Theor. Comput. Fluid Dyn. 18, 443–468. doi:10.1007/s00162-004-0155-z

[166] Schlichting, H., 1979. Boundary-Layer Theory, 7th ed. McGraw-Hill, New York, NY, USA.

[167] Schumann, U., 1977. Realizability of Reynolds-stress turbulence models. Phys. Fluids 20, 721.

doi:10.1063/1.861942

[168] Shih, T., Liu, N., 2008. Assessment of the Partially Resolved Numerical Simulation (PRNS) Approach in the National Combustion Code (NCC) for Turbulent Nonreacting and Reacting Flows (No. NASA/TM-2008-215418).

[169] Shih, T., Zhu, J., Lumley, J.L., 1993. A Realizable Reynolds Stress Algebraic Equation Model (No. 105993), Nasa Technical Memorandum, NASA Technical Memorandum.

[170] Shih, T.-H., Liou, W.W., Shabbir, A., Yang, Z., Zhu, J., 1995. A new k-ϵ eddy viscosity model for high reynolds number turbulent flows. Comput. Fluids 24, 227–238. doi:10.1016/0045-7930(94)00032-T

[171] Shih, T.-H., Liu, N.-S., 2004. Partially resolved numerical simulation. From RANS towards LES for engine turbulent flows, in: 42nd AIAA Aerospace Sciences Meeting & Exhibit, Reno, NV, USA. pp. 1–14.

[172] Shima, E., Kitamura, K., Haga, T., 2013. Green–Gauss/Weighted-Least-Squares Hybrid Gradient Reconstruction for Arbitrary Polyhedra Unstructured Grids. AIAA J. 51, 2740–2747. doi:10.2514/1.J052095

[173] Shur, M., Spalart, P., Strelets, M., Travin, A., 1999. Detached-eddy simulation of an airfoil at high angle of attack. Eng. Turbul. Model. Exp. 4, 669–678.

[174] Shur, M.L., Spalart, P.R., Strelets, M.K., Travin, A.K., 2008. A hybrid RANS-LES approach with delayed-DES and wall-modelled LES capabilities. Int. J. Heat Fluid Flow 29, 1638–1649. doi:10.1016/j.ijheatfluidflow.2008.07.001

[175] Simpson, R.L., 1981. Review—A Review of Some Phenomena in Turbulent Flow Separation. J. Fluids Eng. doi:10.1115/1.3241761

[176] Slotnick, J., Khodadoust, A., Alonso, J., Darmofal, D., Gropp, W., Lurie, E., Mavriplis, D., 2014. CFD Vision 2030 Study: A Path to Revolutionary Computational Aerosciences, Nasa Cr-2014-21878.

[177] Smagorinsky, J., 1963. General circulation experiments wiht the primitive equations I. The basic experiment. Mon. Weather Rev. 91, 99–164. doi:10.1126/science.27.693.594

[178] Smith, B.L., Mahaffy, J.H., Angele, K., Westin, J., 2011. Report of the OECD/NEA-Vattenfall T-Junction Benchmark exercise (No. NEA/CSNI/R(2011)5).

[179] Song, C.-S., Park, S.-O., 2009. Numerical simulation of flow past a square cylinder using Partially-Averaged Navier–Stokes model. J. Wind Eng. Ind. Aerodyn. 97, 37–47. doi:10.1016/j.jweia.2008.11.004

[180] Spalart, P., Jou, W.-H., Strelets, M.K., Allmaras, S., 1997. Comments on the feasibility of LES for wings, and on a hybrid RANS/LES approach, in: Proceedings of the First AFOSR International Conference on DNS/LES, Advances in DNS/LES. Ruston, LA, USA, pp. 137–147.

[181] Spalart, P.R., 2015. Philosophies and fallacies in turbulence modeling. Prog. Aerosp. Sci. 74, 1–15. doi:10.1016/j.paerosci.2014.12.004

[182] Spalart, P.R., 2009. Detached-Eddy Simulation. Annu. Rev. Fluid Mech. 41, 181–202. doi:10.1146/annurev.fluid.010908.165130

[183] Spalart, P.R., 2000. Strategies for turbulence modelling and simulations. Int. J. Heat Fluid Flow 21, 252–263. doi:10.1016/S0142-727X(00)00007-2

[184] Spalart, P.R., Allmaras, S.R., 1992. A One-Equation Turbulence Model for Aerodynamic Flows, in: 30th Aerospace Sciences Meeting & Exhibit. Reno, NV, USA, pp. 1–22.

[185] Spalart, P.R., Deck, S., Shur, M.L., Squires, K.D., Strelets, M.K., Travin, a., 2006. A New Version of Detached-eddy Simulation, Resistant to Ambiguous Grid Densities. Theor. Comput. Fluid Dyn. 20, 181–195. doi:10.1007/s00162-006-0015-0

[186] Speziale, C.G., 1998. Turbulence Modeling for time-dependent RANS and VLES: A Review. AIAA J. 36, 173–184. doi:10.2514/3.14045

[187] Speziale, C.G., 1996. Computing non-equilibrium turbulent flows with time-dependent RANS and VLES, in: Proceedings of 15th International Conference on Numerical Methods in Fluid Dynamics. Monterey, CA, USA, pp. 1–7. doi:10.1007/BFb0107089

[188] Speziale, C.G., 1991. Analytical methods for the development of Reynolds-stress closures in turbulence. Annu. Rev. Fluid Mech. 23, 107–157. doi:10.1146/annurev.fluid.23.1.107

[189] Speziale, C.G., 1987. On nonlinear K-l and K -ε models of turbulence. J. Fluid Mech. 178, 459. doi:10.1017/S0022112087001319

[190] Stokes, G.G., 1845. On the Theories of the Internal Friction of Fluids in Motion, and of the Equilibrium and Motion of Elastic Solids. Trans. Cambridge Philos. Soc. 8, 287–319. doi:10.1017/CBO9780511702242

[191] Strelets, M., 2001. Detached Eddy Simulation of Massively Separated Flows, in: 39th Aerospace Sciences Meeting & Exhibit. Reno, NV, USA, pp. 1–18. doi:10.2514/6.2001-879

[192] Taamallah, S., LaBry, Z. a., Shanbhogue, S.J., Ghoniem, A.F., 2014. Correspondence Between Uncoupled Flame Macrostructures and Thermoacoustic Instability in Premixed Swirl-Stabilized Combustion. Proc. ASME Turbo Expo 2014 Turbine Tech. Conf. Expo. V04BT04A063. doi:10.1115/GT2014-27316

[193] Taylor, G.I., 1935. Statistical Theory of Turbulence. Proc. R. Soc. A Math. Phys. Eng. Sci. 151, 421–444. doi:10.1098/rspa.1935.0158

[194] Taylor, G.I., 1920. Diffusion by continuous movements. Proc. Lond. Math. Soc. Ser. 2, 196–212.

[195] Tennekes, H., Lumley, J.L., 1981. A First Course in Turbulence, MIT Press. ed. Cambridge, MA, USA. doi:10.1017/S002211207321251X

[196] Tokuhiro, A., Kimura, N., 1999. An experimental investigation on thermal striping Mixing phenomena of a vertical non-buoyant jet with two adjacent buoyant jets as measured by ultrasound Doppler velocimetry. Nucl. Eng. Des. 188, 49–73.

[197] Tracey, B.D., Duraisamy, K., Alonso, J.J., 2015. A Machine Learning Strategy to Assist Turbulence Model Development, in: 53rd AIAA Aerospace Sciences Meeting. Kissimmee, FL, USA, pp. 1–22. doi:doi:10.2514/6.2015-1287

[198] Travin, A., M.Shur, Spalart, P., Strelets, M., 2004. On URANS solutions with LES-like behaviour, in: Proceedings of ECCOMAS 2004. pp. 1–20.

[199] Travin, A., Shur, M., Strelets, M., Spalart, P.R., 2002. Physical and numerical upgrades in the detached-eddy simulation of complex turbulent flows. Adv. LES Complex Flows 239–254. doi:10.1007/0-306-48383-1_16

[200] Tryggeson, H., 2007. Analytical Vortex Solutions to the Navier-Stokes Equation, ActaWexionensia. Växjö University Press, Göteborg, Sweden.

[201] Venkatakrishnan, V., 1993. On the accuracy of limiters and convergence to steady state solutions, in: 31st Aerospace Sciences Meeting & Exhibit. Reno, NV, USA, pp. 1–10. doi:10.2514/6.1993-880

[202] von Kármán, T., 1930. Mechanische Ähnlichkeit und Turbulenz. Third Int. Congr. Appl. Mech.

Stock. 85–105.

[203] von Kármán, T., 1921. Uber Laminare und turbulente Reibung. Zeitschrift für Angew. Math. und Mech. 232. doi:10.1002/zamm.19210010401

[204] Wilcox, D., 1988. Reassessment of the scale-determining equation for advanced turbulence models. AIAA J. 26, 1299–1310. doi:10.2514/3.10041

[205] Wilcox, D.C., 1993. Turbulence Modeling for CFD. DCW Publishers, Inc., La Cañada, CA, USA.

[206] Wu, J., Zhou, Y., 1996. Reduced stress tensor and dissipation and the transport of lamb vector (No. 198307). Hampton, VA, USA.

[207] Zhang, J., 2016. Personal communication.

Appendix A: Additional discussions on equations

This appendix provides discussions on equations not covered in the text for the sake of brevity.

A.1 Link between $\overline{II}$ and Poisson's equation for pressure

Many properties of parameter $\overline{II}$ relevant to this work have been presented in Section 4.3. Here, another property is shown, related to the pressure field.

Let us take the divergence of the instantaneous momentum equation. The viscous term vanishes while the resulting equation becomes the following:

$$\boldsymbol{\nabla} \cdot (\boldsymbol{u} \cdot \boldsymbol{\nabla u}) = -\frac{1}{\rho}\boldsymbol{\nabla^2} p \tag{A.1}$$

Re-arranging (Lesieur and Mankbadi, 1988):

$$\frac{1}{2\rho}\boldsymbol{\nabla^2} p = II \tag{A.2}$$

The second invariant is therefore related to pressure through a Poisson's equation. Taking inspiration from the work by Marmanis (1998), we can make an analogy between this equation and the equation of electrostatics. Pressure corresponds to a potential, like voltage, and the second invariant corresponds to a charge, like an electric charge. Interesting analysis of turbulence modeling using potentials and the lamb vector was made by Perot (1999).

An operation similar to that for (A.2) applied to the resolved momentum equation in (2.8) yields:

$$\frac{1}{2\rho}\boldsymbol{\nabla^2}\bar{p} + \frac{1}{2}\frac{\partial^2 \tau_{ij}}{\partial x_i \partial x_j} = \overline{II} \tag{A.3}$$

This equation is similar to (A.2), except that a term containing the residual stress tensor appears in the LHS in addition to the resolved pressure term. High absolute values of $\overline{II}$, needed to define f_r, are expected to appear in regions of strong deformation. Those are regions with strong absolute values of either the resolved pressure "potential", or the contribution of residual stresses, except if those two terms cancel out.

A.2 Properties of the differential operator used in STRUCT-T

Properties of the operator used in STRUCT-T, shown in (8.5), have been investigated by Ducru, Lenci, Abi Akl, and Baglietto (2016). In particular, the mathematical contribution by the two colleagues at MIT Pablo Ducru and Rami Abi Akl has been significant in this investigation. The following sub-section show pages extracted from a manuscript in preparation for journal submission. Permission to show these contents here has been granted by the co-authors of the manuscript.

A.2.1 Definition of the diffusive Lagrangian average

The method presented here generalizes an equation that has been discussed by Germano (2000) as a potential technique for LES filtering. The goal here is to analyze this equation and investigate its properties that could be useful for addressing CFD challenges.

The equation analyzed here proposes to obtain a field $\langle f \rangle$, representing an average in both time and space along the characteristics, by solving for a damped convective-diffusive transport problem driven by a source f, which is the exact field.

The average $\langle f \rangle$ is defined as the solution to the following Vlasov-Poisson-Fokker-Planck problem:

$$\frac{\partial \langle f \rangle}{\partial t} + \boldsymbol{u} \cdot \boldsymbol{\nabla} \langle f \rangle = \boldsymbol{\nabla} \cdot \boldsymbol{\nabla} D \langle f \rangle + \frac{1}{T}(f - \langle f \rangle) \tag{A.4}$$

where D and T are respectively the fields of diffusion coefficients and of characteristic time-scale of the dampening of the system for the mean field $\langle f \rangle$. Let us note that for a given choice of initial and boundary conditions – which will be further discussed hereafter – the Cauchy-Lipschitz theorem ensures existence and uniqueness of the diffusive transport average.

With this definition for the average field $\langle f \rangle$, it is unnecessary to solve for the entire field f and then perform a weighting operation with a weight function g in order to solve for the average field. One only needs to solve directly for the convective-diffusive transport of the mean field, which presents major advantages when it comes to Computational Fluid Dynamics (CFD) since it enables the use of local transport solving techniques. The use of local operations requires significantly reduced computational power compared to explicit averaging.

A.2.2 Properties of the diffusive Lagrangian average

The following sub-sections present significant properties of the averaging operation in A.4.

Linearity

$\forall \ (f_1, f_2)$ scalar fields, and $\lambda \in \mathbb{C}$:

$$\langle \lambda f_1 + f_2 \rangle = \lambda \langle f_1 \rangle + \langle f_2 \rangle \tag{A.5}$$

This stems naturally from the linearity of eq. A.4.

Commutativity with differential operations

From Schwarz's theorem, and given f regularity conditions, differential operators commute with the diffusive transport averaging operator:

$$\frac{\partial}{\partial x_i} \langle f \rangle = \langle \frac{\partial f}{\partial x_i} \rangle, \qquad x_i \in (t, x, y, z) \tag{A.6}$$

Non-projection operator

It is important to notice that the diffusive transport averaging operation is not a projector. Thus, the average of the difference to the value is not zero:

$$\langle f - \langle f \rangle \rangle \neq 0_{\mathcal{F}} \tag{A.7}$$

Conservation of averaged quantity f

BALANCE EQUATIONS

For notation purposes, let $c = \langle f \rangle$. The use of the Green-Ostrodragski theorem yields the following balance equations between volumetric and surface quantities:

$$\forall t \in \mathbb{R}\,, \qquad \frac{\mathrm{d}}{\mathrm{d}t}\int_\Omega c - \int_\Omega \left(\frac{f-c}{T} - c\boldsymbol{\nabla}\cdot\boldsymbol{u}\right) = \int_{\partial\Omega} (D\boldsymbol{\nabla}c\cdot\boldsymbol{n} - c\boldsymbol{u}\cdot\boldsymbol{n}) \tag{A.8}$$

thus yielding the time-integrated:

$$\left[\int_\Omega c\right]_{T_{\text{in.}}}^{T_{\text{end}}} - \int_{T_{\text{in.}}}^{T_{\text{end}}}\int_\Omega \left(\frac{f-c}{T} - c\boldsymbol{\nabla}\cdot\boldsymbol{u}\right) = \int_{T_{\text{in.}}}^{T_{\text{end}}}\int_{\partial\Omega} (D\boldsymbol{\nabla}c\cdot\boldsymbol{n} - c\boldsymbol{u}\cdot\boldsymbol{n}) \tag{A.9}$$

IMPASSABLE BOUNDARY CONDITIONS AND DYNAMIC HYSTERESIS CONSERVATION

In the general case, Ω is an arbitrary control volume. However, the case of most interest is when this volume represents the frontier of a physical domain, which neither the fluid nor the scalar can cross. This entails imposing the following boundary conditions:

$$\begin{aligned} \boldsymbol{v}\cdot\boldsymbol{n} &= 0 \\ \boldsymbol{\nabla}c\cdot\boldsymbol{n} &= 0 \end{aligned} \tag{A.10}$$

Moreover, if the common assumption of incompressible flow is made: $\boldsymbol{\nabla}\cdot\boldsymbol{u} = 0$, then the balance equation can be written as:

$$\frac{\mathrm{d}}{\mathrm{d}t}|c|_{\mathrm{L}_1} + \left|\frac{c}{T}\right|_{\mathrm{L}_1} = \left|\frac{f}{T}\right|_{\mathrm{L}_1} \tag{A.11}$$

with

$$\forall t \in \mathbb{R}\,, \qquad |f|_{\mathrm{L}_1} : t \mapsto \int_\Omega |f(t,\boldsymbol{x})|\,\mathrm{d}\boldsymbol{x} \tag{A.12}$$

This denotes a hysteresis phenomenon of dynamic conservation where the integral quantities are not instantaneously conserved, but will converge to such a conservation property on a timescale of T.

More specifically, if T is a homogeneous field (constant in space), then this dynamic hysteresis conservation solves to:

$$\forall t \in \mathbb{R}\,, \qquad |c|_{\mathrm{L}_1}(t) = |c|_{\mathrm{L}_1}(0)\mathrm{e}^{-\int_0^{t}\frac{1}{T}} + \int_0^t |f|_{\mathrm{L}_1}(w)\frac{e^{-\int_w^{t}\frac{1}{T}}}{T(w)}\mathrm{d}w \tag{A.13}$$

if T is now also assumed constant in time, and if the scalar f is such as its mean over the volume is also invariant in time (i.e. $\forall t,\ |f|_{\mathrm{L}_1}(t) = |f|_{\mathrm{L}_1}(0) = |f|_{\mathrm{L}_1}^0$), then this dynamic conservation yields:

$$\forall t \in \mathbb{R}\,, \qquad |c|_{\mathrm{L}_1}(t) = |c|_{\mathrm{L}_1}(0)\mathrm{e}^{-\int_0^{t}\frac{1}{T}} + |f|_{\mathrm{L}_1}^0\left[1 - \mathrm{e}^{-\frac{t}{T}}\right] \tag{A.14}$$

From this hysteresis dynamic conservation equation, it can be seen that the mean of the diffusive transport average c converges towards the mean of the scalar field f from which it is drawn:

$$\lim_{t\to\infty}|c|_{\mathrm{L}_1}(t) = |f|_{\mathrm{L}_1}^0 \tag{A.15}$$

with a rate of convergence of T, i.e. for $t \gg T$.

Another way of looking at this simple example is to look at the relative difference of the means integrated over time:

$$\int_{T_{\text{in.}}}^{T_{\text{end}}} \frac{|f|_{\text{L}_1}^0 - |c|_{\text{L}_1}(t)}{|f|_{\text{L}_1}^0} \mathrm{d}t \;=\; T\left[\mathrm{e}^{-\frac{T_{\text{in.}}}{T}} - \mathrm{e}^{-\frac{T_{\text{end}}}{T}}\right] \tag{A.16}$$

This means that the smaller the latency time T, the smaller the relative difference integrated among time. Also, for $T_{\text{in.}} \gtrsim T$, this relative difference becomes close to zero, from which one can assume conservation of the mean to be achieved.

Let it be noticed that if the initial condition $c = f$ is chosen, then the mean is always conserved: $\forall t \in \mathbb{R},\ |c|_{\text{L}_1}(t) \;=\; |f|_{\text{L}_1}(0)$. This hints towards numerical acceleration conditions. This initial condition is used in the present thesis work.

MIMICKING THE SCALAR BOUNDARY CONDITIONS FOR A TRANSPORTED SCALAR f

All the above work has been done without taking into account the particularities of the transported scalar field f. However, the specific choice of mimicking the scalar boundary conditions enables the diffusive transport sfumato average to draw more properties from f. Let the mimicking boundary conditions be:

$$\begin{aligned} c|_{\partial\Omega} \quad &= \quad f|_{\partial\Omega} \\ c|_{\partial\Omega} \quad &= \quad f|_{\partial\Omega} \end{aligned} \tag{A.17}$$

Those boundary conditions are used in the present thesis work. The instantaneous balance equation thus becomes:

$$\forall t \in \mathbb{R}\,, \qquad \frac{\mathrm{d}}{\mathrm{d}t}\int_\Omega c - \int_\Omega \frac{f-c}{T} - c\boldsymbol{\nabla}\cdot\boldsymbol{v} \;=\; \int_{\partial\Omega} D\,\boldsymbol{\nabla} f\cdot\boldsymbol{n} - f\boldsymbol{u}\cdot\boldsymbol{n} \tag{A.18}$$

Let us now assume that f itself is being transported through an advecto-diffusive equation, with the same diffusion coefficient D, but without dampening:

$$\frac{\mathrm{D}f}{\mathrm{D}t} = \frac{f}{t} + \boldsymbol{u}\cdot\boldsymbol{\nabla} f = \mathcal{L}[f] = \boldsymbol{\nabla} D \boldsymbol{\nabla} f \tag{A.19}$$

Applying Green's theorem, still with the incompressibility condition $\boldsymbol{\nabla}\cdot\boldsymbol{u} = 0$, then yields the following conservation relation:

$$\frac{\mathrm{d}}{\mathrm{d}t}|c|_{\text{L}_1} + \left|\frac{c}{T}\right|_{\text{L}_1} \;=\; \frac{\mathrm{d}}{\mathrm{d}t}|f|_{\text{L}_1} + \left|\frac{f}{T}\right|_{\text{L}_1} \tag{A.20}$$

For a homogeneous T and an initial condition $|c|_{\text{L}_1}(0) = |f|_{\text{L}_1}(0)$, this equation entails conservation of the mean at all points in time, that is instantaneous average conservation property:

$$\forall t \in \mathbb{R}\,, \qquad |c|_{\text{L}_1}(t) = |f|_{\text{L}_1}(t) \tag{A.21}$$

In other words, the diffusive transport average can conserve the mean at all points in time for a source scalar f being purely transported and diffused, if the boundary conditions are chosen to be the mimicking ones and the initial mean is conserved, regardless of the distribution within the (here arbitrary) control volume.

Equivalence with averaging by means of a weighting function

Let us first re-cast the convective-diffusive transport problem to which $\langle f \rangle$ is the solution as follows:

$$\mathcal{T}[\langle f \rangle] = f \tag{A.22}$$

where the $\mathcal{T}$ operator is defined as:

$$\mathcal{T}:\begin{cases}\mathcal{F}[\mathbb{R}\times\mathbb{R}^d,\mathbb{R}] & \rightarrow & \mathcal{F}[\mathbb{R}\times\mathbb{R}^d,\mathbb{R}] \\ c & \mapsto & T\dfrac{\mathrm{D}c}{\mathrm{D}t}-T\boldsymbol{\nabla}\cdot D\boldsymbol{\nabla}c+c\end{cases} \tag{A.23}$$

The diffusive transport averaging is the result of inverting operator $\mathcal{T}$ into $\mathcal{A}$ with $\mathcal{T}\circ\mathcal{A}=1$, i.e.

$$\langle f\rangle=\mathcal{A}[f] \tag{A.24}$$

In order to solve for the equation $\mathcal{T}[c]=f$, we can resort to the Green's functions method.

Let $(t',\boldsymbol{s})\in\mathbb{R}\times\mathbb{R}^d$ be given, and $G(t,\boldsymbol{x},t',\boldsymbol{s})$ be the Green function, defined as the solution of:

$$\mathcal{T}[G](t,\boldsymbol{x},t',\boldsymbol{s})=\delta(t-t',\boldsymbol{x}-\boldsymbol{s}) \tag{A.25}$$

where δ is the Dirac distribution, which is the neutral element for the convolution product bilinear operation, defined as:

$$f*g:\begin{cases}\mathcal{F}[\mathbb{R}\times\mathbb{R}^d,\mathbb{R}]^2 & \rightarrow & \mathcal{F}[\mathbb{R}\times\mathbb{R}^d,\mathbb{R}] \\ (f,g) & \mapsto & f*g\end{cases} \tag{A.26}$$

with

$$\forall(t,\boldsymbol{x})\in\mathbb{R}\times\mathbb{R}^d, f*g(t,\boldsymbol{x})=\int_{t'\in\mathbb{R}}\int_{\boldsymbol{x}'\in\mathbb{R}^d} f(t',\boldsymbol{s})g(t-t',\boldsymbol{x}-\boldsymbol{s})\mathrm{d}\boldsymbol{s}\mathrm{d}t' \tag{A.27}$$

When solving for $\mathcal{T}[c]=f$, we can use the neutrality of δ with respect to the convolution product to write:

$$\mathcal{T}[c]=f=f*\delta=\int_{\mathbb{R}\times\mathbb{R}^d} f(t',\boldsymbol{s})\mathcal{T}[G](t,\boldsymbol{x},t',\boldsymbol{s})\mathrm{d}\boldsymbol{s}\mathrm{d}t' \tag{A.28}$$

assuming that the operator $\mathcal{T}$ commutes with the integral operation on $\mathbb{R}\times\mathbb{R}^d$, then:

$$\mathcal{T}[c]=\mathcal{T}\left[\int_{\mathbb{R}\times\mathbb{R}^d} f(t',\boldsymbol{s})G(t,\boldsymbol{x},t',\boldsymbol{s})\mathrm{d}\boldsymbol{s}\mathrm{d}t'\right] \tag{A.29}$$

and

$$c=\int_{\mathbb{R}\times\mathbb{R}^d} f(t',\boldsymbol{s})G(t,\boldsymbol{x},t',\boldsymbol{s})\mathrm{d}\boldsymbol{s}\mathrm{d}t' \tag{A.30}$$

is a solution of the problem $\mathcal{T}[c]=f$. It is noteworthy that this solution can be interpreted as an average where f is weighted by the Green function G.

Let us now analyze a heuristic case to illustrate what the Green function physically represents, showing this method to be an appropriate way of defining a local space-time average for our system.

A heuristic, analytically solvable case

Of particular interest is the case where the operator $\mathcal{T}$ is invariant by translation (in $\mathbb{R}\times\mathbb{R}^d$), because in such a case, the Green function also becomes invariant by translation,

$$G(t,\boldsymbol{x},t',\boldsymbol{s})=G(t-t',\boldsymbol{x}-\boldsymbol{s}) \tag{A.31}$$

in which case a solution u to the problem $\mathcal{T}[c]=f$ is given by the convolution product:

$$c=f\star G \tag{A.32}$$

In our case, the property of invariance by translation of $\mathcal{T}$ implies that $\boldsymbol{u}$, D and T are now constant fields in space and time. In this particularly simplified case, the Green function has a well-known analytical expression, derived in Section A.2.3:

$$G(-t,\boldsymbol{x}) = \frac{e^{-\frac{t}{T}}}{T}\mathcal{H}(t)\frac{1}{\sqrt{4\pi Dt}^{d}}\mathrm{e}^{-\frac{(x-vt)^2}{4Dt}} \tag{A.33}$$

This form has strong physical meaning: it is the transported heat kernel, which originates at the source before transport, multiplied by the decaying term of absorption. Thus, if we set $\langle f\rangle = c$, then $\langle f\rangle = f \star G$ indeed represents the average of f with the dampened advecto-diffusive kernel.

It is also noteworthy to mention that in the case of a convolution averaging, Guido Fubini's theorem yields:

$$\| g * f \|_{\mathrm{L}_1} = \| g \|_{\mathrm{L}_1} \cdot \| f \|_{\mathrm{L}_1} \tag{A.34}$$

From which, as long as $\| g \|_{\mathrm{L}_1} = 1$, the total quantity is conserved. In our simple heuristic analytical case, this property is verified.

Limit cases in the heuristic example

Let us examine the case of $d = 1$, and define $L_D = T^2 D$ and $L_{\boldsymbol{u}} = T\boldsymbol{u}$.

Then the following identities exist with the Dirac distribution, for $a \to 0$:

$$\begin{aligned} \delta_a(x) &= \frac{1}{a}\mathrm{e}^{-\frac{x}{a}}\mathcal{H}(t) \\ \delta_a(x) &= \frac{1}{a\sqrt{\pi}}\mathrm{e}^{-\left(\frac{x}{a}\right)^2} \end{aligned} \tag{A.35}$$

In our heuristic case for $d = 1$, the Green function can be expressed:

$$G(-t,\boldsymbol{x}) = \frac{1}{T}\mathrm{e}^{-\frac{t}{T}}\mathcal{H}\left(\frac{t}{T}\right)\frac{1}{2L_D\sqrt{\left(\frac{t}{T}\right)\sqrt{\pi}}}\mathrm{e}^{-\left(\frac{x-L_{\boldsymbol{u}}\left(\frac{t}{T}\right)}{2L_D\sqrt{\left(\frac{t}{T}\right)}}\right)} \tag{A.36}$$

The analysis of this expression exhibits the limiting cases for our averaging:

CASE: $L_D\sqrt{\left(\frac{t}{T}\right)} \to 0$:

$$G(-t,\boldsymbol{x}) = \frac{1}{T}\mathrm{e}^{-\frac{t}{T}}\mathcal{H}\left(\frac{t}{T}\right)\delta\left(\boldsymbol{x} - L_{\boldsymbol{u}}\left(\frac{t}{T}\right)\right) \tag{A.37}$$

Which is exactly the time averaging along the characteristic, as shown in (8.3).

CASE: $T \to 0$, with $D = \frac{L_D^2}{T} \in \mathbb{R}$ and $\boldsymbol{u} = \frac{L_{\boldsymbol{u}}}{T} \in \mathbb{R}^d$.

$$G(-t,\boldsymbol{x}) = \delta_T(t)\frac{1}{\sqrt{4\pi Dt}}\mathrm{e}^{-\frac{(x-\boldsymbol{u}t)^2}{4Dt}} \tag{A.38}$$

Here, we recognize the diffusion kernel with a transported source, times a Dirac distribution. In other terms, in this limiting case, the problem is purely convective-diffusive, with no absorption (i.e. damping).

In the further assumption that $L_D \ll L_{\boldsymbol{u}}$, this becomes the simple diffusion kernel, with no advection. That case can be seen as a form of space averaging corresponding to a spatial diffusion solution.

A.2.3 Derivation of Eq. (A.33) by Fourier transform

In order to find the weighting function g for the specific case analysed in the Green's function approach, we will use a Fourier transform approach.

Let us use the frequency convention for the Fourier transform:

$$\hat{f}(\nu, \boldsymbol{k}) = \int_{\mathbb{R}} \int_{\mathbb{R}^d} f\,(t, \boldsymbol{x}) e^{-\mathrm{i}2\pi(\nu t + \boldsymbol{x}\cdot\boldsymbol{k})} \mathrm{d}\boldsymbol{x}\mathrm{d}t \tag{A.39}$$

for which the inverse is:

$$f(t, \boldsymbol{x}) = \mathcal{TF}^{(-1)}\left[\hat{f}(\nu, \boldsymbol{k})\right] = \int_{\mathbb{R}} \int_{\mathbb{R}^d} \hat{f}\,(\nu, \boldsymbol{k}) e^{\mathrm{i}2\pi(\nu t + \boldsymbol{x}\cdot\boldsymbol{k})} \mathrm{d}\nu\mathrm{d}\boldsymbol{k} \tag{A.40}$$

and which abides by the two following important properties:

$$\widehat{f^{(n)}} = \left(\mathrm{i}2\pi(\nu + \boldsymbol{k}\,\cdot)\right)^n \hat{f} \tag{A.41}$$

and

$$\widehat{f * g} = \hat{f} \cdot \hat{g} \tag{A.42}$$

If we now assume that T is a constant parameter in both time and space, when shifting to Fourier space and using both the convolution and derivation property of the Fourier transform, this yields:

$$\mathrm{i}2\pi\nu\hat{f} \cdot \hat{g} + \left(\widehat{\boldsymbol{u}} * \mathrm{i}2\pi\boldsymbol{k} \cdot \hat{f}\right) \cdot \hat{g} = \left(\widehat{D} * (\mathrm{i}2\pi\boldsymbol{k})^2 \hat{f}\right) \cdot \hat{g} + \frac{1}{T}\left(\hat{f} - \hat{f} \cdot \hat{g}\right) \tag{A.43}$$

i.e.

$$\hat{g} = \frac{1}{1 + i2\pi\nu T + \frac{\left(\widehat{\boldsymbol{u}} * i2\pi T\boldsymbol{k}\cdot\hat{f}\right)}{\hat{f}} + \frac{\left(T\widehat{D} \star (2\pi\boldsymbol{k})^2 \hat{f}\right)}{\hat{f}}} \tag{A.44}$$

Let us now consider the case of constant diffusion coefficient D and velocity $\boldsymbol{u}$ fields, in both time and space. This entails that $\widehat{D} = D\delta$ and $\widehat{\boldsymbol{u}} = \boldsymbol{u}\delta$, where δ is the space-time Dirac distribution, which is the neutral element of the convolution operation.

In this case, the equation in Fourier space becomes:

$$\hat{g}(\nu, \boldsymbol{k}) = \frac{1}{1 + i2\pi T(\nu + \boldsymbol{k}\cdot\boldsymbol{u}) + TD(2\boldsymbol{k})^2} \tag{A.45}$$

So as to find the expression of the weighting function g, we now need to solve for the inverse Fourier transform:

$$g(t, \boldsymbol{x}) = \int_{\mathbb{R}} \int_{\mathbb{R}^d} \hat{g}\,(\nu, \boldsymbol{k}) e^{\mathrm{i}2\pi(\nu t + \boldsymbol{x}\cdot\boldsymbol{k})} \mathrm{d}\boldsymbol{k}\mathrm{d}\nu \tag{A.46}$$

Let us solve for g. Fubini's theorem enables us to write:

$$g(t, \boldsymbol{x}) = \int_{\mathbb{R}^d} \mathrm{d}\,\boldsymbol{k} e^{\mathrm{i}2\pi(\boldsymbol{x}\cdot\boldsymbol{k})} \int_{\mathbb{R}} \frac{e^{i2\pi\nu t}}{1 + i2\pi T(\nu + \boldsymbol{k}\cdot\boldsymbol{u}) + TD(2\pi\boldsymbol{k})^2} \mathrm{d}\nu \tag{A.47}$$

which we write:

$$g(t, \boldsymbol{x}) = \int_{\mathbb{R}^d} e^{\mathrm{i}2\pi(\boldsymbol{x}\cdot\boldsymbol{k})}\, A(t, \boldsymbol{k}) \mathrm{d}\boldsymbol{k} \tag{A.48}$$

with:

$$A(t,\boldsymbol{k}) = \frac{1}{T}\int_{\mathbb{R}} \frac{e^{i2\pi\nu t}}{a(\boldsymbol{k}) + i2\pi\nu}\,\mathrm{d}\nu \tag{A.49}$$

Where

$$a(\boldsymbol{k}) = \frac{1}{T} + \mathrm{i}2\pi(\boldsymbol{k}\cdot\boldsymbol{u}) + D(2\pi\boldsymbol{k})^2 \tag{A.50}$$

$A(t,\boldsymbol{k})$ represents a known Fourier transform:

$$A(t,\boldsymbol{k}) = \frac{1}{T}\mathrm{e}^{a(\boldsymbol{k})t}\mathcal{H}(-t) \tag{A.51}$$

From which we can further integrate

$$g(t,\boldsymbol{x}) = \int_{\mathbb{R}^d} e^{\mathrm{i}2\pi(\boldsymbol{x}\cdot\boldsymbol{k})}\frac{1}{T}\mathrm{e}^{a(\boldsymbol{k})t}\mathcal{H}(-t)\mathrm{d}\boldsymbol{k} \tag{A.52}$$

By replacing $a(\boldsymbol{k})$ in the latter expression and defining $\boldsymbol{\xi} = -(\boldsymbol{x} + \boldsymbol{u}t)$ one finds:

$$g(t,\boldsymbol{x}) = \frac{e^{\frac{t}{T}}}{T}\mathcal{H}(-t)B(\boldsymbol{\xi}) \tag{A.53}$$

Where

$$B(\boldsymbol{\xi}) = \int_{\mathbb{R}^d} \mathrm{e}^{-D(2\pi\boldsymbol{k})^2(-t)}\,\mathrm{e}^{-\mathrm{i}2\pi\boldsymbol{k}\cdot\boldsymbol{\xi}}\mathrm{d}\boldsymbol{k} \tag{A.54}$$

We notice that

$$B(\boldsymbol{\xi}) = \mathcal{TF}\left[\mathrm{e}^{-\alpha\boldsymbol{k}^2}\right] = \sqrt{\frac{\pi}{\alpha}}^d\,\mathrm{e}^{-\frac{(\pi\boldsymbol{\xi})^2}{\alpha}} \tag{A.55}$$

with

$$\alpha = 4\pi^2 D(-t) \tag{A.56}$$

i.e.

$$B(\boldsymbol{\xi}) = \frac{1}{\sqrt{4\pi D(-t)}^d}\,\mathrm{e}^{-\frac{\boldsymbol{\xi}^2}{4D(-t)}} \tag{A.57}$$

from which stems the final form:

$$g(t,\boldsymbol{x}) = \frac{e^{-\frac{(-t)}{T}}}{T}\mathcal{H}(-t)\frac{1}{\sqrt{4\pi D(-t)}^d}\,\mathrm{e}^{-\frac{(\boldsymbol{x}-\boldsymbol{u}(-t))^2}{4D(-t)}} \tag{A.58}$$

Let us note that this form is the exact Green function found above. Indeed, in the assumptions here used, the Green function yields a convolution product since the operator $\mathcal{T}$ is invariant by translation.

A.3 Tests of the STRUCT-T averaging operation in simple configurations

This section applies the differential operation in (8.5), used in the STRUCT-T approach, to demonstrate that, in a numerical solution, the field to be averaged is conserved by the averaging operation when using low time scales. The applications are made in a 2D rectangular domain with 2.5 m width and 1 m height and a constant velocity from left to right of 1 m/s.

In the first set of applications, the transported field f to be averaged has the shape of a cosine wave, as shown in Figure A.1 below. Three tests are made, all using the same averaging length scale L of 0.25 m, as shown in Table A.1 below. The time scale is reduced by one order of magnitude when moving from Test A to Test B and to Test C, as summarized in Table A.1. The same table shows that the deviation between the surface average of f and the surface average of $\bar{f}$, calculated in the whole 2D domain, is reduced when reducing the time scale T.

Table A.1 Details for Tests A, B, C

Variable	Test A	Test B	Test C
L	0.25 m	0.25 m	0.25 m
T	0.5 s	0.05 s	0.005 s
Deviation from average	5×10^{-5}	8×10^{-6}	6×10^{-6}

The fields for $\bar{f}$ resulting from Tests A, B, and C, are shown in Figure A.1 below. We can notice that those results converge to a stable result, demonstrating the low sensitivity of the averaging operation to values of T being low compared to the time scales of the physical phenomenon.

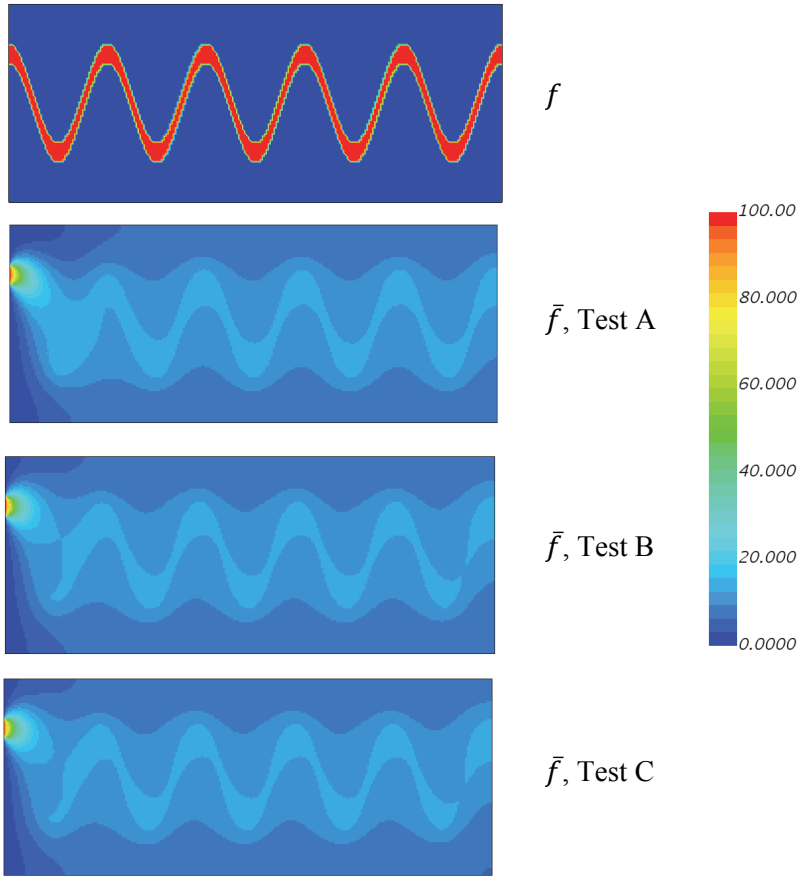

Figure A.1 Instantaneous and averaged fields for Tests A, B, C

Three additional tests are made in which the transported field f has a checkerboard pattern, as shown in Figure A.2 below. The length and time scales for the three tests D, E, and F are the same ones used for A, B, and C, as shown in Table A.2.

Results in Table A.2 confirm the observation that lower time scales T lead to greater conservation of the field to be averaged.

Table A.2 Variables for the test

Variable	Test D	Test E	Test F
L	0.25 m	0.25 m	0.25 m
T	0.5 s	0.05 s	0.005 s
Deviation from average	6×10^{-3}	1×10^{-4}	8×10^{-5}

The averaged fields are shown in Figure A.2 below, where the sensitivity of results to variations of the time scales around low values appears to be very small.

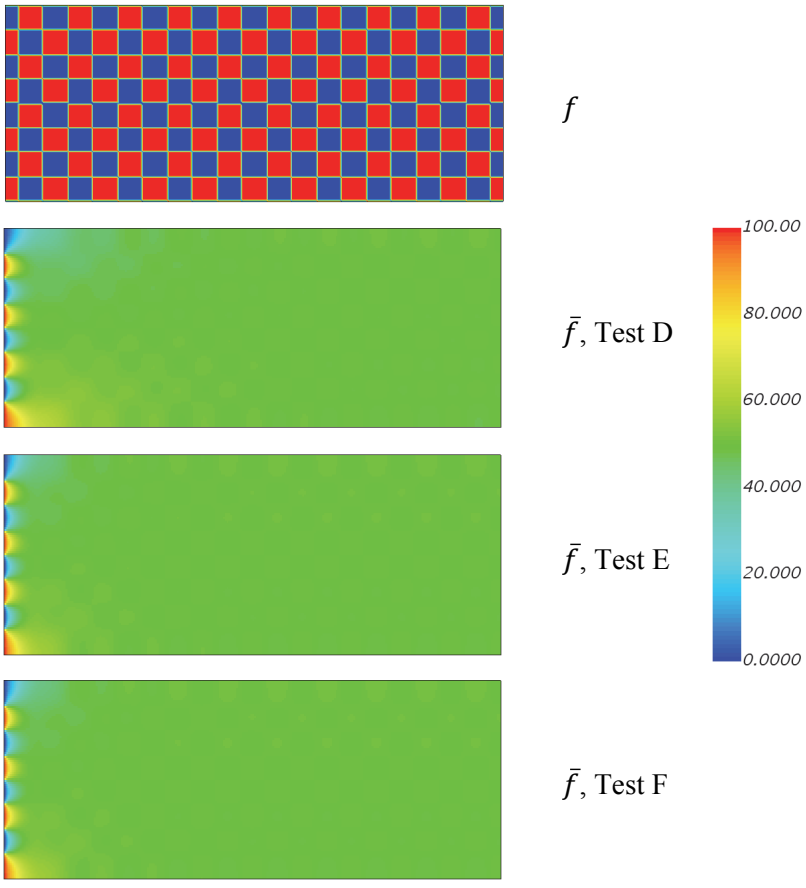

Figure A.2 Instantaneous and averaged function for Tests D, E, F

Appendix B: Applications of the STRUCT models

The main focus of this work has been on the development and assessment of the STRUCT modeling strategy and its complete model formulation. Therefore, the testing has been performed on simple flow cases which allow to evaluate specific challenges of the models, and are particularly demanding. The application of the STRUCT approach to more complex and realistic flows has been performed in collaborative work driven by colleagues at MIT and is useful to evidence the current status of the model applicability. This appendix shows the results of collaborations with Michael J. Acton, Davide Concu, and Jingyong Zhang. The sections below present selected results while complete details can be found in manuscripts published or in preparation for submission.

The first three sections, B.1, B.2, and B.3, show results obtained using the commercial STAR-CCM+ solver, while the latter two sections, B.4, and B.5, present results obtained using the open-source OpenFOAM solver.

B.1 Triple-jet test case

Acton, Lenci, and Baglietto (2015) applied the controlled STRUCT approach to a triple-jet mixing flow test case. This test case represents the oscillatory mixing of non-isothermal flow streams and is useful to detect a potential cause of material damage due to thermal fatigue. For this type of flows, URANS models do not provide the desired level of physical description of the mixing phenomena. On the other hand, the high physical description of LES is related to high computational cost, practically unfeasible for many industrial applications.

An instantaneous qualitative picture of resolved temperature profiles resulting from different simulations is shown in Figure B.1. The figure shows the geometry of this test case, characterized by flow injection from three channels at different temperatures. The figure also compares the qualitative behavior of different turbulence models and shows a photo from the experiment (Tokuhiro and Kimura, 1999). The STRUCT approach appears to provide resolved structures similar to those deriving from LES using a computational grid 64 times smaller, with a base size of 4 mm instead of 1 mm.

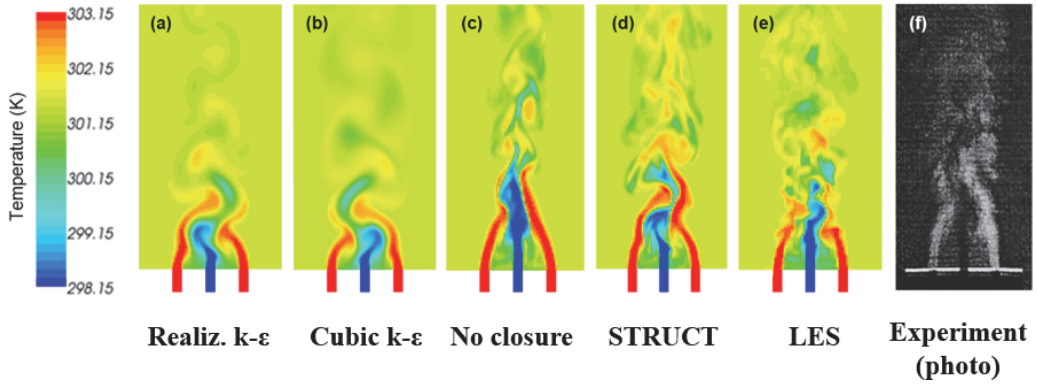

Figure B.1 Triple-jet qualitative results, from Acton, Lenci, and Baglietto (2015). The photo from the experiment was originally published by Tokuhiro and Kimura (1999).

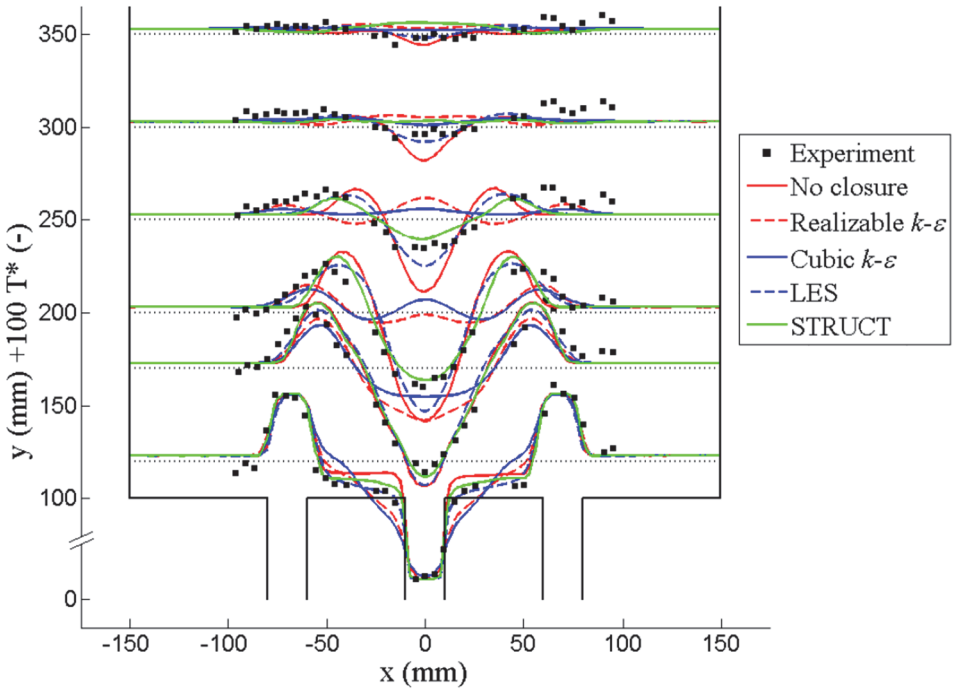

Figure B.2 Time-averaged temperature profiles, from Acton, Lenci and Baglietto (2015)

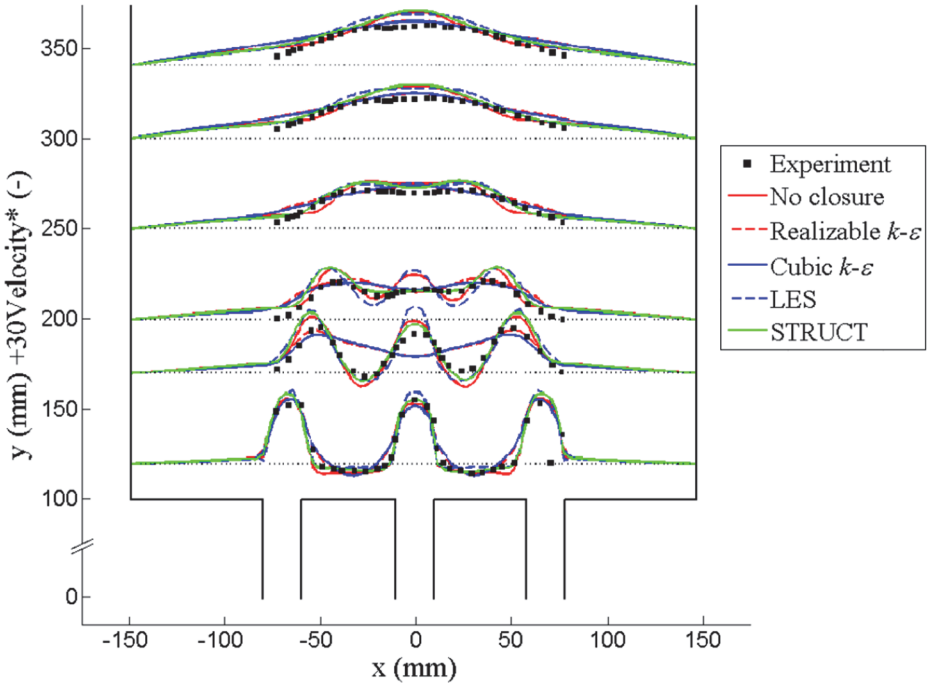

Figure B.3 Time-averaged velocity profiles, from Acton, Lenci and Baglietto (2015)

Profiles of temperature and velocity are shown in Figures B.2 and B.3, comparing results from different turbulence models to experimental data. STRUCT results appear to be in close agreement with experimental data, unlike URANS results.

Observations from results of this work have shown that LES results on the coarser URANS-like grid and results obtained with no closure (i.e. quasi-DNS) also produce profiles in close agreement with the experimental data. However, those two approaches fail in predicting the frequency of temperature fluctuations at the monitor point shown in Figure B.4. On the other hand, both LES run on the fine grid and STRUCT run on the coarse grid provide a close description of this frequency, as shown in the same figure.

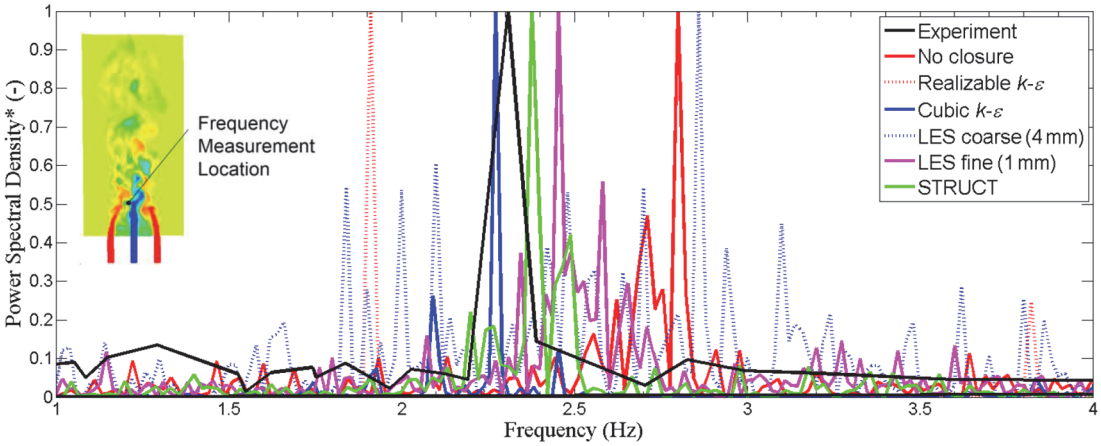

Figure B.4 Temperature fluctuation frequency, from Acton, Lenci, and Baglietto (2015)

B.2 Pressurized water reactor spacer grid analysis

A spacer grid of a pressurized water nuclear reactor was analyzed in a collaborative work conducted by Acton, Demarly, Lenci, Magolan, and Baglietto (2016). The objective of the work was to investigate the grid-to-rod fretting (GTRF) phenomenon, which can be a cause of nuclear fuel cladding failure. The spacer grid analyzed is a characteristic configuration adapted from the literature. Details of the mixing vanes are shown in Figure B.6 below.

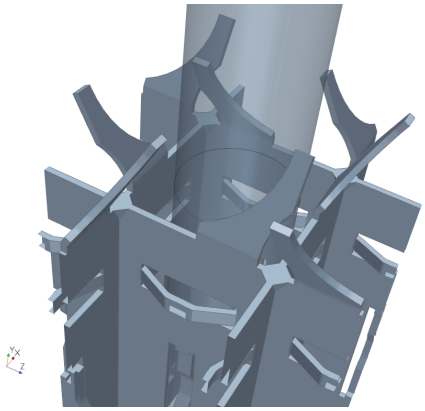

Figure B.5 Spacer grid geometry, from Acton et al. (2016)

The fuel rod downstream the spacer grid was divided into segments of 24.5 mm (1 inch) following the same approach adopted by Elmahdi et al. (2011). Forces acting on the surface of those segments have been monitored in the two main directions, x and z. The forces deriving from LES results have shown to be comparable to the experimental ones reported by Elmahdi et al. (2011), although the spacer grid is different. The figures below show results from simulations run with LES, STRUCT, and the cubic NLEVM by Baglietto and Ninokata (2006). Those results have been run on two grids: a fine LES-suitable one with 40 million cells and a URANS-suitable one with 3.25 million cells.

Due to the similarity with results by Elmahdi et al. (2011), fine-grid LES results are taken as a reference while coarse-grid LES does not provide similar profiles. On the other hand, STRUCT results provide consistent results similar to the reference ones for both grids. URANS results predict very low forces, almost negligible compared to the reference.

Figure B.6 Spacer grid results, from Acton et al. (2016)

B.3 Flow around a simplified car

The use of CFD is very important in the automotive industry. The main parameter of interest is drag, because of its consequences on fuel consumption. However, other variables are also important, such as those affecting noise and vibration, structural integrity of components, lift, and performance under heavy wind. A test case representing flow around a 3D simplified car has been designed by Ahmed, Ramm, and Faltin (1984). The simplified car is a volume with rounded corners in the front and a slant in the upper back. Experimental acquisitions obtained using LDV and hot-wire anemometry (HWA) have been published by Lienhart and Becker (2003).

STRUCT applications on this test case have been performed by the author of this thesis and have benefited from discussions with the visiting student Davide Concu (2016).

Ahmed body simulations have been run on computational grids with 13.4 million cells. Effects of the STRUCT activation on resolved flow structures can be observed in Figure B.7. We can notice that the hybrid activation produces more complex resolved flow structures in that figure.

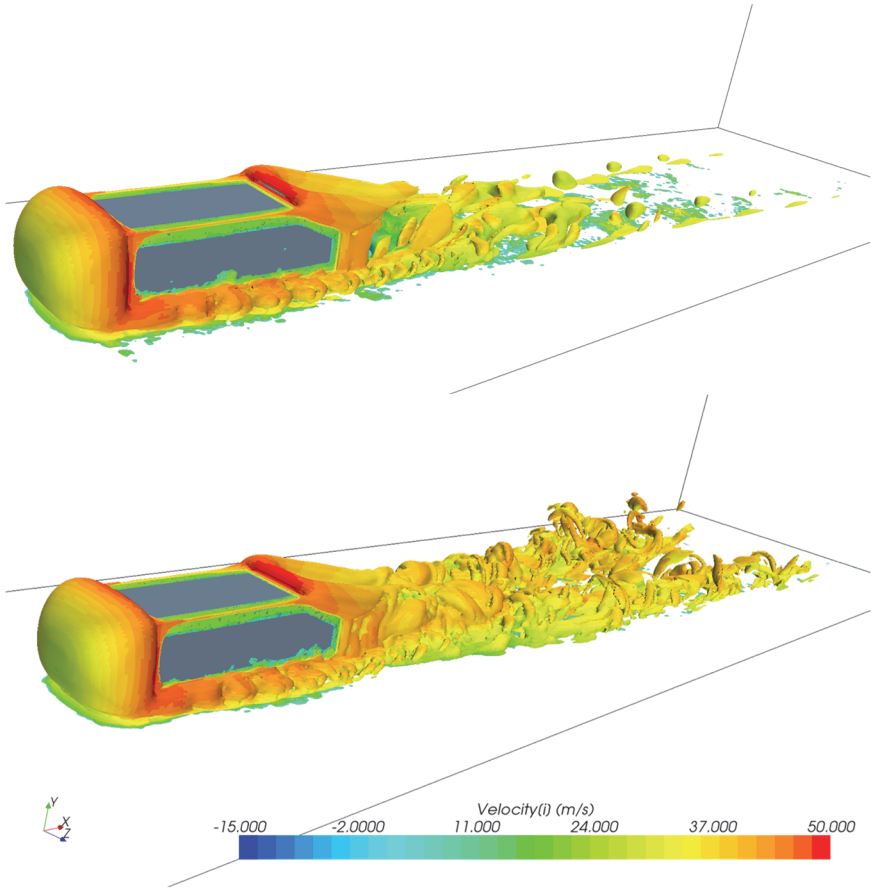

Figure B.7 Iso-Q surfaces colored by velocity for URANS (top) and STRUCT-L (bottom)

The activation regions deriving from application of the complete STRUCT-L and STRUCT-T approaches are shown in Figure B.8. Those regions are located immediately upstream the body and in a longer region downstream. The activation regions deriving from STRUCT-L appear to be longer than the STRUCT-T ones.

Figure B.8 Activation regions for STRUCT-L (top) and STRUCT-T (bottom)

The Ahmed body is a flow case in which URANS models are known to achieve accurate results. Therefore, it is interesting to investigate whether the activation of the STRUCT approach would compromise those results, improve them, or keep them similar. Velocity profiles at the body's symmetry plane for the 35° slant angle are shown in Figure B.9 below. From that figure, we can observe that the introduction of the STRUCT-L and STRUCT-T approaches produces similar results to the baseline NLEVM URANS.

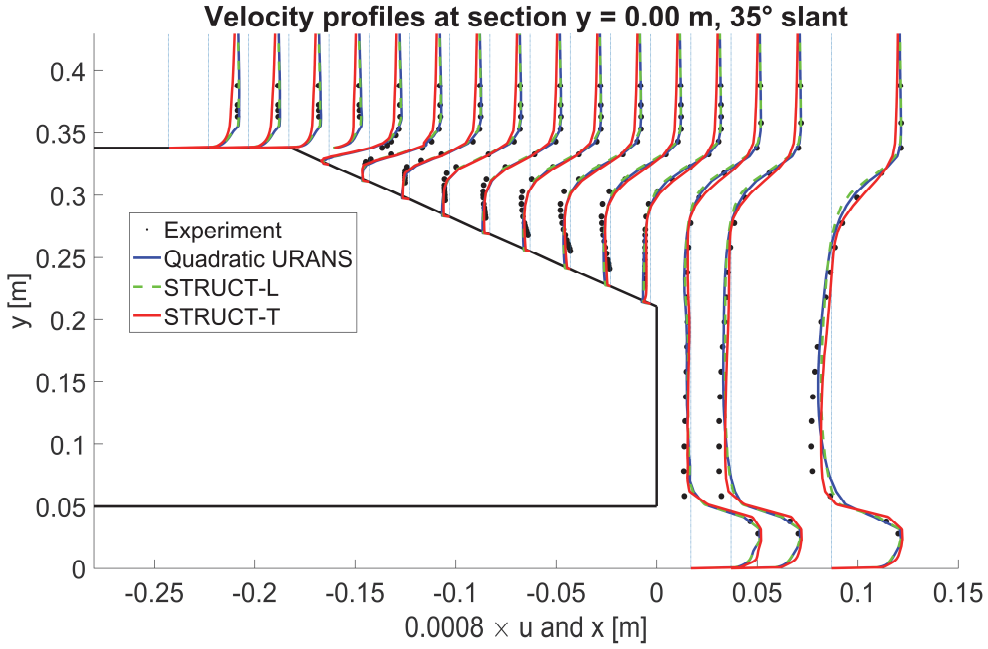

Figure B.9 STRUCT-T activation regions

Simulations in the 25° slant angle configuration are challenging for hybrid models since they do not involve strong separation as for the 35° slant angle. Velocity profiles in Figure B.10 below show that STRUCT-L results are similar to those from the baseline URANS, as observed for the 35° slant angle case. On the other hand, the STRUCT-T approach produces results closer to experimental data above the slant, where a mild recirculation is described correctly. Downstream the slant, the STRUCT-T model produces an underestimate of velocity profiles.

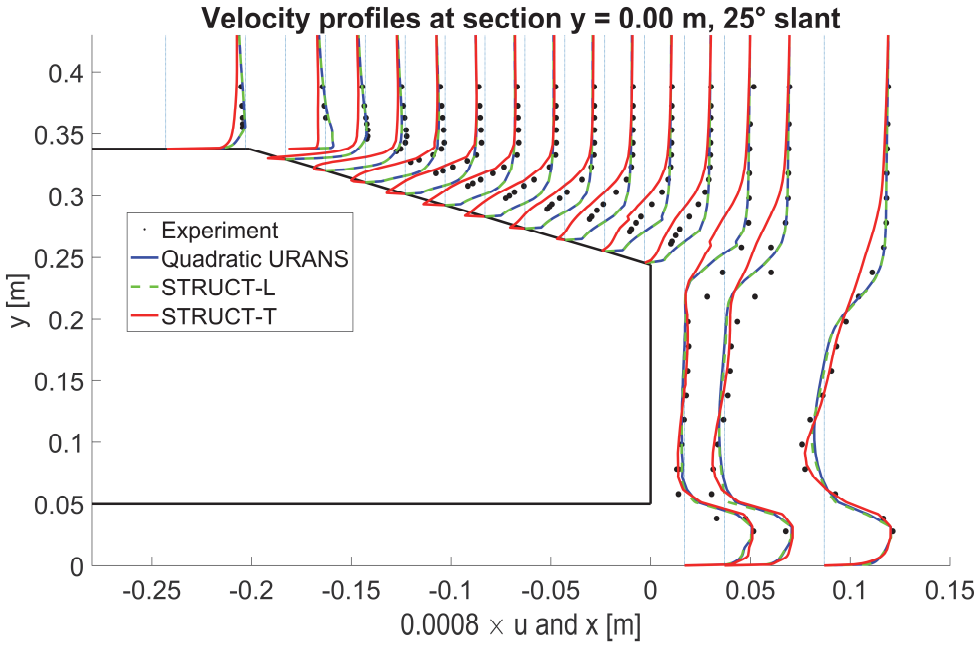

Figure B.10 Velocity profiles for the 25° and 35° slant angles

B.4 Swirl combustor OpenFOAM implementation

The STRUCT approach has been tested in OpenFOAM by the colleague Jingyong Zhang (2016). She has applied the model to a swirl combustor in cold flow simulations. This application has been largely used for validation in previous studies (Kewlani, 2014; Taamallah et al., 2014). The computational grid used was kindly provided by Gaurav Kewlani (2015), a colleague at MIT. The surface representation of this grid is shown below. The grid has a total of 2.1 million cells.

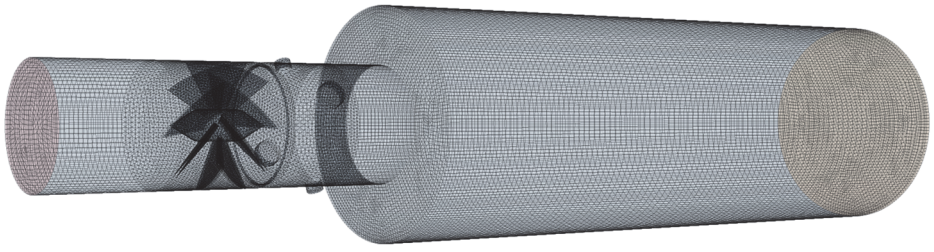

Figure B.11 Swirl combustor geometry and surface grid as provided by Kewlani (2015)

An instantaneous picture of activation regions for the controlled STRUCT approach is shown in Figure B.2 below. The activation regions correspond to those where the strongest flow deformation is expected, i.e. downstream the swirler and the sudden expansion.

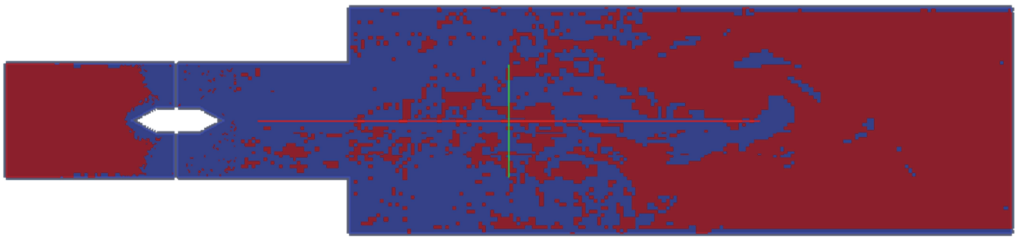

Figure B.12 Swirl combustor, STRUCT activation regions, from Zhang (2016)

Time-averaged profiles for velocity and TKE are shown in Figures B.13 and B.14 below. Those results show that simulation results get closer to experimental data when switching from linear to quadratic to cubic URANS. Enabling the controlled STRUCT approach on top of the cubic URANS produces results that are slightly closer to the experiment.

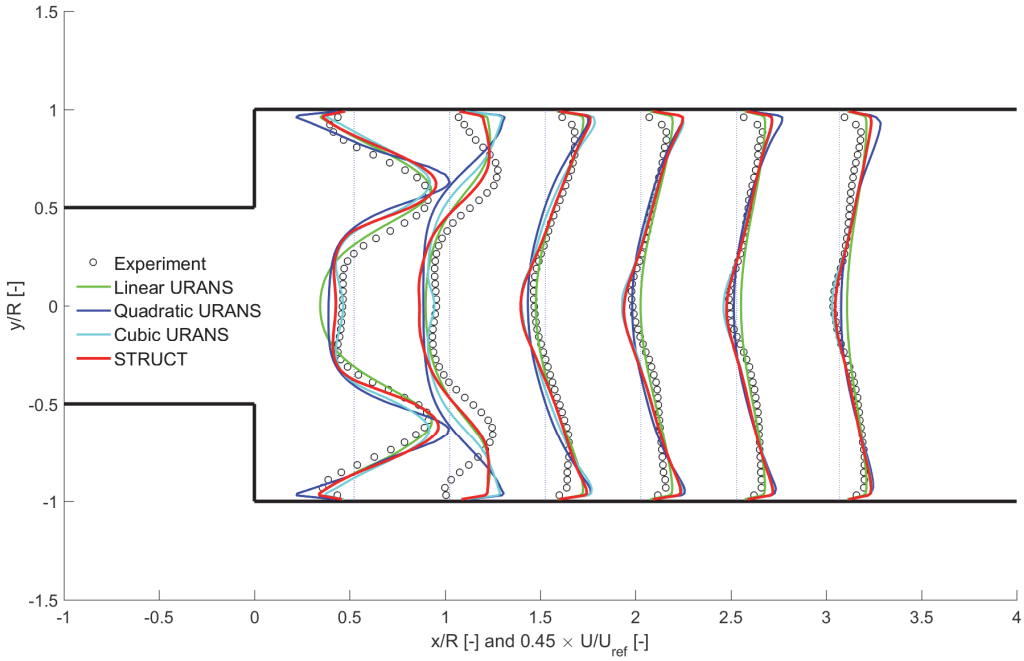

Figure B.13 Swirl combustor, velocity profile, from Zhang (2016)

In particular, TKE Profiles shown in Figure B.14 below show a progressive reduction in the overestimate of TKE immediately downstream the expansion, when changing from linear URANS to quadratic and cubic URANS, and finally to the controlled STRUCT approach. This result demonstrates the capability of STRUCT of reducing an undesired effect of the baseline URANS.

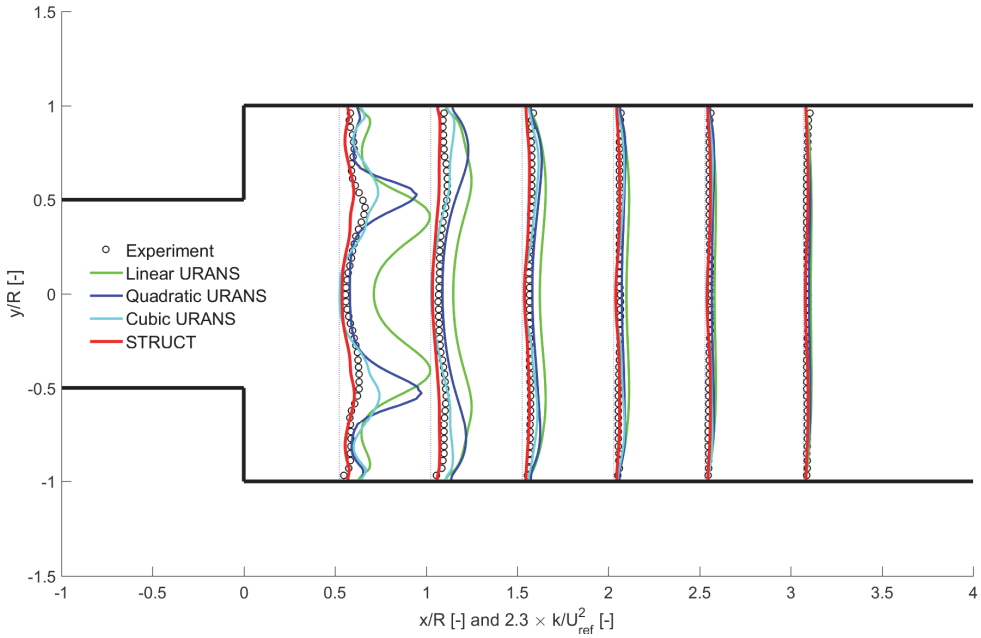

Figure B.14 Swirl combustor, TKE profiles, from Zhang (2016)

B.5 Flow through an asymmetric diffuser OpenFOAM implementation

The colleague Jingyong Zhang (2016) has performed tests of the asymmetric diffuser flow using the OpenFOAM implementation of the controlled STRUCT approach. Those simulations have repeated the tests shown in Section 0, on the same grid with 1.795 million cells and same conditions.

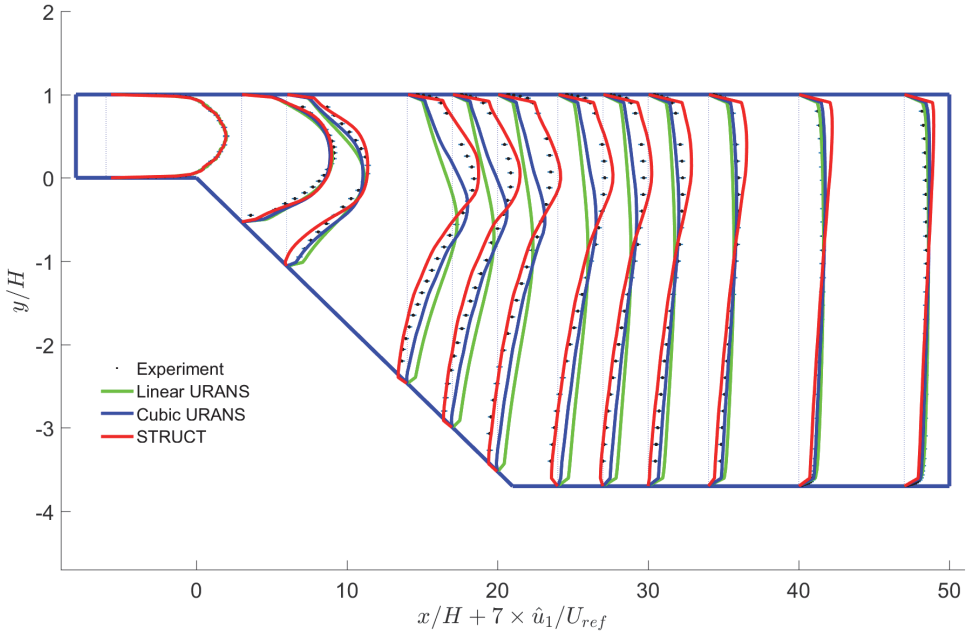

Figure B.15 Asymmetric diffuser, velocity profiles, from Zhang (2016)

Velocity results are shown in Figure B.15 above. Those results are very close to the ones obtained from STAR-CCM+ and shown in Figure 6.47. This result supports the independence of the controlled STRUCT model from the code used.

The STRUCT activation regions obtained are shown in Figure B.16 below. Those regions are very similar to those in Figure 6.43, which have been obtained using STAR-CCM+.

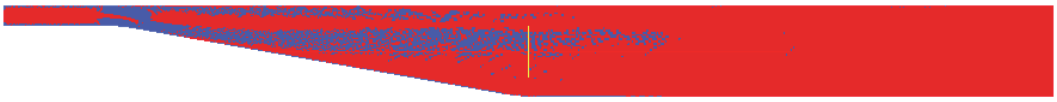

Figure B.16 Asymmetric diffuser, STRUCT activation regions in blue, from Zhang (2016)

Appendix C: Historical highlights

This appendix covers selected historical highlights to characterize the evolution over time of the concepts discussed in this thesis. Steps in such an evolution have typically been initiated by breakthroughs in math, physics, and computer science. It is interesting to notice how so many of the most prominent mathematicians and physicists of all time have contributed to fluid mechanics.

C.1 From ancient civilizations to PDEs

Ancient civilizations demonstrated skills in building devices operating with fluids. Examples are irrigation systems, ships, arrows, aqueducts. Basic principles of fluid statics, including buoyancy, have been formulated by Archimedes (287-212 BC). The complexity of turbulent flows has been represented graphically by Leonardo da Vinci (1452-1519).

Isaac Newton (1687) laid the foundation of classical mechanics introducing the laws of motion. Moreover, he described viscous forces by observing a proportionality law between the shear stress of adjacent fluid layers and the velocity gradient normal to those layers.

During the 18th century, notable scientists studied inviscid fluids, including Jean le Rond D'Alembert, Daniel Bernoulli, Leonhard Euler, Joseph-Louis Lagrange, and Pierre-Simon Laplace. Among them, Euler (1757) published a significant work containing the equations of motion of inviscid fluids. Assuming continuous 3D velocity and pressure fields, Euler applied Newton's second law to infinitesimal fluid elements. This lead to a system of four governing equations: three for momentum and one for mass conservation. The Euler equations have been a breakthrough in fluid mechanics, but also a big challenge for mathematicians and engineers. They were among the first PDEs that have been ever proposed. Nevertheless, they neglected the effects of viscous forces.

Euler's equations for momentum are:

$$\frac{\partial \rho u_i}{\partial t} + \frac{\partial \rho u_i u_j}{\partial x_j} = -\frac{\partial p}{\partial x_i} + F_i \tag{C.1}$$

Euler's mass conservation equation is:

$$\frac{\partial \rho}{\partial t} + \frac{\partial \left(\rho u_j\right)}{\partial x_j} = 0 \tag{C.2}$$

The inviscid equations were very innovative considering the time when they were derived. After many decades of study, the viscous term was added, with the development of the so-called Navier-Stokes equations. The equations have been proposed by the engineer Claude-Louis Navier (1822) for incompressible fluids. Greater theoretical understanding and generalization of the equations was achieved by George Stokes (1845). Deviatory internal stresses in the fluid are described by a viscous term added to the RHS of the momentum equation in (C.1). Those equations have not changed since then and are considered the pillars of fluid mechanics.

C.2 Hydraulics

As introduced in Section 1.2, during the 19th century the equations of fluid motion in their PDE form were not directly usable in engineering applications, including three-dimensional problems. This

motivated the rise and development of the field of hydraulics. Such a field is outside the scope of this work. Let us just recall notable names of contributors to the field: Antoine de Chézy, William and Robert Froude, Gotthilf Heinrich Ludwig Hagen, Lord Kelvin, Lord Rayleigh.

C.3 Turbulence analysis and models

Laminar flow in a straight pipe has a parabolic distribution of axial velocity with wall distance while the other components of velocity are zero. This stable configuration is subject to perturbations due to non-ideal conditions, such as wall imperfections, inlet conditions, vibrations. At low flow velocity, perturbations are dissipated by viscosity. When velocity is increased, inertial forces dominate over viscous forces, generating instability. The flow becomes turbulent.

Attempts to describe turbulence were made by Boussinesq (1877). He treated the momentum transfer caused by eddies by assuming that proportionality exists between turbulent stresses and mean rate of strain. He thus introduced the eddy viscosity, ν_t, thereby analyzing turbulent flows as laminar flows with larger viscosity. This representation treats the effect of eddies in a statistical way, using the same formula that applies to the effect of molecular interactions. For a simple shear flow, turbulent shear stress is:

$$\tau_{12} = \nu_t \frac{\partial U_1}{\partial x_2} \tag{C.4}$$

The transition from laminar to turbulent flow has been studied by Osbourne Reynolds (1883). He observed that streamlines in a pipe transition from direct to sinuous when velocity increases. He identified a dimensionless parameter describing such a transition: the ratio between inertial and viscous forces. Such a parameter was later called Reynolds number (Re).

$$\mathrm{Re} = \frac{\rho u D}{\mu} \tag{C.5}$$

By the end of the nineteenth century, scientists agreed that the Navier-Stokes equations describe laminar flows. However, the applicability of those equations to turbulence was not yet demonstrated. A numerical solution of turbulence would have required computational resources not accessible at that time. The applicability of the Navier-Stokes equations to turbulent flows was shown by Osbourne Reynolds (1895). In his work, he treated the equations statistically and was able to describe averaged turbulent profiles.

These results made it clear that turbulence is a mathematical phenomenon, direct consequence of the Navier-Stokes equations. Since inertial terms are nonlinear, the interaction between those two terms is very complex and produces instabilities (Tennekes and Lumley, 1981) generating turbulence.

Prandtl has made significant advances that allowed for the practical use of the Reynolds-averaged equations with multiple publications spanning about four decades. He first discovered that in fluid motion friction plays an important role only very close to the wall, in the so-called boundary layer (Prandtl, 1904). In a wall-bounded flow, we can distinguish a boundary layer, dominated by viscous effects, and a region in which viscosity can be neglected.

Extensive experimental and theoretical work has provided evidence that boundary layers in simple flows behave according to simple laws.

The near-wall region is usually considered in the literature as divided into three parts: the viscous sublayer, the buffer layer, and the log-law region. Those regions are defined through the dimensionless wall distance:

$$y^+ = \frac{y u_\tau}{\nu} \tag{C.6}$$

The shear velocity is defined based on the wall shear stress and density as:

$$u_\tau = \sqrt{\frac{\tau_w}{\rho}} \tag{C.7}$$

The dimensionless velocity is:

$$u^+ = \frac{u}{u_\tau} \tag{C.8}$$

For simple flows:

- The viscous sublayer is observed for $y^+ < 5$. In such a range, $u^+ \approx y^+$.
- The buffer layer is observed for $5 < y^+ < 30$. Such a region is called "buffer" because it transitions between the behaviors of the two neighboring layers.
- The log-law region was observed by von Kármán (1930) near the wall. In such a range, velocity is proportional to the logarithm of wall distance:

$$u^+ = \frac{1}{\kappa}\ln(y^+) + C \tag{C.9}$$

where κ is the von Kármán constant, which based on observations is commonly taken as 0.41. Further discussion on wall function and a review of selected formulations can be found in the work by Craft and co-workers (2006).

Taylor (1920) and Prandtl (1925) independently introduced the concept of a mixing length, which is similar to mean free path in the kinetic gas theory. Prandtl thus developed a closure for determining the eddy viscosity in a boundary layer.

The momentum integral theory for flat boundary layers was developed by von Kármán (1921). Richardson (1922) described the energy cascade of turbulence, by applying dimensional analysis to the Navier-Stokes equations. Taylor (1935) introduced a statistical theory for homogeneous isotropic turbulence.

A mathematical study of the local structure of homogeneous isotropic turbulence at very high Reynolds number was made by Kolmogorov (1941), who introduced a formulation for the smallest time and length scales. He also proposed (Kolmogorov, 1942) for the first time a complete model in which transport equations are used to compute local properties of turbulence. It is interesting to notice that in his model three transport equations are used.

Independently from Kolmogorov, Prandtl introduced a complete turbulence model with one transport equation (Prandtl, 1945).

Meanwhile, several authors provided contributions to more effective prediction of turbulent flows in engineering applications. Among those are: Blasius, Tollmien, Nikuradse, Colebrook, White, Clausier, Klebanoff, Coles.

A statistical theory for nonhomogeneous turbulence, involving transport equations for all the exact Reynolds stress components, was formulated by Rotta (1951).

Significant discussion was made by Evans and Harlow (1957) on the particle-in-cell method for finite difference numerical solutions of the Navier-Stokes equations.

Starting from the late '60s, CFD calculations have been made possible in civilian applications by the availability of the first suitable computers. After that, the availability of computational resources has grown exponentially in the following half century, following Moore's law.

An important conference, held at Stanford University, took place in 1968. The conference was titled "computing the turbulent boundary layer". At that time, a large variety of incomplete turbulence models was available, requiring prior knowledge of flow properties. The importance of developing complete models was highlighted.

Subsequently, several well-known closures involving transport equations have been formulated. Among those: the standard k-ε (Jones and Launder, 1972), the k-ω of Wilcox (1988), the Spalart-Allmaras (S-A) model (Spalart and Allmaras, 1992). For more details, see Section 2.3.5.

Significant advancements have been made with the introduction of the CFD solution procedure proposed by Patankar and Spalding (1972).

The fundamentals of Reynolds stress models (RSMs) were developed thanks to the contributions of several authors, especially in the late '60s and early '70s. A unified RSM model was proposed by Launder, Recce, and Rodi (1975).

Meanwhile, methods have been proposed that simplify RSMs aiming at achieving new closures simpler to implement and run. Particularly important are nonlinear eddy-viscosity models as proposed by Pope (1975), and algebraic stress models, as proposed by Rodi (1976).

LES methods were introduced by the pioneering work of Smagorinsky (1963). However, the limited computation capability of those times did not allow for 3D solutions. The early uses of LES, including the one of Smagorinsky, were done by meteorologists to predict atmospheric flows. Studies in that field were typically in 2D, and the vertical velocity component was often neglected. A first 3D application to an engineering case was made by Deardorff (1970), simulating a high-Re channel. The filtering concept has been studied and generalized by Leonard (1974). The computational tools of those times only allowed for model applications in very simple flows. Only starting from the late 1980s the availability of faster computers opened the way to a wide development of LES for complex flows. Several authors have improved the theoretical understanding and formulations of LES. Let us just cite the dynamic model by Germano (1991) and its approximation without test filtering, proposed by Chester, Charlette, and Meneveau (2001).

During the late '70s, significant focus was dedicated to the analysis of coherent structures. This effort has brought to significant studies in turbulence topology (Hussain, 1983). However, this concept was not used extensively in turbulence modeling. Substantial exceptions exist (Kobayashi, 2005).

The concept of hybrid turbulence modeling has emerged in the mid-1990s and has evolved quickly. Among a large number of models, let us just mention: the very large-eddy-simulation (VLES) by Speziale (1996), the detached-eddy simulation (DES) introduced by Spalart and co-workers (1997), the partially averaged Navier-Stokes (PANS) by Girimaji and co-workers (2003), and the scale-adaptive simulation (SAS) by Menter and co-workers (2003). Among other important hybrid turbulence models, let us cite limited numerical scales (LNS) (Batten et al., 2000), partially integrated transport model (PITM) (Chaouat and Schiestel, 2013), partially resolved numerical simulation (PRNS) (Shih and Liu, 2008), organized-eddy simulation (OES) (Bourguet et al., 2008), temporal partially integrated transport model (TPITM) (Fadai-Ghotbi et al., 2010b).

Appendix D: STRUCT equations as used here

D.1 Controlled STRUCT

$$r = \begin{cases} 1 & , \quad h \leq 1 \\ \phi & , \quad h > 1 \end{cases} \tag{D.1}$$

$$h \equiv \frac{f_\mathrm{r}}{f_\mathrm{m}} = t_\mathrm{m} f_\mathrm{r} \tag{D.2}$$

$$f_\mathrm{r} \equiv \sqrt{|\bar{I}\bar{I}|} \tag{D.3}$$

$$\frac{1}{f_\mathrm{m}} = t_\mathrm{m} \equiv \langle t_{\mathrm{m},0} \rangle \tag{D.4}$$

$$t_{\mathrm{m},0} = \frac{k_\mathrm{m}}{\varepsilon} \tag{D.5}$$

$$\nu_t = C_\mu \frac{k_\mathrm{m}^2}{\varepsilon} r \tag{D.6}$$

where (D.4) is evaluated by averaging preliminary URANS results and ϕ is optimized a posteriori.

D.2 STRUCT-L

Relations (D.1), (D.2), (D.3), (D.5), (D.6), and:

$$t_\mathrm{m} \approx \exp\left(\ln t_{\mathrm{m},0} + \min\left(\max\left(\frac{R^2}{10}\boldsymbol{\nabla}^2\left(\ln t_{\mathrm{m},0}\right)\right), -\ln(2)\right), \ln(2)\right) \tag{D.7}$$

$$R = C_R \frac{k_\mathrm{m}^{3/2}}{\varepsilon} \tag{D.8}$$

where $C_R = 2$ and $\phi = 0.6$.

D.3 STRUCT-T

Relations (D.2), (D.3), (D.5), (D.6), and:

$$r = \min\left(\frac{1}{\alpha h}, 1\right) \tag{D.9}$$

$$\frac{\mathrm{d}t_\mathrm{m}}{\mathrm{d}t} + \boldsymbol{u} \cdot \boldsymbol{\nabla} t_\mathrm{m} = \frac{L^2}{T}\boldsymbol{\nabla}^2 t_\mathrm{m} + s \tag{D.10}$$

$$s = \min\left(\max\left(\frac{1}{T}\left(t_{\mathrm{m},0} - t_\mathrm{m}\right), -\frac{2t_\mathrm{m}}{\Delta_t}\right), \frac{2t_\mathrm{m}}{\Delta_t}\right) \tag{D.11}$$

$$L = \sqrt{C}\frac{k^{3/2}}{\varepsilon} \tag{D.12}$$

$$T = \frac{1}{\beta}\frac{k}{\varepsilon} \tag{D.13}$$

where $\alpha = 1.35$, $\beta = 0.01$, $C = 0.09$, and the relation $t_\mathrm{m} = t_{\mathrm{m},0}$ is used as initial and boundary condition for solving (D.9).